

# Atomic Level Insights of Non-Noble Metal Catalysts for the Oxygen Evolution Reaction

Présentée le 29 janvier 2021

Faculté des sciences de base  
Laboratoire de synthèse et de catalyse inorganique  
Programme doctoral en chimie et génie chimique

pour l'obtention du grade de Docteur ès Sciences

par

**Lichen BAI**

Acceptée sur proposition du jury

Prof. K. Sivula, président du jury  
Prof. X. Hu, directeur de thèse  
Prof. P. Strasser, rapporteur  
Prof. J. Lloret, rapporteur  
Prof. R. Buonsanti, rapporteuse

---

*Tutte le verità sono facili da capire una volta che sono state rivelate. Il difficile è scoprirle.*

All truths are easy to understand once they are revealed. The difficult thing is to discover them.

*—Galileo Galilei*

---



# Acknowledgements

First of all, I would like to sincerely thank my advisor, Professor Xile Hu, who is the director of the Laboratory of Inorganic Synthesis and Catalysis (LSCI), for offering me the opportunity to conduct research in his group. I am grateful for the frontier research projects he provided me. He taught me how to do the in-depth scientific research in the field of electrocatalysis. His guidance and advice were extremely valuable for me to accomplish my doctoral thesis.

I would also thank the jury president, Prof. Kevin Sivula (EPFL); and the jury members, Prof. Raffaella Buonsanti (EPFL), Prof. Peter Strasser (Technische Universität Berlin, Germany), and Prof. Julio Lloret-Fillol (Institut Català d'Investigació Química, ICIQ, Spain) for reviewing and evaluating the research work in this Thesis. I would greatly thank their valuable comments and suggestions to improve the quality of the Thesis.

Then, I would like to acknowledge all the present and previous members of the LSCI with whom I have worked and spent time. I would like to especially thank Dr. Seunghwa Lee for the collaboration of the *operando* Raman spectroscopy measurements, as well as the fruitful discussions of the research works. I would express my gratitude to Dr. Fang Song, Dr. Lucas Stern, Dr. Elitsa Petkucheva, Dr. Aliki Moysiadou, Dr. Jun Gu, Dr. Pengzuo Chen, Dr. Zhikun Zhang, Mr. Weiyan Ni, Mr. Albert Daubry, Mr. Xingyu Wu, and so on, for all the discussions and experimental help for my research work.

In addition, I would give my especial gratitude to Prof. Hao Ming Chen and Mr. Chia-Shuo Hsu, from National Taiwan University, for their help with *operando* X-ray absorption spectroscopy (XAS) measurements. The work in this Thesis can not be finished without their effort for experiments and data analysis. Great acknowledgement would also be given to Dr. Duncan Alexander (EPFL), for his help and collaboration with aberration corrected transmission electron microscope (TEM) measurements.

I would like to also express gratitude to all the staff of the chemical store, as well as the mechanical and electronic workshop of Institute of Chemistry and Chemical Engineering (ISIC). I also thank the personnel of the Center of Electron Microscope Imaging (CIME) for training me capable of operating TEM, including the aberration corrected TEM. I would acknowledge Dr. Pierre Mettraux for the X-ray photoelectron spectroscopy (XPS) experiments, and Dr. Natalia Gasilova for the inductively coupled plasma atomic emission spectrometry (ICP-AES) measurements.

In terms of the Thesis, I would thank Dr. Seunghwa Lee again for his help to proof part of the Thesis. Dr. Zheng Huang from McGill University, Canada, is acknowledged for proofing the French abstract of this Thesis.

---

I express my gratitude to the secretary of our lab, Mrs. Christina Zamanos-Epremian, for her great help in terms of research and life in EPFL. I would also greatly thank Ms. Anne Lene Odegaard, the administrative assistant in ISIC department, for her generously help and advice to my doctoral studies.

Life is also an important part of my PhD study in EPFL, such like playing basketball in my spare time. I would like to thank my 'good LSCI teammates', including Dr. Runze Mao, Dr. Fang Song, Dr. Chi-Wai Cheung, Dr. Tao Xu, Dr. Pengzuo Chen, and Mr. Xingyu Wu. I have spent a lot of happy time with them.

Last but not least, I would like to sincerely thank my family members and my friends, especially my girlfriend Songlan Sun, for their love, support and constant motivation during my doctoral years. This thesis would not have been possible without them.

# Abstract

The conversion of intermittent renewable energy resources in the form of chemical bond, such as hydrogen production from electrochemical water splitting, is a promising way to satisfy the future global energy demand and address the environmental issues. The oxygen evolution reaction (OER) is the bottleneck among the overall reaction due to its endergonic thermodynamics and complicated  $4\text{H}^+/4\text{e}^-$  transfer process. Despite extensive efforts have been made to develop cheap, efficient and robust heterogeneous electrocatalysts for OER, their heterogeneous nature makes the deep investigation of the active sites and reaction mechanisms challenging, thus impedes the further development of more advanced catalysts. Benefiting from high atomic efficiency, excellent intrinsic activity, and well-defined active motifs, the atomically dispersed catalysts provides an opportunity to get insight of the catalysts. This Thesis aims to use atomically dispersed catalysts as model systems to obtain atomic level insight of the active sites and reaction mechanisms of OER catalysts.

The Chapter 2 demonstrates a Co single-atom precatalyst immobilized on N-doped carbon support (Co-N-C) can be transformed to a Co-Fe double-atom catalyst (Co-Fe-N-C) via electrochemical activation in KOH containing Fe ions impurities. The Co-Fe-N-C exhibited a turnover frequency higher than  $10\text{ s}^{-1}$  at 350 mV overpotential, which is one of the highest values among the state-of-the-art OER catalysts. Electrochemical, microscopic, and spectroscopic data, including atomic-resolution electron microscopy and *operando* X-ray absorption spectroscopy (XAS), reveal an atomically dispersed dimeric Co-Fe moiety as the active site of the Co-Fe-N-C. This work demonstrates double-atom catalysis as a promising approach for the development of well-defined and highly active OER catalysts.

On the basis of Co-Fe-N-C, the Chapter 3 further describes a general synthesis of Co, Fe, and Ni-containing double-atom catalysts from their single-atom precursors via *in situ* electrochemical transformation. All these double-atom catalysts have molecule-like bimetallic active sites, which resembles the possible key active centers of bimetallic heterogeneous catalysts. In Chapter 4, a systematic mechanistic insight of the double-atom catalysts and the catalytic process were provided, by combining both electrokinetic analysis and *operando* XAS results. These mechanisms follow a similar O-O bond forming step and all exhibit bimetallic cooperation. While each mechanisms diverge in the catalytic site and the source of  $\text{OH}^-$  for O-O bond formation as well as the order of proton and electron transfer. These in-depth investigations suggested that the double-atom catalysts not only provide an attractive molecular platform for fundamental studies of heterogeneous OER electrocatalysts, but also establish a bridge between homogeneous and heterogeneous OER catalysis.

The traditional OER catalysts typically occurs via a mechanism involving four consecutive proton-coupled electron transfer (PCET) steps, which has a performance limit imposed by the scaling relationship of various oxygen intermediates. The Chapter 5 describes using *operando* Raman spectroscopy and electrokinetic analysis to study two active model OER catalysts,  $\text{FeOOH-NiOOH}$

---

composite and NiFe layered double hydroxide (LDH). The data support two distinct mechanisms for the two catalysts: FeOOH-NiOOH operates by a bifunctional mechanism where the rate-determining O-O bond forming step is the OH<sup>-</sup> attack on a Fe=O coupled with a hydrogen atom transfer to a nearby Ni<sup>III</sup>-O site, whereas NiFe LDH operates by a conventional mechanism of four consecutive PCET steps. The bifunctional mechanism, hitherto only supported by theoretical computations, has the potential to circumvent the scaling relationship limit of conventional OER mechanism. Thus, this work provides the first experimental evidences to validate such novel mechanisms.

## Keywords

Oxygen evolution reaction; atomically dispersed catalyst; electrocatalysis; *in situ* spectroscopy; electrokinetics; reaction mechanism

---

# Résumé

La conversion des ressources d'énergie renouvelable intermittente sous forme de liaison chimique, comme la production d'hydrogène à partir de la dissociation électrochimique de l'eau, est une méthode prometteuse de satisfaire la future demande énergétique mondiale et de résoudre les problèmes environnementaux. La réaction d'évolution d'oxygène (REO) est le goulot d'étranglement parmi la réaction globale en raison de sa thermodynamique endergonique et de son processus compliqué de transfert en forme de  $4\text{H}^+/4\text{e}^-$ . Malgré des efforts considérables pour développer des électrocatalyseurs hétérogènes bon marché, efficaces et robustes pour la REO, leur nature hétérogène rend difficile l'étude approfondie des sites actifs et des mécanismes de réaction, ce qui empêche le développement ultérieur de catalyseurs plus avancés. Bénéficiant d'une efficacité atomique élevée, d'une excellente activité intrinsèque et de motifs actifs bien définis, les catalyseurs atomiquement dispersés offrent la possibilité d'avoir un aperçu des catalyseurs. Cette Thèse vise à utiliser des catalyseurs atomiquement dispersés comme systèmes modèles pour obtenir un aperçu au niveau atomique des sites actifs et des mécanismes de réaction des catalyseurs REO.

Le Chapitre 2 démontre qu'un précatalyseur mono-atome de Co immobilisé sur un support de carbone dopé d'azote (Co-N-C) peut être transformé en un catalyseur à double-atome de Co-Fe (Co-Fe-N-C) par activation électrochimique dans du KOH contenant des impuretés d'ions Fe. Le Co-Fe-N-C a présenté une fréquence de rotation supérieure à  $10 \text{ s}^{-1}$  à un surpotentiel de 350 mV, ce qui est l'une des valeurs les plus élevées parmi les catalyseurs REO de pointe. Les données électrochimiques, microscopiques et spectroscopiques, y compris la microscopie électronique à résolution atomique et la spectroscopie d'absorption des rayons X (SAX) *operando*, révèlent un fragment Co-Fe dimère dispersé atomiquement comme site actif du Co-Fe-N-C. Ce travail démontre la catalyse à double-atome comme une approche prometteuse pour le développement de catalyseurs REO bien définis et hautement actifs.

Sur la base de Co-Fe-N-C, le Chapitre 3 décrit en outre une synthèse générale de catalyseurs à double-atome contenant du Co, du Fe et du Ni, produisant à partir de leurs précurseurs mono-atomes via une transformation électrochimique *in situ*. Tous ces catalyseurs à double-atome ont des sites actifs bimétalliques analogues à des molécules, qui ressemblent aux centres actifs clés possibles de catalyseurs hétérogènes bimétalliques. Dans le Chapitre 4, une vision mécaniste systématique des catalyseurs à double atome et du processus catalytique a été fournie, en combinant à la fois l'analyse électrocinétique et les résultats SAX *operando*. Ces mécanismes suivent une étape similaire de formation de liaison O-O et présentent tous une coopération bimétallique. Alors que chaque mécanisme diverge dans le site catalytique et la source de l' $\text{OH}^-$  pour la formation de la liaison O-O ainsi que l'ordre du transfert de protons et d'électrons. Ces recherches approfondies suggèrent que les

---

catalyseurs double-atomes non seulement fournissent une plate-forme moléculaire attrayante pour les études fondamentales des électrocatalyseurs REO hétérogènes, mais établissent également un pont entre la catalyse REO homogène et hétérogène.

Les catalyseurs REO traditionnels se produisent généralement via un mécanisme impliquant quatre étapes consécutives de transfert d'électrons couplé aux protons (TECP), qui a une limite de performance imposée par la relation de mise à l'échelle de divers intermédiaires d'oxygène. Le Chapitre 5 décrit utilisant la spectroscopie *operando* Raman et l'analyse électrocinétique pour étudier deux catalyseurs OER modèles actifs, le composite FeOOH-NiOOH et le double hydroxyde laminaire (DHL) NiFe. Les données soutiennent deux mécanismes distincts pour les deux catalyseurs: FeOOH-NiOOH fonctionne par un mécanisme bifonctionnel où l'étape déterminant la vitesse est la formation de liaison O-O via l'attaque OH<sup>-</sup> sur un Fe=O couplée à un transfert d'atome d'hydrogène vers un Ni<sup>III</sup>-O proche site, tandis que DHL NiFe fonctionne par un mécanisme conventionnel de quatre étapes TECP consécutives. Le mécanisme bifonctionnel, jusqu'ici uniquement soutenu par des calculs théoriques, a le potentiel de contourner la limite de relation de mise à l'échelle du mécanisme REO conventionnel. Ainsi, ce travail fournit les premières preuves expérimentales pour valider ces nouveaux mécanismes.

## Mots-clés

réaction d'évolution de l'oxygène; catalyseur atomiquement dispersé; électrocatalyse; spectroscopie *in situ*; électrocinétiques; mécanisme de réaction

---

# 摘要

将分布不均匀的可再生能源转化为可储存的化学能（例如电化学水分解产氢）是一种非常有前景的方法去解决未来的全球能源和环境问题。就水分解反应而言，释氧反应（OER）是整个过程的瓶颈。这是因为这个反应不仅需要很大的外加能量来驱动，而且反应过程涉及到四质子和四电子的转移，动力学过程非常复杂。许多科学工作者花费了很大努力去开发各类廉价，高效和稳定的异相催化剂用于释氧反应。尽管如此，由于异相催化剂的活性位点分布不均匀，对于活性位点和反应机理的深入研究非常具有挑战性，从而使得进一步开发更高效的催化剂十分得困难。得益于高的原子效率，卓越的本征活性，以及明确的反应活性中心，原子级别分散的催化剂为催化过程的深入研究提供了机会。本论文将以原子级别分散的催化剂作为模型系统，对释氧反应的活性中心和反应机理进行原子级别的深入研究。

本论文的第二章阐述了在含有铁杂质的氢氧化钾溶液中，负载在氮掺杂碳基底上的钴单原子催化剂（Co-N-C）可以通过电化学活化的方法转变为钴-铁双原子催化剂（Co-Fe-N-C）。在 350 毫伏的过电位下，该催化剂的转化频率可高达 10 每秒每催化中心 ( $\text{s}^{-1}$ )。这一数值可媲美已报道的最先进的非贵金属 OER 催化剂。电化学，电子显微学以及光谱学数据，包括原子分辨的透射电子显微镜和原位 X 射线吸收谱，揭示了这一催化剂拥有原子级别分散的双金属钴-铁活性中心。这一工作阐明了双原子催化是一个有前景的方法去开发高效并且活性中心明确的 OER 催化剂。

在 Co-Fe-N-C 的基础上，本论文第三章进一步描述了合成包含非贵金属钴，铁，镍的双原子释氧催化剂的方法。这些催化剂可以从对应的单原子催化剂前驱体，通过原位电化学活化的方法制备。一系列电化学，电子显微学以及原位光谱学表征数据证明了所有制备的双原子催化剂均含有分子特征的双金属活性位点。这一活性位点的特征与对应的异相催化剂可能的关键活性中心十分类似。基于这一特性，本论文的第四章将电化学动力学分析和原位 X 射线吸收光谱数据相结合，对这一系列的双原子催化剂进行了全面系统的反应机理和催化过程的研究。这些催化剂拥有类似的 O-O 化学键形成过程，并且都表现出双金属协同作用。但不同催化剂表现出不同的反应机理细节，包括不同的金属催化中心，不同的用于 O-O 键形成的氢氧根来源，以及不同的质子和电子的反应级数。这一系列深入的研究表明了双原子催化剂不仅为异相释氧催化剂的基础性研究提供了引人入胜的平台，而且也均为均相和异相释氧催化架设了一座桥梁。

传统的释氧催化剂的反应机理通常涉及到四步连续的质子耦合电子转移过程。然而，由于不同含氧中间体的能量制约关系，催化剂的活性收到了限制。本论文的第五章结合原位拉曼光谱和电化学反应动力学分析去研究两种不同的镍-铁基 OER 模型催化剂：FeOOH-NiOOH 复

---

合催化剂和镍铁层状双氢氧化物 (NiFe LDH)。实验研究发现这两种催化剂拥有截然不同的反应机理。FeOOH-NiOOH 的催化机理为双功能反应机理。在这个机理中, 决速步骤是 OH<sup>-</sup> 进攻 Fe=O 物种且同时伴随着氢原子转移到邻近 Ni<sup>III</sup>-O 位点的 O-O 键形成过程。而 NiFe LDH 的反应机理为传统的四步连续质子耦合电子转移过程。双功能释氧反应机理被认为有着克服传统机理里的不同含氧中间体的能量制约关系的潜力, 然而迄今为止这一新机理仅仅被理论计算所支持。因此, 本论文第五章的研究工作为双功能释氧反应机理提供了第一例详细的实验证据。

## 关键词

释氧反应; 原子分散的催化剂; 电催化; 原位光谱; 电化学动力学; 反应机理



---

# Symbols and Abbreviations

**$\partial$**  Partial differential

**AC** Aberration Corrected

**AEM** Anion Exchange Membrane; Adsorbates Evolution Mechanism

**BET** Brunauer–Emmett–Teller

***ca.*** Circa

**$C_{dl}$**  Double layer capacitance

**CC** Carbon Cloth

**CN** Coordination Number

**CRR** Carbon-dioxide Reduction Reaction

**CV** Cyclic Voltammetry

**$\Delta$**  Differential (finite)

**$d$**  Differential (infinitely small)

**dec** Decade

**DAC** Double-Atom Catalyst

**DFT** Density Functional Theory

**$E$**  Potential, applied potential

**$E^\circ$**  Standard redox potential

**$e$**  Elementary charge ( $1.602 \times 10^{-19}$  C)

***et al.*** And others

**ECSA** Electrochemical Active Surface Area

**EDX** Energy-Dispersed X-ray

**EXAFS** Extended X-ray Absorption Fine Structure

**$F$**  Faraday constant (96485 C/mol)

**FE** Faradaic Efficiency

**FT** Fourier Transfer

---

**$G^\circ$**  Standard Gibbs free energy

**GC** Gas Chromatography

**$\eta$**  Overpotential

**HAADF-STEM** High-Angle Annular Dark-Field Scanning Transmission Electron Microscopy

**HER** Hydrogen Evolution Reaction

**$i$**  Current

**i.e.** For examples

**ICP-AES** Inductively Coupled Plasma Atomic Emission Spectrometry

**IR** Infrared

**$j$**  Current density

**$j_0$**  Exchange current density

**$K$**  Equilibrium constant

**$k$**  Reaction rate constant

**KIE** Kinetic Isotope Effect

**$\ln$**  Natural logarithm

**$\log$**  Logarithm

**LDH** Layered Double Hydroxide

**LOM** Lattice Oxygen Mechanism

**LSV** Linear Scan Voltammetry

**$m$**  The loading of the active sites

**$n$**  Number of electron transfer

**NP** Nanoparticle

**NRR** Nitrogen Reduction Reaction

**OCP** Open Circuit Potential

**OER** Oxygen Evolution Reaction

**ORR** Oxygen Reduction Reaction

**PES** Pre-Equilibrium Step

**PEM** Polymer Electrolyte Membrane

**R** Resistance

**$R$**  Universal gas constant ( $8.3145 \text{ JK}^{-1}\text{mol}^{-1}$ )

**RDS** Rate-Determining Step

---

**RHE** Reversible Hydrogen Electrode

**RLS** Rate-Limiting Step

**sat.** Saturated

**SAC** Single-Atom Catalyst

**SAED** Selective Area Electron Diffraction

**SERS** Surface-Enhanced Raman Spectroscopy

**SHE** Standard Hydrogen Electrode

**T** Thermodynamic temperature

**TEM** Transmission Electron Microscopy

**TIE** Thermodynamic Isotope Effect

**TOF** Turnover Frequency

**UV-vis** Ultraviolet-visible light

**vs.** versus

**XANES** X-ray Absorption Near Edge Structure

**XAS** X-ray Absorption Spectroscopy

**XPS** X-ray Photoelectron Spectroscopy

**XRD** X-ray Diffraction

**ZPE** Zero-Point Energy

---

# Units and Prefixes

**A** ampere

**C** Coulomb

**°C** degree Celsius

**eV** electron volts

**g** gram

**h/hr** hour

**J** Joule

**L** litre

**m** meter

**m<sup>2</sup>** square-meter

**M** mol/L

**min** minute

**mol** mole

**s** second

**V** volt

**W** watt

**Ω** ohm

**T** tera- ( $10^{12}$ )

**M** mega- ( $10^6$ )

**k** kilo- ( $10^3$ )

**c** centi- ( $10^{-2}$ )

**m** milli- ( $10^{-3}$ )

**μ** micro- ( $10^{-6}$ )

**n** nano- ( $10^{-9}$ )

**p** pico- ( $10^{-12}$ )



---

# Contents

Acknowledgements.....	i
Abstract.....	iii
Résumé .....	v
摘要 .....	vii
Symbols and Abbreviations.....	ix
Units and Prefixes .....	xii
Chapter 1 Introduction and Research Methods .....	1
1.1 The challenge of energy in 21st century .....	2
1.2 Renewable and sustainable energy systems.....	2
1.3 Introduction of OER and OER catalysts .....	6
1.3.1 General concepts of OER catalysis.....	6
1.3.2 General introduction of OER catalysts.....	10
1.3.3 State-of-the-art OER catalysts in alkaline conditions .....	11
1.4 Mechanistic insight of OER catalysis .....	13
1.4.1 Theoretical calculation .....	13
1.4.2 Electrokinetic studies.....	18
1.4.3 <i>in-situ/operando</i> spectroscopy.....	20
1.4.4 Identification of the real active sites of the benchmark catalysts.....	21
1.5 Atomically dispersed catalysts .....	26
1.5.1 General introduction of atomically dispersed catalysts .....	26
1.5.2 Atomically dispersed catalysts for OER .....	28
1.6 Challenges and opportunities in the research field .....	30
1.7 Research methods.....	33
1.8 Outline of the following Chapters .....	35
1.9 References of Chapter 1.....	36
Chapter 2 A Co-Fe double-atom catalyst for the Oxygen Evolution Reaction.....	47
2.1 Introduction.....	48
2.2 Synthesis and characterization of the single-atom Co precatalyst (Co-N-C) .....	49
2.2.1 Synthesis of Co-N-C precatalyst.....	49
2.2.2 Characterization of Co-N-C precatalyst .....	50
2.3 Electrochemical OER performance.....	53
2.4 Characterization of the real catalysts (Co-Fe-N-C) .....	56

---

2.5 <i>Operando</i> XAS study and identification of real active sites .....	60
2.5.1 <i>Operando</i> XAS of Co-N-C and Co-Fe-N-C .....	60
2.5.2 Determination of intrinsic activity of Co-Fe-N-C .....	67
2.6 Conclusions.....	71
2.7 Experimental Details .....	72
2.7.1 Catalyst synthesis and electrolyte preparation .....	72
2.7.2 Physical Characterizations .....	73
2.7.3 Parameters for <i>operando</i> XAS .....	74
2.7.4 Electrochemical Characterizations .....	74
2.8 Contributions.....	76
2.9 References of Chapter 2 .....	76
Chapter 3 The Generality of Double-Atom Catalysis in alkaline Oxygen Evolution Reaction.....	82
3.1 Introduction.....	83
3.2 Characterization of Ni and Fe single-atom precatalysts.....	84
3.3 Characterization of various double-atom catalysts .....	90
3.3.1 Microscopic characterization of various double-atom catalysts.....	90
3.3.2 OER performance of various double-atom catalysts.....	98
3.4 <i>Operando</i> XAS study of double-atom catalysts.....	100
3.4.1 <i>Operando</i> XAS study of Ni-Fe-N-C .....	100
3.4.2 <i>Operando</i> XAS study of Co-Ni-N-C and Co-Co-N-C .....	106
3.4.3 <i>Operando</i> XAS study of Fe-Ni-N-C and Fe-Co-N-C .....	111
3.5 Comparison of intrinsic OER activity .....	123
3.6 Conclusions.....	125
3.7 Experimental Section.....	126
3.7.1 Catalyst synthesis.....	126
3.7.2 Common Physical Characterizations .....	127
3.7.3 XAS measurements.....	128
3.7.4 Electrochemical characterization .....	130
3.8 Contributions.....	132
3.9 References of Chapter 3.....	132
Chapter 4 Double-Atom Catalysts Provide a Molecular Platform for Heterogeneous Oxygen Evolution Electrocatalysis .....	135
4.1 Introduction.....	136
4.2 Methods for electrokinetic analysis .....	137
4.3 Electrokinetic analysis and reaction mechanisms of double-atom catalysts.....	142

---

4.3.1 Electrokinetic analysis and reaction mechanisms of Co-based double atoms.....	142
4.3.2 Electrokinetic analysis and reaction mechanisms of Ni-based double atoms .....	150
4.3.3 Electrokinetic analysis and reaction mechanisms of Fe-based double atoms .....	153
4.4 Comparisons and discussions of the reaction mechanisms .....	158
4.5 Conclusions.....	161
4.6 Experimental Section.....	162
4.7 Contributions.....	162
4.8 References of Chapter 4 .....	163
Chapter 5 Spectroscopic and electrokinetic evidence for a bifunctional mechanism of the oxygen evolution reaction .....	167
5.1 Introduction.....	168
5.2 Basic characterization.....	169
5.3 Activity comparison for OER.....	172
5.4 <i>Operando</i> Raman Spectroscopy .....	175
5.4.1 Potential and position dependent <i>operando</i> Raman Spectroscopy.....	175
5.4.2 $^{18}\text{O}$ isotope labeling and exchange experiments .....	181
5.5 Analysis of the electrokinetics.....	185
5.5.1 Analysis of Tafel slope and reaction order of hydroxyl ions concentration .....	185
5.5.2 Analysis of H-D isotope effect.....	190
5.6 Possible OER mechanisms .....	192
5.7 Conclusions.....	194
5.8 Experimental Sections .....	195
5.8.1 Chemicals and the synthesis of the catalysts .....	195
5.8.2 Characterizations .....	197
5.8.3 Electrochemical test conditions.....	198
5.9 Contributions.....	200
5.10 References of Chapter 5 .....	200
Chapter 6 Conclusions and Outlooks .....	205
References of Chapter 6.....	209
Appendix 1 The quasi-equilibrium model for electrokinetic study .....	211
A1.1 Bultler-Volmer equation .....	211
A1.2 Quasi-Langmuir model.....	212
A1.3 Typical examples for the application of the electrokinetic model.....	215
Appendix 2 H-D isotope effect.....	220
References of the Appendix.....	225



---

Curriculum Vitae .....	226
------------------------	-----

# Chapter 1 Introduction and Research Methods

Part of the Chapter is reformatted from part of the content in a published Perspective:

F. Song, **L. Bai**, A. Moysiadou, S. Lee, C. Hu, L. Liardet, X. Hu: Transition metal oxides as electrocatalysts for the oxygen evolution reaction in alkaline solutions: an application-inspired renaissance. **J. Am. Chem. Soc.** 2018, *140*, 7748–7759.

Reprinted (adapted) with permission from [1]. Copyright (2018) American Chemical Society.

## 1.1 The challenge of energy in 21st century

The development of human society is largely dependent on the utilization of energy.<sup>2,3</sup> The level of technological advancement is highly related to the amount of energy that human are able to use.<sup>2</sup> In the past ages, the fossil fuels (coal, oil and natural gas) are the dominated energy sources of human societies.<sup>2,4,5</sup> With the fast progress of the world and the rapid population increase, the energy consumption of human society is also growing prominently. In 2018, the total world energy consumption was 13.9 billion tons oil equivalents (t.o.e.) or  $1.61 \times 10^5$  TW·h,<sup>6</sup> equivalent to an average power consumption of 18.40 TW. The value will be continuously increased and it is estimated that the average power consumption can exceed 30 TW in 2050.<sup>7</sup> On the one hand, however, fossil energy that is difficult to regenerate in short term will be depleted in the next few hundred years.<sup>2-4</sup> On the other hand, large scale utilization of fossil fuels produces large amounts of CO<sub>2</sub>.<sup>8</sup> The excess emission of CO<sub>2</sub> causes global climate warming and acidification of oceans, resulting the problems such as increments of sea-level and disturbances of the ecosystems.<sup>9,10</sup> In addition, burning fossil fuels also discharges other polluting gases, such like CO, sulfur oxides (SO<sub>x</sub>) and nitric oxides (NO<sub>x</sub>), which are highly detrimental to the environment.<sup>11</sup> In order to alleviate and address the current energy and environmental issues, the fossil fuels need to be substituted by safe, clean and sustainable 'carbon-free' energy sources.<sup>2-5</sup> The exploiting and scaling of such energy systems has become a major scientific and technological challenge in the 21st century.<sup>2,3,12</sup>

## 1.2 Renewable and sustainable energy systems

Up until now, there are several carbon-free energy sources available on Earth, including hydropower, nuclear fission, biomass, wind, tide, geothermal, and solar.<sup>4,13</sup> Among them, nuclear power via nuclear fission is a carbon-free energy source but it is not renewable nor sustainable due to the using of uranium.<sup>4</sup> The nuclear waste is also hazardous to the environment. The other energy sources are renewable. Especially, the solar power is the most abundant energy source. The theoretical amount of energy that reaches the surface of the Earth is estimated to be  $4.3 \times 10^{20}$  J/hr.<sup>2</sup>. This corresponds to a power of approximately  $10^5$  TW, which is over 3000 times higher than the estimated 30 TW that humanity will need in 2050. Generating electricity from renewable energy is a common way that humanity makes use of the renewable energy.<sup>3-5</sup> For instance, a standard commercial solar photovoltaic panel can convert more than 20% of the energy of

sunlight into useable electricity.<sup>4</sup> Despite huge amount of various kinds of potential renewable energy sources are available, their intermittent distribution put an obstacle for the large-scale utilization.<sup>3-5</sup> For example, the solar energy cannot be harnessed at night, and in places with frequent and extensive cloud cover.<sup>4,12</sup> The distribution of solar energy also fluctuates unpredictably during the daytime.<sup>4,12</sup> Similar issues are also encountered for other renewable energy systems.<sup>4</sup> In this regard, the electricity generated from renewable energy is required to be stored, in case to circumvent the mismatch between production and consumption of the energy. One traditional method is to store surplus energy as gravitational potential energy (e.g. using the electricity to pump water to an alpine lake or an artificial reservoir with high sea-level).<sup>14</sup> The advanced energy storage systems include various rechargeable batteries (e.g. Li-ions batteries)<sup>15</sup> and super-capacitors<sup>16</sup>. In comparison to these two approaches, converting intermittent renewable energy resources in the form of chemical bond is more promising since the generated fuels have the advantage to achieve high energy densities.<sup>3,12,13,17</sup>

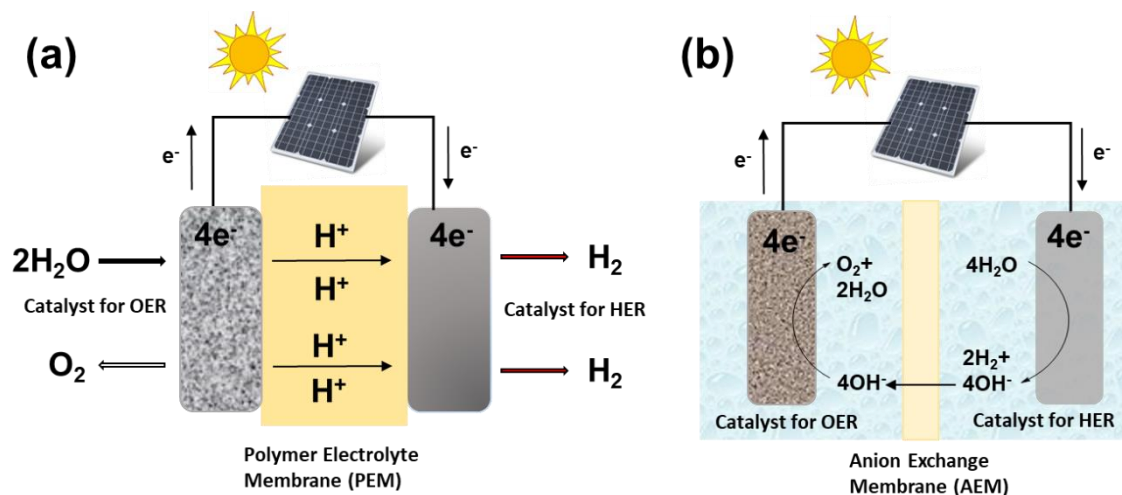


**Figure 1.1** Archetypal electrolysis cells for water splitting. (a) PEM water electrolysis; (b) alkaline water electrolysis.

Hydrogen is a storable fuel with high energy density.<sup>3</sup> The hydrogen can be directly burned as a fuel or used in hydrogen-oxygen fuel cells<sup>18</sup>. The final product in both approaches is only water, which is quite clean and carbon-free.<sup>3,12</sup> These advantages make hydrogen a promising energy carrier. Moreover, hydrogen is also an important substance in chemical industry, serving as the building block to produce many chemicals and fine chemicals.<sup>19</sup> Currently, about 95% of the

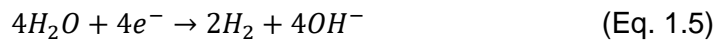
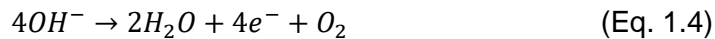
commercial hydrogen is produced from steam reforming of methane (Bosch process).<sup>20</sup> However, the method involves using fossil fuels and produces CO<sub>2</sub>, which is neither renewable nor carbon-neutral. Alternatively, the electrocatalytic water splitting (Eq. 1.1) is a clean approach to produce hydrogen. It is anticipated that in future the electricity input will come from renewable energy sources (Figure 1.1). In this promising way, the intermittent renewable energy resources are converted to clean and storable hydrogen energy.<sup>21-25</sup>



The archetypal electrolysis cells for water splitting are shown in Figure 1.1. Under acidic conditions, water electrolysis is performed in polymer electrolyte membrane (PEM) electrolysis cell (Figure 1.1a)<sup>26</sup>. Water is oxidized at the anode according to the Eq. 1.2, which is known as the oxygen evolution reaction (OER) or water oxidation reaction (WOR). The electrons travel through the external circuit while the protons cross into the cathode compartment through the PEM. The protons are then reduced by the electrons at the cathode, which is the hydrogen evolution reaction (HER, Eq. 3).



Another typical electrochemical cell is the anion exchange membrane (AEM) electrolysis cell (Figure 1.1b)<sup>27</sup>. The operation principle of AEM electrolysis cell is little bit difference compared to that of PEM electrolysis cell.<sup>27</sup> The anodic reaction now is the oxidation of hydroxyl ions to produce oxygen (Eq. 1.4), whereas the cathodic reaction is the reduction of water to hydrogen, with simultaneously generating OH<sup>-</sup> (Eq. 1.5). The OH<sup>-</sup> can traverse the AEM to anode for OER.



In both cases (Figure 1.1), the electricity is supplied by photovoltaics that are driven by solar energy.<sup>2,3,12,13,17</sup> In principle, the electricity can also be provided by other types of intermittent renewable energy sources.

The cathodic reaction in Figure 1.1 can be replaced by other electrochemical reactions, such as CO<sub>2</sub> reduction reaction (CRR)<sup>28,29</sup> and nitrogen reduction reaction (NRR)<sup>30,31</sup>, which are able to generate other important chemicals or fuels. The protons and electrons generated from OER

provide reductive equivalents for CRR and NRR. In this way, the valuable chemicals including  $C_xH_yO_z$  (e.g. CO, ethanol, ethylene, etc.) and  $NH_3$  can be produced via a green and sustainable approach.<sup>17</sup>

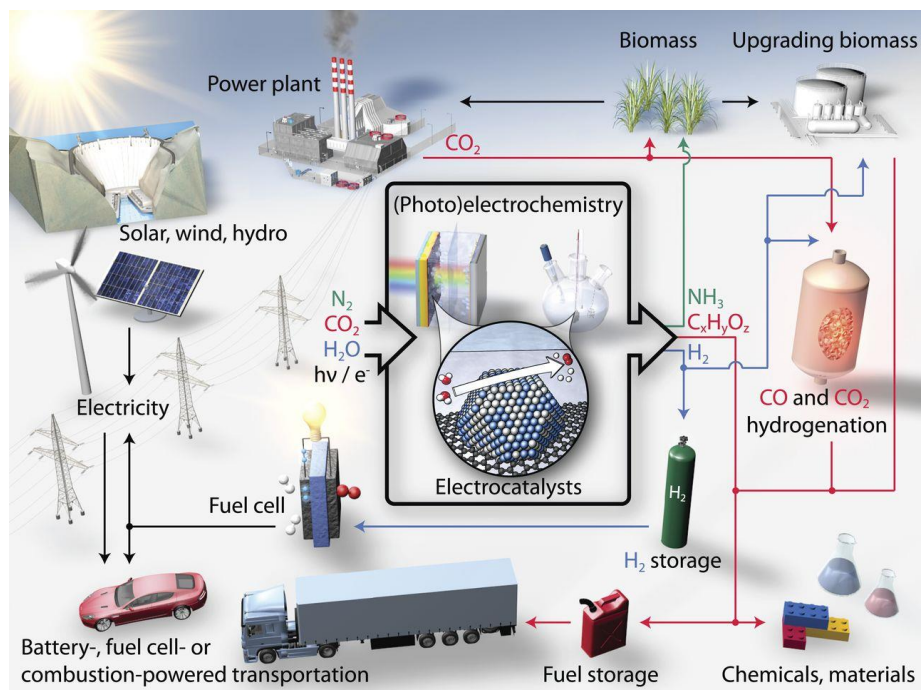


**Figure 1.2** Scheme of possible sustainable energy landscape based on electrocatalysis in future. Reproduced with permission. <sup>[17]</sup> Copyright 2017, American Association for the Advancement of Science (AAAS).

Some researchers have proposed the possible sustainable energy landscape based on electrocatalysis in the future, which can produce important fuels and chemicals, including hydrogen, ammonia, hydrocarbons and their oxygenates (Figure 1.2).<sup>17</sup> Earth's atmosphere provides a universal feedstock of water, carbon dioxide, and nitrogen, which can potentially be converted into the aforementioned products via electrochemical processes coupled to intermittent renewable energy, such as solar, wind, hydro, and so on.  $H_2$  and some hydrocarbon oxygenates like ethanol can be energy carriers to produce clean electricity in fuel cells. Although the oxidized product of hydrocarbons and their oxygenates are  $CO_2$ , these  $CO_2$  can be further concentrated as the raw source to regenerate the fuels with the assistance of renewable energy supply, which is still carbon-neutral.<sup>28,29</sup> Likewise, the  $NH_3$  produced from electroreduction of  $N_2$  facilitates the production of fertilizers sustainably, which is a potential alternative approach to the current energy

consuming and CO<sub>2</sub>-producing Haber-Bosch process in industry.<sup>30,31</sup> The chemical feedstocks produced in the initial stage can be further upgraded to various fine chemicals, polymers, and other materials.

We can see that the electrochemical cells are the central part to realize the sustainable energy landscape.<sup>17</sup> For all kinds of the electrolysis cells, the anodic reaction is the OER, while the cathodic reaction can be HER, CRR, or NRR. Hence, in summary, realizing highly efficient OER is the core to make sustainable energy and sustainable manufacture come true.

Therefore, the following parts of Chapter 1 will provide a brief overview and introduction to the research field of electrocatalytic OER, including the basic concepts, the state-of-the-art catalysts, as well as the mechanistic insights of the active sites of the catalysts. Based on the limitations and challenges in the research field, the key ideas and research methods of this Thesis will be presented.

## 1.3 Introduction of OER and OER catalysts

### 1.3.1 General concepts of OER catalysis

The required standard Gibbs free energy change ( $\Delta G^0$ ) of the water splitting reaction (Eq. 1.1) is 237.2 kJ/mol,<sup>32,33</sup> which means the reaction does not spontaneously proceed without external energy input. According to Eq. 1.6, such standard Gibbs free energy change corresponds to a standard potential ( $E_{Eq}^0$ ) of 1.229 V.<sup>34</sup> In the Equation,  $n$  is the total transferred electrons (four for water splitting reaction, Eq. 1.1), and  $F$  is the Faraday's constant (96485 C/mol). The theoretical potential of OER in standard conditions ( $E_{OER}^0$ , 298.15 K, 1 atm, pH = 0) is 1.229 V versus Standard Hydrogen Electrode (SHE). The theoretical potential of OER ( $E_{OER}$ ) decreased by 59.2 mV/pH (Eq. 1.7), with a value of 0.401 V vs. SHE in pH = 14.<sup>35</sup> The theoretical potential of HER in standard condition is 0 V vs. SHE ( $E_{HER}^0$ ), which is also decreased with pH ( $E_{HER}$ ), with a similar slope as OER (Eq. 1.8).<sup>35</sup> Thus, the theoretical potential of OER relative to Reversible Hydrogen Electrode (RHE) is always 1.229 V.

$$\Delta G^0 = nFE_{Eq}^0 \quad (\text{Eq. 1.6})$$

$$E_{OER} = E_{OER}^0 - 0.0592 \times pH \quad (\text{Eq. 1.7})$$

$$E_{HER} = E_{HER}^0 - 0.0592 \times pH \quad (\text{Eq. 1.8})$$

$$\eta = E - E_{eq} \quad (\text{Eq. 1.9})$$

Additionally, OER involves transfer of four protons and electrons (or four  $\text{OH}^-/\text{e}^-$  in alkaline conditions) and different reaction intermediates (Eq. 1.2 and Eq. 1.4), which impose a large barrier in addition to the theoretical potential.<sup>23,36</sup> To make the reaction proceed in a certain reaction rate, the applied potential ( $E$ ) is always higher than the theoretical potential ( $E_{eq}$ ). This excess required potential is called overpotential ( $\eta$ ), defined as Eq. 1.9. Therefore, due to the endoergic thermodynamics and complicated multiple electrons/protons transfer processes, OER is the bottleneck of the whole water splitting. Employing proper OER catalysts is indispensable to decrease the energy input and thus improve the efficiency of the whole system.<sup>23-25</sup> As depicted in Figure 1.3, the catalysts can change the reaction pathway, and thus significantly decrease the activation energy (or in other words, the required overpotential). Lower required overpotential means higher catalytic performance.

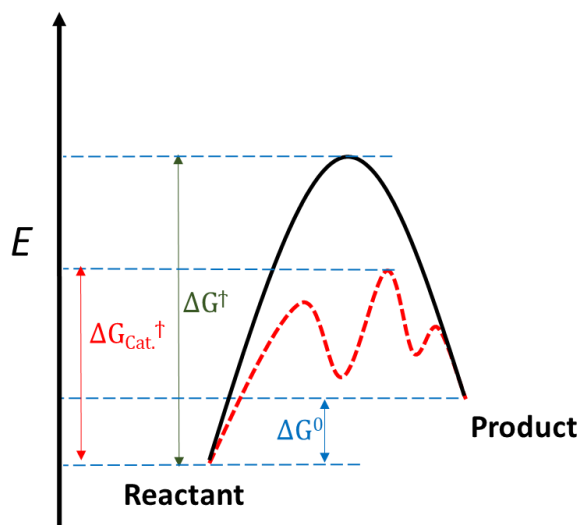


**Figure 1.3** Schematic illustration of the function of the catalysts. Suitable catalysts change the reaction pathway and decrease the activation energy. The required thermodynamic energy is  $\Delta G^0$ . The activation energy with and without catalyst are represented as  $\Delta G_{Cat.}^\ddagger$  and  $\Delta G^\ddagger$ , respectively.

There are several important parameters for evaluating the performance of the OER catalysts, including overpotential, specific activity, turnover frequency (TOF), stability, and Tafel Slope.<sup>23,24,37,38</sup> As mentioned in the last paragraph, overpotential is one of the most important



parameters (Eq. 1.9). Overpotential ( $\eta$ ) is usually defined as to achieve a certain current density.<sup>23,24</sup> Specifically, the value of overpotential at 10 mA/cm<sup>2</sup> is commonly used, which is related to 12.3% solar to hydrogen efficiency when the catalyst is incorporated into the solar water splitting device.<sup>37</sup> The activity (catalytic current density) can also be compared at certain overpotential. It should be cautioned that the actual overpotential includes both the activation overpotential of anodic reaction (for OER) and the potential loss caused by solution resistance (the Ohmic drop),<sup>39</sup> as shown in Eq. 1.10. In Eq. 1.10,  $\eta_a$  represents the activation overpotential of anodic reaction,  $i$  represents catalytic current, while  $R_s$  represents the solution resistance. The Ohmic drop should be taken into consideration in real application, whereas the pure reaction kinetics of the catalysts need to be investigated without Ohmic drop.<sup>34,39</sup> In the case of investigating intrinsic activity and pure reaction kinetics (electrokinetics), the Ohmic drop can be compensated by potentiostat. In the following parts of the Thesis, the mentioned overpotential is always corrected with the Ohmic drop unless otherwise specified.

$$\eta = \eta_a + iR_s \quad (\text{Eq. 1.10})$$

Considering the real application, the catalysts should possess good long-time stability. Typically, the apparent stability of the catalyst can be evaluated via long-time electrolysis at a constant current density (like 10 mA/cm<sup>2</sup>) or at a constant applied potential.<sup>23,24,37,38</sup> Fast multiple cyclic voltammetry (CV) scans is another method to evaluate the stability of the catalysts, in which fluctuated driving force is simulated.<sup>38</sup> It should be noted that the apparent stability of catalytic performance does not necessarily mean a stable catalyst because a catalyst can lose part of its mass or have significant structural change while maintaining the same level of activity. In scientific view, therefore, the structure and composition of the catalyst need to be further checked by various spectroscopic and microscopic characterization methods, while the loading and mass of the catalyst should be examined by ICP-AES (Inductively Coupled Plasma Atomic Emission Spectrometry) or electrochemical quartz crystal microbalance (EQCM).<sup>40,41</sup>

The catalytic activity can be improved by simply increasing the loading or exposing more active sites.<sup>23,37,42</sup> The specific activity and TOF are parameters to evaluate the intrinsic activity of the catalyst.<sup>23,38</sup> There are two main types of specific activity, mass activity and electrochemical active surface area (ECSA) normalized activity, respectively.<sup>23,37</sup> Mass activity ( $J_M$ ) is the catalytic current normalized by mass loading (Eq. 1.11, unit: A/g), while ECSA normalized activity ( $J_{ECSA}$ ) is the performance normalized by ECSA (Eq. 1.12, unit: mA/cm<sup>2</sup>). The ECSA can be estimated from the electrochemical double-layer capacitance of the catalyst ( $C_{dl}$ ) as Eq. 1.13-1.14, where  $C_s$  is the

specific capacitance of the sample or the capacitance of an atomically smooth planar surface of the material per unit area under identical electrolyte conditions.<sup>37</sup> In Eq. 14,  $j_a$  and  $j_c$  are anodic and cathodic double-layer charging and discharging current density, respectively.  $\nu$  is the scan rate.<sup>37</sup>

$$J_M = \frac{j}{M} \quad (\text{Eq. 1.11})$$

$$J_{ECSA} = \frac{j}{ECSA} \quad (\text{Eq. 1.12})$$

$$ECSA = \frac{C_{dl}}{C_s} \quad (\text{Eq. 1.13})$$

$$C_{dl} = \frac{|j_a - j_c|}{2\nu} \quad (\text{Eq. 1.14})$$

The term TOF is used to refer to the catalytic turnover number per unit time.<sup>23,24,38</sup> In OER catalysis, it is defined as evolved oxygen molecules per active sites. TOFs should be compared at a certain applied potential or overpotential.<sup>23,24,38</sup> The TOF value can be calculated via Eq. 1.15, where  $j$  is the catalytic current density,  $n$  is the transferred electrons for OER ( $n = 4$ ),  $F$  is Faraday's Constant (96485 C/mol),  $m$  is the loadings of the active sites.<sup>23,24,38</sup> Sometimes, the determination of the real active sites are difficult. The researchers typically assumed that all the metal species are participating in OER when the real active sites are not clear.<sup>23,38</sup> In this case, the TOF value might be underestimated.

$$TOF = \frac{J \times A}{4 \times F \times m} \quad (\text{Eq. 1.15})$$

Tafel Slope ( $b$ ) is slope of Tafel equation (Eq. 1.16-1.17), which refers to the potential required to achieve 10 times catalytic current density.<sup>23,38</sup> Lower Tafel slope ( $b$ , Eq. 1.17) means a smaller increased applied potential results in higher catalytic current density, which is promising for catalysis. For a multi-step electrochemical reaction, the Tafel slope may provide insightful information of the reaction mechanism.<sup>23,38</sup> The details of mechanistic insight from Tafel slope are provided in Section 1.4.2.

$$\log j = \log j_0 + \frac{\eta}{b} \quad (\text{Eq. 1.16})$$

$$b = \frac{\partial \eta}{\partial \log j} \quad (\text{Eq. 1.17})$$

### 1.3.2 General introduction of OER catalysts

$\text{RuO}_2$  and  $\text{IrO}_2$  had been considered as the benchmarks of OER catalysts because they exhibited high activity at a wide range of pH values.<sup>43</sup> For a reference current density of  $10 \text{ mA/cm}^2$ , an overpotential of ca. 200 mV (in acid) to ca. 300 mV (in base) is required for thin films of  $\text{RuO}_2$  and  $\text{IrO}_2$ . Although these catalysts are employed in PEM water electrolyzers<sup>26</sup>, the reserves of both ruthenium and iridium on Earth are quite limited, making them difficult for large-scale application.

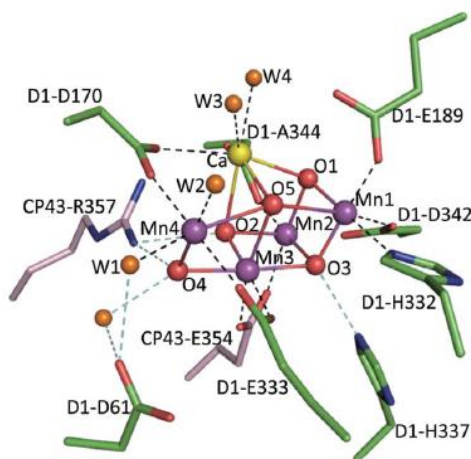


**Figure 1.4** Stereo view of the  $\text{Mn}_4\text{CaO}_5$  cluster and its ligand environment. Manganese, purple; calcium, yellow; oxygen, red; D1, green; CP43, pink. Reproduced with permission.<sup>[44]</sup> Copyright 2011, Springer Nature Publishing AG.

The technological requirement of OER catalysts has motivated intense research efforts on the development of catalysts that are solely composed of Earth-abundant elements.<sup>22-25,38,45,46</sup> Noted that OER is also an important reaction in green plant, which provides protons and reductive species for subsequent  $\text{CO}_2$  conversion.<sup>47</sup> The oxygen evolution complex (OEC) in photosynthetic system (PS) II of green plant exhibits outstanding catalytic performance for OER, with a TOF value as high as 100 to  $400 \text{ s}^{-1}$  under neutral condition.<sup>48</sup> The core structure of the OEC is a multi-nuclear complex called  $\text{Mn}_4\text{CaO}_5$  cluster that is stabilized by the surrounding protein environment (Figure 1.4).<sup>44</sup> However, this natural catalyst is not stable *in vivo* and the activity is not satisfied when the complex is separated and integrated to electrode or photoelectrochemical devices.<sup>49,50</sup> Inspired by the structure properties and working principles of OEC, many OER catalysts composed of non-noble metals were developed. These catalysts might be classified into two categories: homogeneous, molecular complexes and heterogeneous, inorganic solids.<sup>45,46</sup> Molecular catalysts<sup>51</sup> have uniform and easy-to-identify active sites; they are readily characterized

by spectroscopy and X-ray crystallography. Their properties can be finely tuned by ligand modification. The mechanistic understanding of molecular OER catalysts is more facile compared to their heterogeneous counterparts. Notwithstanding these desirable features, molecular catalysts suffer from low long-term stability under the harsh conditions of OER and have the difficulty to be integrated into electrochemical and photoelectrochemical devices.<sup>52,53</sup> In this regard, heterogeneous inorganic catalysts are more practical.

Commercial electrolyzers need to be operated in either concentrated acidic or alkaline conditions, in case to ensure the high conductivity.<sup>26,27</sup> Unfortunately, only platinum metal group based catalysts like Ru and Ir-based materials exhibit substantial stability in acidic medium, where the majority of nonprecious metal oxide OER catalysts gradually or rapidly degrade.<sup>37</sup> Thus, nonprecious metal oxide OER catalysts are mostly studied in alkaline medium.<sup>22-25,37,38</sup> In comparison to acidic water electrolysis or PEM water electrolysis, the alkaline water electrolysis has many advantages<sup>26,27</sup>, such as the catalysts are much cheaper compared to the noble-metal catalysts used for acidic water electrolysis. Moreover, the device has higher durability due to an exchangeable electrolyte and lower dissolution of anodic catalyst.

Scholarly studies of Co-, Ni-, Fe-, and Mn-based oxides or hydroxides in alkaline OER dated back to more than half a century ago.<sup>54-59</sup> The samples used in these early studies were either bulk oxides or electrochemically deposited films. Sample purity and structural homogeneity were not strictly controlled. The characterization was largely limited to electrochemical measurements. As a result, mostly phenomenal findings were reported and the field progressed slowly.

Thanks to developments in nanoscience and nanotechnology, it is now possible to synthesize a wide range of OER electrocatalysts with controlled composition, morphology, size, structure, and surface area. Plenty of OER catalysts based on non-noble metals were developed in recent years.<sup>22-25,37,38</sup> With suitable metal composition, nanostructure, and catalyst loading, now the overpotential to reach 10 mA/cm<sup>2</sup> current density is close or even below 200 mV.<sup>60,61</sup>

### **1.3.3 State-of-the-art OER catalysts in alkaline conditions**

Many metal oxides, hydroxides, and oxyhydroxides based on first-row transition metals can catalyze OER in alkaline conditions.<sup>22-25,37,38</sup> According to the bond strength of HO-M<sup>2+δ</sup>, Markovic and coworkers systematically compared the activity of catalysts composed of 3d single-metal

elements and found that the activities are following the trends as  $\text{Ni} > \text{Co} > \text{Fe} > \text{Mn}$  (Figure 1.5a), of which the trends are inverse with the bond strength of  $\text{HO-M}^{2+\delta}$ .<sup>62</sup> Nevertheless, many researchers suggested even trace amount of Fe impurities in electrolyte can significantly improve the activity of Ni and Co-based OER catalyst, despite pure iron oxide or oxyhydroxide are poor OER catalysts.<sup>59,63-65</sup> Boettcher et al. reexamined the activity trend of first-row transition metal oxyhydroxides after eliminating incidental Fe impurities in electrolyte. A modified OER activity order of  $\text{Ni(Fe)O}_x\text{H}_y > \text{Co(Fe)O}_x\text{H}_y > \text{FeO}_x\text{H}_y\text{-AuO}_x > \text{FeO}_x\text{H}_y > \text{CoO}_x\text{H}_y > \text{NiO}_x\text{H}_y > \text{MnO}_x\text{H}_y$  was obtained (Figure 1.5b).<sup>66</sup> Among them, Fe-based bimetallic materials, like NiFe, CoFe oxides or oxyhydroxides, are the benchmark catalysts for OER in alkaline condition. In recent years, benefiting from the development of material science, NiFe, CoFe bimetallic catalyst with nano-size and porous 3D structure were developed, which showed excellent OER performance.<sup>22-25,37,38</sup>

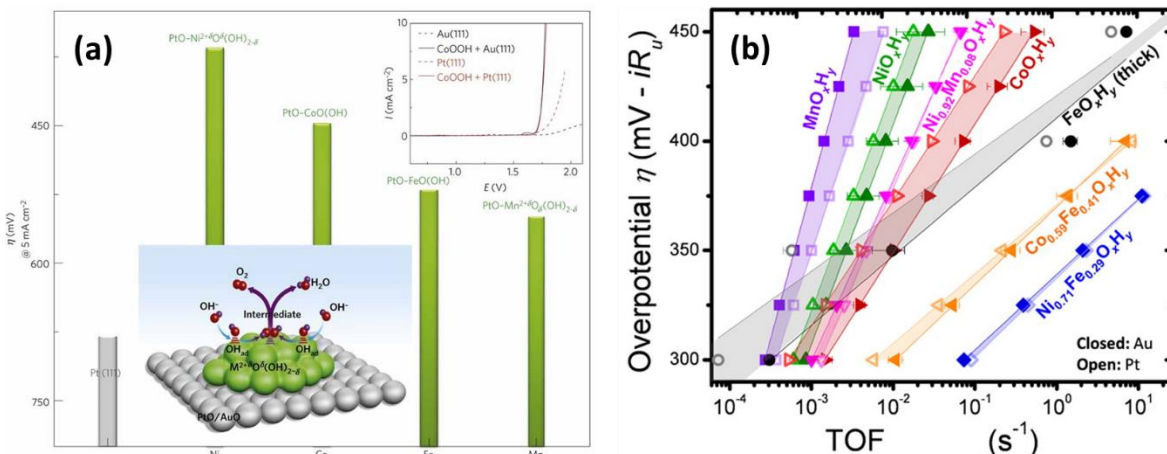


**Figure 1.5** Activity comparison of OER catalysts based on first-row transition metals. (a) Activity comparison of  $\text{MO}_x\text{H}_y$  on PtO substrate, based on the bond strength of  $\text{HO-M}^{2+\delta}$ . Reproduced with permission.<sup>[62]</sup> Copyright 2013, Springer Nature Publishing AG. (b) Comparison of TOF dependence on the overpotential for various bimetallic and single metallic OER catalysts. Reproduced with permission.<sup>[66]</sup> Copyright 2015, American Chemical Society (ACS).

In addition to  $\text{NiFeO}_x\text{H}_y$  and  $\text{CoFeO}_x\text{H}_y$ , some other non-iron-based bimetallic catalysts like  $\text{NiCoO}_x\text{H}_y$ ,  $\text{NiVO}_x\text{H}_y$ ,  $\text{CoMnO}_x\text{H}_y$ , and so on, also showed satisfied performance for OER.<sup>67-69</sup> It should be cautioned that Fe impurities in electrolyte can significantly improve the OER activity. Thus, the activity in Fe-free electrolyte should be evaluated in case to know the real catalytic properties. Actually, some trimetallic hydroxides/oxyhydroxides materials<sup>70-72</sup>, including NiCoFe,

CoFeW, NiFeV, etc., showed more excellent OER activity compared to NiFeO<sub>x</sub>H<sub>y</sub> and CoFeO<sub>x</sub>H<sub>y</sub>. Hu and coworkers developed an amorphous CoV oxide catalyst (CoVO<sub>x</sub>)<sup>73</sup>, which displays good OER performance in both normal KOH (containing Fe impurities) and Fe-free KOH. Control samples including CoO<sub>x</sub> and VO<sub>x</sub> had inferior activity in Fe-free KOH, thus indicating CoVO<sub>x</sub> is a 'real' non-iron-based bimetallic OER catalyst.

In recent years, non-oxide catalysts like selenide, sulfide, nitride, phosphide, etc. were developed and found to exhibit even better activities compared to metal oxyhydroxides.<sup>23,24,74</sup> Nevertheless, in most of the cases, post-catalytic analysis and *in-situ/operando* studies showed that the real active species are actually the metal oxyhydroxides partially or completely transformed from the non-oxide species, while the remained non-oxide species are acted as inner conductor.<sup>23,74</sup> The excellent performance of these materials are due to the porous structure and improved conductivity, comparing to the pure metal oxyhydroxides catalysts. Some materials like CoP, are intrinsically unstable in alkaline electrolyte even without applying potential.<sup>75</sup>

## 1.4 Mechanistic insight of OER catalysis

Understanding the nature of the active sites and getting mechanistic insights of the reaction mechanisms of OER catalysts are indispensable to obtain the knowledge of structure-activity relationships.<sup>23,76,77</sup> Such knowledge is highly crucial to the further design and development of OER catalysts with higher intrinsic activity. There are several research approaches to acquire mechanistic insights of OER catalysts, such as theoretical calculation, electrokinetic analysis and *in-situ/operando* spectroscopy.

### 1.4.1 Theoretical calculation

The general reaction mechanism of metal oxide/oxyhydroxide for OER in alkaline solution can be depicted in Figure 1.6a.<sup>23,76-78</sup> First, the hydroxyl ions are adsorbed on the metal active center (formation of M-OH) along with one electron transfer. Then the M-OH species are converted to metal-oxo species (M=O/M-O<sup>•</sup>) via another one OH<sup>-</sup>/e<sup>-</sup> process. The peroxide intermediates (M-OOH) are formed by the nucleophilic attack of hydroxyl ions on metal-oxo centers. The M-OOH can be further oxidized to M-OO<sup>•</sup> accompanied by oxygen release, after which the catalytic cycles are fulfilled. As suggested by Figure 1.6b, the oxygen evolution can also be accomplished by coupling of two adjacent metal-oxo species. Most other proposed mechanisms include the similar

intermediates, while the major difference is originated from different numbers of transferred electrons or hydroxyl ions in each step. Both mechanisms depicted in Figure 1.6 are called adsorbate evolution mechanism (AEM).

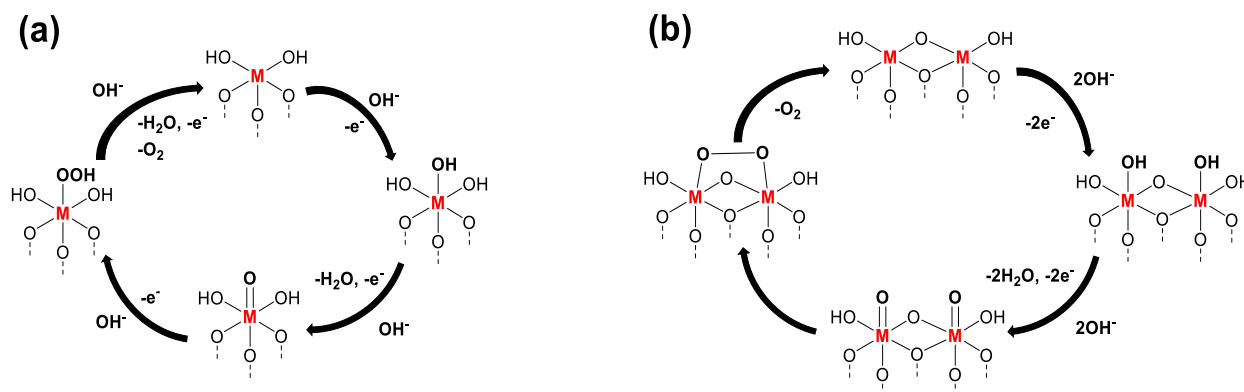


**Figure 1.6** General scheme of conventional OER mechanism in alkaline conditions. (a) A conventional mechanism involving four consecutive proton-coupled electron transfers; (b) A conventional mechanism involving combination of two metal oxo species as the O-O bond forming step.

In some situations, the transfer of electrons and hydroxyl ions is decoupled and does not happen simultaneously.<sup>79</sup> For example, Shao-Horn et al. demonstrated that the covalency of metal-oxygen bond is increased when the energy gap between the metal 3d and O 2p-band centers is reduced. The oxidation of lattice oxygen becomes thermodynamically favorable when O 2p states at the Fermi level lie above the redox energy of the  $\text{O}_2/\text{H}_2\text{O}$  couple (Figure 1.7a), thus the energy level of O 2p orbital is lower than the potential of OER. Based on *in situ*  $^{18}\text{O}$  isotope labelling mass spectrometry, the authors suggested the mechanisms (lattice oxygen mechanism, LOM) related to non-concerted proton–electron transfers during OER, with the oxidation of lattice oxygen (Figure 1.7b and c).<sup>80</sup> It is worth noting that high metal-oxygen covalency is not the only parameter to shift the reaction mechanism from AEM to LOM. To facilitate LOM, the catalyst material also needs to have high tendency to form oxygen vacancy, as well as to have high diffusion rate of  $\text{O}^{2-}$  ions.<sup>81</sup>

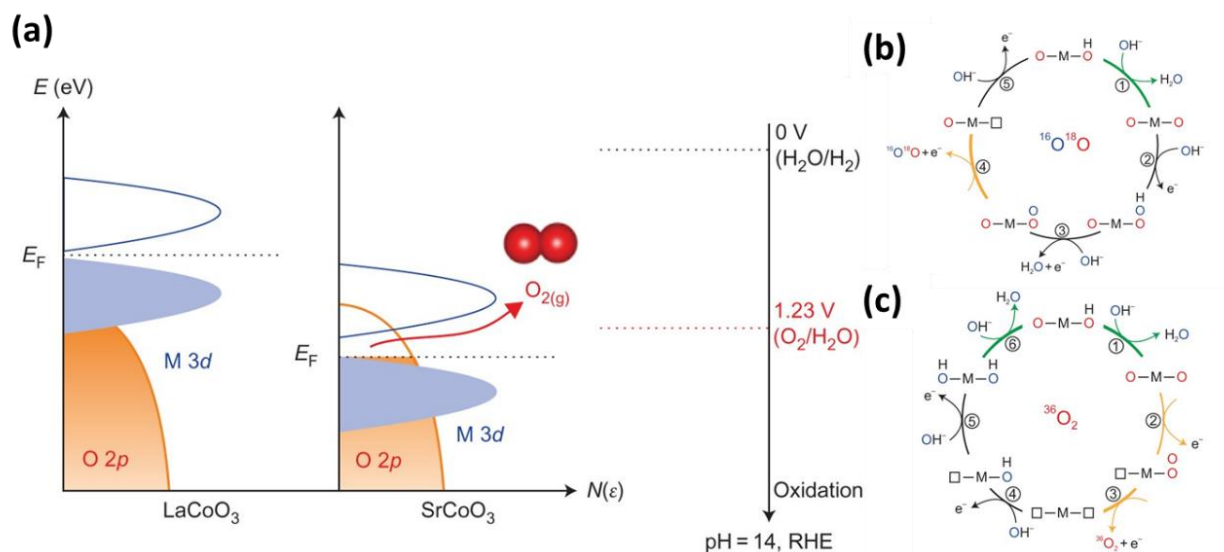


**Figure 1.7** Lattice oxygen participation OER mechanisms. (a) Schematic rigid band diagrams of two representative catalysts, LaCoO<sub>3</sub> and SrCoO<sub>3</sub>. The oxidation of lattice oxygen happens for SrCoO<sub>3</sub> but not LaCoO<sub>3</sub>. (b-c) Two possible OER mechanisms involving the oxidation of lattice oxygen. Reproduced with permission.<sup>[80]</sup> Copyright 2017, Springer Nature Publishing AG.

Although lattice oxygen participation results in non-concerted proton-electron transfer, this view in turn may not be true. The removal of proton can happen either before or after the electron transfer. For example, in a NiOOH catalyst, deprotonation of the surface oxygen groups occurs prior electron transfer.<sup>82</sup> Chorkendorff et al. found that a NiFeO<sub>x</sub>H<sub>y</sub> nanocatalyst exhibited pH-dependent OER activity but there was no lattice oxygen involved in OER processes.<sup>83</sup> Xu et al. also observed similar results for a ZnFe<sub>0.4</sub>Co<sub>1.6</sub>O<sub>4</sub> OER catalyst.<sup>84</sup>

Most of the theoretical calculations, like density functional theory (DFT) calculation assumed that the OER proceeds via the mechanism depicted in Figure 1.6a. In this mechanism model, there are many intermediates such as \*OH, \*OOH, \*O involved in OER catalysis (\* represent adsorbed sites).<sup>85-88</sup> Since the binding energies of the different intermediates are linearly correlated, it seems like descriptors related to adsorption energy of only a single intermediate can predict the activity trend. In early studies, Riutschi and Delahay demonstrated an approximate linear correlation between the rate of oxygen evolution and the M-OH bond energy.<sup>89</sup> Trasatti also suggested the enthalpy change for the lower-to-higher oxide transition (MO<sub>x</sub> → MO<sub>x+1</sub>) as a descriptor.<sup>90,91</sup> As indicated in Figure 1.5a, Markovic and coworkers discovered that the OER



activity of catalysts composed of 3d single-metal elements and found that the activities are inverse with the bond strength of  $\text{HO-M}^{2+}$ .<sup>62</sup>

The OER performance can also be correlated to the other descriptors like electrons filling in  $e_g$  orbital<sup>92</sup> and metal-oxygen covalency<sup>84,93</sup>, since they are scaling with the binding energy of adsorbed oxygen intermediates. For electrons filling in  $e_g$  orbitals, lower  $e_g$  occupancy results stronger binding strength with oxygen-containing intermediates, and vice versa.<sup>92</sup> The optimal OER activity is obtained when the  $e_g$  occupancy is close to unity, in which the binding with oxygen-containing intermediates is neither too strong nor too weak.<sup>92</sup> In the case of metal-oxygen covalency, greater metal-oxygen covalency shifts O p-band center closer to the Fermi level and facilitates the electron transfer between the metal cation and oxygen adsorbates, thus tuning the binding energy of the oxygen-containing intermediates.<sup>84,93</sup>

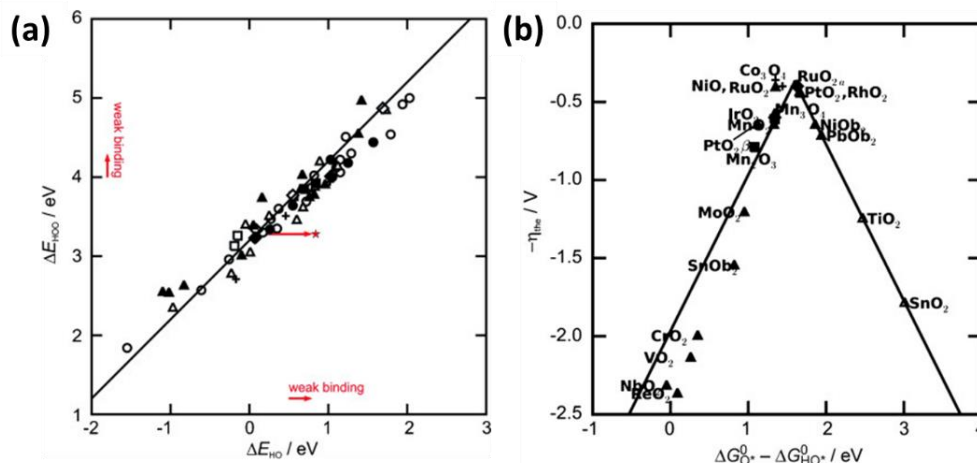


**Figure 1.8** Scaling relationship of OER catalysts. (a) The universal scaling relation between adsorption energies of  $\text{HO}^*$  and  $\text{HOO}^*$  on perovskites, rutiles, anatase,  $\text{Mn}_x\text{O}_y$ ,  $\text{Co}_3\text{O}_4$ , and  $\text{NiO}$  oxides. (b) Volcano plot of the calculated activities trends against descriptor ( $\Delta G_{\text{HO}^*} - \Delta G_{\text{O}^*}$ ) for various metal oxides. Reprinted with permission from [87]. Copyright 2011 Wiley-VCH.

Benefiting from the development of theoretical calculations, the determination of the binding energy of oxygen-containing intermediates was much more accurate. Rossmeisl et al. studied the trends of OER activity using an extensive database of calculated binding energies on surfaces of a large number of metal oxides.<sup>87</sup> A universal scaling relationship between  $\text{HO}^*$  and  $\text{HOO}^*$  was discovered for all the investigated materials, as the difference between the adsorption energies



mechanisms depicted in Figure 1.6b (coupling of two metal-oxo intermediates) and Figure 1.7b (lattice oxygen participation). On the other hand, if the HOO\* is involved, the energy difference between HOO\* and HO\* needs to be lower than 3.2 eV, which means the HOO\* needs to be stabilized compared to HO\*. By employing theoretical calculation, Vojvodic et al. pointed out that \*OOH can be stabilized via a special hydrogen bond interaction with oxygen atom in the nearby opposite surface, when the distance between the surface is 6 Å.<sup>94</sup> This can be realized by creating a nanoscale channel. Follow-up theoretical studies suggested a third-type OER mechanism, the so-called “bifunctional” mechanism, as indicated in Figure 1.9.<sup>95-98</sup> This mechanism involves two catalytic sites, which works in a cooperative manner. One site provides the electrophilic M=O entity, while the other side provides a hydrogen atom acceptor (A). Although the direct nucleophilic attack of an OH<sup>-</sup> on the M=O to form the M-OOH intermediate is energetically too unfavourable, a concerted hydrogen atom transfer to the neighbouring acceptor significantly lowers the energetics. A recent research from Hu and co-workers demonstrated that by choosing suitable catalyst and hydrogen atom acceptor, the theoretical OER overpotential can reach to as low as 0.1 V.<sup>97</sup> Until now, however, this bifunctional mechanism is still only supported by DFT computations.<sup>95-98</sup>

### 1.4.2 Electrokinetic studies

The experimental method to determine reaction mechanism is typically based on electrokinetic analysis. The relationship of current density ( $j$ ) and overpotential ( $\eta$ ) in an electrochemical reaction can be depicted by Butler-Volmer equation (Eq. 1.19).<sup>23,34,99</sup> Here  $j_0$  is the exchange current density,  $n$  is the number of transferred electrons,  $F$  is the Faraday's constant,  $R$  is the universal gas constant,  $T$  is the thermodynamic temperature,  $\alpha_a$  and  $\alpha_c$  is the transfer coefficient of anodic reaction and cathodic reaction, respectively. When the anodic overpotential is high enough, the contribution from the cathodic part is negligible, and thus the Eq. 1.19 can be simplified as Tafel equation (Eq. 1.20; Eq. 1.16 and 1.21 is the logarithm of Eq. 1.20).<sup>23, 34, 90</sup>

$$j = j_0 \left[ \exp \left( \frac{\alpha_a n F \eta}{RT} \right) - \exp \left( - \frac{\alpha_c n F \eta}{RT} \right) \right] \quad (\text{Eq. 1.19})$$

$$j = j_0 \exp \left( \frac{\alpha_a n F \eta}{RT} \right) \quad (\text{Eq. 1.20})$$

$$\log j = \log j_0 + \frac{\eta}{b} \quad (\text{Eq. 1.16})$$

$$b = \frac{\partial \eta}{\partial \log j} = \frac{2.303RT}{\alpha_a n F} \quad (\text{Eq. 1.21})$$

Typically, the overall reaction rate of a multi-step electrochemical reaction depends on the concentration of reactant in the RDS. The concentration of surface adsorbed species for the RDS can be determined by the surface equilibrium equation of the pre-equilibrium step(s) (PES) before the RDS.<sup>99-101</sup> The steps after RDS neither determine the reaction rate nor influence the concentration of surface adsorbed species before RDS, thus do not have the contribution to the overall reaction rate. By adopting this assumption, in 1956, Bockris correlated different Tafel slopes values with the possible RDS of different proposed OER mechanisms.<sup>78</sup> Although some of the proposed reaction pathways were energy unfavorable and difficult to proceed, the methodology was suitable to speculate RDS in any possible OER mechanisms.

Taking conventional OER mechanism in Figure 1.6a as examples, if the initial step is the RDS, the Tafel slope is 120 mV/dec.<sup>99,101</sup> When the second step is the RDS, the Tafel slope is 40 mV/dec.<sup>78,99</sup> If the RDS does not involve the electron transfer, just proceeding after one-electron transfer pre-equilibrium reaction, the Tafel slope becomes 60 mV/dec.<sup>79,99,100</sup> The Tafel slope turns to 24 mV/dec, if the formation of M-OOH is RDS. Similarly, when the RDS is the coupling of metal oxygen or metal-oxo intermediates (Figure 1.6b), the Tafel slope can be either 30 or 15 mV/dec, depending on the antecedent steps.<sup>78,99,101</sup> In general, the Tafel slope decreases when the RDS is close to the end step of the reaction, which is a sign of good electrocatalyst.<sup>23,99</sup> The relationship of apparent transfer coefficient  $\alpha_a$  in Tafel equation can be generally calculated by following equations<sup>23,102</sup>:

$$\alpha_a = n_r \beta + \frac{n_b}{v} \quad (\text{Eq. 1.22})$$

Where  $n_b$  is the number of electrons that transferred before the RDS (or in the PES),  $v$  is the number of RDSs that have taken place in the overall reaction.  $n_r$  is the number of electrons that participate in the RDS,  $\beta$  is the transfer coefficient of the RDS. Thus, the equation provides a simple and rapid approach to identify the RDS of OER.

However, the Tafel analysis is not sufficient to account for the real kinetic behaviors of OER catalysts. The same Tafel values may originate from different reaction pathways. For examples, a Tafel slope of 40 mV/dec is also suitable when the third step is RDS and the second step is in kinetic equilibrium.<sup>79,103</sup> In this case, the first step is fast enough and all the initial active sites (M) are converted to M-OH species. Moreover, the treatment is based on Langmuir isothermal

adsorption model, which assumes a low coverage of the surface intermediate before the RDS. The Tafel slope under low and high overpotential can be quite different even for the same RDS, due to the different coverage degree of the reaction intermediates.<sup>78,99</sup> The transfer coefficient can deviate from 0.5 when the reorganization energy is comparable to overpotential (Eq. 1.23),<sup>34</sup> or when there is a significant barrier in the electron transfer.<sup>103,104</sup> Because of these limitations, a full kinetic analysis for other parameters, including rate orders and isotope effect values, in addition to Tafel slopes, is necessary to establish the detailed reaction mechanism.<sup>79,99,103</sup> To understand which key intermediates are involved, the electrokinetic analysis should combine with *in-situ/operando* spectroscopy.

$$\alpha = \frac{1}{2} \left( 1 + \frac{\eta^F}{\lambda} \right) \quad (\text{Eq. 1.23})$$

### 1.4.3 *in-situ/operando* spectroscopy

Modern analytical tools of spectroscopy and microscopy, especially the access to various *in situ* and *operando* techniques, provide unprecedented fundamental information about the catalytic sites.<sup>76,77,105,106</sup> Many *in situ* and *operando* spectroscopic characterization can probe the key intermediates, active motifs/phase, and dynamic evolution of the catalysts under realistic operating conditions.<sup>76,77,105,106</sup> The acquired information is able to guide further rational design and development of catalysts. The *in-situ/operando* spectroscopies can generally be divided as optical-based techniques (e.g. UV-vis, Raman, IR spectroscopy, etc.) and X-rays techniques (e.g. XAS, XPS, XRD, etc.), which are briefly introduced as below.<sup>105</sup>

IR (Infrared) and Raman spectroscopy are important optical-based techniques, which are sensitive to the catalyst/electrolyte solution interface. IR has higher surface sensitivity and spectral resolution compared to Raman, while Raman is more sensitive to the change of the phase and oxidation state of the materials.<sup>105,106</sup> Therefore, they support and complement with each other. With the assistance of surface-enhanced techniques, people could use Raman and IR to detect different adsorbed key intermediates on electrode surfaces, as well as the potential/time-dependent behavior of the adsorbed species and the active phases. In contrast to IR and Raman spectroscopy, Ultraviolet-visible (UV-vis) spectroscopy reflects information of the whole catalyst film.<sup>77,106</sup> The variation of the position and intensity of the absorption peaks can be associated to the change of the oxidation state or generation of certain active motifs in the bulk material.

X-rays techniques are quite powerful and able to offer more information about oxidation state, phase, orientation and coordination environment of the catalyst materials.<sup>105,106</sup> The experiments are usually performed in synchrotron X-ray light sources. X-ray absorption spectroscopy (XAS) monitors the change of oxidation state (from X-ray Absorption Near Edge Structure, XANES) and coordination structure (from Extended X-ray Absorption Fine Structure, EXAFS) of metal center during catalysis.<sup>107</sup> Although XAS is insensitive towards light elements, adsorbing species can be indirectly detected through monitoring minute changes in the catalyst state and coordination environment of the metal elements.<sup>105-107</sup> Noted that XAS reflected the averaged structural information of the materials. On the contrary, *in situ* X-ray Photoelectron Spectroscopy (XPS) is a technique with more surface sensitivity.<sup>105</sup> The oxidation state of the surface or near surface species of the catalysts could be acquired. *In situ* X-ray diffraction (XRD) is typically performed in synchrotron beamline. The typical setup involves an X-ray detector that can rotate around the sample, providing  $2\theta$  resolution. The technique is useful to provide the change of the active phase during reaction, which is suitable for catalysts with good crystallinity.<sup>105</sup>

#### 1.4.4 Identification of the real active sites of the benchmark catalysts

As mentioned in Section 1.3.3, bimetallic NiFe, CoFe oxyhydroxides ( $\text{NiFeO}_x\text{H}_y$  and  $\text{CoFeO}_x\text{H}_y$ ) are benchmark OER catalysts in alkaline conditions. However, the role of each metal species and the nature of the active sites are still unclear. With the development of *in-situ/operando* techniques and theoretical calculation, in-depth comprehension of the catalysts has been acquired in recent years.<sup>76,77,106</sup> In this sub-section of the Thesis, several important previous studies for the identification of the real active sites of the benchmark OER catalysts will be presented.

Bell and coworkers conducted *operando* XAS using high-energy resolution fluorescence detection (HERFD). The results reveals that Fe(III) in  $\text{Ni}_{1-x}\text{Fe}_x\text{OOH}$  has unusually short Fe-O bond distances (compared to  $\gamma\text{-FeOOH}$ ), occupying octahedral sites, surrounded by edge-sharing  $[\text{NiO}_6]$  octahedral (Figure 1.10a).<sup>108</sup> Additionally, the DFT calculations were performed for pure and Fe doped  $\gamma\text{-NiOOH}$  as well as for pure and Ni doped  $\gamma\text{-FeOOH}$ , based on stepwise proton coupled electron transfer (PCET) OER mechanism. As shown in Figure 1.10a, pure  $\gamma\text{-NiOOH}$  adsorbs all the OER intermediates too weakly, while the adsorption on pure  $\gamma\text{-FeOOH}$  is too strong. The Fe sites that are surrounded by next-nearest Ni show near optimal binding energies for the OER intermediates and the formation of  $\text{OOH}^*$  is the PLS (potential limiting step) or the RLS. In contrast,

the Fe doping actually decreases the activity of the Ni site, and the RLS on Ni site is the formation of  $O^*$  (from  $OH^*$ ). The authors, therefore, pointed out the real active sites of Fe-doped NiOOH are Fe, rather than Ni. Instead, the NiOOH is acting as the supporting conductive substrates.

Stahl and coworkers performed *operando* Mössbauer spectroscopic studies for a NiFe layered double hydroxide (LDH) and a hydrous Fe oxide electrocatalyst on carbon cloth.<sup>109</sup> For NiFe LDH, 21% of the total Fe species were oxidized to Fe(IV) under OER. In contrast, no Fe(IV) was detected in pure Fe catalyst. However, the authors suggested that the OER should occur at reactive Fe species located at edge, corner, or defect sites within Fe-doped NiOOH lattice, while the observed Fe(IV) species were mostly in the bulk and not kinetically competent to serve as the active sites.

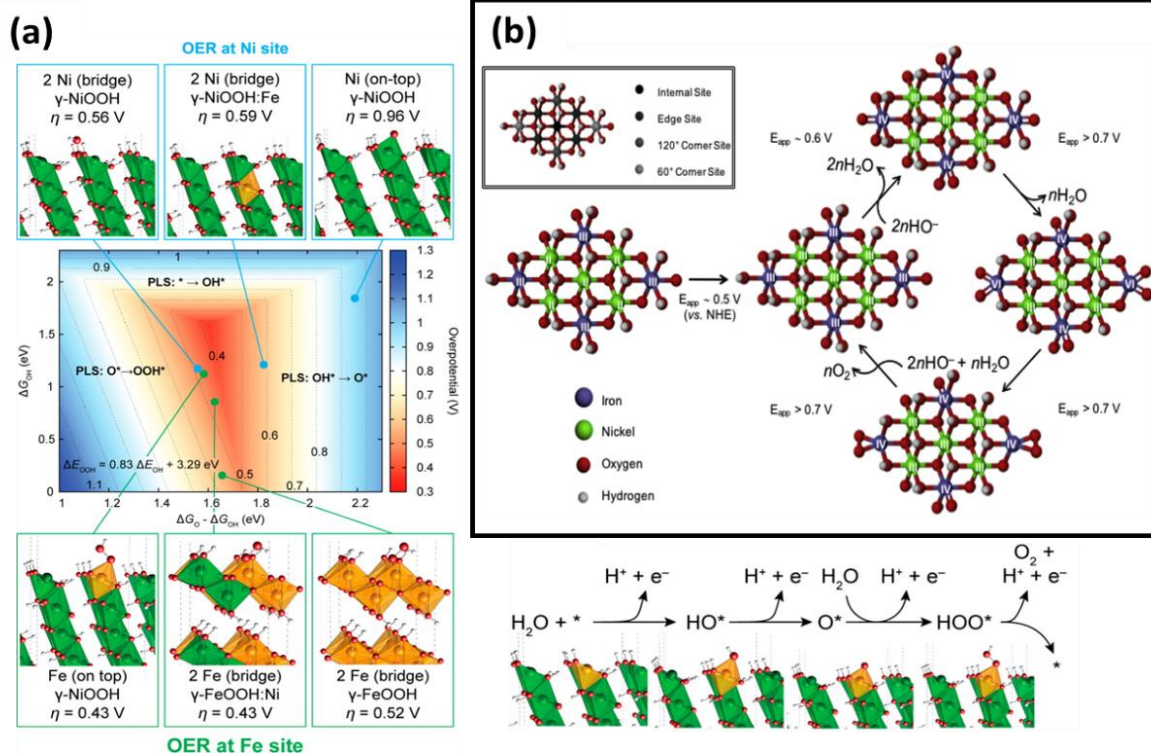


**Figure 1.10** Representative mechanistic studies of  $Ni_{1-x}Fe_xOOH$  OER catalyst. (a) Theoretical OER overpotentials at Ni and Fe surface sites in pure and doped  $\gamma$ -NiOOH and  $\gamma$ -FeOOH model structures based on PCET type OER mechanism. OER activity volcano shows the overpotential is a function of Gibbs free energies of the reaction intermediates. All corresponding model structures are shown with the intermediate whose formation is the PLS. Reproduced with permission.<sup>[108]</sup> Copyright 2015, American Chemical Society (ACS). (b) Proposed OER mechanism and active sites of  $Ni_{1-x}Fe_xOOH$  in non-aqueous electrolyte. Reproduced with permission.<sup>[110]</sup> Copyright 2018, Elsevier.

By using *in situ* XAS, some researchers have also observed Fe(IV) species in both electrodeposited NiFe catalysts and ultrathin NiFe LDH.<sup>111,112</sup> Ahn and Bard employed Surface Interrogation Scanning Electrochemical Microscopy (SI-SECM) to directly measure the surface OER kinetics of Ni(IV) and Fe(IV) in NiOOH, FeOOH, and NiFeO<sub>x</sub>H<sub>y</sub>. They discovered two types of surface sites with fast and slow kinetics, respectively.<sup>113</sup> The fraction of the fast site in NiFeO<sub>x</sub>H<sub>y</sub> matched well with the iron content. Therefore, they concluded that the Fe(IV) site was the active center for OER, with a TOF of 1.7 s<sup>-1</sup> at an overpotential of about 440 mV. As comparisons, the Ni(IV) site in NiOOH has a TOF of 0.04 s<sup>-1</sup>, whereas the Fe(IV) site in FeOOH has a TOF of 0.18 s<sup>-1</sup>. The results are well-consistent with Bell's research<sup>108</sup>.

Considering the life time of key reaction intermediates of Fe-doped NiOOH are too short to be detected in alkaline OER catalytic process, Gray and coworkers studied the behavior of NiFe LDH in non-aqueous medium (acetonitrile). By combining several *in situ* spectroscopic measurements and electrochemical experiments, they identified cis-dioxoiron(VI) as the reactive intermediate (Figure 1.10b).<sup>110</sup> In non-aqueous condition, Fe(III) can be finally oxidized to Fe(VI), while Ni maintains the oxidation state of +3. When the OH<sup>-</sup> is added to solution, Fe(VI) returns back to Fe(III), simultaneously releasing oxygen (Figure 1.10b). Although the properties of the active sites can be quite different in aqueous and non-aqueous conditions, these findings strongly suggested Fe should be the OER active sites of NiFe LDH or NiFeO<sub>x</sub>H<sub>y</sub>.

In sharp contrast to the above-mentioned viewpoints, some researchers demonstrated that Ni is the active sites of NiFeO<sub>x</sub>H<sub>y</sub>, whereas Fe promotes the activity of Ni. Nocera et al. declared that an amorphous Ni oxyhydroxide electrodeposited from Ni-containing borate buffer (Ni-Bi) can be oxidized to an average oxidation state of +3.6 to +3.7 under OER condition.<sup>114</sup> By analyzing the electrokinetic parameters, the authors suggested a chemical coupling of two [Ni(IV)=O] species as the RDS.<sup>101</sup> However, these early experiments did not consider the influence of Fe impurities in electrolyte. In a recent study, after intentionally doping the catalyst with Fe, the same group observed a decreased absorption energy of about 0.8 eV in Ni K-edge XANES (at 60% energy jump level). They assigned this energy decrease as an increased Ni-O covalency, which was correlated to higher formal Ni(IV) character. Thus finally, the authors proposed that Fe doping promoted the access to Ni(IV).<sup>115</sup>



Dau et al. employed *in situ* XAS and spectroelectrochemical study, and they observed a trigonal distortion in di- $\mu$ -hydroxo bridged Ni(II)–Ni(II) motifs as well as in its oxidized form, di- $\mu$ -oxo Ni(IV)–Ni(IV).<sup>116</sup> Incorporation of Fe ions into the structure generates di- $\mu$ -hydroxo Ni(II)–Fe(III) motifs, which decreases the geometric strain in the reduced phase but exacerbates it in the oxidized phase. This inverted effect on the trigonal distortion results in difficulty of oxidation of Ni(II) to Ni(IV) motifs (reflecting by the anodic shift of nickel-based redox peaks). The improved ability to catalyze the OER is attributed to the geometric strain presented in di- $\mu$ -oxo Ni(IV)–Fe(III) sites. The OER activity is thus correlated with introduced geometric distortions caused by redox inactive sites (here is Fe).<sup>116</sup> Similar observation was demonstrated by Durant and the coworkers<sup>117</sup>. By using *in situ* UV-vis spectroelectrochemical study, they pointed out that under OER condition, Fe-doped NiOOH has a RLS related to the oxidized Ni-centered species, with a UV-vis absorption centered at around 610 nm (Figure 1.11a). On the contrary, the oxidized species of FeOOH–NiOOH composite catalyst and pure FeOOH are Fe-centered (the UV-vis absorption centered at around 410 nm, Figure 1.11a).<sup>117</sup> The authors then proposed the OER mechanisms for FeOOH and FeOOH–NiOOH based on Fe as the active centers, while the possible active sites of Fe-doped NiOOH are based on Ni (Figure 1.11b).

By using *in situ* surface-enhanced Raman spectroscopy (SERS), Smith et al. obtained adsorbed nickel active oxygen species ( $\text{NiOO}^\cdot$ , broad Raman peak in the region 900–1150  $\text{cm}^{-1}$ ) on  $\text{NiFeO}_x\text{H}_y$ .<sup>118</sup> The formation of this species seems to support Ni as the active site in  $\text{NiFeO}_x\text{H}_y$ . Very recently, Hu et al. used *operando* Raman spectroscopy and found that Ni sites evolve  $\text{O}_2$  through active oxygen species ( $\text{Ni-OO}^\cdot$ ) and involve lattice oxygen participation. On the contrary, Fe sites produce  $\text{O}_2$  without involving  $\text{Ni-OO}^\cdot$  or lattice oxygen.<sup>119</sup> The authors further systematically studied the OER behavior of exfoliated NiFe LDH with different Fe content by *operando* Raman (Figures 1.11c and 1.11d).<sup>120</sup> When Fe content is below 4.7%, including pure  $\text{Ni(OH)}_2$ , lattice oxygen is involved in OER catalysis, as evidenced by the shift of Raman peaks due to the oxygen isotope exchange (Figure 1.11c). While Fe content is higher than 4.7%, the active sites are Fe dominated and no lattice oxygen participation was observed (Figure 1.11d). Therefore, the active sites may vary depending on the Fe content.

Some DFT calculation studies indicated that both Ni and Fe might participate in OER catalysis together. The possible RLS can be coupling of one  $[\text{Ni(IV)=O}]$  and one  $[\text{Fe(III)-O}^\cdot]$  to release dioxygen.<sup>121</sup> Carter and Martinez suggested the OER of Fe-doped  $\beta$ -NiOOH proceeds through an adsorbed  $\text{OH}^-$  attack to  $[\text{Fe(IV)=O}]$ , simultaneously with hydrogen transfer to nearby Ni(III) site,

thus generating  $[\text{Fe(III)-OO}\cdot]$  (that can be further oxidized to release  $\text{O}_2$ ) and  $\text{Ni(II)}$  species.<sup>96</sup> One evidence of such assumption was reported by Strasser et al. The authors found that a large portion of the Ni ions remained as  $\text{Ni(II)}$  under OER catalytic conditions, whereas the Fe centers remained as  $\text{Fe(III)}$ , regardless of the applied potential.<sup>122</sup>

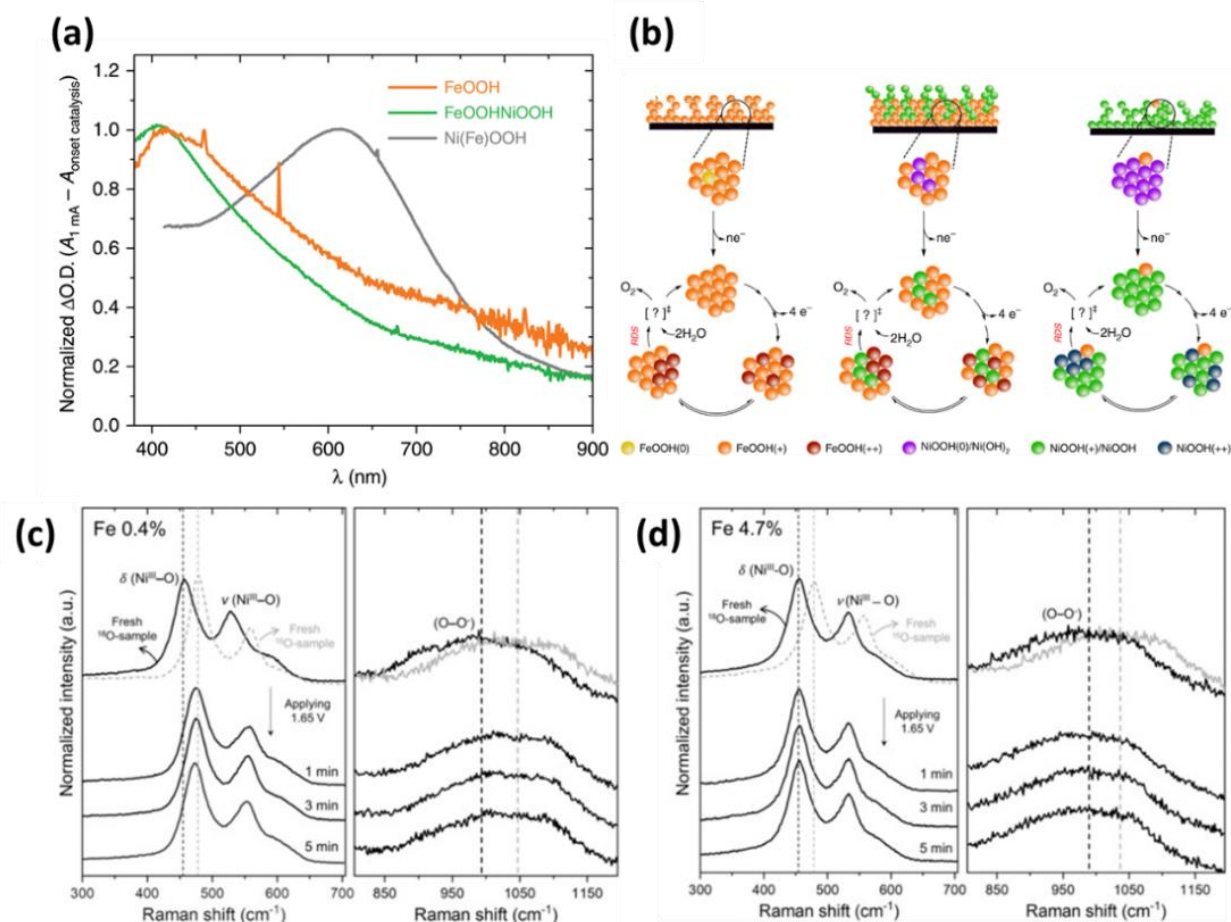


**Figure 1.11** Representative spectroscopic studies of NiFe based OER catalysts. (a) Normalised  $\Delta\text{O.D.}$  UV-vis spectra of the (+/++) oxidation wave correlated with water oxidation for FeOOH (orange), FeOOHNiOOH (green) and Ni(Fe)OOH (grey), obtained by subtracting spectra at OCP after activation from the spectra at  $1\text{ mA/cm}^2$  of current density. (b) Proposed OER mechanism of FeOOH (left), FeOOHNiOOH (middle) and Ni(Fe)OOH (right). Reproduced with permission.<sup>[117]</sup> Copyright 2019, Springer Nature Publishing AG. (c-d) Oxygen isotope exchange experiments. Operando Raman spectra of  $^{18}\text{O}$ -labeled NiFe LDHs containing (c) 0.4% and (d) 4.7% Fe, acquired at 1.65 V in Fe-free  $0.1\text{ M H}_2^{16}\text{O}$  solution of  $\text{K}^{16}\text{OH}$ . Reprinted with permission.<sup>[120]</sup> Copyright 2020, Wiley-VCH.

Similar to  $\text{NiFeO}_x\text{H}_y$ , there are also many debates related to active motifs of  $\text{CoFeO}_x\text{H}_y$ . Both Co and Fe have been proposed as the active centers.<sup>123-126</sup> The assumption was based on the observed species with high oxidation state. For examples, Boettcher et al. observed Fe species with higher than +3 oxidation state under oxidative potential, thus they suggested the oxidized Fe species of  $\text{CoFeO}_x\text{H}_y$  played a key role in the OER mechanism.<sup>124</sup> On the contrary, by using HERFD-XAS, Chen and coworkers detected high-valent Co(IV) species, while Fe was remained as Fe(III). They suggested Fe ions can promote the stabilization of the Co ions under high oxidation state during water oxidation.<sup>123</sup>

In summary, despite the great efforts for investigating the active sites and related OER mechanisms by using *in-situ/operando* spectroscopies and theoretical calculations, the viewpoints of the real active sites of the state-of-the-art OER catalysts are still under debate. The results were quite different and even contradictory between different studies. These discrepancies may result from different experimental conditions and different preparation methods of the catalysts. The different phase, composition, and crystallinity of the catalysts, as well as the heterogeneity of the catalyst structure may result contradict conclusions. Thus, developing catalyst materials with well-defined structure might be a possible way to address the issues.

## 1.5 Atomically dispersed catalysts

### 1.5.1 General introduction of atomically dispersed catalysts

As depicted in Figure 1.12, when the particle size of a certain material gradually reduced, the surface free energy increased simultaneously, and the catalytic properties will significantly change. At the limit, the catalyst can be isolated as single atoms or single ions.<sup>127</sup> The atomically dispersed catalysts (including subnanoclusters and single-atoms) displayed outstanding properties in comparison with traditional bulk and nano materials.<sup>127-129</sup> Single atom catalysts (SACs) are able to achieve up to 100% atomic efficiency because of every metal centers are accessible and can serve as active center. The metal loading of SACs is typically quite low thus economize the cost of the catalysts. The single atom possesses high surface energy, which may have higher activity than traditional nanomaterials. Comparing with nano-catalysts, tuning the activity of atomically dispersed catalysts is more facile by changing the coordination environment. Moreover, the determination of mechanism of SACs is much easier, due to the well-defined structure of the active centers. SACs are like homogeneous catalysts, but they are more stable, because they

don't have unstable fragile organic ligands. Single atom catalysis builds a bridge between homogeneous and heterogeneous catalysis.<sup>127-129</sup> For these reasons, exploiting stable and active SACs is a hot research spot in recent years.<sup>127-130</sup>

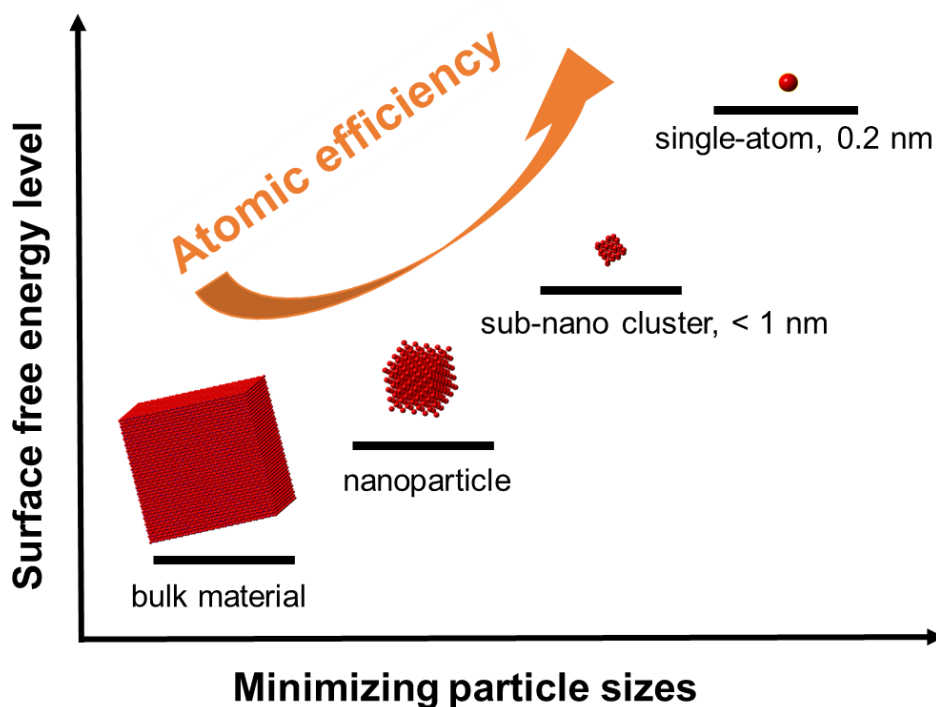


**Figure 1.12** Schematic diagram of the surface free energy level and the atomic efficiency depends on particle sizes.

Due to high surface free energy and highly unsaturated nature, the SACs must be anchored to a certain support, such as metal oxides or carbon based materials, in order to be stabilized and dispersed (Figure 1.13).<sup>127,128</sup> The anchoring sites for SACs are usually vacancies, defects or certain functional groups of the substrates, which means that the single-atom or single-ions should be coordinated by heteroatoms such as O, N, P, S, and so on (Figure 1.13). Heteroatoms doped carbon materials possess large surface area, porous structure, excellent conductivity, and tunable coordination environment, thus rendering them good choices for supporting and stabilizing high loadings of SACs with electrocatalytic activity.<sup>128,129,131</sup> Recent technological advances render many methods for the synthesis of high loadings SACs or catalyst composed of subnano clusters.<sup>127-130</sup>

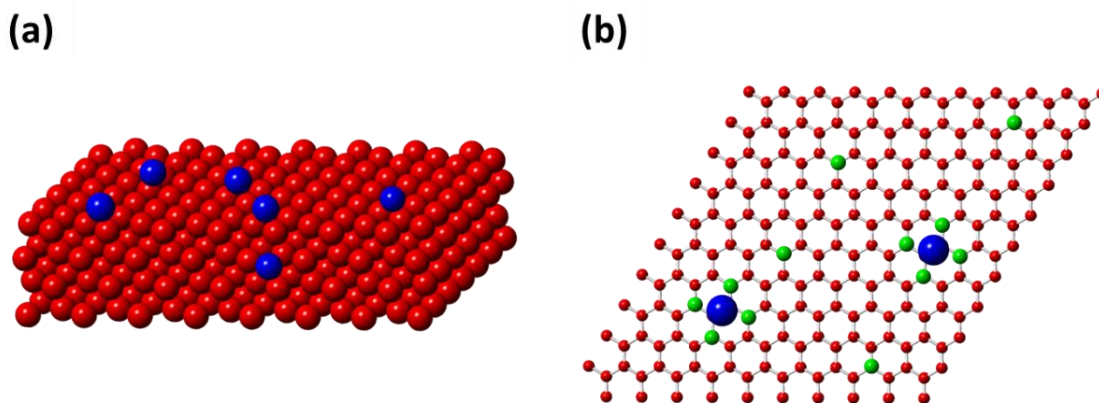


**Figure 1.13** General schematic diagrams for single atoms immobilized on (a) metal oxides and (b) heteroatoms doped carbon. Red: atoms from the substrates; Blue: anchored single atoms; Green: heteroatoms.

In early years, most of the investigated reaction for single-atoms involves the oxidation and hydrogenation of small molecules and organic compounds, water-gas-shift (WGS) and reforming reactions.<sup>127,128,130</sup> These catalysts showed both better activity and higher selectivity compared with traditional nanomaterial catalysts.<sup>127,128,130</sup> Inspired by the great success of SACs in heterogeneous catalysis, some researchers investigated the properties of SACs in the research field of electrocatalysis for energy conversion,<sup>128,129,132-134</sup> like oxygen reduction reaction (ORR), HER, CRR, NRR, and so on. Especially, the Fe-based SACs that coordinated by four nitrogen (Fe-N<sub>4</sub>) exhibit excellent performance for 4-electron ORR.<sup>135</sup> Such Fe SACs may have the potential to substitute Pt, the current cathodic catalysts in fuel cell.<sup>135,136</sup> Moreover, a single-atom Fe SAC coordinated by four pyrrolic type N showed nearly 100% selectivity and an onset overpotential as low as 80 mV for electrocatalytic reduction of CO<sub>2</sub> to CO.<sup>137</sup> The performance even exceeded the benchmark Au-based catalysts.

### 1.5.2 Atomically dispersed catalysts for OER

The research towards SACs that are active for OER did not emerge until recent years.<sup>132-134</sup> In addition to catalyzing ORR and CRR, some theoretical calculation also predicted that the Co and the Ni atoms coordinated by nitrogen or other heteroatoms are promising candidates for OER electrocatalysis.<sup>138,139</sup> Researchers then discovered that some SACs based on non-noble metals

exhibited outstanding activity towards electrocatalytic OER, which are in accordance with theoretical study. As a famous example, Co-C<sub>3</sub>N<sub>4</sub>-CNT whose active sites are Co-N<sub>2</sub> moiety in the g-C<sub>3</sub>N<sub>4</sub> matrix (Figure 1.14a) exhibited comparable activities with precious metal benchmarks for both OER and ORR in 1M KOH.<sup>139</sup> The OER activity of Co-C<sub>3</sub>N<sub>4</sub>-CNT was better than control samples including cobalt oxides, Co atoms that were not modified on C<sub>3</sub>N<sub>4</sub> matrix, and metal-free catalysts, highlighting the importance of the special coordination structure of Co SAC on g-C<sub>3</sub>N<sub>4</sub> (Figure 1.14b).<sup>139</sup>

By introducing second heteroatom other than nitrogen to the substrate can further tune the reactivity of single-atoms. For example, a Co SAC supported on N, S co-doped graphene oxide (Co-NSG) were prepared by simple hydrothermal and impregnation method.<sup>140</sup> The Co-NSG exhibited better OER activity compared to both the catalysts without heteroatoms doping and the catalysts with only one heteroatom (N or S) doping. Two kinds of heteroatoms with different electron-negative properties are beneficial for achieving higher activity. Similarly, Ni SAC immobilized on N, S co-doped porous carbon nanosheet was reported to have prominent performance for electrocatalytic OER.<sup>141</sup> Additionally, it can act as a good cocatalyst for a hematite photoanode.<sup>141</sup>

Huang et al. employed a general process to synthesize Fe, Co, and Ni single-atoms that are anchored on N-doped defect-rich graphene (M-NHGFs).<sup>142</sup> These single-atoms have a common M-N<sub>4</sub>C<sub>4</sub>-O<sub>2</sub> coordination structure (Figure 1.14c). The authors then systematically compared the OER activities, following the trend as Ni SAC > Co SAC > Fe SAC (Figure 1.14d). Specifically, the Ni-NHGF catalyst showed an overpotential of 331 mV to reach 10 mA/cm<sup>2</sup>. The TOF of the catalyst is 0.72 s<sup>-1</sup> at 300 mV overpotential, exceeding many heterogeneous Ni-based OER catalysts. In addition to Fe, Co, Ni SACs, Mn SAC immobilized on N-doped graphene that has Mn-N<sub>4</sub> active site also performed prominent activity for both Ce(IV)-driven (chemical catalytic) and electrochemical OER.<sup>143</sup>

In addition to SACs modified on carbon support, W<sup>144</sup>, Ru<sup>145</sup>, Ir<sup>146</sup>, Au<sup>147</sup> and Pt<sup>148</sup> based single-atoms were anchored on metal (oxy)hydroxides or LDH-based support materials, which also exhibited outstanding OER activity. Unlike carbon-based support materials, these metal (oxy)hydroxides or LDHs (like Co(OH)<sub>2</sub>, Ni(OH)<sub>2</sub>, or NiFe LDH) also have noticeable activity for OER. Theoretical calculation and *in situ* spectroscopic studies suggested that the supported single-atoms can either act as the centers of OER catalysis or just promote the OER activity of the support materials via electronic effect.

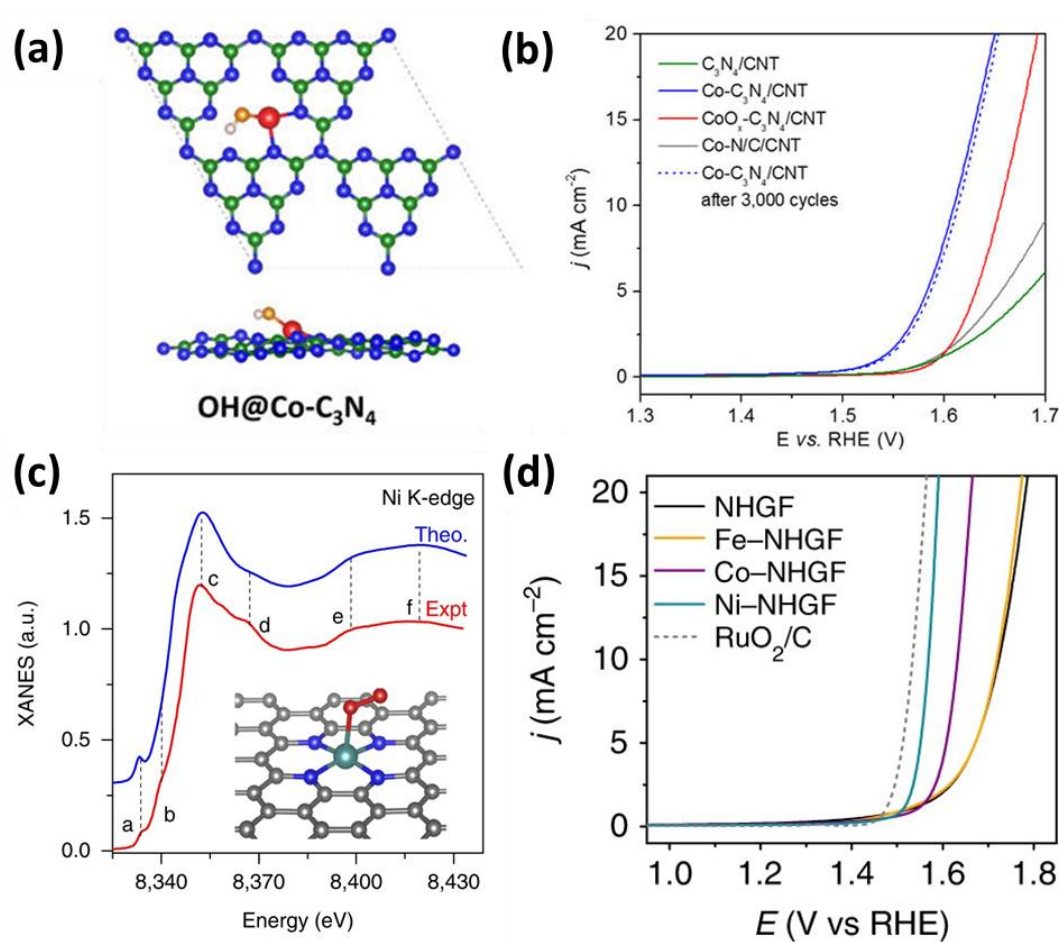


**Figure 1.14** Representative studies of single-atom based OER catalysts. (a) Optimized structure of Co-C<sub>3</sub>N<sub>4</sub>-CNT. C: green; N: blue; Co: red; O: orange; H: grey. (b) Comparison of OER activity of Co-C<sub>3</sub>N<sub>4</sub>-CNT with various control samples. Reproduced with permission.<sup>[139]</sup> Copyright 2017, American Chemical Society (ACS). (c) Comparison between the experimental K-edge XANES spectra of Ni-NHGF and the theoretical spectra calculated based on MN<sub>4</sub>C<sub>4</sub> moieties embedded in the 2D graphene lattice. Some of the main features reproduced are highlighted at points a–f. The teal, blue, red and grey spheres represent Ni, N, O and C, respectively. (d) OER activity comparison of various M-NHGFs and RuO<sub>2</sub>/C reference catalyst. Reproduced with permission.<sup>[142]</sup> Copyright 2019, Springer Nature Publishing AG.

## 1.6 Challenges and opportunities in the research field

After reviewing the development of heterogeneous OER electrocatalysts and the advancement of the deep insight of the active sites and reaction mechanisms, we see that great progress have been made in the research field of OER. Specifically, nanostructured OER catalysts can achieve

lower than 200 mV overpotential to reach a current density of 10 mA/cm<sup>2</sup>. The nature of the active motifs can be probed by state-of-the-art *in-situ/operando* spectroscopy techniques. The catalytic process and activity can be predicted by DFT calculation with certain accuracy. Despite these great efforts and developments, there are still several gaps and limitations in the research field. First, the atomic efficiency of the OER catalysts composed of nanomaterials are not very high. In most of the cases, certain amounts of the active sites are inaccessible during catalysis. Second, the distribution of the active sites in nanomaterials is typically not uniform. As shown in Figure 1.15, different kinds of possible active sites, including steps, kinks, and corners, make the determination of both the properties of active sites and the catalytic reaction mechanisms complicated.<sup>128</sup> Additionally, in Section 1.4.4, we have already seen that the different phase, composition, and crystallinity of the catalysts, as well as the heterogeneity of the catalyst structure may result in debate and even contradict conclusions for mechanistic studies. These limitations impede both the deep investigation of the catalytic nature and the further development of more advanced OER catalysts. Third, the current OER catalysts usually have conventional PCET-type OER mechanisms (Figure 1.6a), in which the performance is limited by scaling relationship of oxygen-containing intermediates. That is why the overpotential of these OER catalysts can not be further decreased. Although a so-called 'bifunctional' OER mechanism was predicted to break the scaling relationship (Figure 1.9), there is no direct experimental evidence so far.

Moreover, although the theoretical calculation is able to predict the reaction mechanisms and catalytic activities, the mismatch between theoretical prediction and experimental data usually happens. This is because the realistic catalytic conditions are influenced by many factors like solvent, electric field, surface adsorbates, and so on. Since the theoretical simulated conditions are usually simplified or idealized, the predicted results can be deviated from real catalysis. The assumptions about the structures and active sites of the catalysts can be erroneous as well. Therefore, the theoretical approach will not replace, but rather require experimental approaches to validate. Both theoretical and experimental methods should be combined to better understand the reaction mechanisms and correlate the performance with certain descriptors.



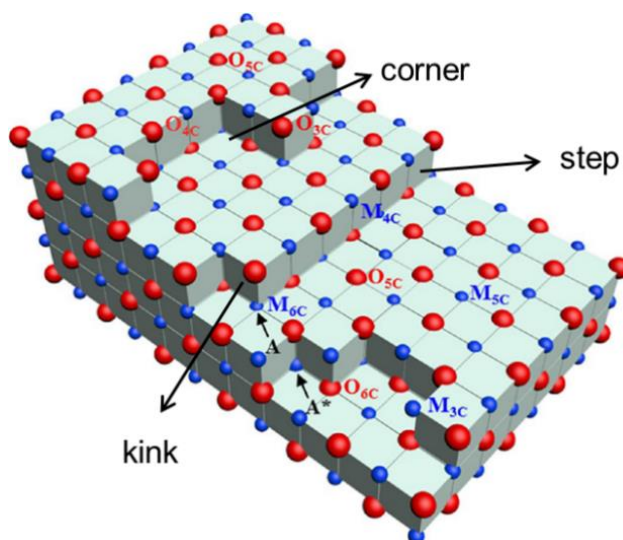


**Figure 1.15** Schematic diagram illustrates the various possible active sites on a metal oxide surface, including steps, kinks, corners, and so on. Blue balls represent metal, while red balls represent oxygen. The coordination numbers (CNs) are indicated. Reproduced with permission.<sup>[128]</sup> Copyright 2016, American Chemical Society (ACS).

The recently developed single-atom OER catalysts provide an opportunity to address the aforementioned issues, due to the nearly 100% atomic efficiency and high intrinsic activity for OER. In addition, due to the well-defined structures and active centers, the single-atom OER catalysts have the potential to be the models for investigating OER mechanism in molecular level. So far, nevertheless, such in-depth studies for SACs were rarely carried out. We still do not know whether the atomically dispersed OER catalysts have similar reaction mechanisms as heterogeneous OER catalysts composed of nanomaterials. On the other hand, it is interesting that whether an atomically dispersed catalysts with the isolated units composed of two metals (so-called double-atom catalysts, DACs) can be made and catalyze OER in alkaline condition. As mentioned in Section 1.3.3, the state-of-the-art OER catalysts in alkaline condition are composed of two metals. Another concern is the stability of atomically dispersed catalysts. People are curious about whether the catalysts are stable or whether there are some compositional and structural evolutions during catalytic process.

## 1.7 Research methods

According to the current limitations of the research in OER, this Thesis aims to fill the gap of the research field from the following aspects. (1) Development of atomically dispersed catalysts with well-defined active sites that can catalyze OER in alkaline condition with high intrinsic activity. Specifically, the Thesis will try to make the DACs and examine if they have higher intrinsic activity compared to SACs. The compositional and structural stability of the atomically dispersed catalysts will be inspected. (2) If the atomically dispersed catalysts (including both SACs and DACs) are stable or dynamically stable, they will be employed as molecular platforms to study the OER mechanisms. The properties of the key intermediates and the details of the reaction pathways will be systematically studied. The mechanistic details will be compared with similar homogeneous metal complexes and heterogeneous metal oxyhydroxides that have similar metal compositions. (3) Providing experimental evidences to validate the 'bifunctional' OER mechanism (hitherto only predicted by DFT calculation), for which can break the overpotential limitation imposed by scaling relationship of conventional OER mechanism. To perform this experiment, the Thesis will first investigate the model catalyst that is predicted to possibly have bifunctional mechanism. Then the difference of the catalytic behavior between this model catalyst and another catalyst that operated by conventional OER mechanism will be systematically compared.

Some specific research methods are required to realize the above-mentioned goals. The research methods of this Thesis are summarized in Figure 1.16. Generally, this Thesis will combine various characterization approaches to have a systematic study. In first stage, the suitable catalysts will be synthesized. The synthetic conditions will be optimized to obtain the desired materials. Next, various *ex situ* physical methods, including XRD, Raman, XPS, TEM (Transmission Electron Microscopy), ICP-AES, and so on, will characterize the catalysts. These characterizations provide the information like crystallinity, phase, morphology, oxidation state, composition and the loading of catalyst. Simultaneously, the OER activity will be measured and evaluated in conventional three-electrode system. Importance will be given to quantitative values such as specific activity, TOF, overpotential to reach 10 mA/cm<sup>2</sup>, and Tafel Slope. From the basic characterization, the initial view of whether the atomically dispersed catalysts are stable or whether there are some compositional and structural changes during OER catalysis will be acquired.

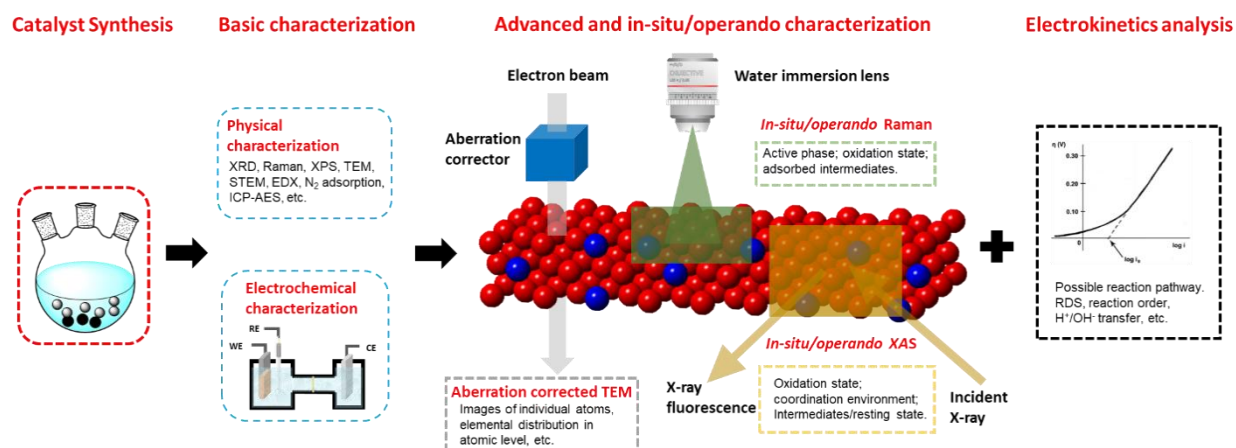


**Figure 1.16** Illustration of the main research methods and techniques adopted in this Thesis, as well as the key information that can be obtained.

In the third stage, by cooperating with other colleagues and collaborators in other institute, advanced characterization will be performed. Specifically, spherical aberration corrected TEM in HAADF-STEM (High-Angle Annular Dark-Field Scanning Transmission Electron Microscopy) mode is a powerful technique to image single atoms and clusters with several atoms (sub-nano clusters).<sup>128, 129</sup> The atomically dispersed species can be distinguished with the support by atomic weight contrast. In addition, *in-situ/operando* spectroscopy, including Raman (sensitive to catalyst/electrolyte interface) and XAS (reflect the information of bulk material) will offer dynamic information of the catalysts. The evolution of the catalysts under different applied potential and reaction durations can be traced. It is also possible to detect the high-valent key intermediates. After *in-situ/operando* experiments, the important electrokinetic parameters including Tafel slope, reaction orders, hydrogen-deuterium isotope effect will be analyzed. From the results, we will know the possible RDS,  $H^+/OH^-$  transfer properties, as well as the possible reaction pathways. The combination of *in-situ/operando* techniques and electrokinetic analysis can lead to comprehensive understanding of the dynamic evolution of the catalysts/active motifs and the catalytic mechanisms.

The design of the electrochemical cells (ECs) for *in-situ/operando* measurements is crucial for obtaining reasonable data.<sup>105</sup> The most important part is to fit the working electrode to various light sources and detectors. For Raman, the key point is using lens with long-working-distance water-immersion objective to allow sufficient amount of electrolyte to be placed over catalyst

(Figure 1.17a).<sup>119,120</sup> The general design of the EC for XAS measurements is in Figure 1.17b.<sup>149</sup> Normally, XAS studies of electrocatalysts are performed in fluorescence mode. The Kapton window (Kapton polyimide film) in the EC allows the incident X-ray to transmit and interact with the samples.<sup>149</sup> Thin water layer is necessary to minimize the attenuation of X-ray while ensure the catalysis happen in a certain reaction rate.

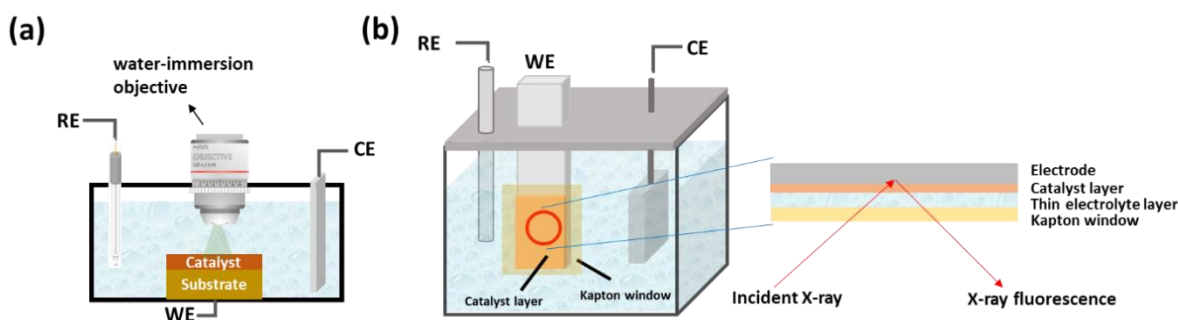


**Figure 1.17** General design of ECs for collecting Raman and XAS data under OER catalytic conditions. (a) ECs for *in-situ/operando* Raman; (b) ECs for *in-situ/operando* XAS.

## 1.8 Outline of the following Chapters

According to the aforementioned research methods, in the following Chapters, the Thesis will employ atomically dispersed catalysts as molecular models to reveal the OER mechanisms and dynamic evolution of the active sites in atomic level. Chapter 2 describes that a Co single-atom precatalyst can be transformed to a Co-Fe DAC via electrochemical activation in Fe-containing KOH. This DAC has atomically dispersed well-defined structure. Its intrinsic activity for OER is among the best-reported OER catalysts in alkaline conditions. The Chapter 3 further reveals that the double-atom catalysis is general and ubiquitous in alkaline OER catalysis, many DACs with similar coordination environment as the Co-Fe DAC were developed. All these DACs contain well-defined structure, which resembles the possible key active centers of bimetallic heterogeneous catalysts. Therefore, in Chapter 4, the Thesis presents a systematic mechanistic insight of DACs and the related catalytic process. The similarity and difference of the mechanisms compared to homogeneous and heterogeneous OER catalysts are discussed.

In addition to the research work related to atomically dispersed catalysts, this Thesis also provides experimental methods to validate a novel 'bifunctional' OER mechanism (Chapter 5). This mechanism is different from conventional OER mechanism and hitherto only proposed by DFT calculation. The Chapter confirms that a composite catalyst (FeOOH-NiOOH) operated by this mechanism exhibited much higher intrinsic activity compared to conventional NiFe LDH. The mechanistic difference of the two catalysts is systematically compared.

The last Chapter of the Thesis (Chapter 6) provides overall conclusions as well as the outlook and perspectives in the research field.

Last but not the least, the Appendix, the final part of the Thesis, provides detailed knowledge about the related electrochemical methods and models adopted in this Thesis. The mathematical derivation of some important equations are also demonstrated.

## 1.9 References of Chapter 1

- (1) Song, F.; Bai, L.; Moysiadou, A.; Lee, S.; Hu, C.; Liardet, L.; Hu, X. Transition Metal Oxides as Electrocatalysts for the Oxygen Evolution Reaction in Alkaline Solutions: An Application-Inspired Renaissance. *J. Am. Chem. Soc.* **2018**, *140*, 7748-7759.
- (2) Lewis, N. S.; Nocera, D. G. Powering the planet: Chemical challenges in solar energy utilization. *Proc. Natl. Acad. Sci. USA* **2006**, *103*, 15729-15735.
- (3) Cook, T. R.; Dogutan, D. K.; Reece, S. Y.; Surendranath, Y.; Teets, T. S.; Nocera, D. G. Solar energy supply and storage for the legacy and nonlegacy worlds. *Chem. Rev.* **2010**, *110*, 6474-6502.
- (4) Schiermeier, Q.; Tollefson, J.; Scully, T.; Witze, A.; Morton, O. Energy alternatives: Electricity without carbon. *Nature News* **2008**, *454*, 816-823.
- (5) Chu, S.; Majumdar, A. Opportunities and challenges for a sustainable energy future. *Nature* **2012**, *488*, 294-303.
- (6) BP, B. P. Statistical Review of World Energy 2019. **2019**.
- (7) Petroleum, B. Statistical review of world energy 2009. *BP, London* **2009**.
- (8) Peters, G. P.; Le Quéré, C.; Andrew, R. M.; Canadell, J. G.; Friedlingstein, P.; Ilyina, T.; Jackson, R. B.; Joos, F.; Korsbakken, J. I.; McKinley, G. A. Towards real-time verification of CO<sub>2</sub> emissions. *Nat. Climate Change* **2017**, *7*, 848-850.
- (9) Ekwurzel, B.; Boneham, J.; Dalton, M. W.; Heede, R.; Mera, R. J.; Allen, M. R.; Frumhoff, P. C. The rise in global atmospheric CO<sub>2</sub>, surface temperature, and sea level from emissions traced to major carbon producers. *Climatic Change* **2017**, *144*, 579-590.

- (10) Licker, R.; Ekwurzel, B.; Doney, S.; Cooley, S.; Lima, I.; Heede, R.; Frumhoff, P. Attributing ocean acidification to major carbon producers. *Environ. Res. Lett.* **2019**, *14*, 124060.
- (11) Omer, A. M. Energy, environment and sustainable development. *Renew. Sust. Energ. Rev.* **2008**, *12*, 2265-2300.
- (12) Lewis, N. S. Research opportunities to advance solar energy utilization. *Science* **2016**, *351*, aad1920.
- (13) Jacobson, M. Z.; Delucchi, M. A.; Bauer, Z. A. F.; Goodman, S. C.; Chapman, W. E.; Cameron, M. A.; Bozonnat, C.; Chobadi, L.; Clonts, H. A.; Enevoldsen, P.; Erwin, J. R.; Fobi, S. N.; Goldstrom, O. K.; Hennessy, E. M.; Liu, J.; Lo, J.; Meyer, C. B.; Morris, S. B.; Moy, K. R.; O'Neill, P. L.; Petkov, I.; Redfern, S.; Schucker, R.; Sontag, M. A.; Wang, J.; Weiner, E.; Yachanin, A. S. 100% Clean and Renewable Wind, Water, and Sunlight All-Sector Energy Roadmaps for 139 Countries of the World. *Joule* **2017**, *1*, 108-121.
- (14) Rehman, S.; Al-Hadhrami, L. M.; Alam, M. M. Pumped hydro energy storage system: A technological review. *Renew. Sust. Energ. Rev.* **2015**, *44*, 586-598.
- (15) Etacheri, V.; Marom, R.; Elazari, R.; Salitra, G.; Aurbach, D. Challenges in the development of advanced Li-ion batteries: a review. *Energy Environ. Sci.* **2011**, *4*, 3243-3262.
- (16) González, A.; Goikolea, E.; Barrena, J. A.; Mysyk, R. Review on supercapacitors: Technologies and materials. *Renew. Sust. Energ. Rev.* **2016**, *58*, 1189-1206.
- (17) Seh, Z. W.; Kibsgaard, J.; Dickens, C. F.; Chorkendorff, I.; Nørskov, J. K.; Jaramillo, T. F. Combining theory and experiment in electrocatalysis: Insights into materials design. *Science* **2017**, *355*, eaad4998.
- (18) Wang, T.; Xie, H.; Chen, M.; D'Aloia, A.; Cho, J.; Wu, G.; Li, Q. Precious metal-free approach to hydrogen electrocatalysis for energy conversion: From mechanism understanding to catalyst design. *Nano Energy* **2017**, *42*, 69-89.
- (19) Ramachandran, R.; Menon, R. K. An overview of industrial uses of hydrogen. *Int. J. Hydrog.* **1998**, *23*, 593-598.
- (20) Ogden, J. M. Prospects for building a hydrogen energy infrastructure. *Annu. Rev. Energ. Environ.* **1999**, *24*, 227-279.
- (21) Morales-Guio, C. G.; Stern, L. A.; Hu, X. Nanostructured hydrotreating catalysts for electrochemical hydrogen evolution. *Chem. Soc. Rev.* **2014**, *43*, 6555-6569.
- (22) Hunter, B. M.; Gray, H. B.; Muller, A. M. Earth-Abundant Heterogeneous Water Oxidation Catalysts. *Chem. Rev.* **2016**, *116*, 14120-14136.
- (23) Suen, N. T.; Hung, S. F.; Quan, Q.; Zhang, N.; Xu, Y. J.; Chen, H. M. Electrocatalysis for the oxygen evolution reaction: recent development and future perspectives. *Chem. Soc. Rev.* **2017**, *46*, 337-365.

- (24) Tahir, M.; Pan, L.; Idrees, F.; Zhang, X.; Wang, L.; Zou, J.-J.; Wang, Z. L. Electrocatalytic oxygen evolution reaction for energy conversion and storage: A comprehensive review. *Nano Energy* **2017**, *37*, 136-157.
- (25) Roger, I.; Shipman, M. A.; Symes, M. D. Earth-abundant catalysts for electrochemical and photoelectrochemical water splitting. *Nat. Rev. Chem.* **2017**, *1*, 0003.
- (26) Carmo, M.; Fritz, D. L.; Mergel, J.; Stolten, D. A comprehensive review on PEM water electrolysis. *Int. J. Hydrog.* **2013**, *38*, 4901-4934.
- (27) Vincent, I.; Bessarabov, D. Low cost hydrogen production by anion exchange membrane electrolysis: A review. *Renew. Sust. Energ. Rev.* **2018**, *81*, 1690-1704.
- (28) Zhu, D. D.; Liu, J. L.; Qiao, S. Z. Recent Advances in Inorganic Heterogeneous Electrocatalysts for Reduction of Carbon Dioxide. *Adv. Mater.* **2016**, *28*, 3423-3452.
- (29) Gao, D.; Arán-Ais, R. M.; Jeon, H. S.; Roldan Cuenya, B. Rational catalyst and electrolyte design for CO<sub>2</sub> electroreduction towards multicarbon products. *Nat. Catal.* **2019**, *2*, 198-210.
- (30) Qing, G.; Ghazfar, R.; Jackowski, S. T.; Habibzadeh, F.; Ashtiani, M. M.; Chen, C. P.; Smith, M. R., 3rd; Hamann, T. W. Recent Advances and Challenges of Electrocatalytic N<sub>2</sub> Reduction to Ammonia. *Chem. Rev.* **2020**, *120*, 5437-5516.
- (31) Guo, W.; Zhang, K.; Liang, Z.; Zou, R.; Xu, Q. Electrochemical nitrogen fixation and utilization: theories, advanced catalyst materials and system design. *Chem. Soc. Rev.* **2019**, *48*, 5658-5716.
- (32) Qi, J.; Zhang, W.; Cao, R. Solar-to-Hydrogen Energy Conversion Based on Water Splitting. *Adv. Energy Mater.* **2018**, *8*, 1701620.
- (33) Jiang, C.; Moniz, S. J. A.; Wang, A.; Zhang, T.; Tang, J. Photoelectrochemical devices for solar water splitting - materials and challenges. *Chem. Soc. Rev.* **2017**, *46*, 4645-4660.
- (34) Bard, A. J.; Faulkner, L. R.; Leddy, J.; Zoski, C. G.: *Electrochemical methods: fundamentals and applications*; Wiley New York, 1980; Vol. 2.
- (35) Delahay, P.; Pourbaix, M.; Van Rysselberghe, P. Potential-pH diagrams. *J. Chem. Educ.* **1950**, *27*, 683.
- (36) Gagliardi, C. J.; Vannucci, A. K.; Concepcion, J. J.; Chen, Z.; Meyer, T. J. The role of proton coupled electron transfer in water oxidation. *Energy Environ. Sci.* **2012**, *5*, 7704-7717.
- (37) McCrory, C. C.; Jung, S.; Peters, J. C.; Jaramillo, T. F. Benchmarking heterogeneous electrocatalysts for the oxygen evolution reaction. *J. Am. Chem. Soc.* **2013**, *135*, 16977-16987.
- (38) Han, L.; Dong, S.; Wang, E. Transition-Metal (Co, Ni, and Fe)-Based Electrocatalysts for the Water Oxidation Reaction. *Adv. Mater.* **2016**, *28*, 9266-9291.
- (39) Hernández-Pagán, E. A.; Vargas-Barbosa, N. M.; Wang, T.; Zhao, Y.; Smotkin, E. S.; Mallouk, T. E. Resistance and polarization losses in aqueous buffer-membrane electrolytes for water-splitting photoelectrochemical cells. *Energy Environ. Sci.* **2012**, *5*, 7582-7589.

- (40) Hillman, A. R. The EQCM: electrogravimetry with a light touch. *J. Solid State Electrochem.* **2011**, *15*, 1647-1660.
- (41) Moysiadou, A.; Hu, X. Stability profiles of transition metal oxides in the oxygen evolution reaction in alkaline medium. *J. Mater. Chem. A* **2019**, *7*, 25865-25877.
- (42) Morales-Guio, C. G.; Liardet, L.; Hu, X. Oxidatively Electrodeposited Thin-Film Transition Metal (Oxy)hydroxides as Oxygen Evolution Catalysts. *J. Am. Chem. Soc.* **2016**, *138*, 8946-8957.
- (43) Park, S.; Shao, Y.; Liu, J.; Wang, Y. Oxygen electrocatalysts for water electrolyzers and reversible fuel cells: status and perspective. *Energy Environ. Sci.* **2012**, *5*, 9331.
- (44) Umena, Y.; Kawakami, K.; Shen, J. R.; Kamiya, N. Crystal structure of oxygen-evolving photosystem II at a resolution of 1.9 Å. *Nature* **2011**, *473*, 55-60.
- (45) Dau, H.; Limberg, C.; Reier, T.; Risch, M.; Roggan, S.; Strasser, P. The Mechanism of Water Oxidation: From Electrolysis via Homogeneous to Biological Catalysis. *ChemCatChem* **2010**, *2*, 724-761.
- (46) Singh, A.; Spiccia, L. Water oxidation catalysts based on abundant 1st row transition metals. *Coord. Chem. Rev.* **2013**, *257*, 2607-2622.
- (47) Lubitz, W.; Reijerse, E. J.; Messinger, J. Solar water-splitting into H<sub>2</sub> and O<sub>2</sub>: design principles of photosystem II and hydrogenases. *Energy Environ. Sci.* **2008**, *1*, 15.
- (48) Duan, L.; Bozoglian, F.; Mandal, S.; Stewart, B.; Privalov, T.; Llobet, A.; Sun, L. A molecular ruthenium catalyst with water-oxidation activity comparable to that of photosystem II. *Nat. Chem.* **2012**, *4*, 418-423.
- (49) Efrati, A.; Tel-Vered, R.; Michaeli, D.; Nechushtai, R.; Willner, I. Cytochrome c-coupled photosystem I and photosystem II (PSI/PSII) photo-bioelectrochemical cells. *Energy Environ. Sci.* **2013**, *6*, 2950.
- (50) Zhang, J. Z.; Bombelli, P.; Sokol, K. P.; Fantuzzi, A.; Rutherford, A. W.; Howe, C. J.; Reisner, E. Photoelectrochemistry of Photosystem II in Vitro vs in Vivo. *J. Am. Chem. Soc.* **2018**, *140*, 6-9.
- (51) Karkas, M. D.; Verho, O.; Johnston, E. V.; Akerman, B. Artificial photosynthesis: molecular systems for catalytic water oxidation. *Chem. Rev.* **2014**, *114*, 11863-12001.
- (52) Limburg, B.; Bouwman, E.; Bonnet, S. Molecular water oxidation catalysts based on transition metals and their decomposition pathways. *Coord. Chem. Rev.* **2012**, *256*, 1451-1467.
- (53) Li, F.; Yang, H.; Li, W.; Sun, L. Device Fabrication for Water Oxidation, Hydrogen Generation, and CO<sub>2</sub> Reduction via Molecular Engineering. *Joule* **2018**, *2*, 36-60.
- (54) Bode, H.; Dehmelt, K.; Witte, J. Zur kenntnis der nickelhydroxidelektrode—I. Über das nickel (II)-hydroxidhydrat. *Electrochim. Acta* **1966**, *11*, 1079-1071.
- (55) Morita, M.; Iwakura, C.; Tamura, H. The anodic characteristics of manganese dioxide electrodes prepared by thermal decomposition of manganese nitrate. *Electrochim. Acta* **1977**, *22*, 325-328.



- (56) El Wakkad, S.; Hickling, A. The anodic behaviour of metals. Part VI.—Cobalt. *Trans. Faraday Soc.* **1950**, *46*, 820-824.
- (57) Schultze, J.; Mohr, S.; Lohrengel, M. Electrode reactions at modified surfaces dependent on the reaction site:  $\gamma$ -FeOOH as example. *J. Electroanal. Chem. Interf. Electrochem.* **1983**, *154*, 57-68.
- (58) Młynarek, G.; Paszkiewicz, M.; Radniecka, A. The effect of ferric ions on the behaviour of a nickelous hydroxide electrode. *J. Appl. Electrochem.* **1984**, *14*, 145-149.
- (59) Corrigan, D. A. The catalysis of the oxygen evolution reaction by iron impurities in thin film nickel oxide electrodes. *J. Electrochem. Soc.* **1987**, *134*, 377-384.
- (60) Qian, M.; Cui, S.; Jiang, D.; Zhang, L.; Du, P. Highly Efficient and Stable Water-Oxidation Electrocatalysis with a Very Low Overpotential using FeNiP Substitutional-Solid-Solution Nanoplate Arrays. *Adv. Mater.* **2017**, *29*, 1704075.
- (61) Xu, X.; Song, F.; Hu, X. A nickel iron diselenide-derived efficient oxygen-evolution catalyst. *Nat. Commun.* **2016**, *7*, 12324.
- (62) Subbaraman, R.; Tripkovic, D.; Chang, K. C.; Strmcnik, D.; Paulikas, A. P.; Hirunsit, P.; Chan, M.; Greeley, J.; Stamenkovic, V.; Markovic, N. M. Trends in activity for the water electrolyser reactions on 3d M(Ni,Co,Fe,Mn) hydr(oxy)oxide catalysts. *Nat. Mater.* **2012**, *11*, 550-557.
- (63) Burke, M. S.; Kast, M. G.; Trotochaud, L.; Smith, A. M.; Boettcher, S. W. Cobalt-iron (oxy)hydroxide oxygen evolution electrocatalysts: the role of structure and composition on activity, stability, and mechanism. *J. Am. Chem. Soc.* **2015**, *137*, 3638-3648.
- (64) Trotochaud, L.; Young, S. L.; Ranney, J. K.; Boettcher, S. W. Nickel-iron oxyhydroxide oxygen-evolution electrocatalysts: the role of intentional and incidental iron incorporation. *J. Am. Chem. Soc.* **2014**, *136*, 6744-6753.
- (65) Klaus, S.; Cai, Y.; Louie, M. W.; Trotochaud, L.; Bell, A. T. Effects of Fe Electrolyte Impurities on Ni(OH)<sub>2</sub>/NiOOH Structure and Oxygen Evolution Activity. *J. Phys. Chem. C* **2015**, *119*, 7243-7254.
- (66) Burke, M. S.; Zou, S.; Enman, L. J.; Kellon, J. E.; Gabor, C. A.; Pledger, E.; Boettcher, S. W. Revised Oxygen Evolution Reaction Activity Trends for First-Row Transition-Metal (Oxy)hydroxides in Alkaline Media. *J. Phys. Chem. Lett.* **2015**, *6*, 3737-3742.
- (67) Bao, J.; Zhang, X.; Fan, B.; Zhang, J.; Zhou, M.; Yang, W.; Hu, X.; Wang, H.; Pan, B.; Xie, Y. Ultrathin Spinel-Structured Nanosheets Rich in Oxygen Deficiencies for Enhanced Electrocatalytic Water Oxidation. *Angew. Chem. Int. Ed.* **2015**, *54*, 7399-7404.
- (68) Song, F.; Hu, X. Ultrathin Cobalt–Manganese Layered Double Hydroxide Is an Efficient Oxygen Evolution Catalyst. *J. Am. Chem. Soc.* **2014**, *136*, 16481-16484.
- (69) Fan, K.; Chen, H.; Ji, Y.; Huang, H.; Claesson, P. M.; Daniel, Q.; Philippe, B.; Rensmo, H.; Li, F.; Luo, Y.; Sun, L. Nickel-vanadium monolayer double hydroxide for efficient electrochemical water oxidation. *Nat. Commun.* **2016**, *7*, 11981.

- (70) Jiang, J.; Sun, F.; Zhou, S.; Hu, W.; Zhang, H.; Dong, J.; Jiang, Z.; Zhao, J.; Li, J.; Yan, W.; Wang, M. Atomic-level insight into super-efficient electrocatalytic oxygen evolution on iron and vanadium co-doped nickel (oxy)hydroxide. *Nat. Commun.* **2018**, *9*, 2885.
- (71) Smith, R. D.; Prevot, M. S.; Fagan, R. D.; Zhang, Z.; Sedach, P. A.; Siu, M. K.; Trudel, S.; Berlinguette, C. P. Photochemical route for accessing amorphous metal oxide materials for water oxidation catalysis. *Science* **2013**, *340*, 60-63.
- (72) Zhang, B.; Zheng, X.; Voznyy, O.; Comin, R.; Bajdich, M.; García-Melchor, M.; Han, L.; Xu, J.; Liu, M.; Zheng, L. Homogeneously dispersed multimetal oxygen-evolving catalysts. *Science* **2016**, *352*, 333-337.
- (73) Liardet, L.; Hu, X. Amorphous Cobalt Vanadium Oxide as a Highly Active Electrocatalyst for Oxygen Evolution. *ACS Catal.* **2018**, *8*, 644-650.
- (74) Anantharaj, S.; Ede, S. R.; Sakthikumar, K.; Karthick, K.; Mishra, S.; Kundu, S. Recent Trends and Perspectives in Electrochemical Water Splitting with an Emphasis on Sulfide, Selenide, and Phosphide Catalysts of Fe, Co, and Ni: A Review. *ACS Catal.* **2016**, *6*, 8069-8097.
- (75) Hung, S.-F.; Zhu, Y.; Tzeng, G.-Q.; Chen, H.-C.; Hsu, C.-S.; Liao, Y.-F.; Ishii, H.; Hiraoka, N.; Chen, H. M. In Situ Spatially Coherent Identification of Phosphide-Based Catalysts: Crystallographic Latching for Highly Efficient Overall Water Electrolysis. *ACS Energy Lett.* **2019**, *4*, 2813-2820.
- (76) Song, J.; Wei, C.; Huang, Z. F.; Liu, C.; Zeng, L.; Wang, X.; Xu, Z. J. A review on fundamentals for designing oxygen evolution electrocatalysts. *Chem. Soc. Rev.* **2020**, *49*, 2196-2214.
- (77) Hu, C.; Zhang, L.; Gong, J. Recent progress made in the mechanism comprehension and design of electrocatalysts for alkaline water splitting. *Energy Environ. Sci.* **2019**, *12*, 2620-2645.
- (78) Bockris, J. O. M. Kinetics of activation controlled consecutive electrochemical reactions: anodic evolution of oxygen. *J. Chem. Phys.* **1956**, *24*, 817-827.
- (79) Doyle, R.; Lyons, M. Kinetics and mechanistic aspects of the oxygen evolution reaction at hydrous iron oxide films in base. *J. Electrochem. Soc.* **2013**, *160*, H142-H154.
- (80) Grimaud, A.; Diaz-Morales, O.; Han, B.; Hong, W. T.; Lee, Y.-L.; Giordano, L.; Stoerzinger, K. A.; Koper, M. T. M.; Shao-Horn, Y. Activating lattice oxygen redox reactions in metal oxides to catalyze oxygen evolution. *Nat. Chem.* **2017**, *9*, 457-465.
- (81) Mefford, J. T.; Rong, X.; Abakumov, A. M.; Hardin, W. G.; Dai, S.; Kolpak, A. M.; Johnston, K. P.; Stevenson, K. J. Water electrolysis on  $\text{La}_{1-x}\text{Sr}_x\text{CoO}_{3-\delta}$  perovskite electrocatalysts. *Nat. Commun.* **2016**, *7*, 11053.
- (82) Diaz-Morales, O.; Ferrus-Suspedra, D.; Koper, M. T. M. The importance of nickel oxyhydroxide deprotonation on its activity towards electrochemical water oxidation. *Chem. Sci.* **2016**, *7*, 2639-2645.
- (83) Roy, C.; Sebok, B.; Scott, S. B.; Fiordaliso, E. M.; Sørensen, J. E.; Bodin, A.; Trimarco, D. B.; Damsgaard, C. D.; Vesborg, P. C. K.; Hansen, O.; Stephens, I. E. L.; Kibsgaard, J.; Chorkendorff, I. Impact of nanoparticle size and lattice oxygen on water oxidation on  $\text{NiFeOxHy}$ . *Nat. Catal.* **2018**, *1*, 820-829.

- (84) Zhou, Y.; Sun, S.; Song, J.; Xi, S.; Chen, B.; Du, Y.; Fisher, A. C.; Cheng, F.; Wang, X.; Zhang, H.; Xu, Z. J. Enlarged CoO Covalency in Octahedral Sites Leading to Highly Efficient Spinel Oxides for Oxygen Evolution Reaction. *Adv. Mater.* **2018**, *30*, e1802912.
- (85) Rossmeisl, J.; Logadottir, A.; Nørskov, J. K. Electrolysis of water on (oxidized) metal surfaces. *Chem. Phys.* **2005**, *319*, 178-184.
- (86) Rossmeisl, J.; Qu, Z. W.; Zhu, H.; Kroes, G. J.; Nørskov, J. K. Electrolysis of water on oxide surfaces. *J. Electroanal. Chem.* **2007**, *607*, 83-89.
- (87) Man, I. C.; Su, H.-Y.; Calle-Vallejo, F.; Hansen, H. A.; Martínez, J. I.; Inoglu, N. G.; Kitchin, J.; Jaramillo, T. F.; Nørskov, J. K.; Rossmeisl, J. Universality in Oxygen Evolution Electrocatalysis on Oxide Surfaces. *ChemCatChem* **2011**, *3*, 1159-1165.
- (88) Koper, M. T. M. Thermodynamic theory of multi-electron transfer reactions: Implications for electrocatalysis. *J. Electroanal. Chem.* **2011**, *660*, 254-260.
- (89) Rüetschi, P.; Delahay, P. Influence of Electrode Material on Oxygen Overvoltage: A Theoretical Analysis. *J. Chem. Phys.* **1955**, *23*, 556-560.
- (90) Trasatti, S. Electrocatalysis by oxides — Attempt at a unifying approach. *J. Electroanal. Chem. Interf. Electrochem.* **1980**, *111*, 125-131.
- (91) Trasatti, S. Electrocatalysis in the anodic evolution of oxygen and chlorine. *Electrochim. Acta* **1984**, *29*, 1503-1512.
- (92) Suntivich, J.; May, K. J.; Gasteiger, H. A.; Goodenough, J. B.; Shao-Horn, Y. A perovskite oxide optimized for oxygen evolution catalysis from molecular orbital principles. *Science* **2011**, *334*, 1383-1385.
- (93) Hwang, J.; Rao, R. R.; Giordano, L.; Katayama, Y.; Yu, Y.; Shao-Horn, Y. Perovskites in catalysis and electrocatalysis. *Science* **2017**, *358*, 751-756.
- (94) Doyle, A. D.; Montoya, J. H.; Vojvodic, A. Improving Oxygen Electrochemistry through Nanoscopic Confinement. *ChemCatChem* **2015**, *7*, 738-742.
- (95) Halck, N. B.; Petrykin, V.; Krtil, P.; Rossmeisl, J. Beyond the volcano limitations in electrocatalysis--oxygen evolution reaction. *Phys. Chem. Chem. Phys.* **2014**, *16*, 13682-13688.
- (96) Martinez, J. M. P.; Carter, E. A. Unraveling Oxygen Evolution on Iron-Doped beta-Nickel Oxyhydroxide: The Key Role of Highly Active Molecular-like Sites. *J. Am. Chem. Soc.* **2019**, *141*, 693-705.
- (97) Song, F.; Busch, M. M.; Lassalle-Kaiser, B.; Hsu, C.-S.; Petkucheva, E.; Bensimon, M.; Chen, H. M.; Corminboeuf, C.; Hu, X. An Unconventional Iron Nickel Catalyst for the Oxygen Evolution Reaction. *ACS Cent. Sci.* **2019**, *5*, 558-568.
- (98) Busch, M.; Halck, N. B.; Kramm, U. I.; Siahrostami, S.; Krtil, P.; Rossmeisl, J. Beyond the top of the volcano? – A unified approach to electrocatalytic oxygen reduction and oxygen evolution. *Nano Energy* **2016**, *29*, 126-135.
- (99) Fang, Y.-H.; Liu, Z.-P. Tafel Kinetics of Electrocatalytic Reactions: From Experiment to First-Principles. *ACS Catal.* **2014**, *4*, 4364-4376.

- (100) Surendranath, Y.; Kanan, M. W.; Nocera, D. G. Mechanistic studies of the oxygen evolution reaction by a cobalt-phosphate catalyst at neutral pH. *J. Am. Chem. Soc.* **2010**, *132*, 16501-16509.
- (101) Bediako, D. K.; Surendranath, Y.; Nocera, D. G. Mechanistic studies of the oxygen evolution reaction mediated by a nickel-borate thin film electrocatalyst. *J. Am. Chem. Soc.* **2013**, *135*, 3662-3674.
- (102) Bockris, J. O. M.; Reddy, A. K.: *Modern electrochemistry 2B: electrocatalysis in chemistry, engineering, biology and environmental science*; Springer Science & Business Media, 1998; Vol. 2.
- (103) Lyons, M. E. G.; Brandon, M. P. A comparative study of the oxygen evolution reaction on oxidised nickel, cobalt and iron electrodes in base. *J. Electroanal. Chem.* **2010**, *641*, 119-130.
- (104) Meyer, R. E. Cathodic processes on passive zirconium. *J. Electrochem. Soc.* **1960**, *107*, 847-853.
- (105) Handoko, A. D.; Wei, F.; Jenndy; Yeo, B. S.; Seh, Z. W. Understanding heterogeneous electrocatalytic carbon dioxide reduction through *operando* techniques. *Nat. Catal.* **2018**, *1*, 922-934.
- (106) Zhu, K.; Zhu, X.; Yang, W. Application of In Situ Techniques for the Characterization of NiFe-Based Oxygen Evolution Reaction (OER) Electrocatalysts. *Angew. Chem. Int. Ed.* **2019**, *58*, 1252-1265.
- (107) Wang, M.; Árnadóttir, L.; Xu, Z. J.; Feng, Z. In Situ X-ray Absorption Spectroscopy Studies of Nanoscale Electrocatalysts. *Nano-Micro Lett.* **2019**, *11*, 47.
- (108) Friebe, D.; Louie, M. W.; Bajdich, M.; Sanwald, K. E.; Cai, Y.; Wise, A. M.; Cheng, M. J.; Sokaras, D.; Weng, T. C.; Alonso-Mori, R.; Davis, R. C.; Bargar, J. R.; Nørskov, J. K.; Nilsson, A.; Bell, A. T. Identification of highly active Fe sites in (Ni,Fe)OOH for electrocatalytic water splitting. *J. Am. Chem. Soc.* **2015**, *137*, 1305-1313.
- (109) Chen, J. Y.; Dang, L.; Liang, H.; Bi, W.; Gerken, J. B.; Jin, S.; Alp, E. E.; Stahl, S. S. *Operando* Analysis of NiFe and Fe Oxyhydroxide Electrocatalysts for Water Oxidation: Detection of Fe(4)(+) by Mossbauer Spectroscopy. *J. Am. Chem. Soc.* **2015**, *137*, 15090-15093.
- (110) Hunter, B. M.; Thompson, N. B.; Müller, A. M.; Rossman, G. R.; Hill, M. G.; Winkler, J. R.; Gray, H. B. Trapping an Iron(VI) Water-Splitting Intermediate in Nonaqueous Media. *Joule* **2018**, *2*, 747-763.
- (111) Wang, D.; Zhou, J.; Hu, Y.; Yang, J.; Han, N.; Li, Y.; Sham, T.-K. In Situ X-ray Absorption Near-Edge Structure Study of Advanced NiFe(OH)<sub>x</sub> Electrocatalyst on Carbon Paper for Water Oxidation. *J. Phys. Chem. C* **2015**, *119*, 19573-19583.
- (112) Kuai, C.; Zhang, Y.; Wu, D.; Sokaras, D.; Mu, L.; Spence, S.; Nordlund, D.; Lin, F.; Du, X.-W. Fully Oxidized Ni-Fe Layered Double Hydroxide with 100% Exposed Active Sites for Catalyzing Oxygen Evolution Reaction. *ACS Catal.* **2019**, *9*, 6027-6032.
- (113) Ahn, H. S.; Bard, A. J. Surface Interrogation Scanning Electrochemical Microscopy of Ni(1-x)Fe(x)OOH (0 < x < 0.27) Oxygen Evolving Catalyst: Kinetics of the "fast" Iron Sites. *J. Am. Chem. Soc.* **2016**, *138*, 313-318.

- (114) Bediako, D. K.; Lassalle-Kaiser, B.; Surendranath, Y.; Yano, J.; Yachandra, V. K.; Nocera, D. G. Structure-activity correlations in a nickel-borate oxygen evolution catalyst. *J. Am. Chem. Soc.* **2012**, *134*, 6801-6809.
- (115) Li, N.; Bediako, D. K.; Hadt, R. G.; Hayes, D.; Kempa, T. J.; Cube, F. v.; Bell, D. C.; Chen, L. X.; Nocera, D. G. Influence of iron doping on tetravalent nickel content in catalytic oxygen evolving films. *Proc. Natl. Acad. Sci. USA* **2017**, *114*, 1486-1491.
- (116) Smith, R. D. L.; Pasquini, C.; Loos, S.; Chernev, P.; Klingan, K.; Kubella, P.; Mohammadi, M. R.; González-Flores, D.; Dau, H. Geometric distortions in nickel (oxy)hydroxide electrocatalysts by redox inactive iron ions. *Energy Environ. Sci.* **2018**, *11*, 2476-2485.
- (117) Francas, L.; Corby, S.; Selim, S.; Lee, D.; Mesa, C. A.; Godin, R.; Pastor, E.; Stephens, I. E. L.; Choi, K. S.; Durrant, J. R. Spectroelectrochemical study of water oxidation on nickel and iron oxyhydroxide electrocatalysts. *Nat. Commun.* **2019**, *10*, 5208.
- (118) Trzesniewski, B. J.; Diaz-Morales, O.; Vermaas, D. A.; Longo, A.; Bras, W.; Koper, M. T.; Smith, W. A. In Situ Observation of Active Oxygen Species in Fe-Containing Ni-Based Oxygen Evolution Catalysts: The Effect of pH on Electrochemical Activity. *J. Am. Chem. Soc.* **2015**, *137*, 15112-15121.
- (119) Lee, S.; Banjac, K.; Lingenfelder, M.; Hu, X. Oxygen Isotope Labeling Experiments Reveal Different Reaction Sites for the Oxygen Evolution Reaction on Nickel and Nickel Iron Oxides. *Angew. Chem. Int. Ed.* **2019**, *58*, 10295-10299.
- (120) Lee, S.; Bai, L.; Hu, X. Deciphering Iron-Dependent Activity in Oxygen Evolution Catalyzed by Nickel-Iron Layered Double Hydroxide. *Angew. Chem. Int. Ed.* **2020**, *59*, 8072-8077.
- (121) Xiao, H.; Shin, H.; Goddard, W. A. Synergy between Fe and Ni in the optimal performance of (Ni, Fe) OOH catalysts for the oxygen evolution reaction. *Proc. Natl. Acad. Sci. USA* **2018**, *115*, 5872-5877.
- (122) Gorlin, M.; Chernev, P.; Ferreira de Araujo, J.; Reier, T.; Dresp, S.; Paul, B.; Krahner, R.; Dau, H.; Strasser, P. Oxygen Evolution Reaction Dynamics, Faradaic Charge Efficiency, and the Active Metal Redox States of Ni-Fe Oxide Water Splitting Electrocatalysts. *J. Am. Chem. Soc.* **2016**, *138*, 5603-5614.
- (123) Hung, S. F.; Chan, Y. T.; Chang, C. C.; Tsai, M. K.; Liao, Y. F.; Hiraoka, N.; Hsu, C. S.; Chen, H. M. Identification of Stabilizing High-Valent Active Sites by *Operando* High-Energy Resolution Fluorescence-Detected X-ray Absorption Spectroscopy for High-Efficiency Water Oxidation. *J. Am. Chem. Soc.* **2018**, *140*, 17263-17270.
- (124) Enman, L. J.; Stevens, M. B.; Dahan, M. H.; Nellist, M. R.; Toroker, M. C.; Boettcher, S. W. *Operando* X-Ray Absorption Spectroscopy Shows Iron Oxidation Is Concurrent with Oxygen Evolution in Cobalt-Iron (Oxy)hydroxide Electrocatalysts. *Angew. Chem. Int. Ed.* **2018**, *57*, 12840-12844.
- (125) Smith, R. D. L.; Pasquini, C.; Loos, S.; Chernev, P.; Klingan, K.; Kubella, P.; Mohammadi, M. R.; Gonzalez-Flores, D.; Dau, H. Spectroscopic identification of active sites for the oxygen evolution reaction on iron-cobalt oxides. *Nat. Commun.* **2017**, *8*, 2022.

- (126) Gong, L.; Chng, X. Y. E.; Du, Y.; Xi, S.; Yeo, B. S. Enhanced Catalysis of the Electrochemical Oxygen Evolution Reaction by Iron(III) Ions Adsorbed on Amorphous Cobalt Oxide. *ACS Catal.* **2018**, *8*, 807-814.
- (127) Yang, X.-F.; Wang, A.; Qiao, B.; Li, J.; Liu, J.; Zhang, T. Single-atom catalysts: a new frontier in heterogeneous catalysis. *Acc. Chem. Res.* **2013**, *46*, 1740-1748.
- (128) Liu, J. Catalysis by Supported Single Metal Atoms. *ACS Catal.* **2016**, *7*, 34-59.
- (129) Bayatsarmadi, B.; Zheng, Y.; Vasileff, A.; Qiao, S. Z. Recent Advances in Atomic Metal Doping of Carbon-based Nanomaterials for Energy Conversion. *Small* **2017**, *13*, 1700191.
- (130) Zhang, W.; Zheng, W. Single Atom Excels as the Smallest Functional Material. *Adv. Funct. Mater.* **2016**, *26*, 2988-2993.
- (131) Liu, K.; Zhong, H.; Meng, F.; Zhang, X.; Yan, J.; Jiang, Q. Recent advances in metal–nitrogen–carbon catalysts for electrochemical water splitting. *Mater. Chem. Front.* **2017**, *1*, 2155-2173.
- (132) Zhu, C.; Fu, S.; Shi, Q.; Du, D.; Lin, Y. Single-Atom Electrocatalysts. *Angew. Chem. Int. Ed.* **2017**, *56*, 13944-13960.
- (133) Zhao, D.; Zhuang, Z.; Cao, X.; Zhang, C.; Peng, Q.; Chen, C.; Li, Y. Atomic site electrocatalysts for water splitting, oxygen reduction and selective oxidation. *Chem. Soc. Rev.* **2020**, *49*, 2215-2264.
- (134) Chen, Y.; Ji, S.; Chen, C.; Peng, Q.; Wang, D.; Li, Y. Single-Atom Catalysts: Synthetic Strategies and Electrochemical Applications. *Joule* **2018**, *2*, 1242-1264.
- (135) Liu, M.; Wang, L.; Zhao, K.; Shi, S.; Shao, Q.; Zhang, L.; Sun, X.; Zhao, Y.; Zhang, J. Atomically dispersed metal catalysts for the oxygen reduction reaction: synthesis, characterization, reaction mechanisms and electrochemical energy applications. *Energy Environ. Sci.* **2019**, *12*, 2890-2923.
- (136) Asset, T.; Atanasov, P. Iron-Nitrogen-Carbon Catalysts for Proton Exchange Membrane Fuel Cells. *Joule* **2020**, *4*, 33-44.
- (137) Gu, J.; Hsu, C.-S.; Bai, L.; Chen, H. M.; Hu, X. Atomically dispersed Fe<sup>3+</sup> sites catalyze efficient CO<sub>2</sub> electroreduction to CO. *Science* **2019**, *364*, 1091-1094.
- (138) Li, X.; Cui, P.; Zhong, W.; Li, J.; Wang, X.; Wang, Z.; Jiang, J. Graphitic carbon nitride supported single-atom catalysts for efficient oxygen evolution reaction. *Chem. Commun.* **2016**, *52*, 13233-13236.
- (139) Zheng, Y.; Jiao, Y.; Zhu, Y.; Cai, Q.; Vasileff, A.; Li, L. H.; Han, Y.; Chen, Y.; Qiao, S.-Z. Molecule-Level g-C<sub>3</sub>N<sub>4</sub> Coordinated Transition Metals as a New Class of Electrocatalysts for Oxygen Electrode Reactions. *J. Am. Chem. Soc.* **2017**, *139*, 3336-3339.
- (140) Wang, J.; Ge, X.; Liu, Z.; Thia, L.; Yan, Y.; Xiao, W.; Wang, X. Heterogeneous Electrocatalyst with Molecular Cobalt Ions Serving as the Center of Active Sites. *J. Am. Chem. Soc.* **2017**, *139*, 1878-1884.

- (141) Hou, Y.; Qiu, M.; Kim, M. G.; Liu, P.; Nam, G.; Zhang, T.; Zhuang, X.; Yang, B.; Cho, J.; Chen, M.; Yuan, C.; Lei, L.; Feng, X. Atomically dispersed nickel-nitrogen-sulfur species anchored on porous carbon nanosheets for efficient water oxidation. *Nat. Commun.* **2019**, *10*, 1392.
- (142) Fei, H.; Dong, J.; Feng, Y.; Allen, C. S.; Wan, C.; Voloskiy, B.; Li, M.; Zhao, Z.; Wang, Y.; Sun, H.; An, P.; Chen, W.; Guo, Z.; Lee, C.; Chen, D.; Shakir, I.; Liu, M.; Hu, T.; Li, Y.; Kirkland, A. I.; Duan, X.; Huang, Y. General synthesis and definitive structural identification of MN<sub>4</sub>C<sub>4</sub> single-atom catalysts with tunable electrocatalytic activities. *Nat. Catal.* **2018**, *1*, 63-72.
- (143) Guan, J.; Duan, Z.; Zhang, F.; Kelly, S. D.; Si, R.; Dupuis, M.; Huang, Q.; Chen, J. Q.; Tang, C.; Li, C. Water oxidation on a mononuclear manganese heterogeneous catalyst. *Nat. Catal.* **2018**, *1*, 870-877.
- (144) Yan, J.; Kong, L.; Ji, Y.; White, J.; Li, Y.; Zhang, J.; An, P.; Liu, S.; Lee, S. T.; Ma, T. Single atom tungsten doped ultrathin  $\alpha$ -Ni(OH)<sub>2</sub> for enhanced electrocatalytic water oxidation. *Nat. Commun.* **2019**, *10*, 2149.
- (145) Li, P.; Wang, M.; Duan, X.; Zheng, L.; Cheng, X.; Zhang, Y.; Kuang, Y.; Li, Y.; Ma, Q.; Feng, Z.; Liu, W.; Sun, X. Boosting oxygen evolution of single-atomic ruthenium through electronic coupling with cobalt-iron layered double hydroxides. *Nat. Commun.* **2019**, *10*, 1711.
- (146) Wang, Q.; Huang, X.; Zhao, Z. L.; Wang, M.; Xiang, B.; Li, J.; Feng, Z.; Xu, H.; Gu, M. Ultrahigh-Loading of Ir Single Atoms on NiO Matrix to Dramatically Enhance Oxygen Evolution Reaction. *J. Am. Chem. Soc.* **2020**, *142*, 7425-7433.
- (147) Zhang, J.; Liu, J.; Xi, L.; Yu, Y.; Chen, N.; Sun, S.; Wang, W.; Lange, K. M.; Zhang, B. Single-Atom Au/NiFe Layered Double Hydroxide Electrocatalyst: Probing the Origin of Activity for Oxygen Evolution Reaction. *J. Am. Chem. Soc.* **2018**, *140*, 3876-3879.
- (148) Lin, C.; Zhao, Y.; Zhang, H.; Xie, S.; Li, Y. F.; Li, X.; Jiang, Z.; Liu, Z. P. Accelerated active phase transformation of NiO powered by Pt single atoms for enhanced oxygen evolution reaction. *Chem. Sci.* **2018**, *9*, 6803-6812.
- (149) Tung, C. W.; Hsu, Y. Y.; Shen, Y. P.; Zheng, Y.; Chan, T. S.; Sheu, H. S.; Cheng, Y. C.; Chen, H. M. Reversible adapting layer produces robust single-crystal electrocatalyst for oxygen evolution. *Nat. Commun.* **2015**, *6*, 8106.

# Chapter 2 A Co-Fe double-atom catalyst for the Oxygen Evolution Reaction

The results presented in this chapter were published in:

**L. Bai**, C. S. Hsu, D. T. L. Alexander, H. M. Chen, X. Hu A Cobalt-Iron Double-Atom Catalyst for the Oxygen Evolution Reaction. **J. Am. Chem. Soc.** 2019, 141, 14190-14199.

Reprinted (adapted) with permission from [1]. Copyright (2019) American Chemical Society.

An early version of the results were also published as a preprint:

**L. Bai**, C. S. Hsu, D. T. L. Alexander, H. M. Chen, X. Hu A Cobalt-Iron Double-Atom Catalyst for the Oxygen Evolution Reaction. Chemrxiv, preprint, link: <https://doi.org/10.26434/chemrxiv.8131235.v1>



## 2.1 Introduction

As introduced in Section 1.5, Chapter 1, single-atom catalysts (SACs) have been widely applied in various electrocatalytic reactions.<sup>2-4</sup> These catalysts are attractive because they exhibit maximum atomic efficiency, high selectivity and intrinsic activity towards certain reactions. Moreover, SACs possess well-defined active sites, which facilitates mechanistic understanding of the reaction processes. In recent years, SACs for the oxygen evolution reaction (OER), including Ru<sup>5-7</sup>, Ir<sup>8-10</sup>, Co<sup>11-13</sup>, Ni<sup>14-17</sup>, Fe<sup>18,19</sup>, Mn<sup>20,21</sup> were reported. These catalysts indeed exhibited good performance for OER, however, the deep insights of the mechanisms were still insufficient.

Structural or compositional changes were usually observed in electrocatalysts under catalytic conditions.<sup>22-24</sup> Some researchers also indicated that there are significant structural changes for SACs in reductive electrocatalysis, including hydrogen evolution reaction (HER) and CO<sub>2</sub> reduction reaction (CRR). For examples, Wei and coworkers reported that a Co SAC with Co-N<sub>4</sub> structure (the Co is coordinated by 4 nitrogen atoms) is transformed to Co-N<sub>2</sub>-OH (the Co is coordinated by 2 nitrogen atoms and one OH group) under HER catalytic conditions.<sup>25</sup> Similar decreases of the coordination numbers (CNs) were also observed in a Pt SAC for HER.<sup>26</sup> Fontecave et al. showed that a Cu-N<sub>4</sub> SAC can reversibly transform to Cu nanoparticles (NPs) during CRR, which is the reason for good Faradaic efficiency (FE) of ethanol.<sup>27</sup> Nevertheless, whether the structural or compositional transformations are existed in OER SACs are yet to explore.

Moreover, OER in alkaline medium is an archetypical electrochemical reaction for which bimetallic catalysts are often more active than monometallic catalysts.<sup>28-31</sup> Based on the time-resolved spectroscopic measurements of intermediates in a photochemical OER catalyzed by Co<sub>3</sub>O<sub>4</sub>, Frei and co-workers proposed that an oxygen-bridged Co-Co moiety reacted much faster than a single Co site.<sup>32</sup> Moreover, benchmark works showed that the nickel-iron oxyhydroxide (NiFeO<sub>x</sub>H<sub>y</sub>) and cobalt-iron oxyhydroxide (CoFeO<sub>x</sub>H<sub>y</sub>) are among the most active OER catalysts in alkaline solutions.<sup>28-31</sup> Incorporation of a trace amount of iron will significantly enhance the activity of pure nickel or cobalt oxide/oxyhydroxide (NiO<sub>x</sub> or CoO<sub>x</sub>), while pure iron oxides (FeO<sub>x</sub>) has low activity.<sup>22,33</sup> It follows that instead of SACs, a so-called double-atom catalyst (DAC) would be more active for OER. Recently, some DACs were reported to exhibit higher activity than SACs for electrocatalytic oxygen reduction reaction (ORR)<sup>34</sup>, CRR<sup>35</sup>, and co-catalyst for photoanode<sup>36</sup>.

However, double-atom OER electrocatalysts composed of only earth-abundant elements are hitherto unknown.

In this Chapter, we show that a single-atom Co precatalyst (Co-N-C) can be transformed to a Co-Fe double-atom catalyst (Co-Fe-N-C) under OER in Fe-containing KOH, in which the Fe is dynamically bound to Co via oxygen bridge. This Co-Fe DAC exhibits a turnover frequency (TOF) value comparable to the state-of-the-art OER catalysts ( $>10\text{ s}^{-1}$  at 350 mV overpotential). The work presents, to our knowledge, the first example of double-atom electrocatalyst that is highly efficient for OER. Such well-defined double-atom OER catalyst would also provide a promising platform for further mechanistic investigations.

## 2.2 Synthesis and characterization of the single-atom Co precatalyst (Co-N-C)

### 2.2.1 Synthesis of Co-N-C precatalyst

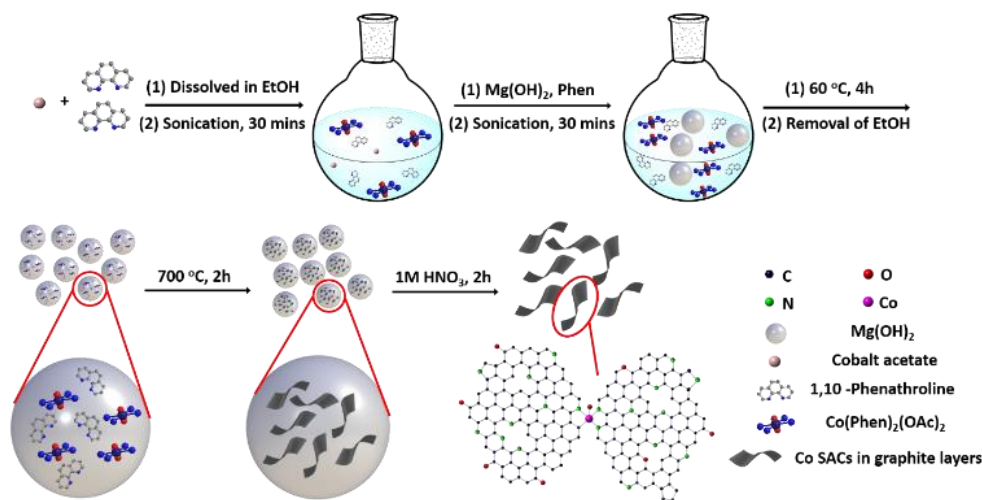


**Figure 2.1** Synthetic process of Co-N-C. A proposed, indicative structure of the Co-N-C precatalyst is shown in the graph by taking account of the results from the XAS study (see Section 2.5 for detailed explanations).

In this study, a hard template method based on  $\text{Mg}(\text{OH})_2$  is employed to synthesize Co-based single-atoms dispersed on N-doped carbon (Co-N-C). The  $\text{Mg}(\text{OH})_2$  serves as both a template and a dispersing reagent. As indicated in previous literatures<sup>37</sup>,  $\text{Mg}(\text{OH})_2$  is an appropriate support material for dispersing single-atoms and preventing aggregation of the metal species, due to the moderate interaction of  $\text{Mg}(\text{OH})_2$  with the metal species and inertness towards the reaction with

metal ions during high temperature pyrolysis. Figure 2.1 shows the synthetic process of Co-N-C. The detailed synthetic procedure is mentioned in Section 2.7.1. Generally, a Co(II) complex of phenanthroline (Phen) is first synthesized and then mixed with extra Phen ligands and commercial Mg(OH)<sub>2</sub> nanoparticles. The mixture is dispersed in ethanol by sonication and further reacted in ethanol. After removal of the solvent and drying, the solid mixture is heated to 700 °C. During pyrolysis, the organic ligands are condensed and polymerized to N-doped carbon on the surface of MgO, in which the Co is coordinated by nitrogen and carbon (Figure 2.1). The Co-N-C is obtained by removing MgO and small amount of Co nanoparticles via acid washing. The metal contents of Co-N-C were measured by inductively coupled plasma atomic emission spectrometry (ICP-AES). The weight percentage of Co is 2.2±0.2 %, while that of Mg was only 0.06±0.02 %, indicating that nearly all MgO was removed by acid leaching.

## 2.2.2 Characterization of Co-N-C precatalyst

The X-ray diffraction (XRD) pattern of Co-N-C showed only broad peaks at 26.2° and 42.9°, corresponding to the (002) and (101) planes of graphitic carbon,<sup>38,39</sup> but the crystallinity of the material is poor (Figure 2.2a). No peaks from either crystalline metal oxides or metallic species were present. Raman spectrum of Co-N-C showed only two bands characteristic of graphite carbon (G band at 1600 cm<sup>-1</sup>) and defective carbon (D band at 1350 cm<sup>-1</sup>, Figure 2.2b), respectively.<sup>15,37</sup> According to the N<sub>2</sub> physical adsorption-desorption measurement (Figure 2.2c), the Co-N-C exhibited a high BET (Brunauer-Emmett-Teller) surface area of 496 m<sup>2</sup>/g and a mesoporous feature (type IV isotherm with a hysteresis loop).<sup>40</sup>

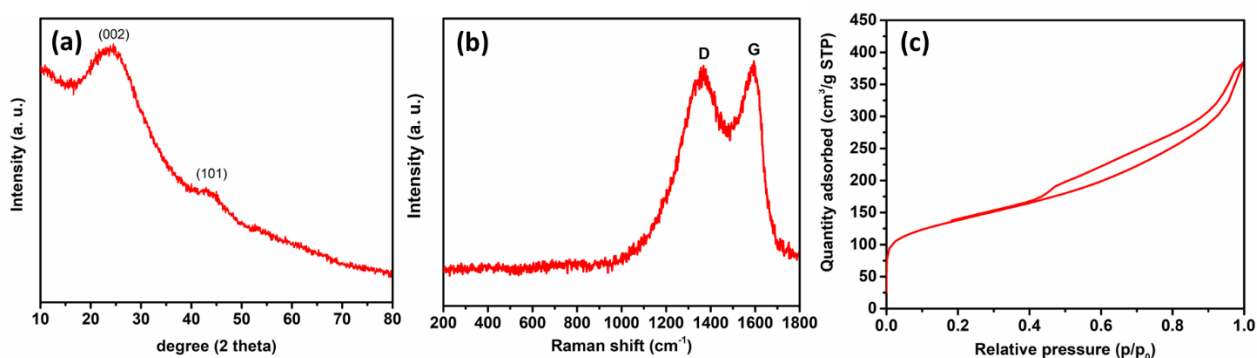


**Figure 2.2** Basic physical characterization of Co-N-C. (a) XRD; (b) Raman; (c) N<sub>2</sub> physical adsorption-desorption isotherms curve.

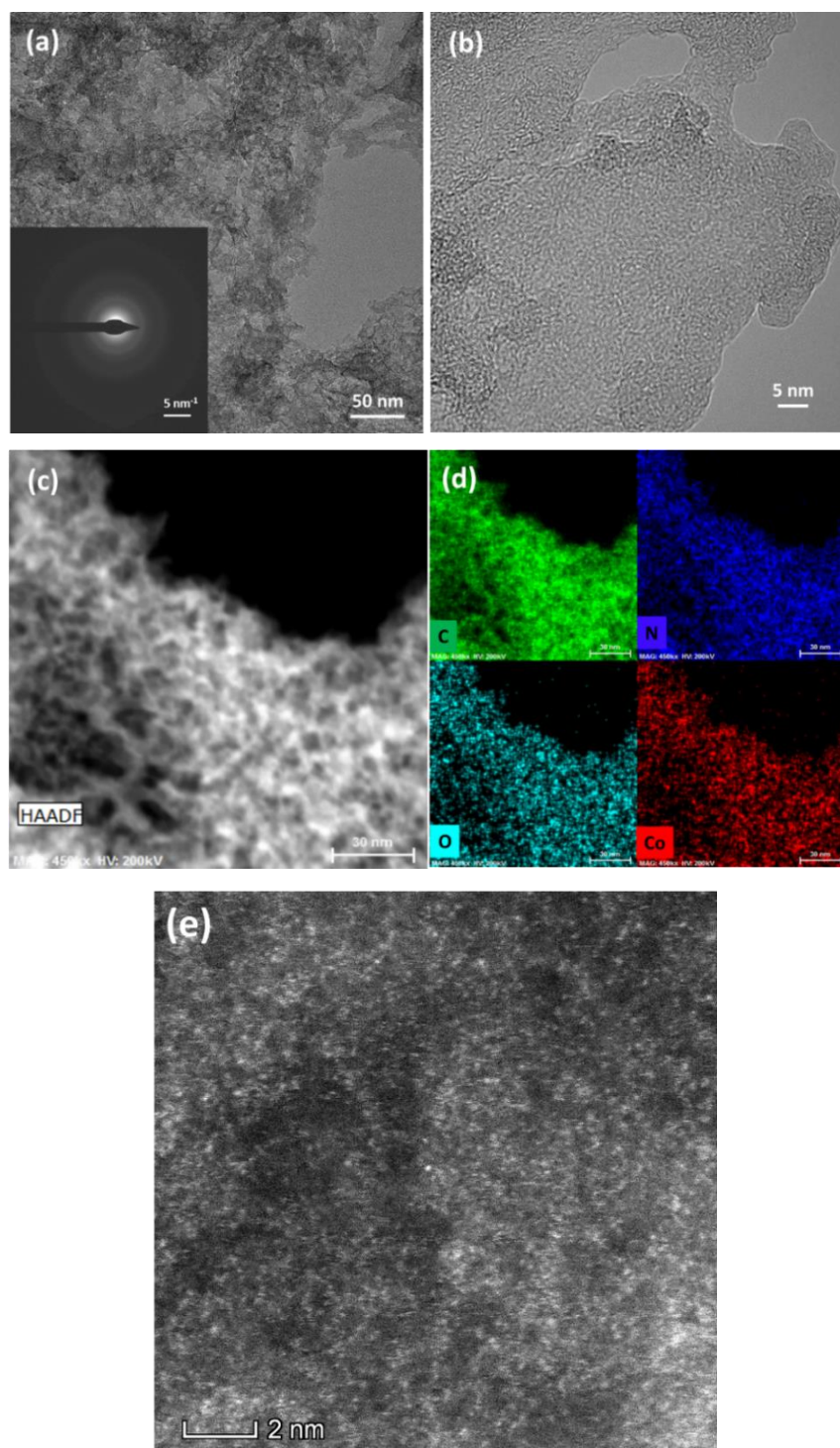


**Figure 2.3** Microscopic characterization of Co-N-C. (a) TEM image, inset: corresponding SAED pattern; (b) HRTEM image; (c) HAADF-STEM image; (d) corresponding EDX mapping of (c); (e) Spherical aberration corrected HAADF-STEM image.

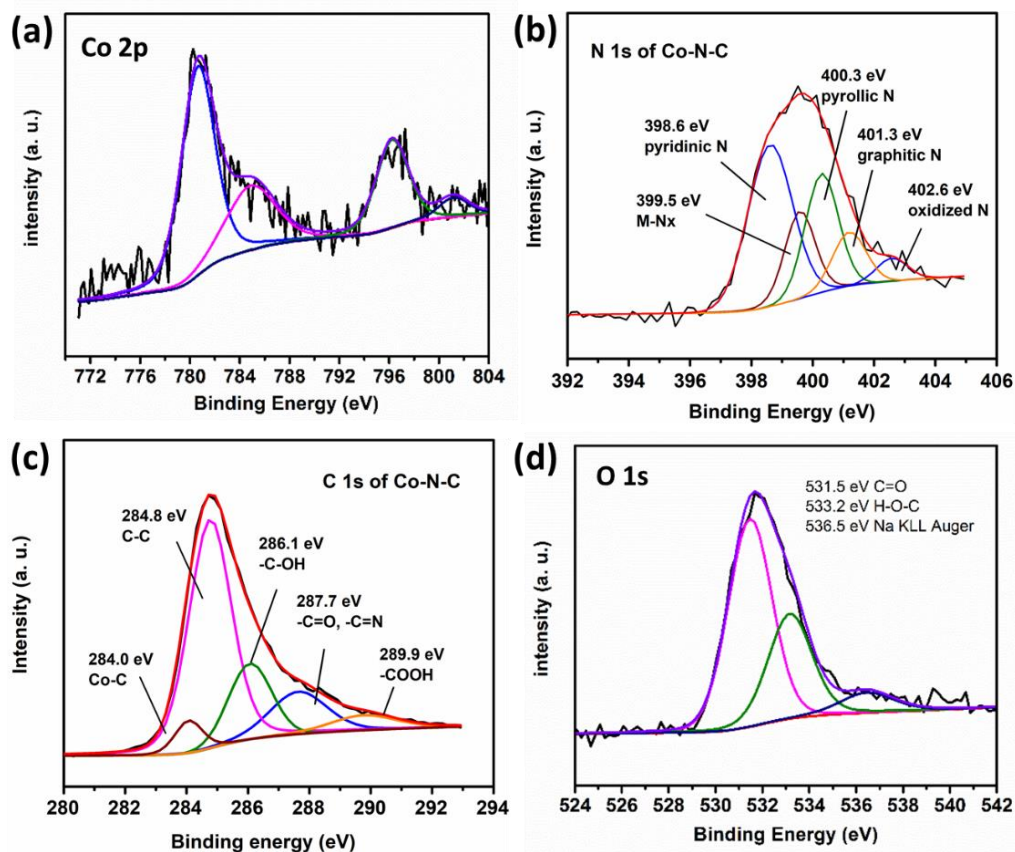


**Figure 2.4** High resolution of XPS of Co-N-C: (a) Co 2p; (b) N 1s; (c) C 1s and (d) O 1s.

Transmission electron microscopy (TEM) images showed that Co-N-C is multilayered and porous (Figure 2.3a). The corresponding selective area electron diffraction (SAED) pattern (Figure 2.3a inset) indicated poor crystallinity, which was in accordance with the XRD result (Figure 2.2a). The high resolution TEM (HRTEM) image also revealed a mostly amorphous carbon support, with only some irregular lattice fringes (Figure 2.3b). Neither Co oxides nor metallic Co nanoparticles were observed. In HAADF-STEM (high-angle annular dark field scanning transmission electrode microscopy) mode, Energy dispersed X-ray (EDX) mapping images showed the material is composed of C, N, O, and Co (Figures 2.3c and 2.3d), in which Co is homogeneously distributed across the whole material. Spherical aberration corrected (AC) HAADF-STEM image (Figure 2.3e) showed many well-dispersed bright dots, each having a size of about 0.2 nm. These dots are attributed to single Co atoms dispersed on the carbon support.<sup>41,42</sup> Note that as the Co atoms are distributed through a carbon support that is amorphous,

multi-layered, and non-flat, only the Co atoms which are at the focal height of the electron probe appear sharp, while Co atoms at other heights are imaged as blurry spots.<sup>13,18</sup>

X-ray photoelectron spectroscopy (XPS) revealed the chemical compositions and oxidation states of Co-N-C. In Co 2p region, the Co2p<sub>3/2</sub> (780.7 eV) and Co2p<sub>1/2</sub> (796.3 eV) subpeaks and two satellite peaks at 785.1 and 801.3 eV suggested that the oxidation state of Co is +2 (Figure 2.4a).<sup>12,37,43</sup> The high-resolution N 1s XPS spectrum (Figure 2.4b) was deconvoluted into five different types of N species including pyridinic N (398.6 eV), pyrrolic N (400.3 eV), graphitic N (401.3 eV), and oxidized N (402.6 eV).<sup>44,45</sup> A peak at 399.5 eV, which is attributed to metal-nitrogen bond, was also observed.<sup>45,46</sup> The subpeaks at 286.1, 287.8, 289.9 eV in C1s region (Figure 2.4c) suggested that the material contains hydroxyl (-C-OH), -C-N; carbonyl (-C=O), -C=N; and carboxylic functional groups.<sup>44,47</sup> A small peak deconvoluted with low binding energy (284.0 eV) is the possible metal-carbon bond (see Section 2.5.1 for details).<sup>48</sup> The O 1s spectrum was deconvoluted into two peaks at 531.5 and 533.2 eV, which were attributed to -C=O and -C-OH groups, respectively (Figure 2.4d).<sup>37,49</sup> The oxygen groups were inadvertently introduced during the synthetic process.

All of the above results indicated that the Co-N-C is composed of single Co atoms imbedded on N-doped amorphous carbon.

## 2.3 Electrochemical OER performance

We drop-casted Co-N-C on carbon-cloth (CC) electrode to evaluate the OER performance. We found that the potential of Co-N-C was gradually decreased under a constant applied current density of 2 mA/cm<sup>2</sup> (Figure 2.5a), which means the activity was gradually improved with the activation time. The potential was stabilized after ca. 3h activation. The activated Co-N-C on CC exhibited an overpotential of 321±5 mV to reach 10 mA/cm<sup>2</sup>, with a Tafel slope of 40±2 mV/dec (Figures 2.5b and 2.5c).

The activation process of Co-N-C led to incorporation of Fe ions, as confirmed by ICP-AES. Typically, the loadings of Co and Fe were 9.4(±1.4) ×10<sup>-8</sup> mol/cm<sup>2</sup> and 8.6(±1.6) ×10<sup>-9</sup> mol/cm<sup>2</sup> after activation, respectively. According to previous reports, trace amount of iron ions are essential for the high activity of NiO<sub>x</sub> and CoO<sub>x</sub> pre-catalysts.<sup>22,33</sup> To verify the role of Fe in the activity of Co-N-C, a number of experiments were conducted (Figures 2.5b and 2.5c). First, the Co-N-C was

tested in an Fe-free KOH solution (1 M, obtained by treating with  $\text{Ni(OH)}_2$ , see Section 2.7.1). The initial activity of the sample was low, with an overpotential of  $495 \pm 19$  mV at  $10 \text{ mA/cm}^2$  and a Tafel slope of  $72 \pm 4$  mV/dec. The activity could be improved by prolonged electrolysis to reach an overpotential of  $443 \pm 15$  mV at  $10 \text{ mA/cm}^2$  and a Tafel slope of  $58 \pm 4$  mV/dec. The reason of the activity improvement in Fe-free but Ni-containing KOH will be demonstrated in Chapter 3. Noted that the activities of Co-N-C in Fe-free KOH (even after electrochemical activation) are much lower than that of the activated Co-N-C in a "normal" KOH solution which contains a trace amount of iron ions (0.18 ppm), likely in the form of  $[\text{Fe(OH)}_4]^-$ .<sup>50,51</sup> Addition of 10 ppm of  $\text{Fe(NO}_3)_3 \cdot 9\text{H}_2\text{O}$  (assuming some of it would be converted into  $[\text{Fe(OH)}_4]^-$ ) into the "normal" KOH further improved the activity. The overpotential at  $10 \text{ mA/cm}^2$  was decreased to  $309 \pm 4$  mV, while Tafel slope is  $37 \pm 2$  mV/dec. These results (Figures 2.5b and 2.5c) support the hypothesis that iron incorporation is essential for the high activity of Co-N-C. A new reduction peak at 1.189 V emerged after activation in Fe-containing "normal" KOH, while the corresponding oxidation peak was hidden by background capacitive current (Figure 2.5d). This feature was absent for the catalyst activated in Fe-free KOH. This new redox feature indicates the presence of a new Co species formed upon Fe incorporation. The activated Co-N-C catalyst is then labeled as Co-Fe-N-C.

Both accelerated degradation measurements and galvanostatic electrolysis were adopted to evaluate the stability of the Co-Fe-N-C (Figures 2.5e and 2.5f). The polarization curve of the catalyst obtained after 3000 fast continuous cyclic voltammetry scans (CVs) exhibited a negligible increase in overpotential (4 mV) for  $10 \text{ mA/cm}^2$  compared to the initial curve, indicating excellent stability (Figure 2.5e). Moreover, no significant overpotential increase was observed during 16 h of electrolysis at  $10 \text{ mA/cm}^2$  (Figure 2.5f). The FE of OER was determined as 98%, implying almost all of the current was in charge of catalytic water oxidation (Figure 2.5g). Detailed procedure of determining FE is in Section 2.7.4.



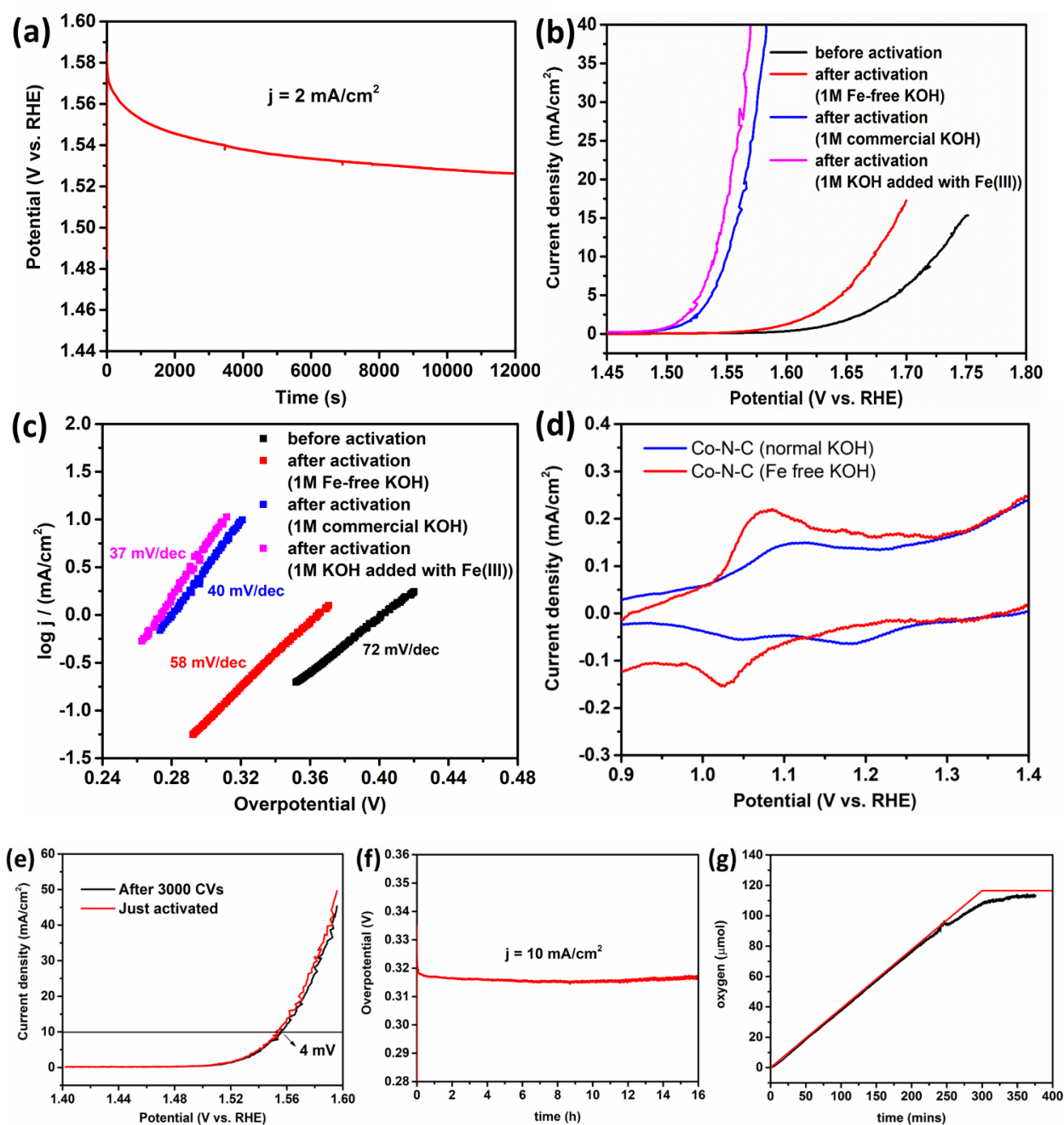


**Figure 2.5** Electrochemical OER performance of Co-N-C. (a) Chronopotential activation plot of Co-N-C at  $2 \text{ mA/cm}^2$ . (b) Linear scan voltammetry curves (LSVs) of Co-N-C at different conditions. (c) Corresponding Tafel plots derived from (b). (d) The CVs of Co-N-C (in precatalytic region) after activated in normal KOH (blue), Fe-free KOH (red). Scan rate =  $50 \text{ mV/s}$ . (e) Comparison of LSVs of activated Co-N-C before (red) and after (black) 3000 fast CVs (scan rate =  $50 \text{ mV/s}$ ). (f) Stability test of Co-N-C by long-time electrolysis at  $10 \text{ mA/cm}^2$ . (g) Oxygen evolution curve (black) of the activated Co-N-C detected by fluorescence type  $\text{O}_2$  sensor, the red curve is the theoretical oxygen evolution curve with assumed 100% Faradaic efficiency.



## 2.4 Characterization of the real catalysts (Co-Fe-N-C)

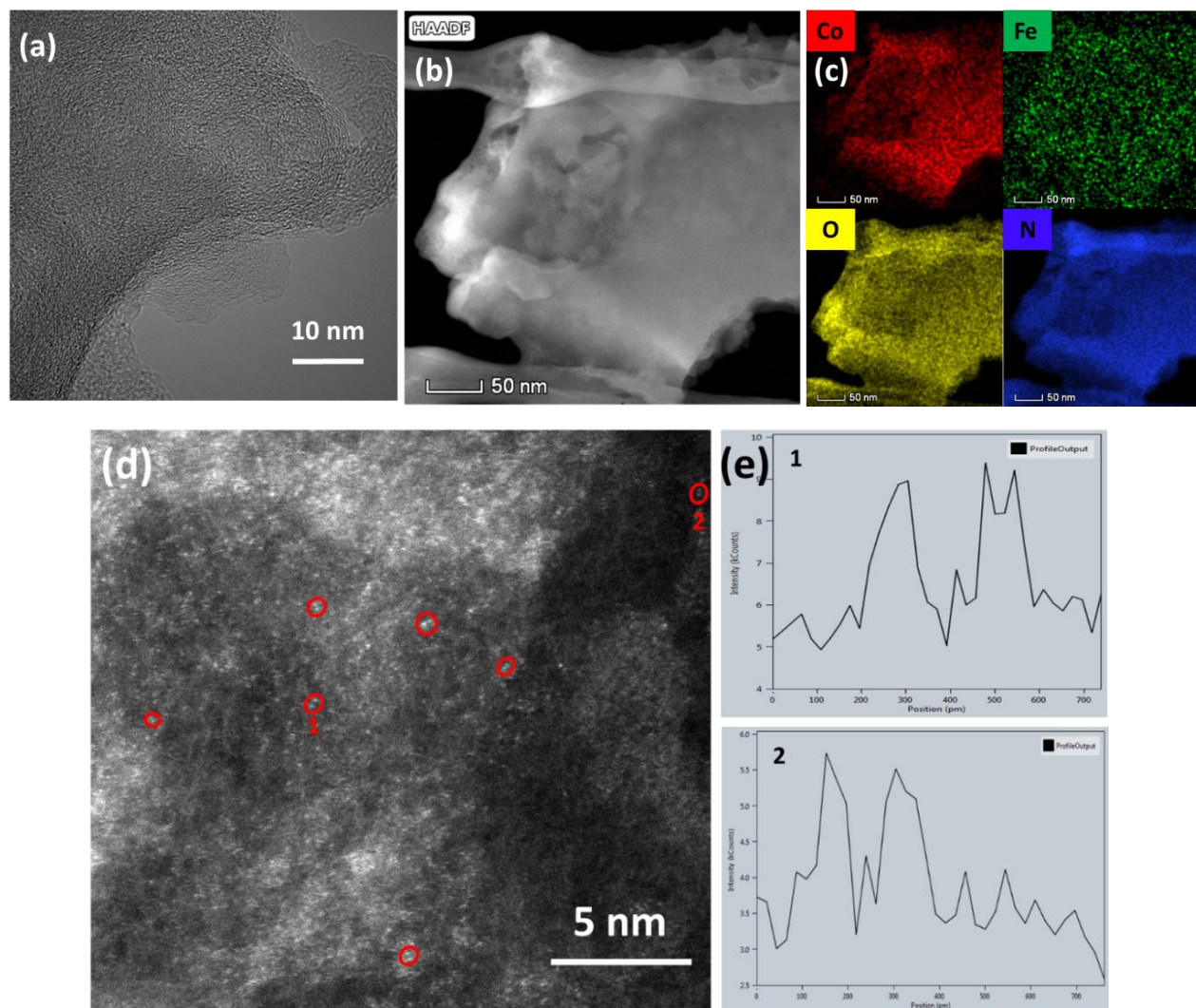


**Figure 2.6** Microscopic characterization of Co-Fe-N-C. (a) HR-TEM image. (b) HAADF-STEM image. (c) Corresponding EDX mapping of (b). (d) Spherical aberration corrected HAADF-STEM image. Red circles indicate possible double-atom pairs. (e) Analysis of the atomic distance and intensity profile of possible double-atom pairs.

We examined the activated materials (Co-Fe-N-C) by microscopies. The HRTEM image of Co-Fe-N-C revealed a morphology similar to Co-N-C, with amorphous carbon and no obvious aggregated nanoparticles (Figure 2.6a). EDX mapping images (Figures 2.6b and 2.6c) showed that both Co and Fe were homogeneously distributed throughout the material. Figure 2.6d showed that the materials were still atomically dispersed, with some possible double-atom pairs (Figure 2.6d, red circles). Intensity profiles analysis exhibited that the apparent distance of the double-

atom pairs is about 0.2-0.3 nm, which is in the range of the distance between two metals connected by oxygen-bridge. The intensity of two atoms are similar (Figure 2.6e). Therefore, these double-atom pairs can be regarded as possible Co-Fe dimers. However, it should be noted that while it is tempting to assign them to the Co-Fe dimers, unambiguous confirmation is not possible. As those images correspond to a 2D projection of a 3D structure, they might also originate from Co atoms that are separated by height in the amorphous carbon but which nearly overlap in the imaging projection.

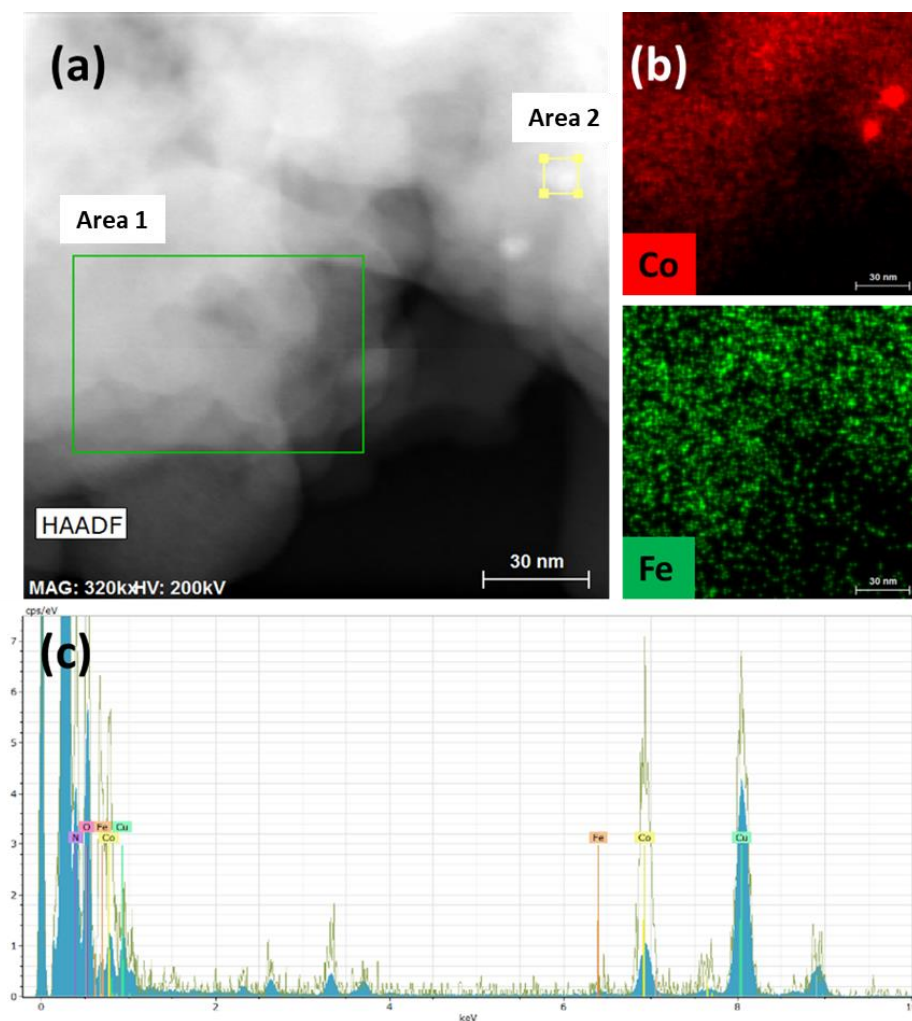


**Figure 2.7** Microscopic characterization of Co-Fe-N-C in an area containing small amount of nanoparticles. (a) HAADF-STEM image, (b) EDX mapping images and (c) corresponding EDX spectra. The spectra showed that the content of Co is higher for the region containing a nanoparticle (Area 2, yellow hollow) but the content of Fe is similar to the area without nanoparticles (Area 1, blue filled). The Cu signals came from the Cu grid on which the sample was casted.

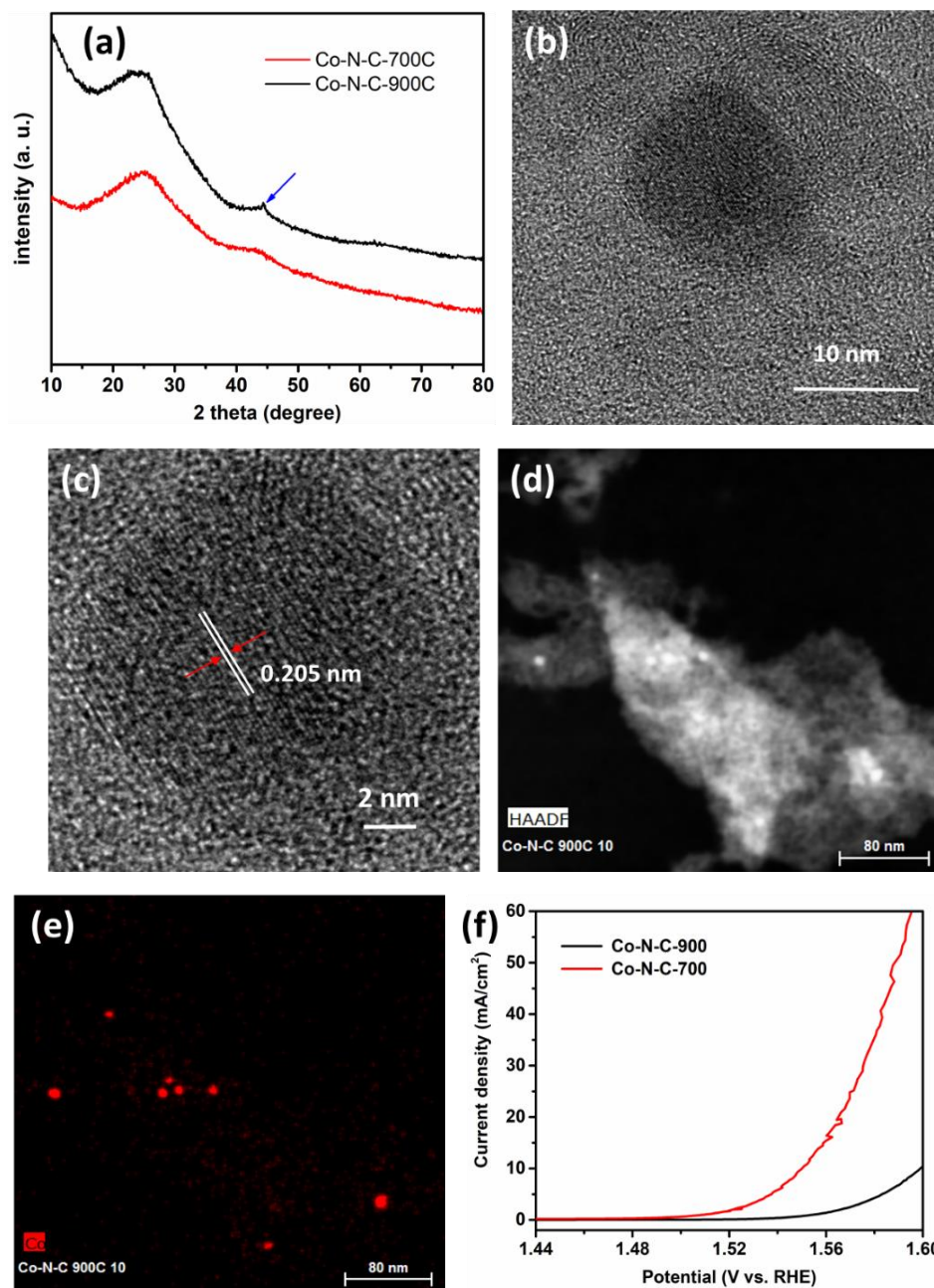


**Figure 2.8** Characterization of Co-N-C-900. (a) XRD comparison of Co-N-C (red) and Co-N-C-900 (black). The blue arrow indicated the diffraction peak of (111) facet of metallic Co (Reference code: 00-015-0806). (b) TEM and (c) HRTEM images of Co-N-C-900. The marked distance of the lattice fringes corresponds to (111) planes of metallic Co (Reference code: 00-015-0806). (d) HAADF-STEM image and (e) corresponding EDX mapping of Co-N-C-900. (f) OER activity comparison of activated Co-N-C/Co-Fe-N-C (red) and activated Co-N-C-900 (black).

Only a very small amount of Co-containing NPs were observed in a small region of Co-Fe-N-C (Figure 2.7). Although Fe species may also adsorb on the surface of Co NPs, the latter's tiny quantity and large size made them unlikely to be the active species in Co-Fe-N-C for OER. To better evaluate the activity of these Co-containing NPs, they were purposely prepared at a higher pyrolysis temperature of the precursors at 900 °C. Figures 2.8a-e are the characterization for the resulting material, termed as Co-N-C-900, including XRD, TEM and EDX mapping. These results suggested that many Co NPs and less atomically dispersed Co were existed in the material. Co-N-C-900 exhibited much lower OER activity than Co-N-C after similar activation process (Figure 2.8f), despite having similar loadings of Co and Fe (Co:  $6.1(\pm 0.7) \times 10^{-8}$  mol/cm<sup>2</sup>, Fe:  $1.1(\pm 0.2) \times 10^{-8}$  mol/cm<sup>2</sup>) to those of Co-Fe-N-C. Such results further support that the observed tiny amount of Co NPs are not responsible for the main contribution of the OER activity of Co-Fe-N-C.

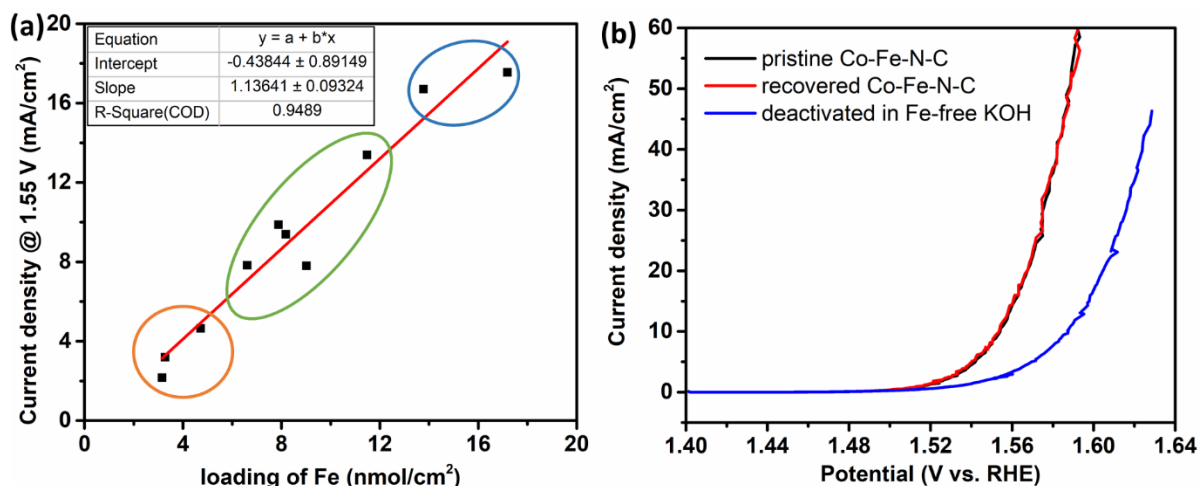


**Figure 2.9** The relationship between the OER activity of Co-Fe-N-C and the Fe loadings. (a) The current density at 1.55 V vs. RHE for the catalysts with different Fe loadings. The circles with different colors pointed the samples activated in different electrolyte. Orange: activated in 1M KOH for 90 mins. Green: activated in 1M KOH until stabilized performance. Blue: activated in 1M KOH added with 10 ppm Fe(III) until stabilized performance. (b) LSVs of Co-Fe-N-C before (black curve) and after (blue curve) electrolysis in 1M Fe free KOH for 2h. The activity can be recovered by re-activating the catalyst in fresh unpurified 1M KOH (red curve).

The activity of Co-Fe-N-C depends critically on the number of iron sites. The current density at 1.55 V vs. RHE is roughly proportional to the loadings of Fe (Figure 2.9a). The loadings of Fe could be roughly controlled by changing the activation time and the Fe concentration in KOH.

Interestingly, the adsorption of Fe ions from Fe-containing solution is reversible. When OER electrolysis was conducted over a long period of time (2 h) using Co-Fe-N-C in a Fe-free KOH solution, the amount of Fe in the catalyst decreased, and the OER activity became worse. The activity could be recovered in KOH solutions containing even a trace amount of Fe ions, suggesting a fast equilibrium between absorption and desorption of Fe ions (Figure 2.9b). Such phenomenon is similar to a recent study of the metal oxides, in which Fe active sites are dynamic.<sup>52</sup> The above characterization and electrochemistry experiments suggested some of the Co single-atoms were dynamically transformed to possible Co-Fe double-atoms, which might be the real active center for OER.

## **2.5 Operando XAS study and identification of real active sites**

### **2.5.1 Operando XAS of Co-N-C and Co-Fe-N-C**

*Operando* X-ray absorption spectroscopy (XAS) was applied to characterize the detailed coordination structures of the catalyst and probe the changes of the structures of the catalytic sites during OER catalysis. Figure 2.10a shows the *operando* Co K-edge X-ray absorption near edge spectroscopy (XANES) of the as-prepared Co-N-C, the Co-N-C activated by 5 CVs (0.2-0.6 V vs. Ag/AgCl, scan rate: 20 mV/s), and Co-N-C in various OER durations, together with reference samples of metallic Co, CoO, Co<sub>3</sub>O<sub>4</sub> and CoOOH.<sup>53,54</sup> The spectroscopic features of Co-N-C under different conditions are significantly different from the standard reference samples. The oxidation state of Co ion in Co-N-C is close to +2, since the energy of main absorption edge coincides with that of Co(2+)O and is slightly lower than that of Co<sub>3</sub>(8/3+)O<sub>4</sub> (Figures 2.10a right and 2.10b). This result is consistent with the observation from the XPS study (Figure 2.4a). Noted that the oxidation state of Co increases to +3 when the catalyst is immersed in 1 M KOH, manifesting probable coordination environment change (see below for detailed illustration).



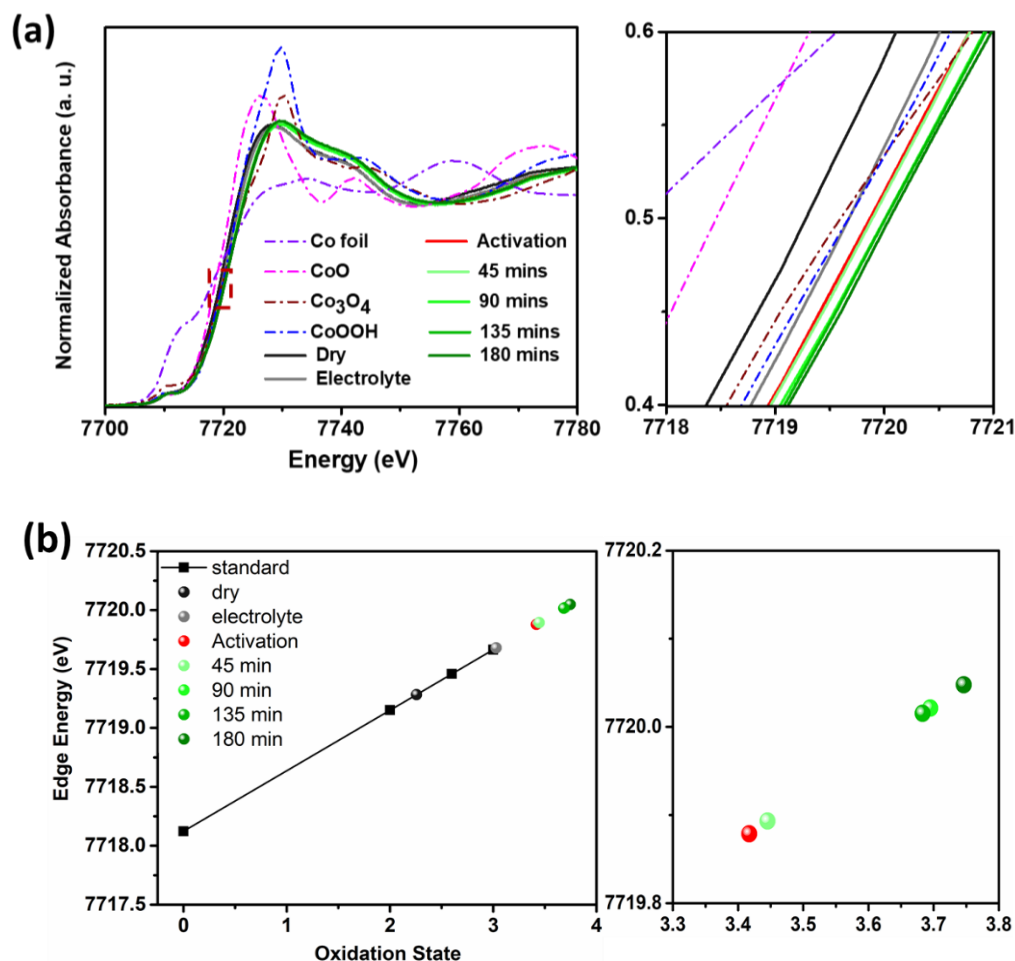


**Figure 2.10** *Operando* XANES of Co-N-C in different conditions. (a) Left: Co K-edge XANES spectra of Co-N-C precatalyst (black), Co-N-C in electrolyte (grey), after 5 CVs activation (red) and under OER with various duration (green, 45-180 mins). Co standard samples: Co foil (purple), CoO (pink),  $\text{Co}_3\text{O}_4$  (brown), CoOOH (blue) are showed in dashed lines. Right: The enlargement image of the dark-red dashed box in left image, for determination of the change of the oxidation state. (b) Left: K-edge energies (at 50% level) of XANES spectra in Fig. (a), and cobalt references compounds containing Co(0), Co(II), or Co(III), showed in black squares. Right: The enlarged graph of left image with apparent oxidation state higher than +3.3.

The structural evolution and the formation of Co-Fe DAC were further revealed by *operando* extended X-ray absorption fine structure (EXAFS) spectra at the Co K-edge (Figure 2.11a, the fitting parameters of the data is in Table 2.1). The first coordinated shell ranging from 1.5–2 Å is attributed to the single scattering paths of Co ions with closest C, N, or O, while the second coordinated shell with a range from 2–3 Å results from the single scattering paths of outer neighboring C and metal surrounding the Co ions. In the dry sample of Co-N-C, the Co ions are

five-coordinated and are surrounded by about three N, one C, and one O atoms (Figures 2.11a right and 2.11b). The O atom likely comes from an absorbed hydroxyl or water group. Although distinguishing the scattering paths among Co-C, Co-N and Co-O is challenging, the characteristic features of these paths are slightly different. Accordingly, the multipath fitting for the first shell is necessary. Once the Co-N-C sample is in contact with alkaline electrolyte (1 M KOH), two of the coordinated N atoms, or one N and one C atom, are replaced by three new O atoms, as indicated by the extracted structural parameters (Figures 2.11a right, 2.11b, and Table 2.1). The coordinated oxygen groups are assigned as OH<sup>-</sup> and H<sub>2</sub>O from the electrolyte. Apparent distances of all paths are slightly shorter than those of the as-prepared Co-N-C precatalyst (dry powder), which might be ascribed to the oxidation of Co ions (Figure 2.10a). We assumed that the heteroatoms of one graphite layer are no longer coordinated to Co and the graphite layer is away from the Co center. Once the coordination environment is changed, the +2 oxidation state of Co is no longer stable, which can be oxidized by ambient oxygen to form Co(+3) species.

Most interestingly, after CVs activation and Fe incorporation, a new scattering path (Co-Fe) was observed at 2.53 Å with a CN value of ~0.22. This apparent distance is significantly shorter than that of Co-Fe in spinel oxide<sup>55</sup> and slightly larger than the atomic radius of metallic Co(0)-Fe(0)<sup>56</sup>, indicating a newly formed Co-Fe interaction with a specific geometry (Figures 2.11a right, 2.11b, and Table 2.1). For an ideal dimer structure, the expected CN of M-M should be 1. However, since the XAS result is referred to the assembly nature of probed sample, which means the average CN of target element will be diluted by the atoms that did not form the double atom pairs and further be decreased to a lower value than the ideal case of 1.0. The CN value of 0.22 suggests about one-fifth Co ions interact with Fe ions in Co-Fe-N-C.

To probe the structures of the active sites in Co-Fe-N-C during OER activation ( $j = 1 \text{ mA/cm}^2$ ), *operando* XAS was conducted (Figure 2.11a). Even after OER for 180 min, no significant structural change was found in all interaction paths except for a minor change in the Co-Fe path, indicating the present double-atom electrocatalyst is robust. As compared to that of the sample activated by 5 CVs, the apparent distance of Co-Fe path during OER increases by approximately 0.1 Å, while the CN value of Co-Fe path remains almost the same. The increase in the bond length of the Co-Fe path might be due to the enhanced interaction of OH<sup>-</sup>/H<sub>2</sub>O with Co ions during OER, which weakens the Co-Fe interaction.

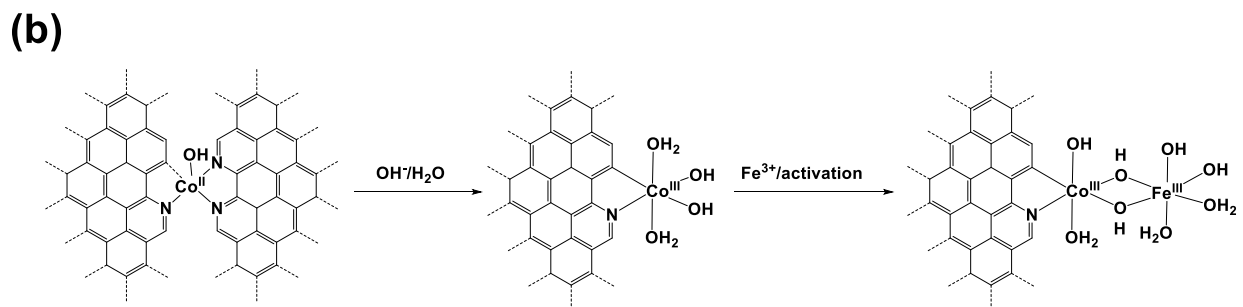
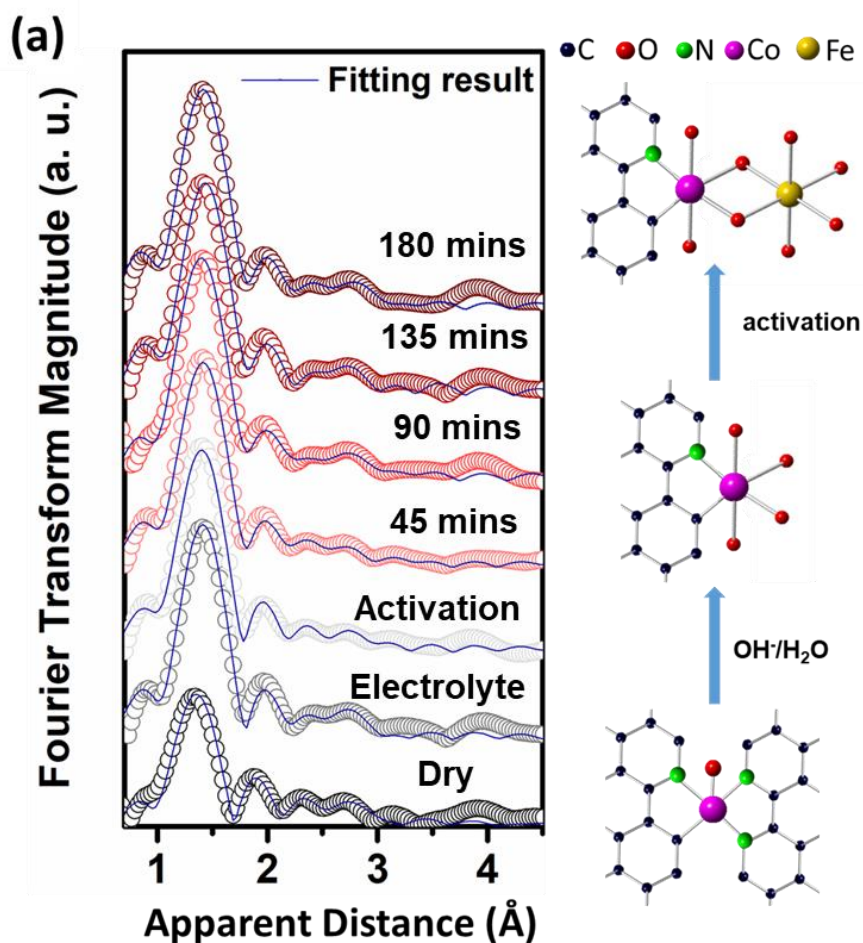


**Figure 2.11** Operando EXAFS of Co-N-C in different conditions. (a) Fourier transform of Co K-edge EXAFS spectra w/o phase correction for as-prepared Co-N-C, and the catalyst after 5 CVs, activation as well as under OER for various durations. The fitting results are showed in solid curve. The proposed evolution process of the catalysts are showed in the right. H atoms were removed for clarity. (b) Proposed model for the formation of Co-Fe double-atom catalyst; after immersing the pre-catalyst in the electrolyte solution, either two N or one N and one C were replaced by O. For simplicity, only the model where two N were replaced is shown.



The observed CN value of Co-Fe path after 5 CVs activation and under OER is higher than the Fe/Co ratio determined by post-catalytic ICP-AES. The discrepancy is attributed to the higher surface sensitivity of the fluorescence-yield XAS (< 100 nm) compared to ICP-AES (bulk). Furthermore, considering the error of the fitting of the second coordination shells, such discrepancy is acceptable. It is noted that the first coordinated shell of Co-Fe-N-C remains nearly identical during OER at various times, indicating that the *in situ* formed Co-Fe-N-C double-atomic structure is stable during extended OER. Notably, the possibilities of the formation of CoOOH and any type of cobalt oxides can be excluded even after reacting for 5 h, since the spectroscopic features of Co-N-C and Co-Fe-N-C are evidently different from those cases (Figure 2.12).

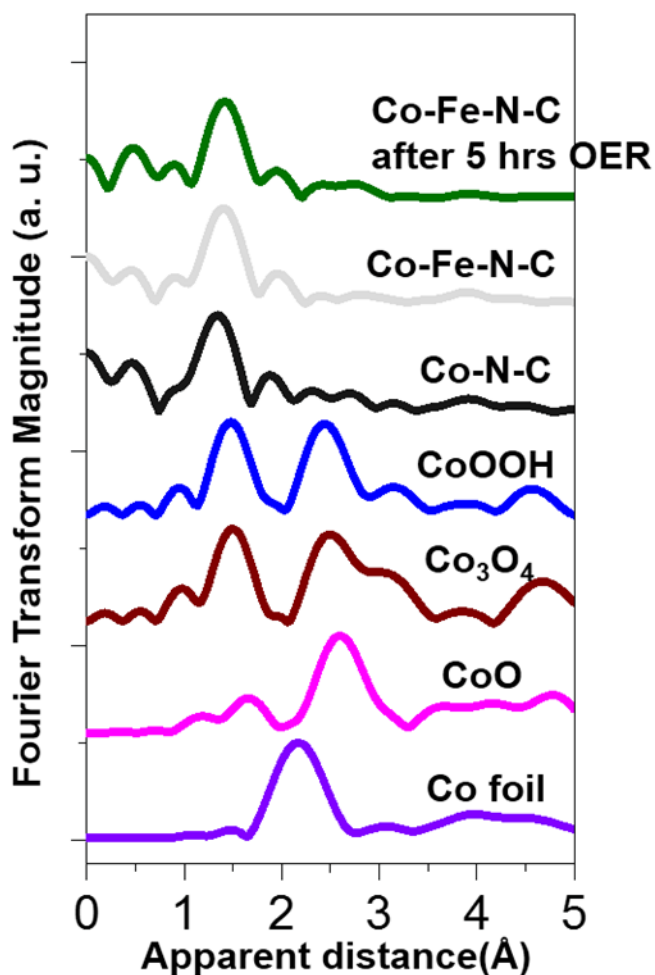


**Figure 2.12** Fourier transform Co K-edge EXAFS spectra of as-prepared Co-N-C, Co-Fe-N-C and Co-Fe-N-C after OER for 5 hours in comparison with various Co reference samples.

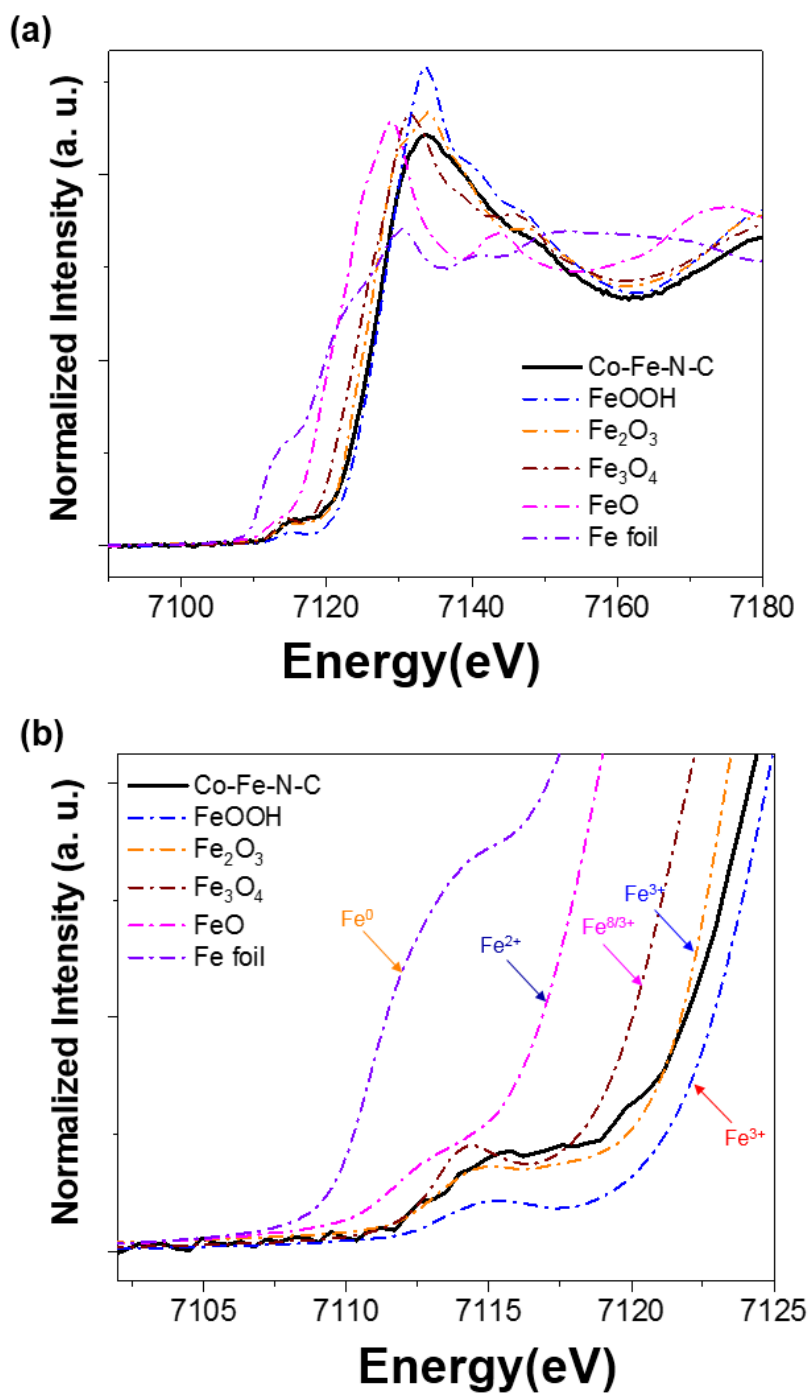


**Figure 2.13** *Ex situ* XANES of Fe in Co-Fe-N-C. (a) XANES spectra of Fe K-edge for Co-Fe-N-C and references including iron oxides and foil. (b) Magnified XANES with the energy range below 7125 eV.

As illustrated in Figure 2.10b, the oxidation state of Co is significantly higher than +3 after 45 min of OER and it reaches an even higher value after 180 min of OER. This observation would be consistent with a probable Co(IV)=O species acting as the key intermediate of OER.

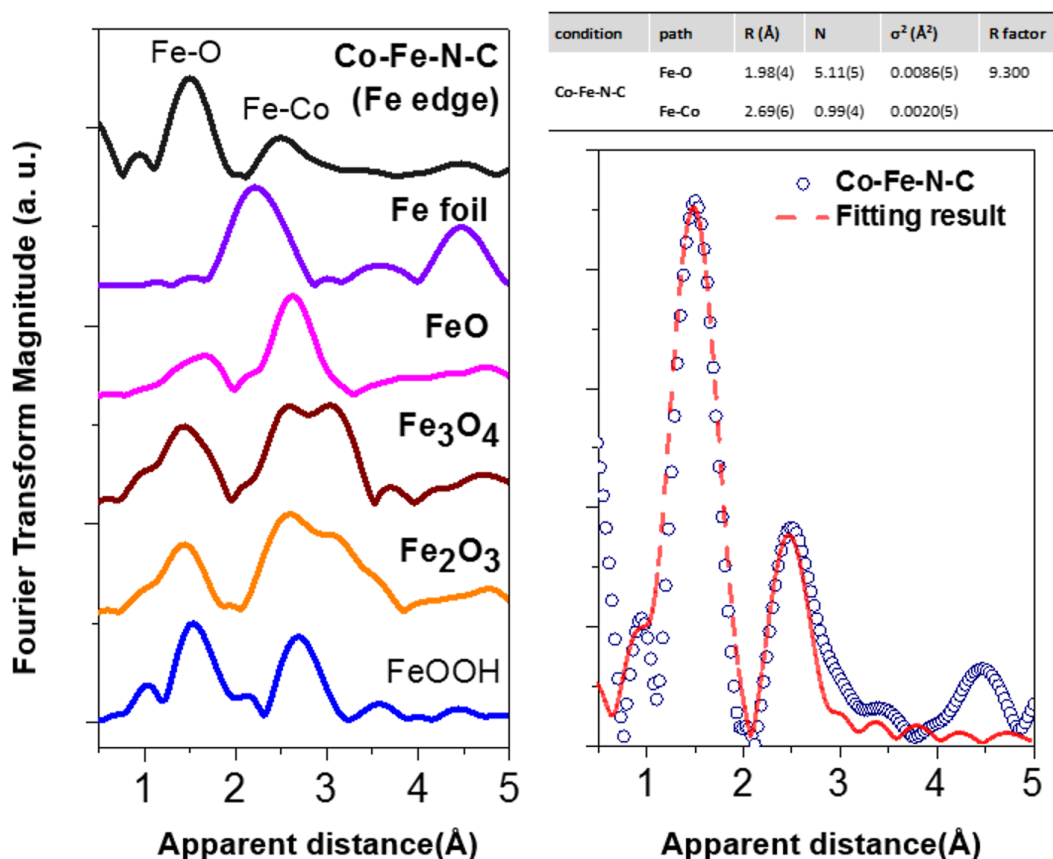


**Figure 2.14** *Ex situ* EXAFS spectra of Fe in Co-Fe-N-C. Left: EXAFS spectra of Fe K-edge for Co-Fe-N-C and references including iron oxides and foil. Right: r-space EXAFS spectra of Fe K-edge for Co-Fe-N-C sample (experimental data; blue hollow circle) and the corresponding fitting result (red line). Fitting structural parameters are demonstrated in the Table.

Because of the fundamental challenges to obtain the *in-situ/operando* XAS spectrum of Fe ions in Co-Fe-N-C due to the extremely low Fe amount, XAS analysis of Fe K edge was conducted on the post-catalytic samples of Co-Fe-N-C. Both the XANES and EXAFS spectra are characteristic of a divergent feature from those of reference cases including the FeOOH, Fe<sub>2</sub>O<sub>3</sub>, Fe<sub>3</sub>O<sub>4</sub>, FeO and Fe foil (Figures 2.13 and 2.14), while the oxidation state of Fe is approximately

+3 (Figure 2.13b). The major coordinated element in the first shell is oxygen. The CN is close to 5 (Figure 2.14). Considering the possible dehydration of the dry activated sample, we suggested a probable Fe-O6 structure. The presence of a rather weak peak at the second scattering shell is attributed to the single-scattering path of Fe-Co, in which the CN and the apparent distance is ~0.96 and 2.69 Å, respectively (Figure 2.14). The CN value indicates that most Fe ions are bonded with Co ions to form the double-atom moiety as proposed in Figure 2.11b. The distance of Fe-Co obtained from the Fe K edge data is well consistent with that obtained from the Co K edge data (Table 2.1).

Summing up, the XAS data reveals the following structural evolution of the single-atom Co precatalyst during OER activation (Figure 2.11). The as-prepared sample comprised of atomically dispersed Co atoms stabilized by three N and one C atoms from the N-doped carbon support and one oxygen from OH<sup>-</sup>/H<sub>2</sub>O. Upon immersion into an alkaline electrolyte, the ligand environment of Co ions changes significantly, and the Co ions are now coordinated to 1 C and 1 N or 2N from the support and 4 OH<sup>-</sup>/H<sub>2</sub>O groups coming from the electrolyte. After electrochemical activation, Fe is incorporated and a dimeric Co-Fe moiety is formed, probably through two bridging hydroxyl groups. This structure remains stable during OER. Taking into consideration of the essential role of Fe in catalysis and the activity scales with the amount of Fe, we attributed this dimeric, Co-Fe double-atom pair as the active site of Co-Fe-N-C.

## 2.5.2 Determination of intrinsic activity of Co-Fe-N-C

As the *operando* XAS results indicated the active site of Co-Fe-N-C is the Co-Fe dimeric unit, the TOFs of the catalyst could be calculated using the total amount of such Co-Fe unit. The activity is linearly dependent of the Fe content (Figure 2.9a). Nearly all of the Fe species are uniformly distributed (Figure 2.6c) and connected with single-atom Co sites (Figures 2.6d, 2.6e, 2.11 and 2.14). Therefore, the number of Co-Fe unit can be estimated by the Fe loadings. The TOF could be calculated as Eq. 2.1, where  $J$  is the anodic current density at certain overpotential,  $A$  is the geometrical surface area of the electrode,  $F$  is the Faraday constant (96485 C/mol), and  $m$  is the amount of dimeric active sites.

$$TOF = \frac{J \times A}{4 \times F \times m} \quad (\text{Eq. 2.1})$$

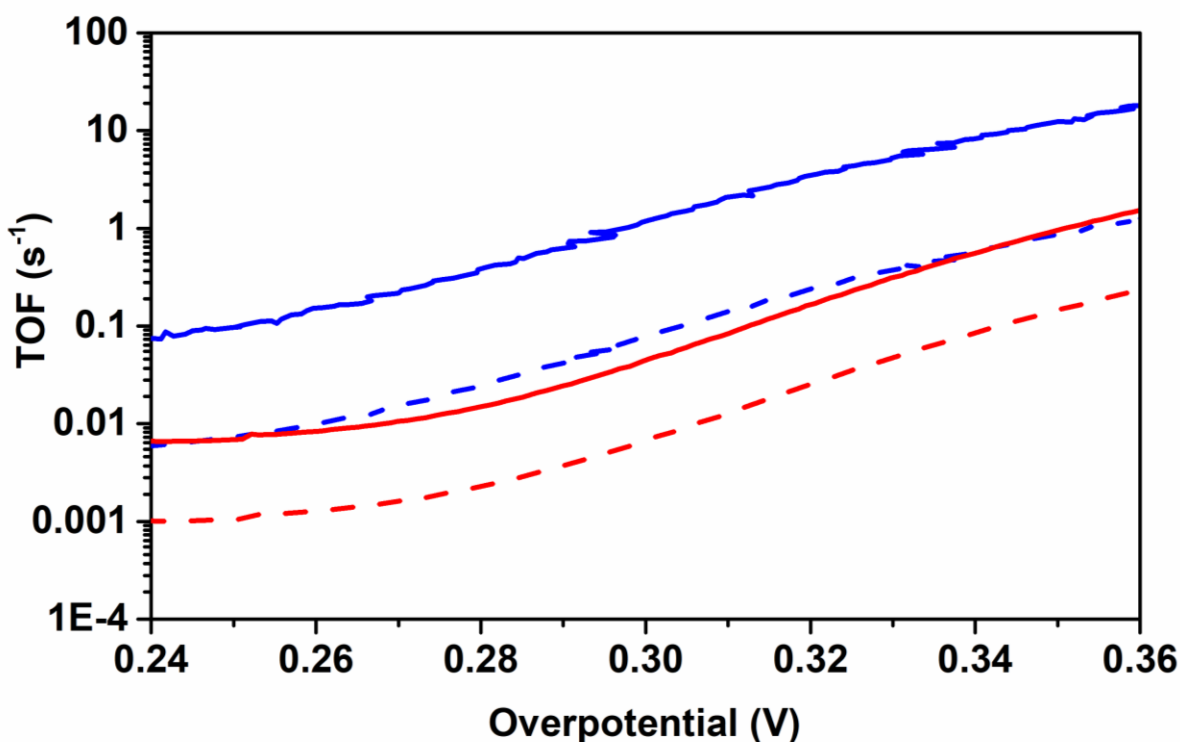


**Figure 2.15** Potential dependent TOFs of Co-Fe-N-C (blue curve) and activated Co-N-C-900 (in normal KOH, red curve). The solid line is based on the loading of dimetric Co-Fe sites, the dashed line is based on the loadings of total metals (Co and Fe).

With TOFs (Figure 2.15) of higher than  $1 \text{ s}^{-1}$  at 300 mV and about  $12 \text{ s}^{-1}$  at 350 mV, the Co-Fe-N-C has activity comparable to the most active nanomaterials based on transition metals (Table 2.2). It is noteworthy that the Co-Fe-N-C also exhibited the best OER performance compared to previously reported OER catalysts consisted of single atoms or sub-nano clusters (Table 2.2). The TOFs of Co-Fe-N-C are much higher than Co-N-C-900 (Figure 2.15), suggesting that in activated Co-N-C-900 (the control sample with more Co NPs), the absorbed Fe ions were connected mostly to Co NPs rather than single-atom Co sites.

**Table 2.1** Structural parameters of Co-N-C extracted from *operando* Co K-edge EXAFS refinement for as-prepared Co-N-C, Co-N-C after 5 CVs activation, as well as Co-N-C under OER for various duration. The blue area indicates the first shell coordination parameters.

condition	path	R (Å)	N	$\sigma^2$ (Å <sup>2</sup> )	R factor
As-prepared	Co-C	1.61(4)	1.10(5)	0.0097(3)	9.899
	Co-N	1.89(5)	3.36(2)	0.0085(6)	
	Co-O	2.15(2)	0.75(2)	0.0039(4)	
	Co-C1	2.92(3)	3.43(9)	0.0100(4)	
	Co-C2	3.16(4)	3.99(9)	0.0091(7)	
	Co-Fe	-	-	-	
In electrolyte	Co-C	1.36(3)	0.43(4)	0.0090(9)	3.962
	Co-N	1.64(6)	1.53(3)	0.0099(3)	
	Co-O	1.86(3)	3.21(5)	0.0055(4)	
	Co-C1	2.81(7)	2.27(5)	0.0077(9)	
	Co-C2	3.31(6)	2.17(8)	0.0072(3)	
	Co-Fe	-	-	-	
Activation (after 5 CVs)	Co-C	1.48(7)	0.47(3)	0.0097(5)	2.978
	Co-N	1.67(4)	1.48(6)	0.0094(4)	
	Co-O	1.86(5)	3.32(5)	0.0062(4)	
	Co-C1	2.84(3)	2.23(5)	0.0075(8)	
	Co-C2	3.38(7)	2.11(8)	0.0086(9)	
	Co-Fe	2.53(3)	0.22(2)	0.0095(7)	
45 min	Co-C	1.48(3)	0.46(5)	0.0098(6)	2.881
	Co-N	1.67(4)	1.51(3)	0.0085(2)	
	Co-O	1.86(5)	3.45(4)	0.0061(5)	
	Co-C1	2.81(3)	2.26(3)	0.0092(6)	
	Co-C2	3.37(7)	2.15(8)	0.0098(9)	
	Co-Fe	2.65(3)	0.26(2)	0.0089(4)	
90 min	Co-C	1.46(4)	0.44(3)	0.0023(6)	4.059
	Co-N	1.66(4)	1.51(5)	0.0062(2)	
	Co-O	1.86(5)	3.43(4)	0.0049(3)	
	Co-C1	2.80(2)	2.25(2)	0.0056(7)	
	Co-C2	3.39(7)	2.13(7)	0.0049(9)	
	Co-Fe	2.65(3)	0.24(3)	0.0097(6)	

<b>135 min</b>	<b>Co-C</b>	<b>1.48(4)</b>	<b>0.46(5)</b>	0.0032(7)	4.014
	<b>Co-N</b>	<b>1.68(2)</b>	<b>1.52(3)</b>	0.0025(2)	
	<b>Co-O</b>	<b>1.87(3)</b>	<b>3.44(2)</b>	0.0051(4)	
	<b>Co-C1</b>	2.81(2)	2.26(3)	0.0037(6)	
	<b>Co-C2</b>	3.38(7)	2.15(8)	0.0074(9)	
	<b>Co-Fe</b>	2.64(3)	0.23(2)	0.0059(5)	
<b>180 min</b>	<b>Co-C</b>	<b>1.40(6)</b>	<b>0.46(2)</b>	0.0091(7)	3.039
	<b>Co-N</b>	<b>1.68(2)</b>	<b>1.52(4)</b>	0.0096(2)	
	<b>Co-O</b>	<b>1.87(3)</b>	<b>3.25(3)</b>	0.0047(4)	
	<b>Co-C1</b>	2.82(2)	2.11(3)	0.0084(7)	
	<b>Co-C2</b>	3.37(8)	2.08(8)	0.0063(9)	
	<b>Co-Fe</b>	2.68(2)	0.27(2)	0.0095(4)	

**Table 2.2** Comparison of OER activity of Co-Fe-N-C with other state-of-the-art OER catalysts, including nanomaterials and atomically dispersed catalysts based on first-row transition metals.

Catalysts	Electrolyte	Overpotential (mV) @ 10 mA/cm <sup>2</sup>	Tafel slope (mV/dec)	TOF (s <sup>-1</sup> ) /overpotential (mV)	Reference
Co-N-C activated*	1 M KOH	321	40	12/350	<b>This work.</b>
CoOOH nanosheet	1 M KOH	300	38	0.09/340	<sup>57</sup>
Fe adsorbed CoO <sub>x</sub>	1 M KOH	309	28	1.6/350	<sup>58</sup>
CoAl LDH-graphene	1 M KOH	252	36	1.14/350	<sup>59</sup>
FeO <sub>x</sub> clusters on Ni foam	1M KOH	215	34	0.82/270	<sup>60</sup>
NiFe LDH-rGO	1 M KOH	207	39	0.99/300	<sup>61</sup>
NiFe LDH-CNT	1 M KOH	245	31	0.56/300	<sup>62</sup>
NiFeO <sub>x</sub>	1 M KOH	297	37	1.9/300	<sup>63</sup>
Exfoliated NiFe LDH	1 M KOH	301	40	0.11/300	<sup>64</sup>
Plasma-assisted Exfoliated CoFe LDH	1 M KOH	267	38	4.78/300	<sup>65</sup>
Co-g-C <sub>3</sub> N <sub>4</sub> -CNT	1 M KOH	370	62	-	<sup>13</sup>
Co-N,S-graphene	1 M KOH	370	62	0.27/350	<sup>12</sup>
Plasma treated ZIF-67	1 M KOH	319	70	0.082/320	<sup>66</sup>
Plasma treated ZIF-67	1 M KOH	310	54	0.462/300	<sup>67</sup>
Fe-N,S-CNT	1 M KOH	370	82	-	<sup>18</sup>
Ni <sub>4</sub> (PET) <sub>8</sub>	0.1 M KOH	330	38	-	<sup>68</sup>
Ni <sub>6</sub> (PET) <sub>12</sub>	0.1 M KOH	430	69	10/470	<sup>69</sup>
Ni-NHGF	1M KOH	331	63	0.72/300	<sup>16</sup>
Mn-GO	1 M KOH	337	55	-	<sup>21</sup>

\* In a KOH adding with 10 ppm Fe(III), the overpotential is 309 mV (@10 mA/cm<sup>2</sup>) while the Tafel slope is 37 mV/dec.

## 2.6 Conclusions

Electrochemical activation of Co species atomically dispersed on nitrogen-doped carbon (Co-N-C) in Fe-containing alkaline electrolyte led to incidental Fe-incorporation and the formation of a Co-Fe double-atom catalyst (Co-Fe-N-C). Fe is essential for the enhanced activity of Co-Fe-N-C



compared to Co-N-C, and the activity of the former scales with the amount of Fe loading. *Operando* XAS data indicated that Co-N-C undergoes major structural changes upon immersion into an alkaline electrolyte, followed by Fe incorporation during electrochemical activation to yield a dimeric Co-Fe structural motif that is the real active site for OER. This double-atom active site appears to be stable during OER. Its TOF, over 10 s<sup>-1</sup> at 350 mV overpotential, is among the highest for non-precious OER catalysts. This work introduces an easily accessed, molecularly defined, and earth-abundant bimetallic electrocatalysts for OER. Such double-atom catalyst bridges the transitionally separated molecular and solid-state catalysts, thereby offering an attractive platform for the fundamental studies of metal oxides in OER.

## 2.7 Experimental Details

### 2.7.1 Catalyst synthesis and electrolyte preparation

All the chemicals (including metal salts and organic ligands) were purchased from Sigma-Aldrich unless otherwise noted. The solvents include ultra-pure water (18.2 MΩ/cm), ethanol (Fluka), and isopropanol (Fluka).

**Synthesis of the Co-N-C precatalyst.** 0.5 mmol Co(OAc)<sub>2</sub>·4H<sub>2</sub>O (125 mg, Ac = acetate) was dissolved in 30 mL ethanol. An ethanol solution (20 mL) of 1,10-phenanthroline (Phen, 1.0 mmol, 180 mg) was added drop-wise and the reaction mixture was sonicated for 30 min. 90 mg of Phen and 4 g of commercial Mg(OH)<sub>2</sub> were then added and the reaction mixture was further sonicated for 30 min. The mixture was then refluxed at 60 °C for 4 h. The ethanol solvent was removed by rotary evaporation and the remaining solids were dried overnight in air and finely ground. The powder was calcinated at 700 °C for 2 h under a nitrogen atmosphere (ramping rate: 2 °C/min). A black solid was obtained. It was stirred in a 1 M HNO<sub>3</sub> solution at room temperature for 2 h to remove the MgO support and residual cobalt nanoparticles. The solid was further washed with ultra-pure water until the filtrate became neutral. The solid was dried in air at room temperature overnight (see Figure 2.1 for illustration).

**Synthesis of the Co-N-C-900C reference.** The synthetic procedure is the same as Co-N-C precatalyst except the temperature of pyrolysis is 900 °C.

**Preparation of Fe-free (Ni-containing) KOH.** The Fe impurities in normal KOH solutions can be removed by treating with high-purity Ni(OH)<sub>2</sub>.<sup>22</sup> In a clean 50 mL polypropylene centrifuge tube, 2

g of  $\text{Ni}(\text{NO}_3)_2 \cdot 6\text{H}_2\text{O}$  (99.99%) was dissolved in 5 mL of ultrapure water. 20 mL of 1 M KOH solution was added to give a  $\text{Ni}(\text{OH})_2$  precipitate. The suspension was agitated and centrifuged, and the supernatant was decanted. The  $\text{Ni}(\text{OH})_2$  precipitate was washed with ultrapure water for three times by centrifugation. The solid was dispersed in 10 mL of 1 M KOH by centrifugation, and the supernatant was decanted. This solid was used as the Fe-absorber. The cleaning procedure involves adding KOH solution in this  $\text{Ni}(\text{OH})_2$  solid, mechanically agitated over-night, followed by at least 3 h of resting. The Fe content of the electrolyte after treatment was at the detection limit of ICP-AES (ca. 2 ppb).

### 2.7.2 Physical Characterizations

XRD measurements were carried out on an X'Pert Philips diffractometer in Bragg-Brentano geometry with monochromatic  $\text{CuK}\alpha$  radiation (0.1541 nm) and a fast Si-PIN multi-strip detector. The step size was  $0.02^\circ \text{ s}^{-1}$ . Raman spectrum was recorded on a LabRAM high resolution Raman spectrometer. The power of laser was set as 0.1% in order to alleviate the damage of carbon matrix caused by stronger laser beam.  $\text{N}_2$ -physisorption measurements were performed on a Micromeritics 3Flex apparatus at liquid nitrogen temperature between  $10^{-5}$  and 0.99 relative  $\text{N}_2$  pressure. Samples (ca. 100 mg) were dried at  $120^\circ\text{C}$  under vacuum ( $< 10^{-3}$  mbar) for 4 h and a leak test was performed prior to analysis. TEM was performed on an FEI Talos microscope operated at 200 kV high tension. EDX mapping was used for elemental characterization, with simultaneously acquired HAADF-STEM images showing atomic number and thickness contrast. For atomic resolution imaging, the measurements were performed on an FEI Titan Themis 60-300 operated at 200 kV with an aberration-corrected electron probe and using HAADF-STEM conditions. Samples for TEM were prepared by drop-drying the samples from their diluted ethanol suspensions onto carbon-coated copper grids. XPS measurements were performed on a PHI5000 VersaProbe II XPS system by Physical Electronics (PHI) with a detection limit of 1 atomic percent. Monochromatic X-rays were generated by an  $\text{Al K}\alpha$  source (1486.7 eV). The diameter of the analyzed area is 10  $\mu\text{m}$ . ICP-AES results were obtained by a Nexlon 350 (Perkin Elmer) machine. Before dissolving in ultra-pure nitric acid (65%, Merck KGaA), all the samples were put in muffle oven and then heated at  $600^\circ\text{C}$  for 12 h in air to remove carbon support and make sure all of the metal ions were exposed to be digested by nitric acid. The concentration of nitric acid of the samples were diluted to 2% before the measurements.

### 2.7.3 Parameters for *operando* XAS

The *operando* XAS were recorded at SP8 (Japan) 12B2 Taiwan beamline of National Synchrotron Radiation Research Center (NSRRC), the electron storage ring was operated at 8.0 GeV with a constant current of ~100 mA. The *operando* XAS measurements were performed at the desired condition with a special electrochemical cell (EC) designed for these experiments, and the data were collected in fluorescence mode. During the measurements, the oxygen and hydrogen could be detected with close to 100% FE. Additionally, the activity trend of the catalysts was similar to that in EC for normal OER performance measurements. Thus, our XAS measurements can be considered as '*operando* experiments'.

**XAS data analysis.** An  $E_0$  values of 7709.0 eV was used to calibrate all data with respect to the first inflection point of the absorption K-edge of Co foil, respectively. The backscattering amplitude and phase shift functions for specific atom pairs were calculated ab initio using the FEFF8 code. X-ray absorption data were analyzed using standard procedures, including pre-edge and post-edge background subtraction, normalization with respect to edge height, Fourier transformation, and nonlinear least-squares curve fitting. The normalized  $k^3$ -weighted EXAFS spectra,  $k^3\chi(k)$ , were Fourier-transformed in a  $k$  range from 1.5 to 11 Å<sup>-1</sup>, to evaluate the contribution of each bond pair to the Fourier transform (FT) peak. The experimental Fourier-filtered spectra were obtained by performing an inverse Fourier transformation with a Hanning window function with  $r$  between 0.8–2 Å for first coordinated shell and 1.8–3.1 Å for second coordinated shell. The  $S_0^2$  (amplitude reduction factor) values of the Co was fixed at 0.88, to determine the structural parameters of each bond pair.

### 2.7.4 Electrochemical Characterizations

The catalyst ink was prepared by mixing of 1 mL water, 0.25 mL isopropanol, 0.01 mL 5 wt% Nafion solution and 3 mg catalysts. The ink was sonicated for at least 1 h. Then 40 µL of the ink was uniformly loaded onto a carbon cloth electrode (plasma treated to increase hydrophilicity, 0.25 cm<sup>2</sup>). The electrodes were dried in a 70 °C oven for 30 mins before measurements.

The electrochemical measurements were performed in a three-electrode electrochemical cell, in which Pt wire and Ag/AgCl electrode were used as counter and reference electrode,

respectively. The working electrode and reference electrode were separated with counter electrode by a glass frit. 1M KOH standard solution (Merck KGaA, pH = 13.6) and polypropylene beakers were adapted in order to make our measurements rigorous. All potentials were reported versus RHE unless otherwise specified by using the follow equation:  $E(\text{RHE}) = E(\text{Ag}/\text{AgCl}) + 0.197 \text{ V} + 0.0592 \times 13.6 \text{ V}$ . The solution was stirred by a magnetic stirring bar in all of the electrochemical measurements. All of the electrochemical results were compensated with solution resistance (95% degree). The polarization curves were recorded by the LSV, the scan rate was 0.5 mV/s. To investigate redox peaks, the scan rate was set to 50 mV/s in order to obtain higher signal to background ratio. The activation curves were measured in chronopotential mode with a current density of 2 mA/cm<sup>2</sup>, via the stability test were measured at a current density of 10 mA/cm<sup>2</sup>. Five CV scans should be carried out before galvanic static activation in case to oxidize the carbon surface. Accelerated degradation studies were performed in continuous CV scans at a scan rate of 50 mV/s for 3000 cycles (electrochemical window: 0.2–0.6 V vs. Ag/AgCl). FE were determined in a gas-tight H-type electrochemical cell. The cell was filled with 1M KOH solution until the headspace of the compartment containing the working electrode was about 9.2 ml. The oxygen probe was inserted into this headspace. The quantification of oxygen was performed using an Ocean Optics Multifrequency Phase Fluorimeter (MFPF-100) with a FOXY-OR 125 probe. A linear two-point calibration curve was created using air (20.9% O<sub>2</sub>) and the headspace purged with N<sub>2</sub> for more than 1 h (0% O<sub>2</sub>). A constant oxidation current of 2.5 mA (corresponding to a current density of 10 mA/cm<sup>2</sup>) was passed for 300 mins. It should be mentioned that the final volume increased to 12 mL due to the increased pressure. The Faradaic yield was calculated from Eq. 2.2, where  $P$  is the pressure of atmosphere ( $1.013 \times 10^5 \text{ Pa}$ ),  $V$  is the volume of the headspace,  $R$  is the universal gas constant ( $8.314 \text{ J}/(\text{mol K})$ ),  $T$  is the environmental temperature (298.15K),  $w(\text{O}_2)$  is the volume concentration of oxygen measured by the oxygen sensor,  $I$  is the constant current (2.5 mA),  $t$  is the time (s) for the galvanic static electrolysis, and  $F$  is the Faraday constant. The volume of the head space was assumed to increase linearly with the concentration of oxygen, that is  $w(\text{O}_2)/0.232 \times (12.0 - 9.2) + 9.2$  (23.2% was the final oxygen concentration read by oxygen sensor).

$$FE\% = \frac{PV \times w(\text{O}_2) \times 4F}{RT \times It} \times 100\% \quad (\text{Eq. 2.2})$$

## 2.8 Contributions

L. Bai performed the synthesis, the majority of characterization, and electrochemical tests. C.-S. Hsu performed the *operando* X-ray absorption experiments. D. T. L. Alexander performed the spherical aberration corrected HAADF-STEM measurements. All authors analyzed the data. L. Bai and X. Hu wrote the paper, with inputs from other authors. H. M. Chen and X. Hu directed the research.

The following individuals from EPFL were acknowledged for experimental assistance: Dr. Fang Song (TEM and Raman) Dr. Lucas-Alexandre Stern (TEM), Mr. Weiyan Ni (XRD), Dr. Florent E. H  roguel and Prof. Jeremy Luterbacher (N<sub>2</sub> adsorption), Dr. Pierre Mettraux (XPS), Dr. Natalia Gasilova (ICP-AES). Dr. Yen-Fa Liao (from NSRRC) is acknowledged for help with *operando* XAS. We thank Mr. Yongpeng Liu (EPFL) for help with graphics.

## 2.9 References of Chapter 2

- (1) Bai, L.; Hsu, C. S.; Alexander, D. T. L.; Chen, H. M.; Hu, X. A Cobalt-Iron Double-Atom Catalyst for the Oxygen Evolution Reaction. *J. Am. Chem. Soc.* **2019**, *141*, 14190-14199.
- (2) Zhu, C.; Fu, S.; Shi, Q.; Du, D.; Lin, Y. Single-Atom Electrocatalysts. *Angew. Chem. Int. Ed.* **2017**, *56*, 13944-13960.
- (3) Zhao, D.; Zhuang, Z.; Cao, X.; Zhang, C.; Peng, Q.; Chen, C.; Li, Y. Atomic site electrocatalysts for water splitting, oxygen reduction and selective oxidation. *Chem. Soc. Rev.* **2020**, *49*, 2215-2264.
- (4) Chen, Y.; Ji, S.; Chen, C.; Peng, Q.; Wang, D.; Li, Y. Single-Atom Catalysts: Synthetic Strategies and Electrochemical Applications. *Joule* **2018**, *2*, 1242-1264.
- (5) Yu, H.; Hui, L.; Xue, Y.; Liu, Y.; Fang, Y.; Xing, C.; Zhang, C.; Zhang, D.; Chen, X.; Du, Y.; Wang, Z.; Gao, Y.; Huang, B.; Li, Y. 2D graphdiyne loading ruthenium atoms for high efficiency water splitting. *Nano Energy* **2020**, *72*, 104667.
- (6) Yao, Y.; Hu, S.; Chen, W.; Huang, Z.-Q.; Wei, W.; Yao, T.; Liu, R.; Zang, K.; Wang, X.; Wu, G.; Yuan, W.; Yuan, T.; Zhu, B.; Liu, W.; Li, Z.; He, D.; Xue, Z.; Wang, Y.; Zheng, X.; Dong, J.; Chang, C.-R.; Chen, Y.; Hong, X.; Luo, J.; Wei, S.; Li, W.-X.; Strasser, P.; Wu, Y.; Li, Y. Engineering the electronic structure of single atom Ru sites via compressive strain boosts acidic water oxidation electrocatalysis. *Nat. Catal.* **2019**, *2*, 304-313.
- (7) Cao, L.; Luo, Q.; Chen, J.; Wang, L.; Lin, Y.; Wang, H.; Liu, X.; Shen, X.; Zhang, W.; Liu, W.; Qi, Z.; Jiang, Z.; Yang, J.; Yao, T. Dynamic oxygen adsorption on single-atomic Ruthenium catalyst with high performance for acidic oxygen evolution reaction. *Nat. Commun.* **2019**, *10*, 4849.

- (8) Wang, Q.; Huang, X.; Zhao, Z. L.; Wang, M.; Xiang, B.; Li, J.; Feng, Z.; Xu, H.; Gu, M. Ultrahigh-Loading of Ir Single Atoms on NiO Matrix to Dramatically Enhance Oxygen Evolution Reaction. *J. Am. Chem. Soc.* **2020**, *142*, 7425-7433.
- (9) Babu, D. D.; Huang, Y.; Anandhababu, G.; Wang, X.; Si, R.; Wu, M.; Li, Q.; Wang, Y.; Yao, J. Atomic iridium@cobalt nanosheets for dinuclear tandem water oxidation. *J. Mater. Chem. A* **2019**, *7*, 8376-8383.
- (10) Jiang, K.; Luo, M.; Peng, M.; Yu, Y.; Lu, Y. R.; Chan, T. S.; Liu, P.; de Groot, F. M. F.; Tan, Y. Dynamic active-site generation of atomic iridium stabilized on nanoporous metal phosphides for water oxidation. *Nat. Commun.* **2020**, *11*, 2701.
- (11) Su, H.; Zhao, X.; Cheng, W.; Zhang, H.; Li, Y.; Zhou, W.; Liu, M.; Liu, Q. Hetero-N-Coordinated Co Single Sites with High Turnover Frequency for Efficient Electrocatalytic Oxygen Evolution in an Acidic Medium. *ACS Energy Lett.* **2019**, *4*, 1816-1822.
- (12) Wang, J.; Ge, X.; Liu, Z.; Thia, L.; Yan, Y.; Xiao, W.; Wang, X. Heterogeneous Electrocatalyst with Molecular Cobalt Ions Serving as the Center of Active Sites. *J. Am. Chem. Soc.* **2017**, *139*, 1878-1884.
- (13) Zheng, Y.; Jiao, Y.; Zhu, Y.; Cai, Q.; Vasileff, A.; Li, L. H.; Han, Y.; Chen, Y.; Qiao, S. Z. Molecule-Level g-C<sub>3</sub>N<sub>4</sub> Coordinated Transition Metals as a New Class of Electrocatalysts for Oxygen Electrode Reactions. *J. Am. Chem. Soc.* **2017**, *139*, 3336-3339.
- (14) Zhang, H.; Liu, Y.; Chen, T.; Zhang, J.; Zhang, J.; Lou, X. W. D. Unveiling the Activity Origin of Electrocatalytic Oxygen Evolution over Isolated Ni Atoms Supported on a N-Doped Carbon Matrix. *Adv. Mater.* **2019**, *31*, e1904548.
- (15) Hou, Y.; Qiu, M.; Kim, M. G.; Liu, P.; Nam, G.; Zhang, T.; Zhuang, X.; Yang, B.; Cho, J.; Chen, M.; Yuan, C.; Lei, L.; Feng, X. Atomically dispersed nickel-nitrogen-sulfur species anchored on porous carbon nanosheets for efficient water oxidation. *Nat. Commun.* **2019**, *10*, 1392.
- (16) Fei, H.; Dong, J.; Feng, Y.; Allen, C. S.; Wan, C.; Voloskiy, B.; Li, M.; Zhao, Z.; Wang, Y.; Sun, H.; An, P.; Chen, W.; Guo, Z.; Lee, C.; Chen, D.; Shakir, I.; Liu, M.; Hu, T.; Li, Y.; Kirkland, A. I.; Duan, X.; Huang, Y. General synthesis and definitive structural identification of MN<sub>4</sub>C<sub>4</sub> single-atom catalysts with tunable electrocatalytic activities. *Nat. Catal.* **2018**, *1*, 63-72.
- (17) Zhang, L.; Jia, Y.; Gao, G.; Yan, X.; Chen, N.; Chen, J.; Soo, M. T.; Wood, B.; Yang, D.; Du, A.; Yao, X. Graphene Defects Trap Atomic Ni Species for Hydrogen and Oxygen Evolution Reactions. *Chem* **2018**, *4*, 285-297.
- (18) Chen, P.; Zhou, T.; Xing, L.; Xu, K.; Tong, Y.; Xie, H.; Zhang, L.; Yan, W.; Chu, W.; Wu, C.; Xie, Y. Atomically Dispersed Iron-Nitrogen Species as Electrocatalysts for Bifunctional Oxygen Evolution and Reduction Reactions. *Angew. Chem. Int. Ed.* **2017**, *56*, 610-614.
- (19) Lei, C.; Chen, H.; Cao, J.; Yang, J.; Qiu, M.; Xia, Y.; Yuan, C.; Yang, B.; Li, Z.; Zhang, X.; Lei, L.; Abbott, J.; Zhong, Y.; Xia, X.; Wu, G.; He, Q.; Hou, Y. Fe-N<sub>4</sub> Sites Embedded into Carbon Nanofiber Integrated with Electrochemically Exfoliated Graphene for Oxygen Evolution in Acidic Medium. *Adv. Energy Mater.* **2018**, *8*, 1801912.

- (20) Shang, H.; Sun, W.; Sui, R.; Pei, J.; Zheng, L.; Dong, J.; Jiang, Z.; Zhou, D.; Zhuang, Z.; Chen, W.; Zhang, J.; Wang, D.; Li, Y. Engineering Isolated Mn-N<sub>2</sub>C<sub>2</sub> Atomic Interface Sites for Efficient Bifunctional Oxygen Reduction and Evolution Reaction. *Nano Lett.* **2020**, *20*, 5443-5450.
- (21) Guan, J.; Duan, Z.; Zhang, F.; Kelly, S. D.; Si, R.; Dupuis, M.; Huang, Q.; Chen, J. Q.; Tang, C.; Li, C. Water oxidation on a mononuclear manganese heterogeneous catalyst. *Nat. Catal.* **2018**, *1*, 870-877.
- (22) Trotochaud, L.; Young, S. L.; Ranney, J. K.; Boettcher, S. W. Nickel-iron oxyhydroxide oxygen-evolution electrocatalysts: the role of intentional and incidental iron incorporation. *J. Am. Chem. Soc.* **2014**, *136*, 6744-6753.
- (23) Xu, X.; Song, F.; Hu, X. A nickel iron diselenide-derived efficient oxygen-evolution catalyst. *Nat. Commun.* **2016**, *7*, 12324.
- (24) Hung, S.-F.; Zhu, Y.; Tzeng, G.-Q.; Chen, H.-C.; Hsu, C.-S.; Liao, Y.-F.; Ishii, H.; Hiraoka, N.; Chen, H. M. In Situ Spatially Coherent Identification of Phosphide-Based Catalysts: Crystallographic Latching for Highly Efficient Overall Water Electrolysis. *ACS Energy Lett.* **2019**, *4*, 2813-2820.
- (25) Cao, L.; Luo, Q.; Liu, W.; Lin, Y.; Liu, X.; Cao, Y.; Zhang, W.; Wu, Y.; Yang, J.; Yao, T.; Wei, S. Identification of single-atom active sites in carbon-based cobalt catalysts during electrocatalytic hydrogen evolution. *Nat. Catal.* **2018**, *2*, 134-141.
- (26) Fang, S.; Zhu, X.; Liu, X.; Gu, J.; Liu, W.; Wang, D.; Zhang, W.; Lin, Y.; Lu, J.; Wei, S.; Li, Y.; Yao, T. Uncovering near-free platinum single-atom dynamics during electrochemical hydrogen evolution reaction. *Nat. Commun.* **2020**, *11*, 1029.
- (27) Karapinar, D.; Huan, N. T.; Ranjbar Sahraie, N.; Li, J.; Wakerley, D.; Touati, N.; Zanna, S.; Taverna, D.; Galvão Tizei, L. H.; Zitolo, A. Electroreduction of CO<sub>2</sub> on Single-Site Copper-Nitrogen-Doped Carbon Material: Selective Formation of Ethanol and Reversible Restructuration of the Metal Sites. *Angew. Chem. Int. Ed.* **2019**, *58*, 15098-15103.
- (28) Suen, N. T.; Hung, S. F.; Quan, Q.; Zhang, N.; Xu, Y. J.; Chen, H. M. Electrocatalysis for the oxygen evolution reaction: recent development and future perspectives. *Chem. Soc. Rev.* **2017**, *46*, 337-365.
- (29) Song, F.; Bai, L.; Moysiadou, A.; Lee, S.; Hu, C.; Liardet, L.; Hu, X. Transition Metal Oxides as Electrocatalysts for the Oxygen Evolution Reaction in Alkaline Solutions: An Application-Inspired Renaissance. *J. Am. Chem. Soc.* **2018**, *140*, 7748-7759.
- (30) McCrory, C. C.; Jung, S.; Peters, J. C.; Jaramillo, T. F. Benchmarking heterogeneous electrocatalysts for the oxygen evolution reaction. *J. Am. Chem. Soc.* **2013**, *135*, 16977-16987.
- (31) Morales-Guio, C. G.; Liardet, L.; Hu, X. Oxidatively Electrodeposited Thin-Film Transition Metal (Oxy)hydroxides as Oxygen Evolution Catalysts. *J. Am. Chem. Soc.* **2016**, *138*, 8946-8957.
- (32) Zhang, M.; de Respinis, M.; Frei, H. Time-resolved observations of water oxidation intermediates on a cobalt oxide nanoparticle catalyst. *Nat. Chem.* **2014**, *6*, 362-367.

- (33) Burke, M. S.; Kast, M. G.; Trotochaud, L.; Smith, A. M.; Boettcher, S. W. Cobalt-iron (oxy)hydroxide oxygen evolution electrocatalysts: the role of structure and composition on activity, stability, and mechanism. *J. Am. Chem. Soc.* **2015**, *137*, 3638-3648.
- (34) Wang, J.; Huang, Z.; Liu, W.; Chang, C.; Tang, H.; Li, Z.; Chen, W.; Jia, C.; Yao, T.; Wei, S.; Wu, Y.; Li, Y. Design of N-Coordinated Dual-Metal Sites: A Stable and Active Pt-Free Catalyst for Acidic Oxygen Reduction Reaction. *J. Am. Chem. Soc.* **2017**, *139*, 17281-17284.
- (35) Jiao, J.; Lin, R.; Liu, S.; Cheong, W. C.; Zhang, C.; Chen, Z.; Pan, Y.; Tang, J.; Wu, K.; Hung, S. F.; Chen, H. M.; Zheng, L.; Lu, Q.; Yang, X.; Xu, B.; Xiao, H.; Li, J.; Wang, D.; Peng, Q.; Chen, C.; Li, Y. Copper atom-pair catalyst anchored on alloy nanowires for selective and efficient electrochemical reduction of CO<sub>2</sub>. *Nat. Chem.* **2019**, 222-228.
- (36) Zhao, Y.; Yang, K. R.; Wang, Z.; Yan, X.; Cao, S.; Ye, Y.; Dong, Q.; Zhang, X.; Thorne, J. E.; Jin, L.; Materna, K. L.; Trimpalis, A.; Bai, H.; Fakra, S. C.; Zhong, X.; Wang, P.; Pan, X.; Guo, J.; Flytzani-Stephanopoulos, M.; Brudvig, G. W.; Batista, V. S.; Wang, D. Stable iridium dinuclear heterogeneous catalysts supported on metal-oxide substrate for solar water oxidation. *Proc. Natl. Acad. Sci. USA* **2018**, *115*, 2902-2907.
- (37) Liu, W.; Zhang, L.; Yan, W.; Liu, X.; Yang, X.; Miao, S.; Wang, W.; Wang, A.; Zhang, T. Single-atom dispersed Co–N–C catalyst: structure identification and performance for hydrogenative coupling of nitroarenes. *Chem. Sci.* **2016**, *7*, 5758-5764.
- (38) Li, Q.; Chen, W.; Xiao, H.; Gong, Y.; Li, Z.; Zheng, L.; Zheng, X.; Yan, W.; Cheong, W. C.; Shen, R.; Fu, N.; Gu, L.; Zhuang, Z.; Chen, C.; Wang, D.; Peng, Q.; Li, J.; Li, Y. Fe Isolated Single Atoms on S, N Codoped Carbon by Copolymer Pyrolysis Strategy for Highly Efficient Oxygen Reduction Reaction. *Adv. Mater.* **2018**, *30*, e1800588.
- (39) Ren, W.; Tan, X.; Yang, W.; Jia, C.; Xu, S.; Wang, K.; Smith, S. C.; Zhao, C. Isolated Diatomic Ni-Fe Metal–Nitrogen Sites for Synergistic Electroreduction of CO<sub>2</sub>. *Angew. Chem. Int. Ed.* **2019**, *58*, 6972-6976.
- (40) Cychosz, K. A.; Guillet-Nicolas, R.; Garcia-Martinez, J.; Thommes, M. Recent advances in the textural characterization of hierarchically structured nanoporous materials. *Chem. Soc. Rev.* **2017**, *46*, 389-414.
- (41) Liu, J. Catalysis by Supported Single Metal Atoms. *ACS Catal* **2016**, *7*, 34-59.
- (42) Bayatsarmadi, B.; Zheng, Y.; Vasileff, A.; Qiao, S. Z. Recent Advances in Atomic Metal Doping of Carbon-based Nanomaterials for Energy Conversion. *Small* **2017**, *13*, 1700191.
- (43) Zhang, L.; Wang, A.; Wang, W.; Huang, Y.; Liu, X.; Miao, S.; Liu, J.; Zhang, T. Co–N–C Catalyst for C–C Coupling Reactions: On the Catalytic Performance and Active Sites. *ACS Catal.* **2015**, *5*, 6563-6572.
- (44) Fei, H.; Dong, J.; Arellano-Jimenez, M. J.; Ye, G.; Dong Kim, N.; Samuel, E. L.; Peng, Z.; Zhu, Z.; Qin, F.; Bao, J.; Yacaman, M. J.; Ajayan, P. M.; Chen, D.; Tour, J. M. Atomic cobalt on nitrogen-doped graphene for hydrogen generation. *Nat. Commun.* **2015**, *6*, 8668.



- (45) Ju, W.; Bagger, A.; Hao, G. P.; Varela, A. S.; Sinev, I.; Bon, V.; Roldan Cuenya, B.; Kaskel, S.; Rossmeisl, J.; Strasser, P. Understanding activity and selectivity of metal-nitrogen-doped carbon catalysts for electrochemical reduction of CO<sub>2</sub>. *Nat. Commun.* **2017**, *8*, 944.
- (46) Yang, H. B.; Hung, S.-F.; Liu, S.; Yuan, K.; Miao, S.; Zhang, L.; Huang, X.; Wang, H.-Y.; Cai, W.; Chen, R.; Gao, J.; Yang, X.; Chen, W.; Huang, Y.; Chen, H. M.; Li, C. M.; Zhang, T.; Liu, B. Atomically dispersed Ni(i) as the active site for electrochemical CO<sub>2</sub> reduction. *Nat. Energy* **2018**, *3*, 140-147.
- (47) Wang, G.; Wang, H.; Lu, X.; Ling, Y.; Yu, M.; Zhai, T.; Tong, Y.; Li, Y. Solid-state supercapacitor based on activated carbon cloths exhibits excellent rate capability. *Adv. Mater.* **2014**, *26*, 2676-2682.
- (48) Tian, Z.; Wang, C.; Yue, J.; Zhang, X.; Ma, L. Effect of a potassium promoter on the Fischer–Tropsch synthesis of light olefins over iron carbide catalysts encapsulated in graphene-like carbon. *Catal. Sci. Tech.* **2019**, *9*, 2728-2741.
- (49) Lu, X.; Yim, W. L.; Suryanto, B. H.; Zhao, C. Electrocatalytic oxygen evolution at surface-oxidized multiwall carbon nanotubes. *J. Am. Chem. Soc.* **2015**, *137*, 2901-2907.
- (50) Peng, H.; Luo, W.; Wu, D.; Bie, X.; Shao, H.; Jiao, W.; Liu, Y. Study on the Effect of Fe<sup>3+</sup> on Zircon Flotation Separation from Cassiterite Using Sodium Oleate as Collector. *Minerals* **2017**, *7*, 108.
- (51) Channei, D.; Phanichphant, S.; Nakaruk, A.; Mofarah, S.; Koshy, P.; Sorrell, C. Aqueous and Surface Chemistries of Photocatalytic Fe-Doped CeO<sub>2</sub> Nanoparticles. *Catalysts* **2017**, *7*, 45.
- (52) Chung, D. Y.; Lopes, P. P.; Farinazzo Bergamo Dias Martins, P.; He, H.; Kawaguchi, T.; Zapol, P.; You, H.; Tripkovic, D.; Strmcnik, D.; Zhu, Y.; Seifert, S.; Lee, S.; Stamenkovic, V. R.; Markovic, N. M. Dynamic stability of active sites in hydr(oxy)oxides for the oxygen evolution reaction. *Nat. Energy* **2020**, *5*, 222-230.
- (53) Hsu, C. S.; Suen, N. T.; Hsu, Y. Y.; Lin, H. Y.; Tung, C. W.; Liao, Y. F.; Chan, T. S.; Sheu, H. S.; Chen, S. Y.; Chen, H. M. Valence- and element-dependent water oxidation behaviors: in situ X-ray diffraction, absorption and electrochemical impedance spectroscopies. *Phys. Chem. Chem. Phys.* **2017**, *19*, 8681-8693.
- (54) Wang, H. Y.; Hung, S. F.; Chen, H. Y.; Chan, T. S.; Chen, H. M.; Liu, B. In *Operando* Identification of Geometrical-Site-Dependent Water Oxidation Activity of Spinel Co<sub>3</sub>O<sub>4</sub>. *J. Am. Chem. Soc.* **2016**, *138*, 36-39.
- (55) Aquilanti, G.; Cognigni, A.; Anis-ur-Rehman, M. Cation Distribution in Zn Doped Cobalt Nanoferrites Determined by X-ray Absorption Spectroscopy. *J. Supercond. Novel Magn.* **2010**, *24*, 659-663.
- (56) Pearson, W. B.: *Crystal chemistry and physics of metals and alloys*; Wiley, 1972.
- (57) Huang, J.; Chen, J.; Yao, T.; He, J.; Jiang, S.; Sun, Z.; Liu, Q.; Cheng, W.; Hu, F.; Jiang, Y.; Pan, Z.; Wei, S. CoOOH Nanosheets with High Mass Activity for Water Oxidation. *Angew. Chem. Int. Ed.* **2015**, *54*, 8722-8727.

- (58) Gong, L.; Chng, X. Y. E.; Du, Y.; Xi, S.; Yeo, B. S. Enhanced Catalysis of the Electrochemical Oxygen Evolution Reaction by Iron(III) Ions Adsorbed on Amorphous Cobalt Oxide. *ACS Catal.* **2018**, *8*, 807-814.
- (59) Ping, J.; Wang, Y.; Lu, Q.; Chen, B.; Chen, J.; Huang, Y.; Ma, Q.; Tan, C.; Yang, J.; Cao, X.; Wang, Z.; Wu, J.; Ying, Y.; Zhang, H. Self-Assembly of Single-Layer CoAl-Layered Double Hydroxide Nanosheets on 3D Graphene Network Used as Highly Efficient Electrocatalyst for Oxygen Evolution Reaction. *Adv. Mater.* **2016**, *28*, 7640-7645.
- (60) Song, F.; Busch, M. M.; Lassalle-Kaiser, B.; Hsu, C.-S.; Petkucheva, E.; Bensimon, M.; Chen, H. M.; Corminboeuf, C.; Hu, X. An Unconventional Iron Nickel Catalyst for the Oxygen Evolution Reaction. *ACS Cent. Sci.* **2019**, *5*, 558-568.
- (61) Long, X.; Li, J.; Xiao, S.; Yan, K.; Wang, Z.; Chen, H.; Yang, S. A strongly coupled graphene and FeNi double hydroxide hybrid as an excellent electrocatalyst for the oxygen evolution reaction. *Angew. Chem. Int. Ed.* **2014**, *53*, 7584-7588.
- (62) Gong, M.; Li, Y.; Wang, H.; Liang, Y.; Wu, J. Z.; Zhou, J.; Wang, J.; Regier, T.; Wei, F.; Dai, H. An advanced Ni-Fe layered double hydroxide electrocatalyst for water oxidation. *J. Am. Chem. Soc.* **2013**, *135*, 8452-8455.
- (63) Fominykh, K.; Chernev, P.; Zaharieva, I.; Sicklinger, J.; Stefanic, G.; Dobliger, M.; Muller, A.; Pokharel, A.; Bocklein, S.; Scheu, C.; Bein, T.; Fattakhova-Rohlfing, D. Iron-doped nickel oxide nanocrystals as highly efficient electrocatalysts for alkaline water splitting. *ACS Nano* **2015**, *9*, 5180-5188.
- (64) Song, F.; Hu, X. Exfoliation of layered double hydroxides for enhanced oxygen evolution catalysis. *Nat. Commun.* **2014**, *5*, 4477.
- (65) Wang, Y.; Zhang, Y.; Liu, Z.; Xie, C.; Feng, S.; Liu, D.; Shao, M.; Wang, S. Layered Double Hydroxide Nanosheets with Multiple Vacancies Obtained by Dry Exfoliation as Highly Efficient Oxygen Evolution Electrocatalysts. *Angew. Chem. Int. Ed.* **2017**, *56*, 5867-5871.
- (66) Dou, S.; Dong, C.-L.; Hu, Z.; Huang, Y.-C.; Chen, J.-I.; Tao, L.; Yan, D.; Chen, D.; Shen, S.; Chou, S.; Wang, S. Atomic-Scale CoO<sub>x</sub> Species in Metal-Organic Frameworks for Oxygen Evolution Reaction. *Adv. Funct. Mater.* **2017**, *27*, 1702546.
- (67) Tao, L.; Lin, C.-Y.; Dou, S.; Feng, S.; Chen, D.; Liu, D.; Huo, J.; Xia, Z.; Wang, S. Creating coordinatively unsaturated metal sites in metal-organic-frameworks as efficient electrocatalysts for the oxygen evolution reaction: Insights into the active centers. *Nano Energy* **2017**, *41*, 417-425.
- (68) Joya, K. S.; Sinatra, L.; AbdulHalim, L. G.; Joshi, C. P.; Hedhili, M. N.; Bakr, O. M.; Hussain, I. Atomically monodisperse nickel nanoclusters as highly active electrocatalysts for water oxidation. *Nanoscale* **2016**, *8*, 9695-9703.
- (69) Kauffman, D. R.; Alfonso, D.; Tafen, D. N.; Lekse, J.; Wang, C.; Deng, X.; Lee, J.; Jang, H.; Lee, J.-s.; Kumar, S.; Matraga, C. Electrocatalytic Oxygen Evolution with an Atomically Precise Nickel Catalyst. *ACS Catal.* **2016**, *6*, 1225-1234.

# Chapter 3 The Generality of Double-Atom Catalysis in alkaline Oxygen Evolution Reaction

The results presented in this chapter were partly reformatted from a published preprint<sup>1</sup>:

**L. Bai**, C. S. Hsu, D. T. L. Alexander, H. M. Chen, X. Hu: Double-Atom Catalysts Provide a Molecular Platform for Oxygen Evolution. ChemRxiv. Preprint (2019). Link:

<https://doi.org/10.26434/chemrxiv.11341961.v1>

### 3.1 Introduction

Due to the importance of oxygen evolution reaction (OER) for many carbon-neutral energy conversion process, tremendous efforts have been spent in developing efficient and scalable OER electrocatalysts.<sup>2-5</sup> It is now established that mixed metal oxides containing Co, Fe, or Ni are the most active heterogeneous OER catalysts in alkaline medium.<sup>2-3, 5-7</sup> As demonstrated in Chapter 1 of this Thesis, however, the heterogeneous nature of these metal oxides makes it difficult to study and understand the fundamental properties and mechanisms of these catalysts.<sup>2-</sup>

3, 8-9

Atomically dispersed catalysts including single-atom catalysts (SACs) and discrete sub-nano clusters are emerging class of heterogeneous electrocatalysts with high atomic efficiency.<sup>10-14</sup> These catalysts possess uniform and well-defined active sites, providing a unique opportunity for mechanistic understanding. Although some atomically dispersed OER catalysts were recently reported<sup>10-14</sup>, the structures of their active sites during OER remained unclear. In Chapter 2 of this Thesis, we already found that a purposely-made single-atom Co catalyst (Co-N-C) was in reality a Co-Fe double-atom catalyst (Co-Fe-N-C), due to *in situ* catalyst transformation in KOH containing Fe ions impurities. This double-atom Co-Fe catalyst exhibited much higher intrinsic OER activity than the pristine Co SAC, which is quite similar to the fact that heterogeneous bimetallic OER catalysts have better performance than single-metallic ones. Thus, it would be intriguing that some other non-noble metal double-atom catalysts (DACs) with higher intrinsic OER activity could be prepared by similar methods.

In this Chapter, a series of DACs are produced from Co, Fe, and Ni-containing single-atom pre-catalysts via similar electrochemical activation methods, manifesting the generality of double-atom catalysis in alkaline OER. All of these DACs possess two to three magnitude higher intrinsic activities in comparison to the single-atom pre-catalysts. The structures of these catalysts are well characterized by *operando* X-ray absorption spectroscopy (XAS), complemented by aberration-corrected (AC) high-angle annular dark field scanning transmission electron microscopy (HAADF-STEM) analysis. They all have molecularly defined bimetallic active centers, stabilized by N and C from the N-doped carbon support, of which the coordination structures are resemble of the possible key active motifs of the related heterogeneous OER catalysts.

### 3.2 Characterization of Ni and Fe single-atom precatalysts

Single-atom Ni and Fe pre-catalysts (Ni-N-C and Fe-N-C) were prepared by a similar method as single-atom Co pre-catalyst (Co-N-C) mentioned in Chapter 2 (see Figure 2.1 in Chapter 2 for details). The powdered X-ray diffraction (XRD) patterns of both Ni-N-C and Fe-N-C samples showed only two broad peaks at  $26^\circ$  and  $43^\circ$  (Figure 3.1a), which were assigned to the (002) and (101) planes of graphite carbon.<sup>15-16</sup> No peaks from either crystalline metal oxides or metallic species were observed. Raman spectra (Figure 3.1b) of Ni-N-C and Fe-N-C showed only two bands characteristic of graphite carbon (G band at  $1600\text{ cm}^{-1}$ ) and defective carbon (D band at  $1350\text{ cm}^{-1}$ ).<sup>17-18</sup>  $\text{N}_2$  adsorption experiments showed that the BET (Brunauer-Emmett-Teller) surface area of Ni-N-C and Fe-N-C was 168 and  $742\text{ m}^2/\text{g}$ , respectively, with mesoporous characteristics (type IV isotherm with a hysteresis loop) (Figures 3.1c and 3.1d).<sup>19</sup>

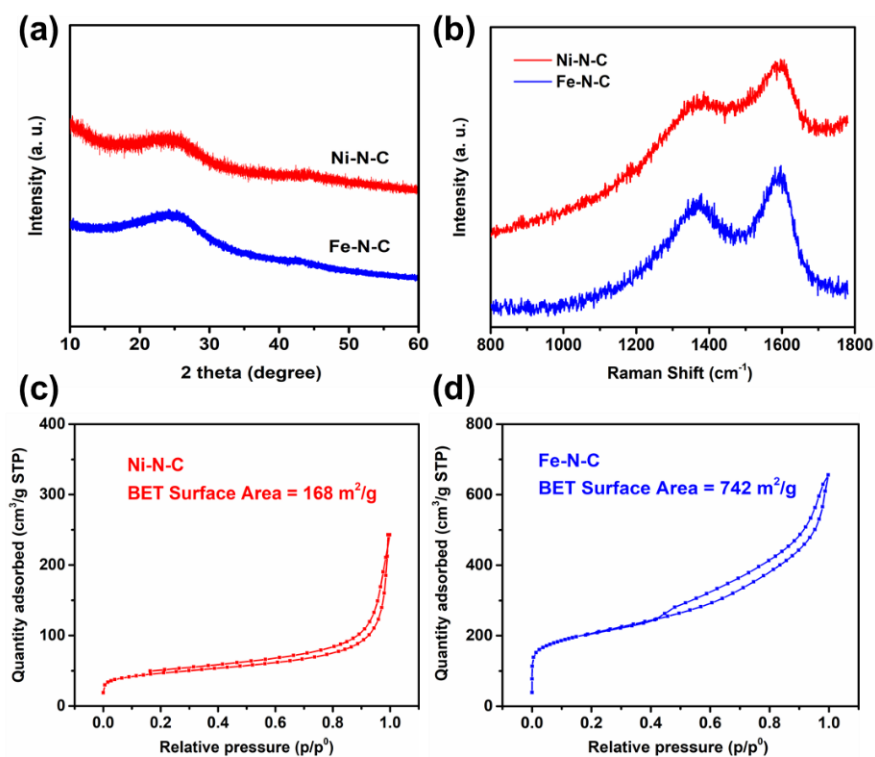


**Figure 3.1** XRD, Raman, and physical adsorption characterization of Ni-N-C (red) and Fe-N-C (blue). (a) XRD; (b) Raman.  $\text{N}_2$  adsorption experiments of (c) Ni-N-C and (d) Fe-N-C.

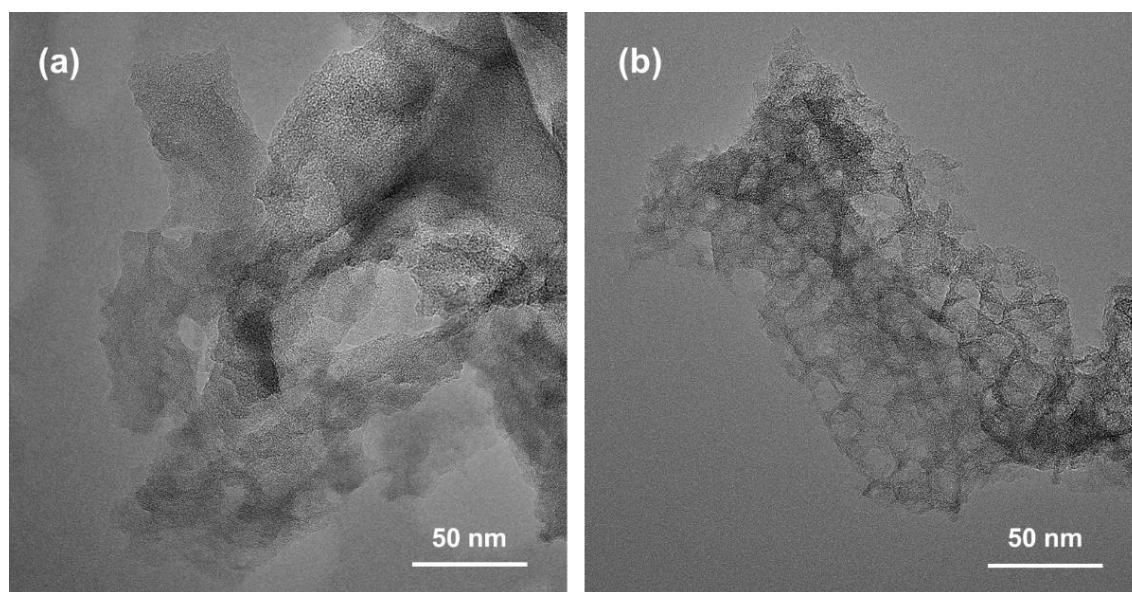


**Figure 3.2** TEM images of (a) Ni-N-C and (b) Fe-N-C.

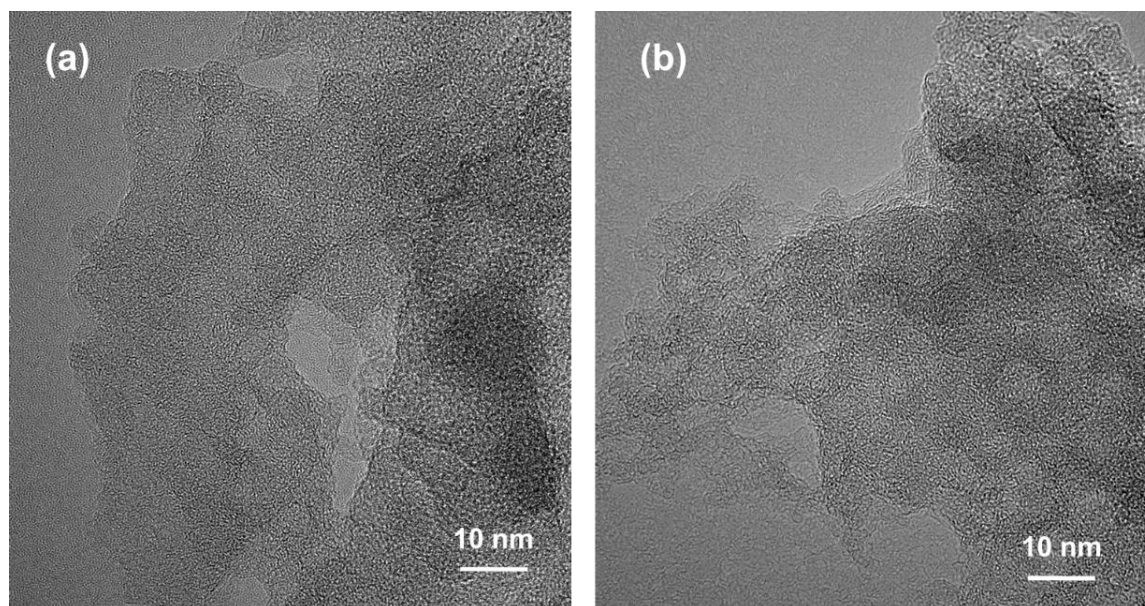


**Figure 3.3** HR-TEM images of (a) Ni-N-C and (b) Fe-N-C.

The carbon structures in both Ni-N-C and Fe-N-C are porous and amorphous, as revealed by transmission electron microscopy (TEM) images (Figure 3.2). No obvious metal atom clusters or nanoparticles were observed in either Ni-N-C or Fe-N-C by high-resolution TEM and standard HAADF-STEM (Figures 3.3-3.5). Energy dispersed X-ray (EDX) mapping images indicated a

homogeneous distribution of both metal (Ni or Fe) and non-metal elements (N, O, and C) (Figures 3.4 and 3.5). For both Ni-N-C and Fe-N-C, similar as Co-N-C in Chapter 2, AC HAADF-STEM images revealed many single atoms as bright dots uniformly distributed on the carbon substrates (Figure 3.6).

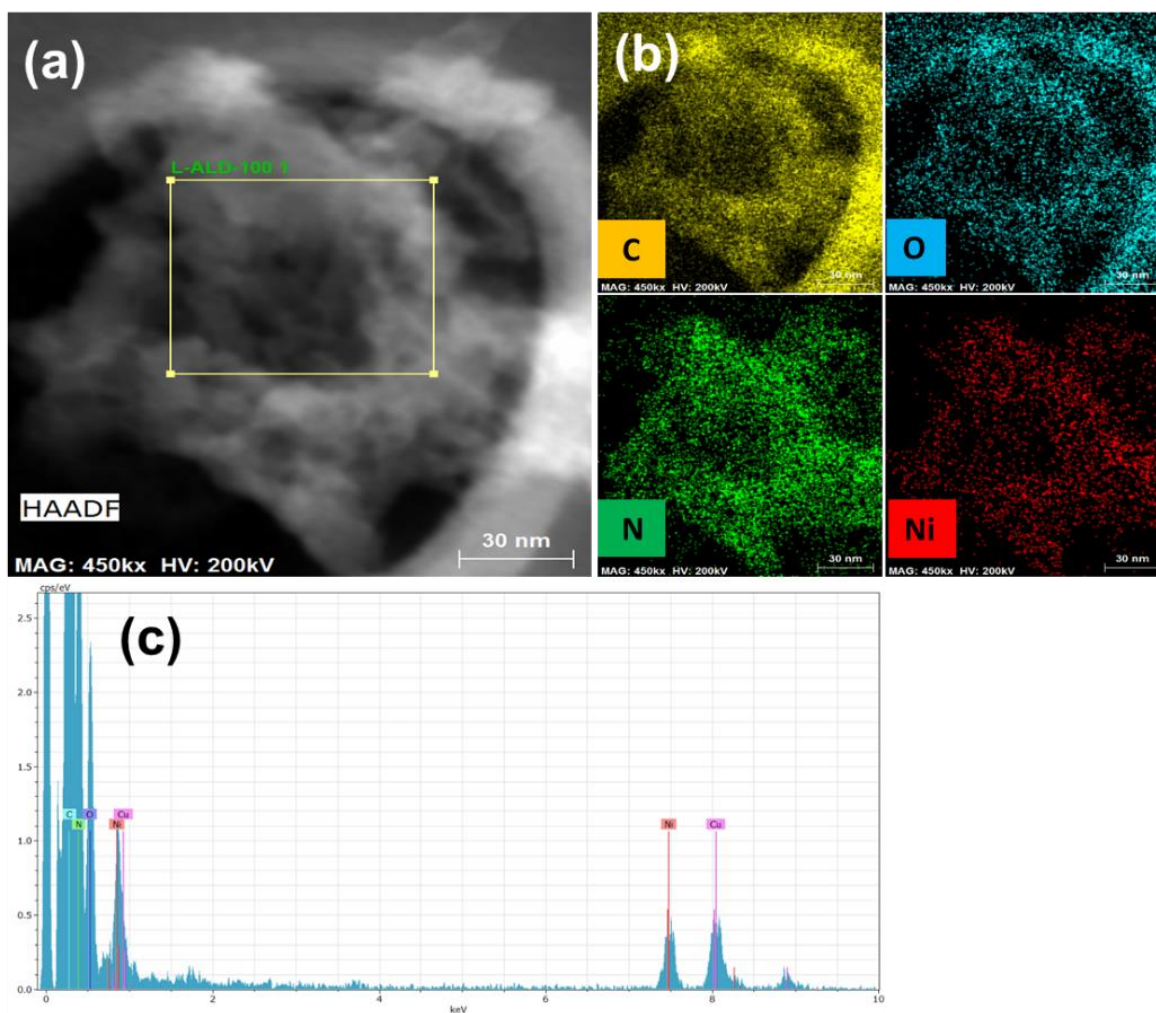


**Figure 3.4** (a) HAADF-STEM image, (b) corresponding elemental mapping and (c) EDX spectrum of Ni-N-C.



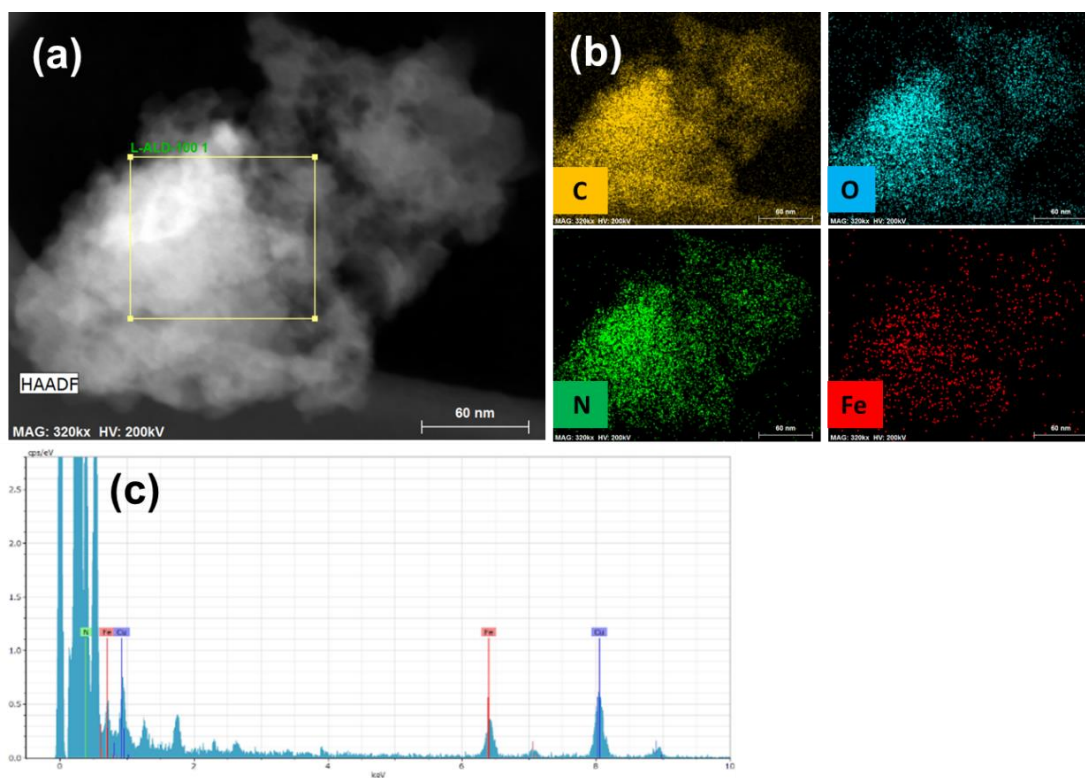


**Figure 3.5** (a) HAADF-STEM image, (b) corresponding elemental mapping and (c) EDX spectrum of Fe-N-C.

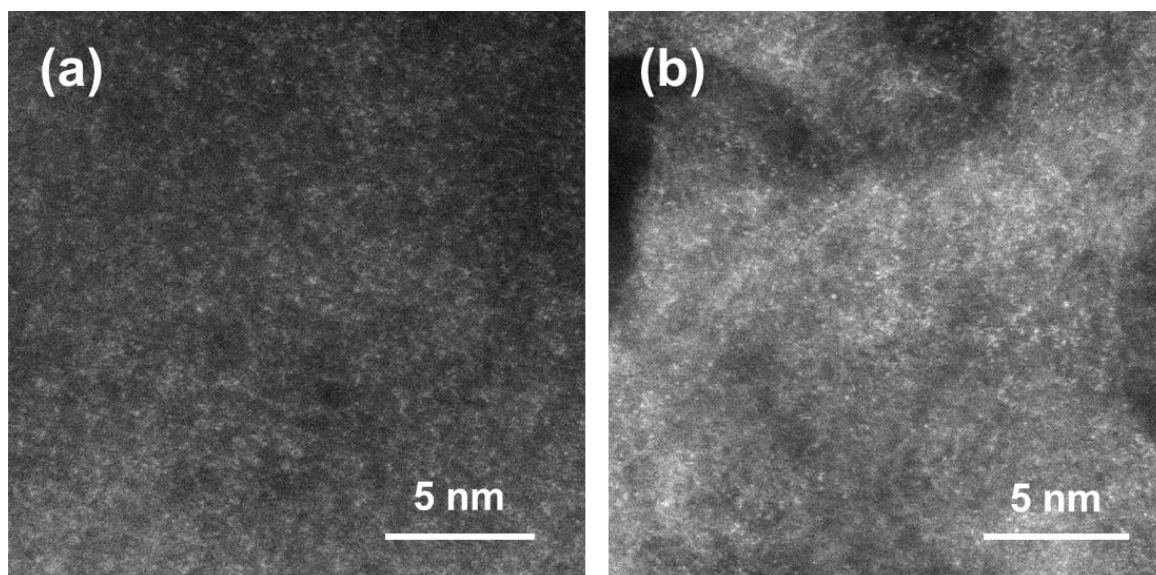


**Figure 3.6** Aberration corrected HAADF-STEM images of (a) Ni-N-C and (b) Fe-N-C.



The chemical states of Ni-N-C and Fe-N-C were characterized by X-ray photoelectron spectroscopy (XPS). The Ni 2p XPS spectra showed two peaks with binding energies of 855.4 eV (Ni 2p<sub>3/2</sub>) and 872.7 eV (Ni 2p<sub>1/2</sub>), respectively (Figure 3.7a). These values, in combination with two satellite peaks at 860.4 and 880.4 eV (Figure 3.7a), suggest a +2 oxidation state for Ni.<sup>20-21</sup> For Fe 2p XPS of Fe-N-C, the binding energies of 711.0 eV (Fe 2p<sub>3/2</sub>) and 724.1 eV (Fe 2p<sub>1/2</sub>) and the associated satellite peaks point to an oxidation state of about +3 for Fe (Figure 3.7b).<sup>22-23</sup> The XPS spectra of N 1s of Ni-N-C were deconvoluted into five peaks with binding energies of 398.6, 399.6, 400.4, 401.4, 402.8 eV, which were respectively assigned to pyridinic N, M-N<sub>x</sub> (nitrogen that is coordinated to metal ions), pyrrolic N, graphitic N, and oxidized N (Figure 3.7c).<sup>24-25</sup> Similar results were also obtained for Fe-N-C (Figure 3.7d). In both cases, pyridinic N was the major N species (Table 3.1). Previous works suggested pyridinic N sites are important in stabilizing SACs.<sup>25-26</sup> The pyridinic N that is coordinated to metal has ~1 eV blue shift of the binding energy, well consistent with similar reported material.<sup>25</sup> The XPS spectra of C1s and O1s were similar for both Ni-N-C and Fe-N-C (Figure 3.8).<sup>18, 26-28</sup> In both cases, small peaks at around 284 eV, corresponding to metal-carbon bond, could be deconvoluted (Figures 3.8a and 3.8c).<sup>29</sup> The features indicated the possible existence of metal-carbon coordination, which are similar to that of Co-N-C in Chapter 2. The relative concentrations of different N, O, C species in single-atom pre-catalysts (including the results of Co-N-C in Chapter 2) are summarized in Tables 3.1-3.3.

**Table 3.1** The results of deconvoluted subpeaks of N 1s XPS of Ni-N-C, Fe-N-C and Co-N-C (Chapter 2). The results are listed as Binding energy (eV)/Atomic content (%).

Type of the catalysts	Pyridinic N	Metal-nitrogen bond (M-N <sub>x</sub> )	Pyrrolic N	Graphite N	Oxidized N
Ni-N-C	398.6/52.5	399.6/16.8	400.4/19.4	401.4/9.0	402.8/2.3
Fe-N-C	398.5/50.2	399.7/18.9	400.3/19.7	401.3/9.8	402.7/1.4
Co-N-C	398.6/44.0	399.5/16.7	400.3/24.0	401.3/10.9	402.6/4.4

**Table 3.2** The results of deconvoluted subpeaks of C 1s XPS of Ni-N-C, Fe-N-C and Co-N-C (Chapter 2). The results are listed as Binding energy (eV)/Atomic content (%).

Type of the catalysts	Metal-carbon bond (M-C <sub>x</sub> )	-C-C	-C-OH	-C=O/-C=N	-COOH
Ni-N-C	284.0/4.4	284.8/61.1	286.1/17.3	287.8/10.2	289.9/7.0
Fe-N-C	283.9/5.1	284.7/55.5	286.1/20.9	287.9/12.5	289.9/6.0
Co-N-C	284.0/5.3	284.8/57.1	286.1/17.8	287.7/14.0	289.9/5.8

**Table 3.3** The results of deconvoluted subpeaks of O 1s XPS of Ni-N-C, Fe-N-C and Co-N-C (Chapter 2). The results are listed as Binding energy (eV)/Atomic content (%).

Type of the catalysts	-C=O	-C-OH
Ni-N-C	531.5/64.7	533.0/35.3
Fe-N-C	531.5/68.8	533.0/31.2
Co-N-C	531.5/65.5	533.2/34.5

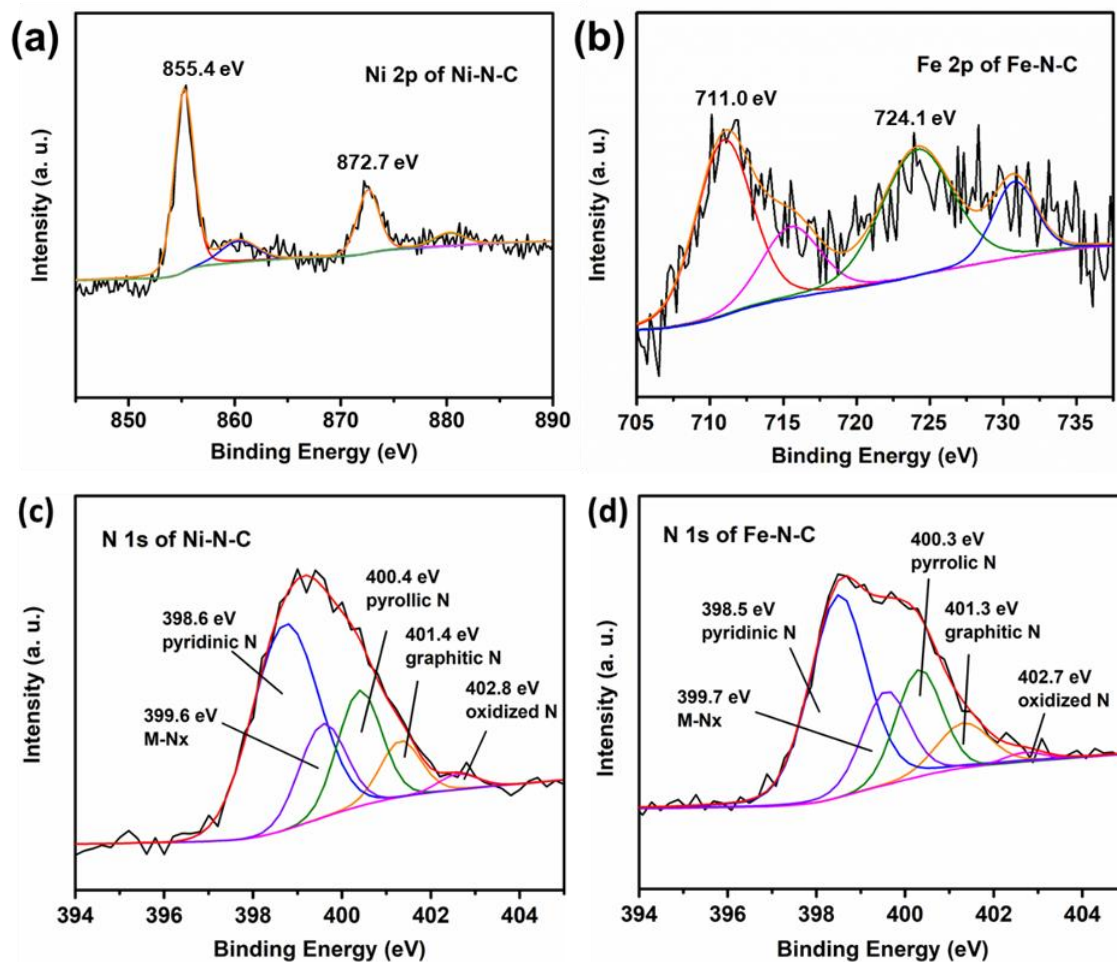


**Figure 3.7** High-resolution XPS of (a) Ni 2p of Ni-N-C, (b) Fe 2p of Fe-N-C. (c) N 1s of Ni-N-C, (d) N 1s of Fe-N-C.

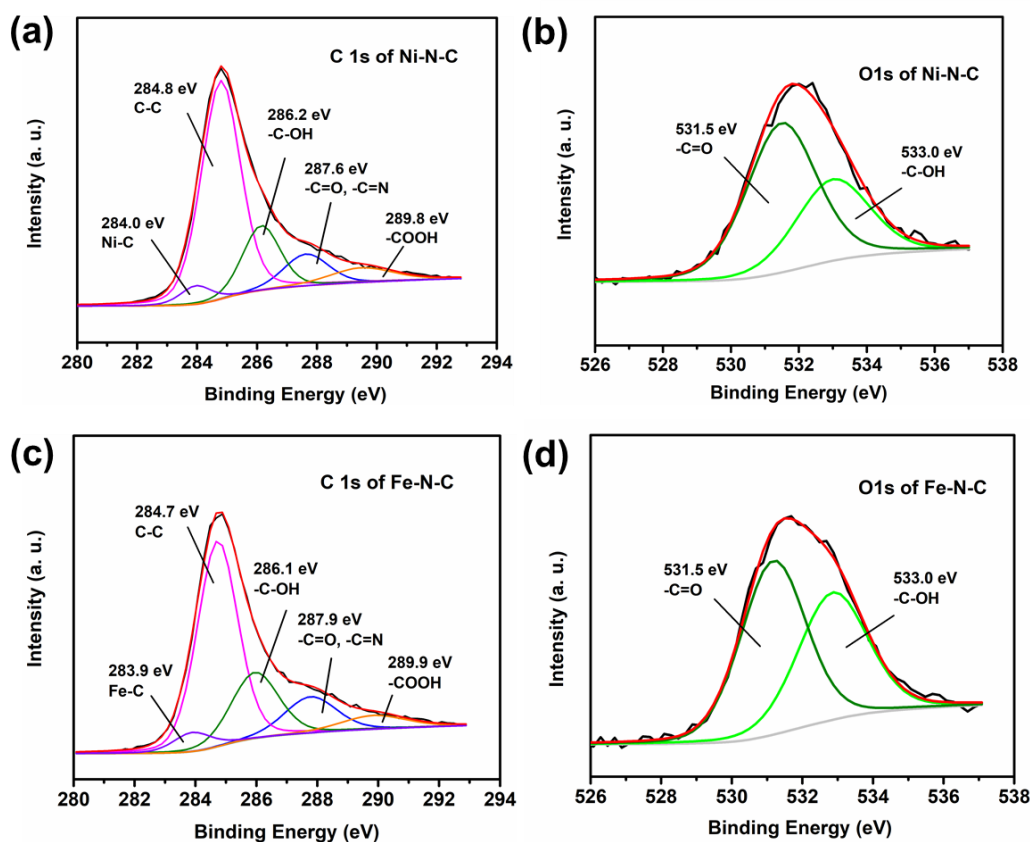


**Figure 3.8** High resolution XPS of Ni-N-C for (a) C 1s region and (b) O 1s region; high resolution XPS of Fe-N-C for (c) C 1s region and (d) O 1s region.

### 3.3 Characterization of various double-atom catalysts

#### 3.3.1 Microscopic characterization of various double-atom catalysts

In Chapter 2, we found that under OER conditions, a Co single-atom pre-catalyst (Co-N-C) was converted to a Co-Fe DAC by incorporating Fe ions from the electrolyte solution. This unexpected finding encouraged us to probe whether analogous DACs might be formed using similar *in situ* electrochemical activation in KOH containing various metal ions impurities. We treated normal KOH with pure Ni(OH)<sub>2</sub> and Co(OH)<sub>2</sub> (detailed methods and procedures of the sample preparation are depicted in Section 3.7.1) to remove Fe impurities while simultaneously introducing Ni and Co impurities, respectively.<sup>30-31</sup>

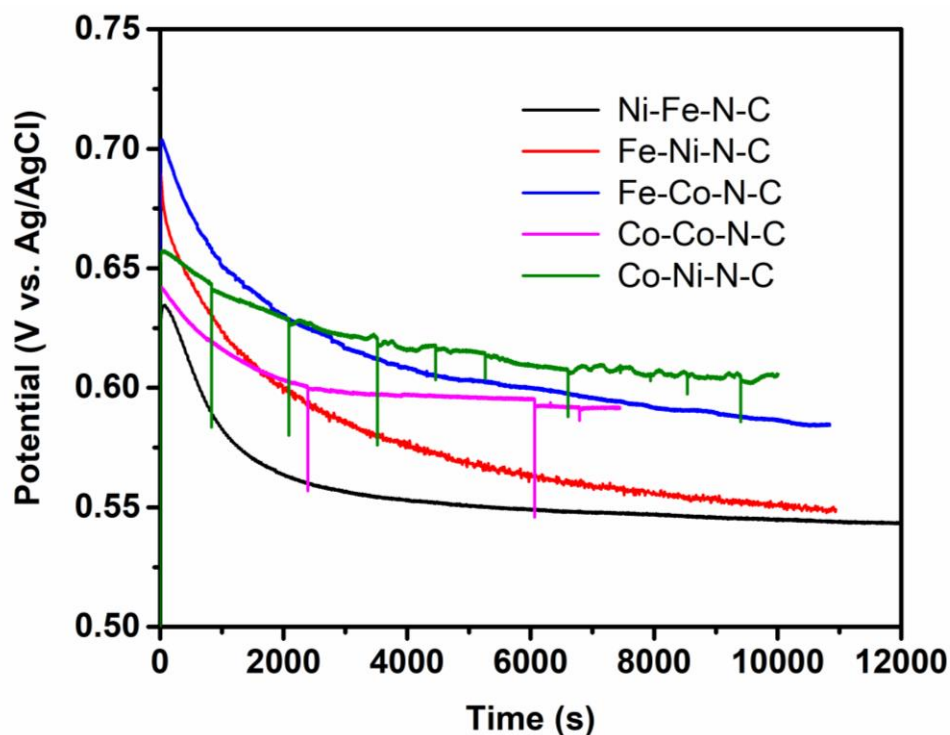


**Figure 3.9** Constant current activation of single-atom pre-catalysts to various double-atom catalysts. For M1-M2-N-C, M1 represents initial type of single-atom pre-catalysts, while M2 represents the metal ions to be adsorbed from 1 M KOH. The current density is 2 mA/cm<sup>2</sup> for Ni-Fe-N-C and 1 mA/cm<sup>2</sup> for the others. All the catalysts were loaded on carbon-cloth electrodes. No correction for solution resistance was applied.

Similar as generating Co-Fe-N-C, it is anticipated that Co-N-C precatalyst can transform to Co-Ni-N-C (binding Ni) and Co-Co-N-C (binding another distal Co) from Ni-containing and Co-containing KOH, respectively. In both cases, the applied potential for constant current density of 1 mA/cm<sup>2</sup> was indeed gradually decreased within time, indicating activation of the catalysts (Figure 3.9). The result is well consistent with the phenomenon that the Co-N-C can also be activated in Fe-free KOH (see Chapter 2, Section 2.3). We further found that Ni-N-C can also be activated in Fe containing KOH (Figure 3.9), like Co-N-C. In a similar way, Fe-N-C was activated in Ni-containing and Co-containing KOH (Figure 3.9). We named those three activated catalysts as Ni-Fe-N-C, Fe-Ni-N-C and Fe-Co-N-C, respectively.

The activated materials were then characterized by HR-TEM, common HAADF-STEM and EDX mapping, as well as AC HAADF-STEM. Taking Co-Ni-N-C as an example, HR-TEM and HAADF-STEM images indicated the absence of aggregated nanoparticles (Figures 3.10a and 3.10b). In addition to Co, a small amount of Ni was detected by the corresponding EDX mapping

images and spectra (Figures 3.10c and 3.10d). Both metal elements were homogeneously distributed (Figure 3.10c). Inductively coupled plasma atomic emission spectrometry (ICP-AES) results confirmed the incorporation of Ni, with a loading of about 5% relative to Co (Table 3.4). AC HAADF-STEM image showed that the catalyst remained atomically dispersed (Figure 3.10e). Possible Co-Ni dimers were observed, with a separation of around 0.2-0.3 nm, similar as Co-Fe double-atoms mentioned in the previous Chapter (Figure 3.10f). These results support the possible formation of a Co-Ni DAC.

Similar to Co-Ni-N-C, the formation of other possible double-atoms were confirmed as Figures 3.11-3.14, including Co-Co-N-C (Figure 3.11), Ni-Fe-N-C (Figure 3.12), Fe-Co-N-C (Figure 3.13), and Fe-Ni-N-C (Figure 3.14). All double-atom pairs have a separation of metals as around 0.2-0.3 nm (similar as Co-Ni-N-C). The ratio of distal metals to single-atoms were little bit different between each DACs (ranging from about 5% to 40%), as shown in Table 3.4.

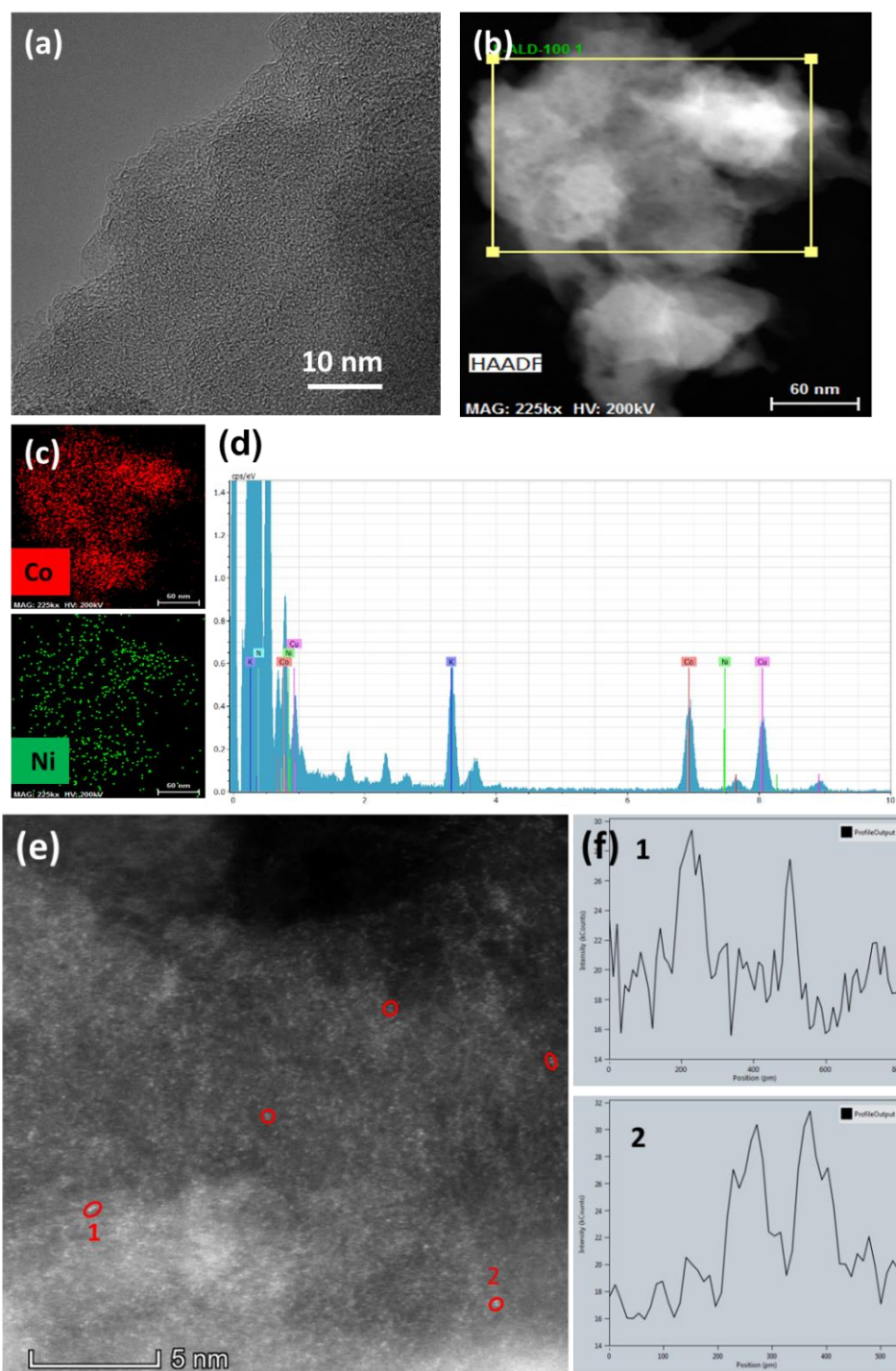


**Figure 3.10** Microscopic characterization of Co-Ni-N-C. (a) HR-TEM image. (b) HAADF-STEM image. (c) Corresponding EDX mapping images of (b). (d) Corresponding EDX spectrum of the indicated area in (b). (e) AC HAADF-STEM image. Some closely-located atom pairs are marked with red circles. (f) The intensity profiles (e.g., for region 1 and 2) indicated they are possibly Co-Ni dimers. In principle, some of the observed dimers can originate from single Co atoms in different depths of the 3D carbon support. However, the majority of the dimers might be assigned to double-atom species based on similar intensity and appropriate distance (2-3 Å).



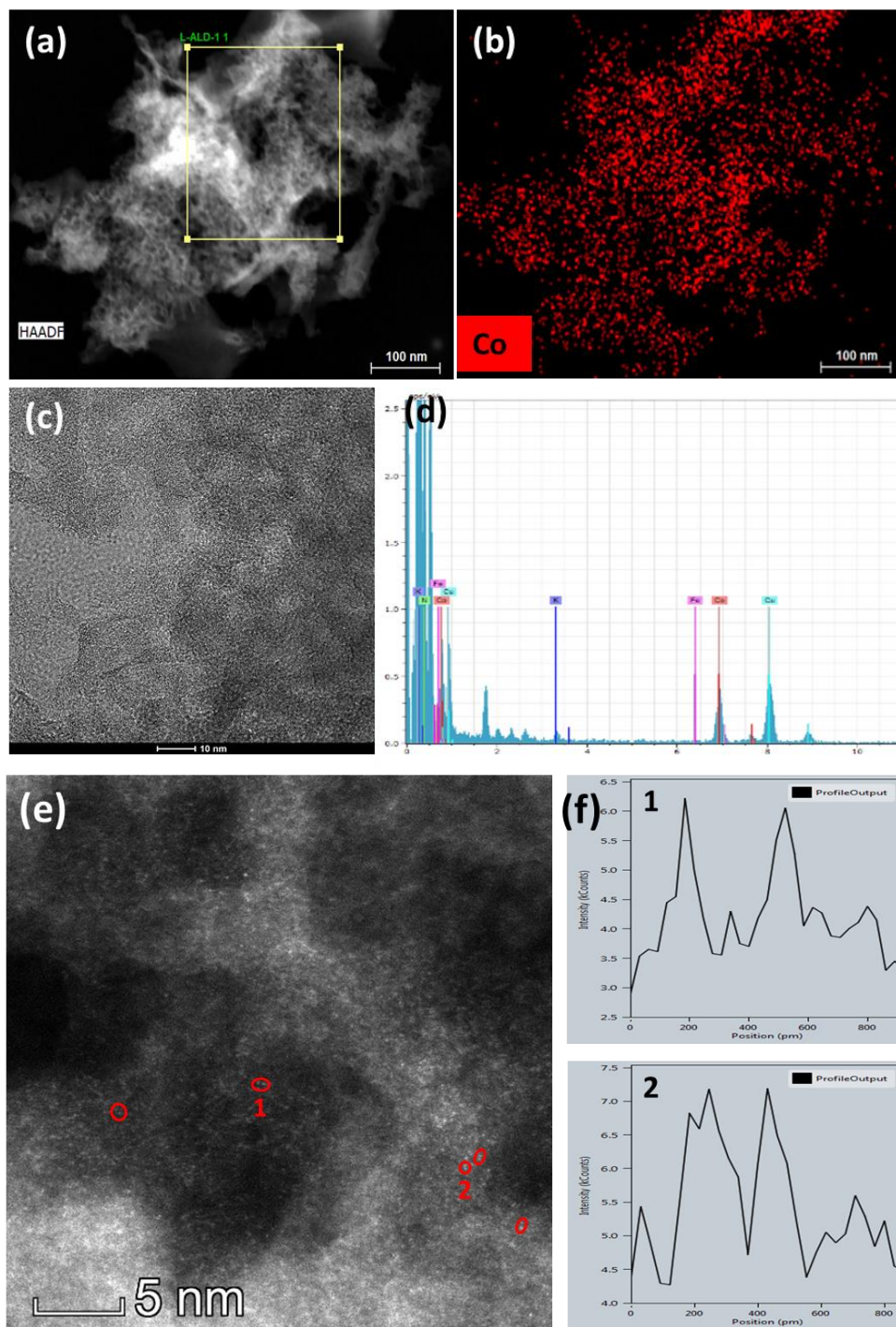


**Figure 3.11** Microscopic characterization of Co-Co-N-C. (a) HAADF-STEM image. (b) Corresponding EDX mapping image of (a). (d) Corresponding EDX spectrum of the indicated area in (a). (c) HR-TEM image. (e) AC HAADF-STEM image. Some closely-located atom pairs are marked with red circles. (f) The intensity profiles (e.g., for region 1 and 2) indicated they are possibly Co-Co dimers. In principle, some of the observed dimers can originate from single Co atoms in different depths of the 3D carbon support. However, the majority of the dimers might be assigned to double-atom species based on similar intensity and appropriate distance (2-3 Å).

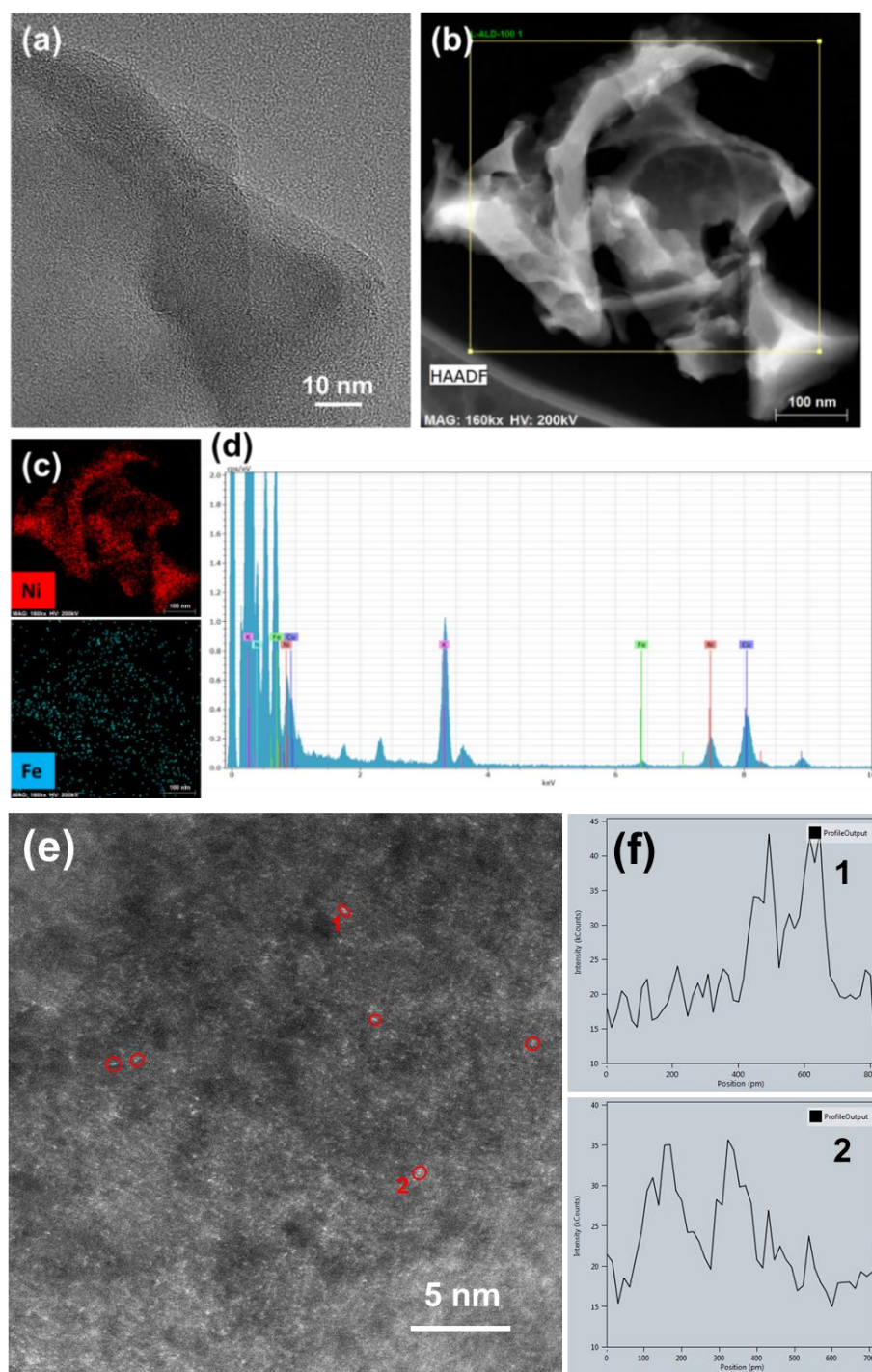


**Figure 3.12** Microscopic characterization of Ni-Fe-N-C. (a) HR-TEM image. (b) HAADF-STEM image. (c) Corresponding EDX mapping images of (b). (d) Corresponding EDX spectrum of the indicated area in (b). (e) AC HAADF-STEM image. Some closely-located atom pairs are marked with red circles. (f) The intensity profiles (e.g., for region 1 and 2) indicated they are possibly Ni-Fe dimers. In principle, some of the observed dimers can originate from single Ni atoms in different depths of the 3D carbon support. However, the majority of the dimers might be assigned to double-atom species based on similar intensity and appropriate distance (2-3 Å).



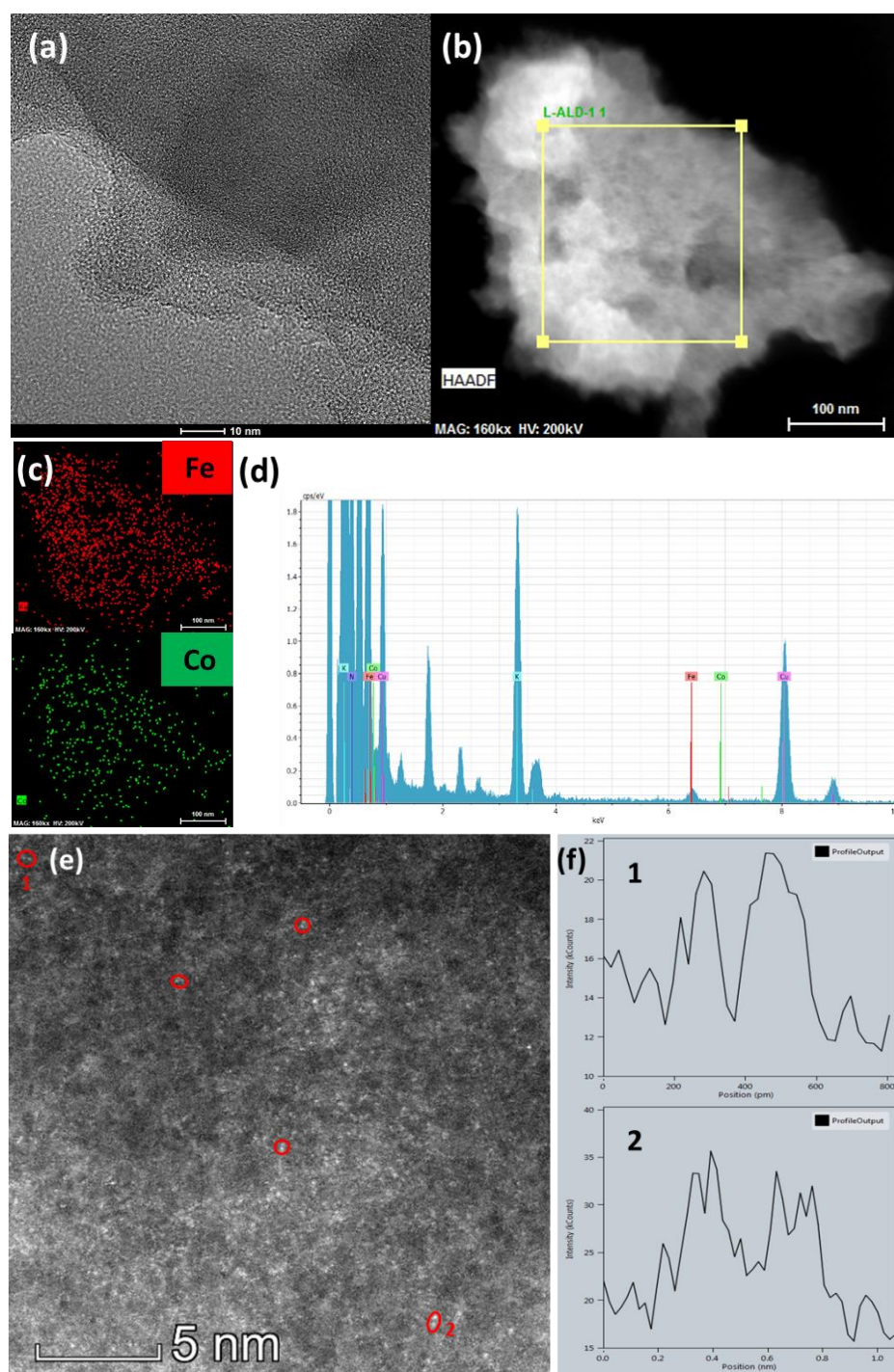


**Figure 3.13** Microscopic characterization of Fe-Co-N-C. (a) HR-TEM image. (b) HAADF-STEM image. (c) Corresponding EDX mapping images of (b). (d) Corresponding EDX spectrum of the indicated area in (b). (e) AC HAADF-STEM image. Some closely-located atom pairs are marked with red circles. (f) The intensity profiles (e.g., for region 1 and 2) indicated they are possibly Fe-Co dimers. In principle, some of the observed dimers can originate from single Fe atoms in different depths of the 3D carbon support. However, the majority of the dimers might be assigned to double-atom species based on similar intensity and appropriate distance (2-3 Å).

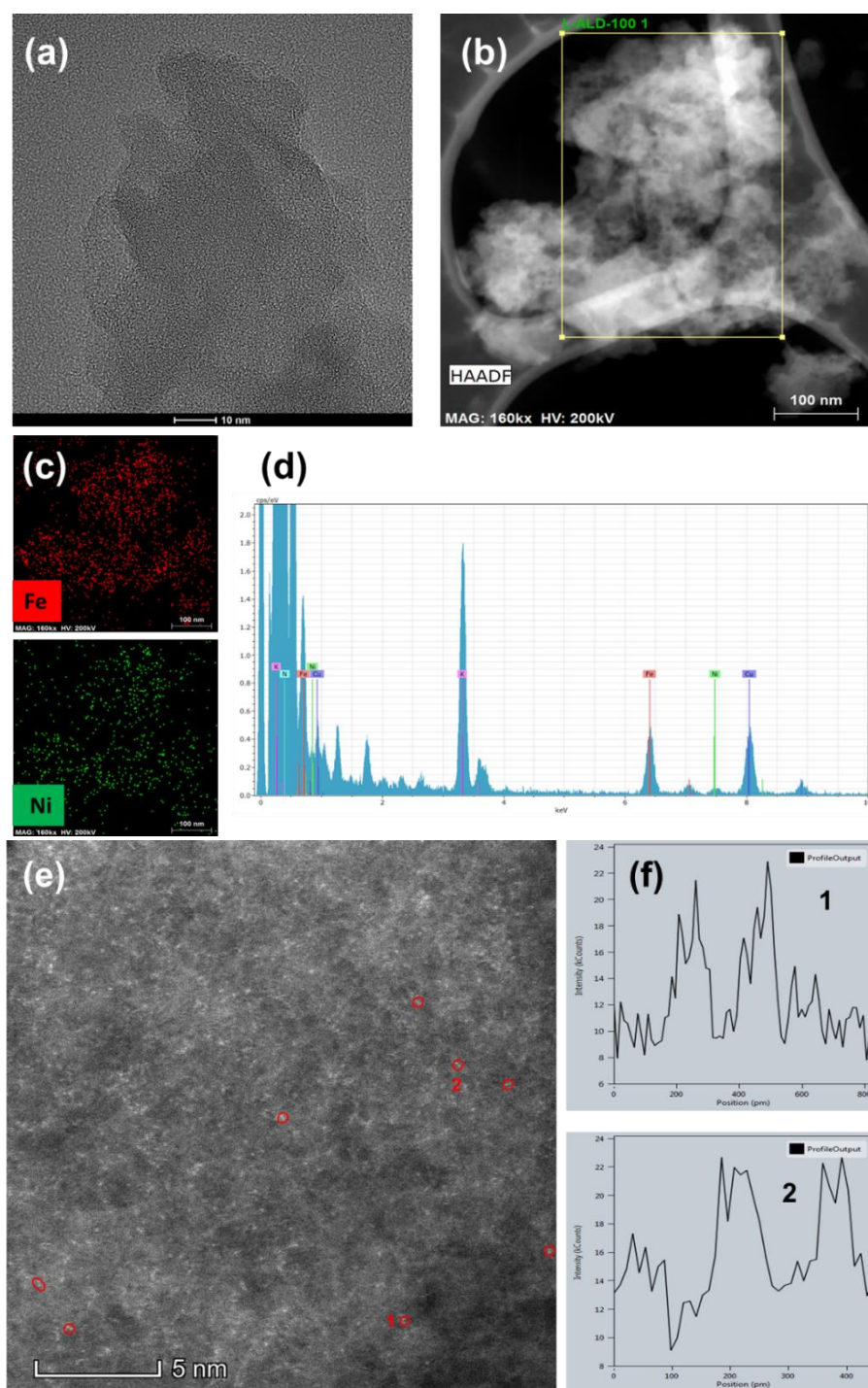


**Figure 3.14** Microscopic characterization of Fe-Ni-N-C. (a) HR-TEM image. (b) HAADF-STEM image. (c) Corresponding EDX mapping images of (b). (d) Corresponding EDX spectrum of the indicated area in (b). (e) AC HAADF-STEM image. Some closely-located atom pairs are marked with red circles. (f) The intensity profiles (e.g., for region 1 and 2) indicated they are possibly Fe-Ni dimers. In principle, some of the observed dimers can originate from single Fe atoms in different depths of the 3D carbon support. However, the majority of the dimers might be assigned to double-atom species based on similar intensity and appropriate distance (2-3 Å).

**Table 3.4.** The metal loadings of different double-atom catalysts calculated by ICP-AES.

Type of the catalysts	Co (nmol)	Fe (nmol)	Ni (nmol)	Loading of dimers (nmol)
Co-Fe-N-C <sup>a</sup>	94 ± 14	8.6 ± 1.6	-	8.6 ± 1.6
Ni-Fe-N-C	-	13.5 ± 3.3	125 ± 9.9	13.5 ± 3.3
Co-Ni-N-C	105 ± 21	-	4.0 ± 1.7	4.0 ± 1.7
Co-Co-N-C <sup>b</sup>	130 ± 20	-	-	52 ± 5.0
Fe-Co-N-C	6.4 ± 0.8	63 ± 6.0	-	6.4 ± 0.8
Fe-Ni-N-C	-	59 ± 4.5	20 ± 7.2	20 ± 7.2

- a. The data of Co-Fe-N-C is referred to Chapter 2.  
b. The Co loading increased about 40% after activation, we assumed the increased Co are bound to Co single-atom pre-catalyst then form Co-Co double atoms.

### 3.3.2 OER performance of various double-atom catalysts

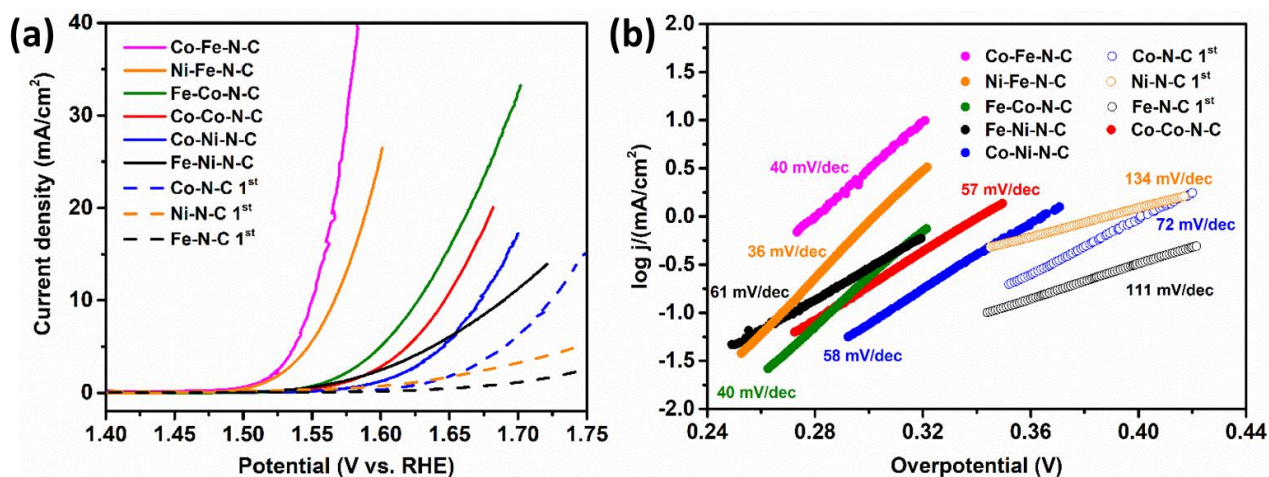


**Figure 3.15** Electrochemical OER performance of double-atom catalysts and single-atom pre-catalysts. (a) Linear scanning voltammetry (LSV) curves of single-atom pre-catalysts (dashed lines) and double-atom catalysts (solid lines) in 1 M KOH (containing various metal impurities). The LSV curves of Co, Ni, Fe single-atom pre-catalysts were recorded on the first scans in Fe-free 1 M KOH. (b) Corresponding Tafel plots derived from (a). The Tafel slopes of double-atom catalysts are in solid circles, and those of single-atom pre-catalysts are in hollow circles.

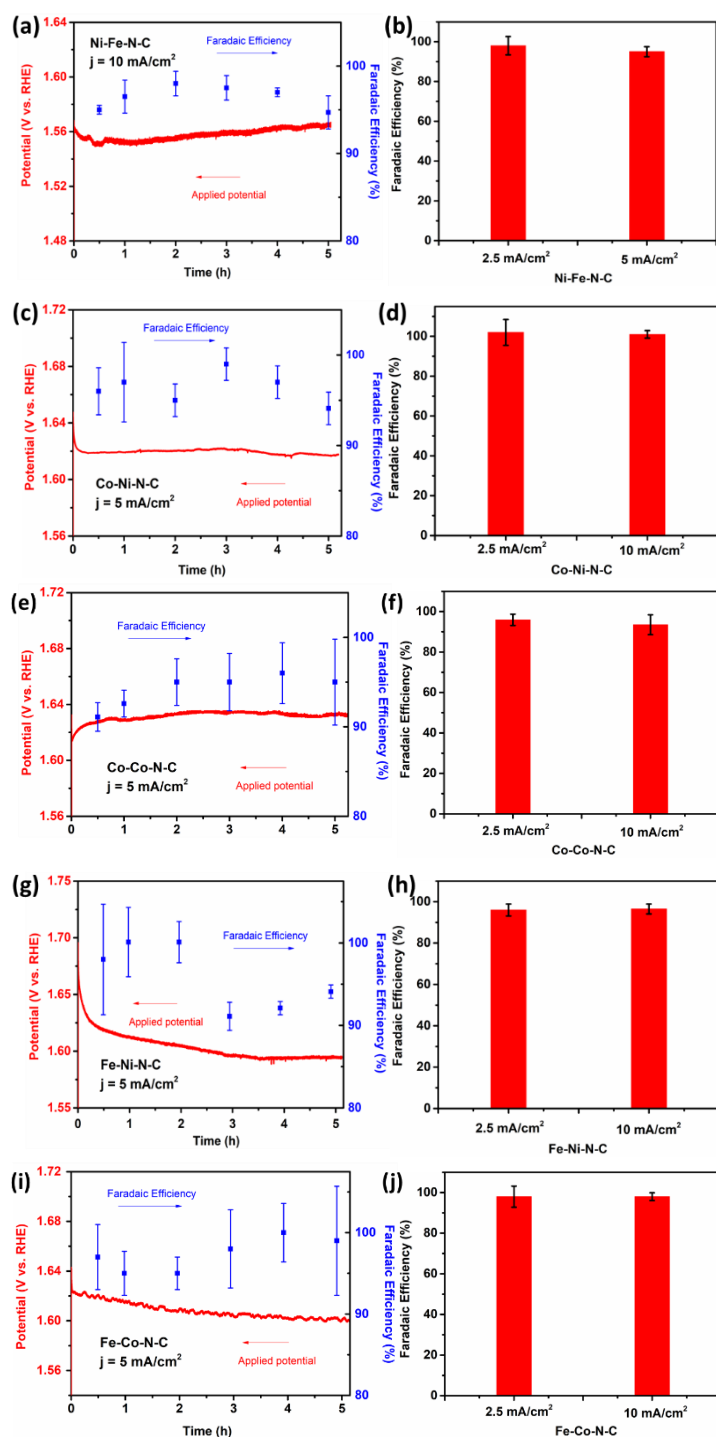


**Figure 3.16** Faradaic efficiency of the double-atom catalysts. (a, b) Ni-Fe-N-C; (c, d) Co-Ni-N-C; (e, f) Co-Co-N-C; (g, h) Fe-Ni-N-C; (i, j) Fe-Co-N-C. (a, c, e, g, i) Faradaic efficiency measured at different time duration of constant current electrolysis (10  $\text{mA/cm}^2$  for Ni-Fe-N-C, 5  $\text{mA/cm}^2$  for other catalysts). The plots of time-dependent applied potential are shown in red curves. (b, d, f, h, j) Faradaic efficiency measured at different current density (after constant current electrolysis for 15 mins).



From Figure 3.15, it is evidenced that all of the double-atoms exhibited higher activity compared to the initial single-atom precatalysts. The LSV curve of Co-Fe-N-C is also added for comparison (see Chapter 2, Section 2.3 for detailed OER performance). We found Co-Fe and Ni-Fe double-atoms exhibited the best performance among all of these catalysts.

Co-Fe, Ni-Fe, Fe-Co have similar Tafel slope as close to 40 mV/dec, suggesting they should have similar reaction mechanisms. While Fe-Ni, Co-Ni, Co-Co also have similar reaction process, as all of them showed close to 60 mV/dec Tafel slope. Single-atom precatalysts like Ni-N-C and Fe-N-C exhibited Tafel slope closed to 120 mV/dec. The detailed analysis of the reaction mechanisms will be presented in next Chapter of this Thesis (Chapter 4).

All of the possibly generated DACs exhibited stable performance for at least 5h chronopotential electrolysis (Figure 3.16). Additionally, the O<sub>2</sub> Faradaic efficiency (FE) of these catalysts are close to 100% at various duration and different current density (Figure 3.16), indicative of nearly all the current is in charge of catalyzing OER. The detailed procedure of O<sub>2</sub> FE measurements is depicted in Section 3.7.4.

### **3.4 Operando XAS study of double-atom catalysts**

#### **3.4.1 Operando XAS study of Ni-Fe-N-C**

*Operando* XAS experiments were performed to both further verify the generation of double-atom species and to reveal the local environments of the core metals. First considering Ni-Fe-N-C, XANES indicated that the oxidation state of Ni in the dry sample was between +2 and +3, since the energy of the main absorption edge was located between those of Ni(2+)O and LiNi(3+)O<sub>2</sub> reference samples (Figure 3.17). The energy of the absorption edge of Ni only increased slightly upon formation of Ni-Fe-N-C (Figure 3.17), suggesting that only some of the Ni<sup>2+</sup> ions in Ni-N-C were oxidized to Ni<sup>3+</sup> upon electrochemical activation (at constant current of 1 mA/cm<sup>2</sup>). The average oxidation state of Ni ions then remained nearly the same during the extended electrolysis.

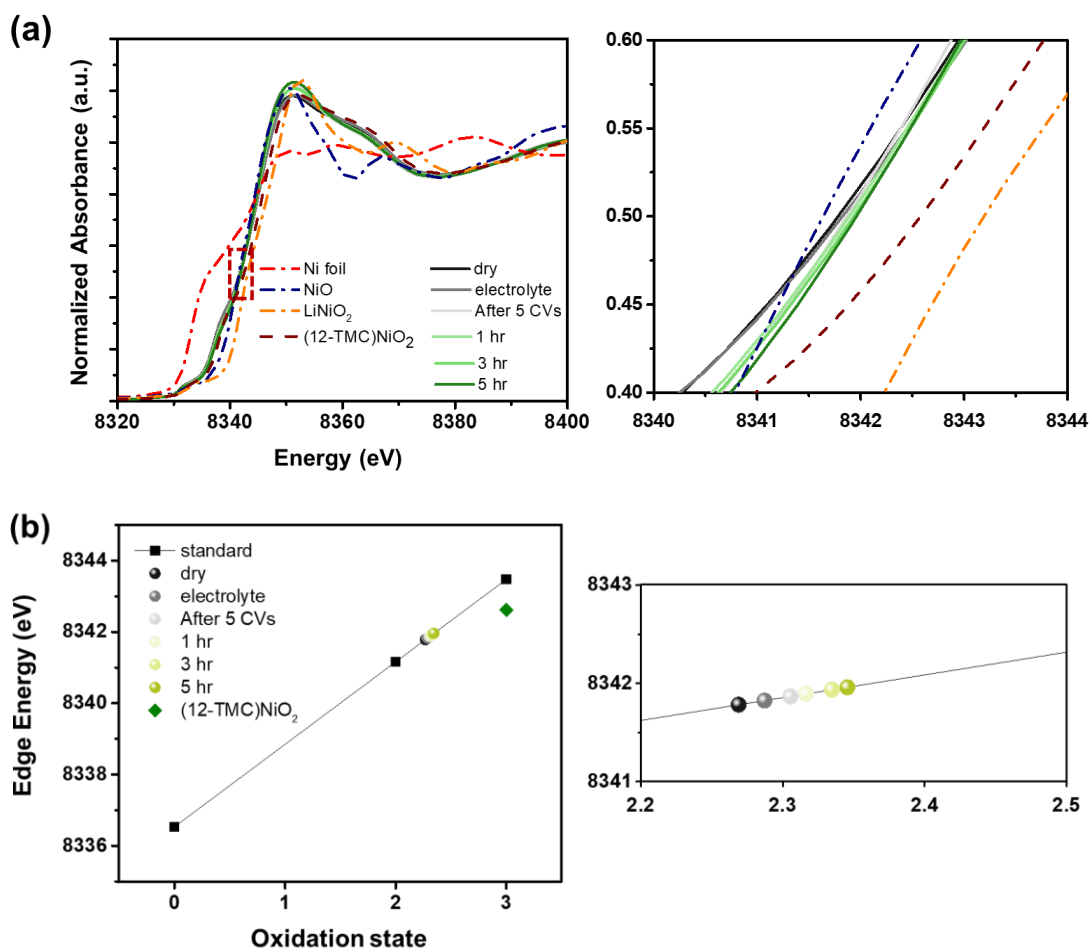


**Figure 3.17** Ni K-edge *operando* XANES of Ni-Fe-N-C. (a) Left: Ni K-edge XANES spectra of Ni-N-C precatalyst (black), Ni-N-C in electrolyte (grey), after 5 CVs activation (light grey) and under OER with various duration (green, 1, 3, 5 hr). Ni standard samples: Ni foil (red), NiO (blue), LiNiO<sub>2</sub> (orange), (12-TMC)NiO<sub>2</sub> (brown) are showed in dashed lines. Right: The enlargement image of the dark red dashed box in left image, for determination of the change of the oxidation state. (b) Left: K-edge energies (at 50% level) of XANES spectra in Fig. (a), and Ni references compounds containing Ni(0), Ni(II), or Ni(III), showed in black squares (or green square for (12-TMC)NiO<sub>2</sub>). Right: The enlarged graph of left image with apparent oxidation state ranging from +2.2-2.5.

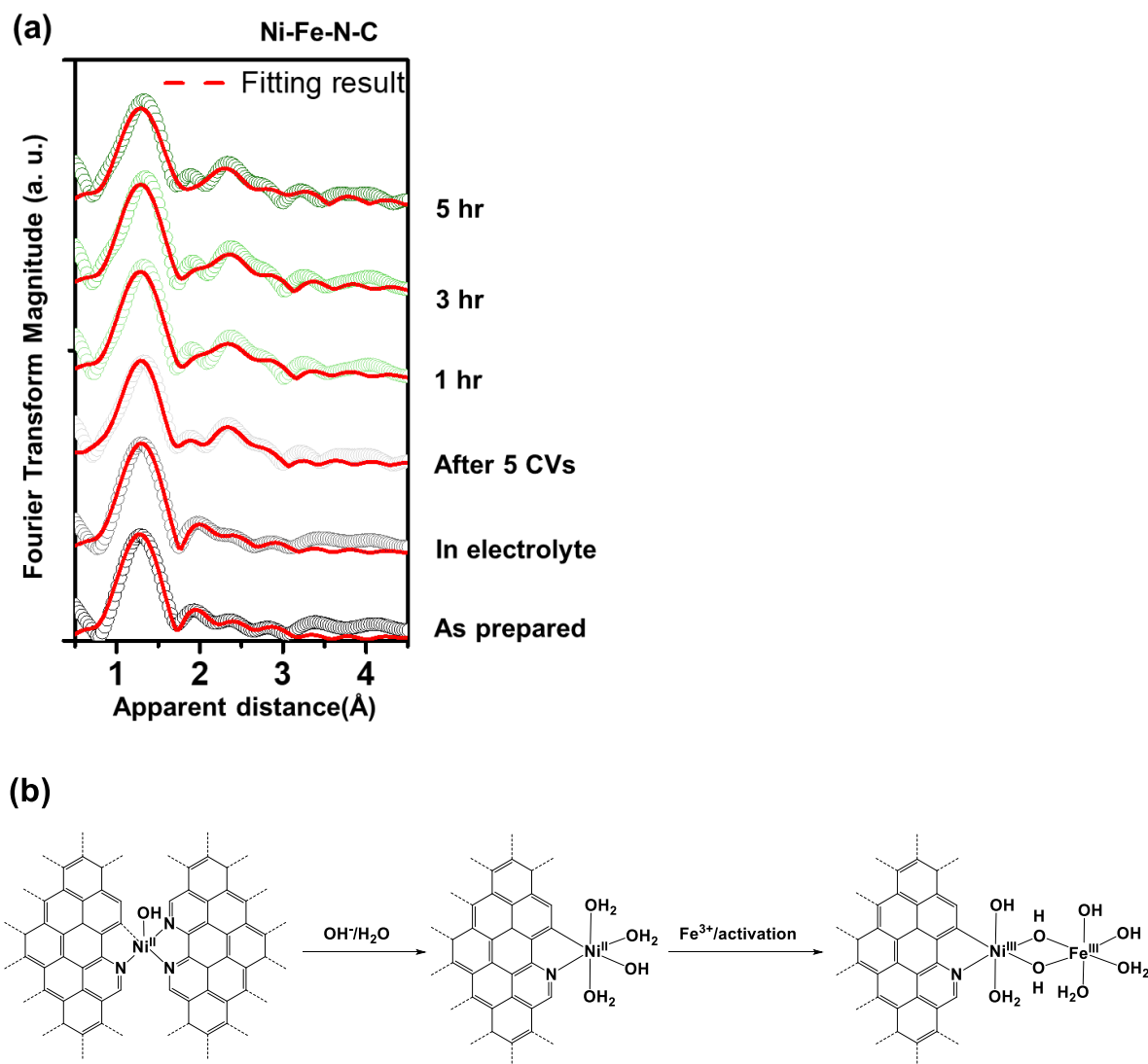


**Figure 3.18** Ni K-edge *operando* EXAFS of Ni-Fe-N-C. (a) Fourier transform of Ni K-edge EXAFS spectra w/o phase correction for as-prepared Ni-N-C and the catalyst after 5 CVs activation as well as under OER for various durations (1, 3, 5 hr). The fitting results are showed in red solid curve. (b) Proposed model for the formation of Ni-Fe double-atom catalyst.

Ni is coordinated by 3 N, 1 C, 1 O, as revealed by Ni K-edge EXAFS (Figure 3.18, Table 3.5). Thus, the Ni-N-C pre-catalyst has a similar structure as Co-N-C (see Chapter 2, Section 2.5.1). The N and C donors come from the N-doped carbon support, and the O donor is assumed to be an adsorbed hydroxyl group or water. When Ni-N-C was immersed in alkaline electrolyte (1 M KOH), two N donors were replaced by three new O donors ( $\text{OH}^-/\text{H}_2\text{O}$ ), as indicated by the extracted structural parameters (Table 3.5). After 5 CVs activation, the first shell coordination

structure of Ni remained nearly the same, while a single-scattering path of  $\sim 2.9$  Å appeared in the second scattering shell (coordination number, CN = 0.2). This distance is in the range of the observed separation of double-atom pairs in AC HAADF-STEM image (Figure 3.13). We attributed this scattering path to an Fe ion connected to the Ni ion via oxygen-bridge(s). We noted that the apparent distance of Ni-Fe is different from that of M1-O-M2 units in NiFe LDH<sup>32</sup>, amorphous NiFeO<sub>x</sub><sup>33</sup>, and NiFe<sub>2</sub>O<sub>4</sub><sup>34</sup>. Formation of NiO and metallic Ni clusters were also excluded based on their different spectroscopic features (Figure 3.19). Both the first shell and the second shell coordination structures of Ni-Fe-N-C remained stable under OER conditions in the time scale of 5 hr (Figure 3.18a, Table 3.5). A proposed process for generation of Ni-Fe-N-C was provided in Figure 3.18b.

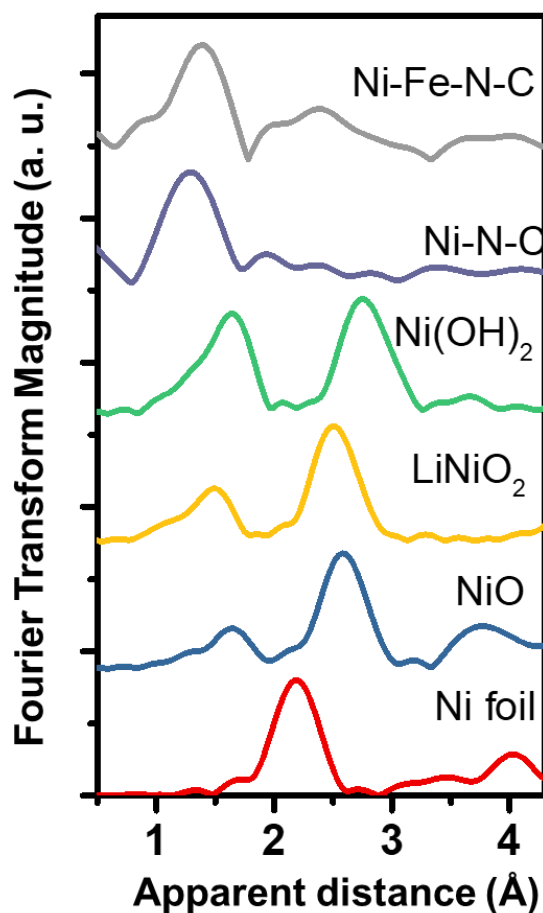


**Figure 3.19** Fourier transform Ni K-edge EXAFS spectra of as-prepared Ni-N-C and Ni-Fe-N-C in comparison with various Ni reference samples.



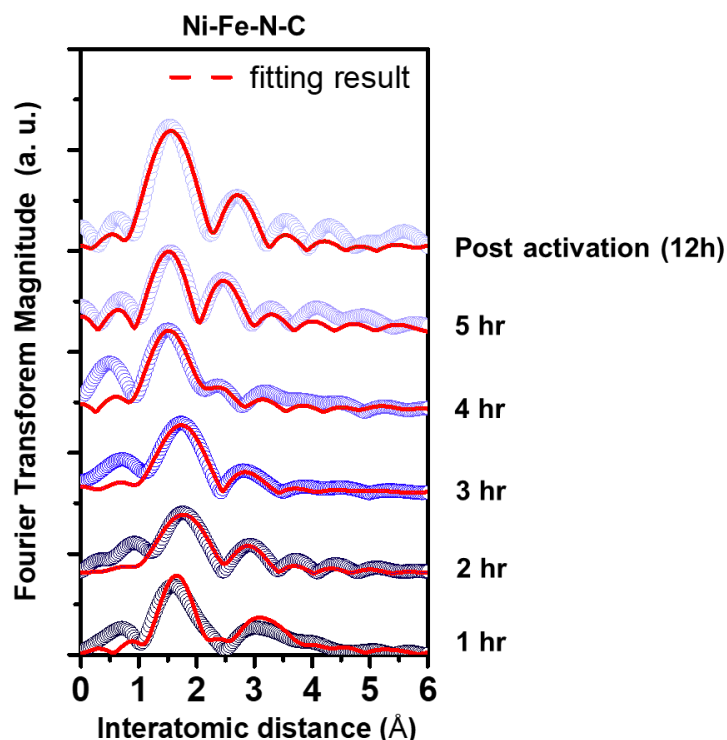


**Figure 3.20** Fourier transform of Fe K-edge *operando* EXAFS spectra w/o phase correction for Ni-Fe-N-C under OER in various durations (1-5 hr and post activation). The fitting results are showed in red solid curve.

The coordination environment and the oxidation state of the distal Fe atom of Ni-Fe-N-C were also examined by *operando* XAS (Figures 3.20 and 3.21). After 1 hour activation, *operando* Fe K-edge EXAFS showed that the distal iron was surrounded by close to 4 oxygen in first shell and a Fe-Ni path in second shell with a CN value of about 1.0 was presented (Figures 3.20a and 3.20b). This CN strongly indicated the formation of Ni-Fe double atoms (all of the Fe is in the form of double-atom while some of Ni is still in the form of single-atom). In the early stage, there were four coordinated oxygen around distal Fe, in which half of them resulted from the bridged oxygen with Ni atoms (Table 3.6). With increasing the activation duration, the CN value in first shell remarkably increased and reached a saturated six oxygen-coordinated configuration, which can be ascribed to attaching additional OH<sup>-</sup>/H<sub>2</sub>O from electrolyte. The CN of Fe-Ni remained nearly constant as close to 1.0 at different time duration (Table 3.6), indicating the gradual increment of Ni-Fe CN in Ni-K edge EXAFS was related to more Fe adsorption rather than generation of Fe-doped NiOOH. Concurrently, the oxidation state of Fe was gradually increased with the activation time (Figure 3.21), demonstrating accumulation of more Fe(IV) species due to the formation of

more Ni-Fe double-atom pairs. The apparent oxidation state of Fe could reach to higher than +3 after the sample still kept in the electrolyte with applying the potential for another 12 hours. Noted that the initial apparent oxidation state of Fe is a bit lower than +3, this is due probable to the different coordination environment compared to the Fe oxide reference samples. In general, the first shell around distal Fe only contained the oxygen from both bridged oxygen and aqueous OH<sup>-</sup>/H<sub>2</sub>O through whole duration, while in second shell only Fe-Ni path could be detected with a constant CN value of about 1.0, confirming the formation of double-atom structures.

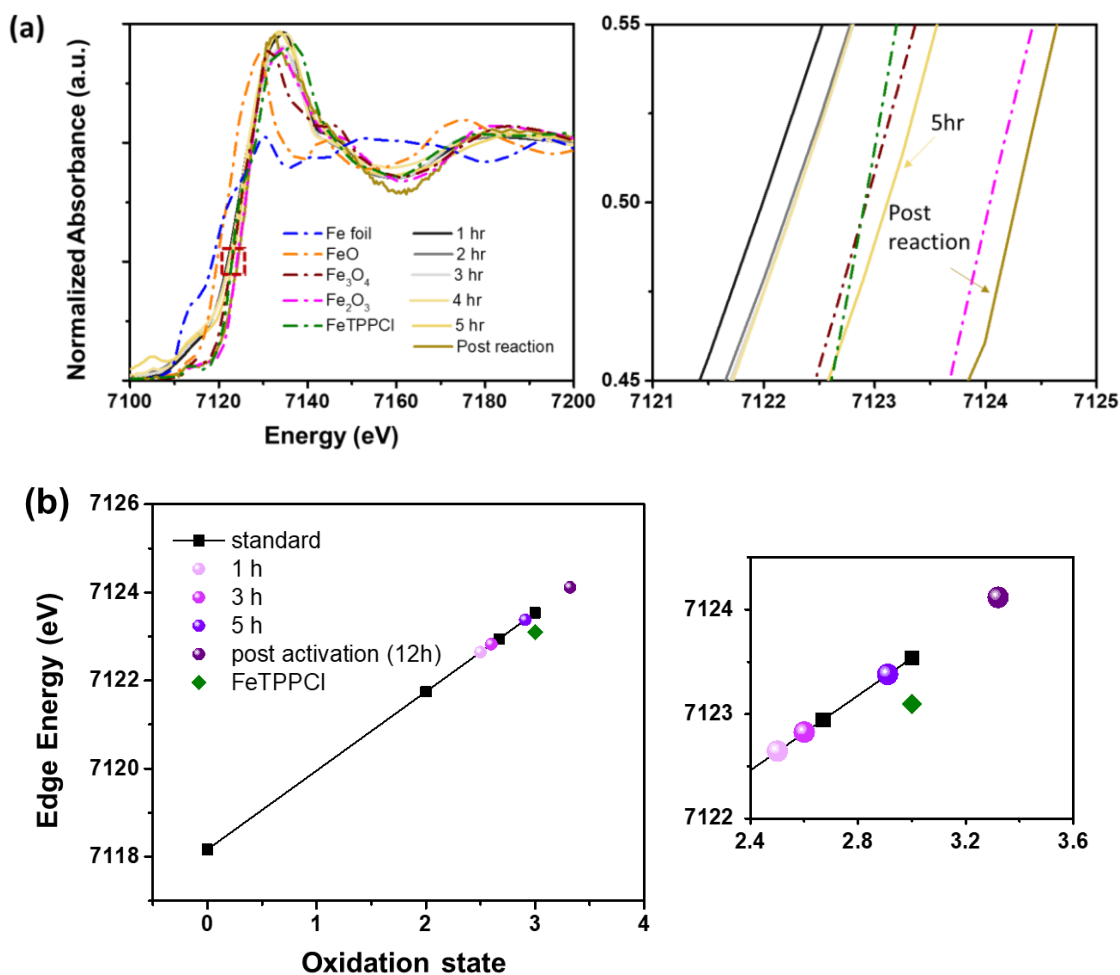


**Figure 3.21** Fe K-edge *operando* XANES of Ni-Fe-N-C. (a) Left: Fe K-edge XANES spectra of Ni-Fe-N-C under OER with various duration (grey and yellow, 1-5 hr and post activation). Fe standard samples: Fe foil (blue), FeO (orange), Fe<sub>3</sub>O<sub>4</sub> (brown), Fe<sub>2</sub>O<sub>3</sub> (pink), FeTPPCI (green) are showed in dashed lines. Right: The enlargement image of the dark red dashed box in the Left image, for determination of the change of the oxidation state. (b) Left: K-edge energies (at 50% level) of XANES spectra in Figure (a), and Fe references compounds containing Fe(0), Fe(II), or Fe(III), showed in black squares (with FeTPPCI shown in green square). Right: The enlarged graph of left image with apparent oxidation state ranging from +2.4-3.6.

### 3.4.2 Operando XAS study of Co-Ni-N-C and Co-Co-N-C

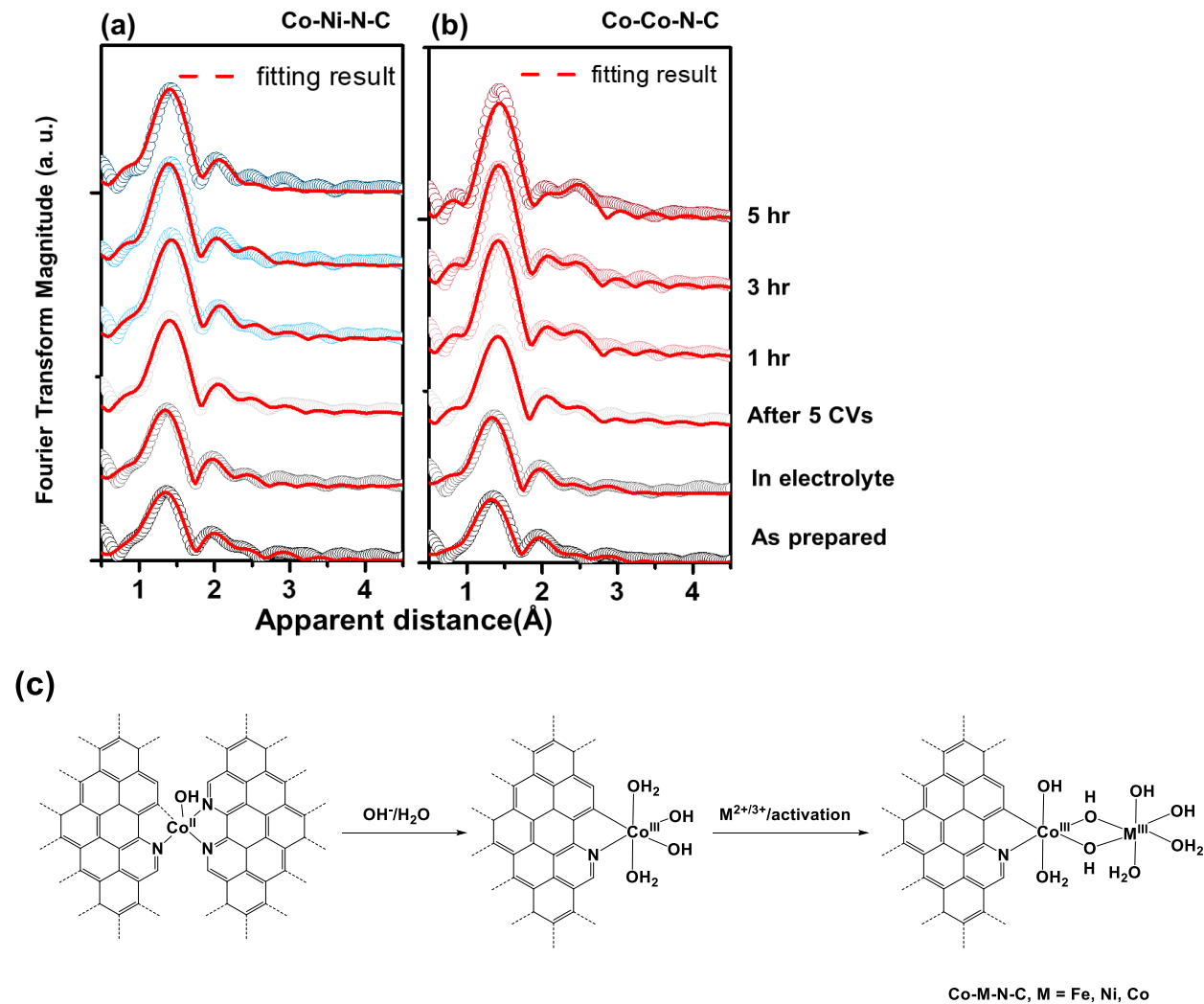


**Figure 3.22** Fourier transform of *operando* Co K-edge EXAFS spectra w/o phase correction for as-prepared Co-N-C and the catalyst after 5 CVs activation as well as under OER for various durations (1, 3, 5 hr) in (a) Ni containing and (b) Co containing Fe free KOH. The fitting results are showed in red solid curves. (c) Proposed model for the formation of Co-based double-atom catalyst.

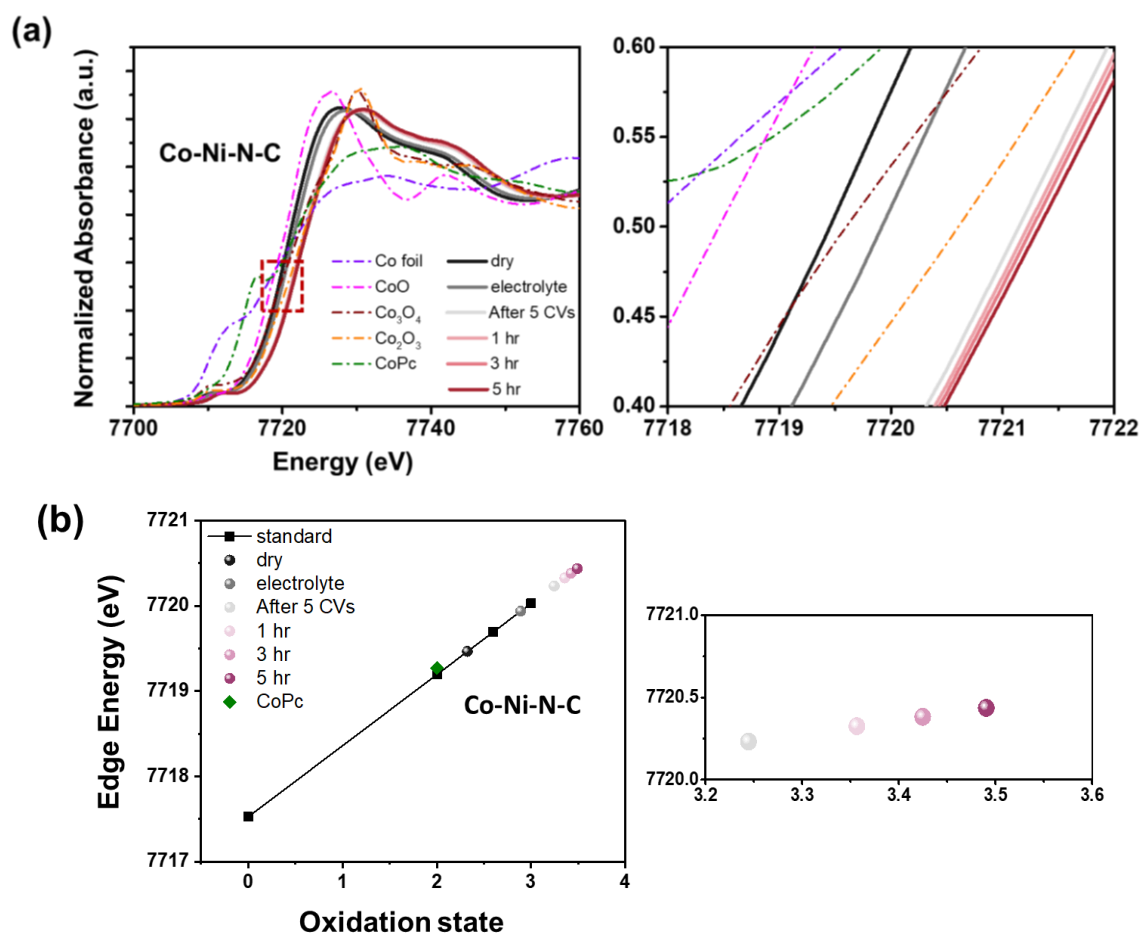


**Figure 3.23** *Operando* XANES of Co-Ni-N-C. (a) Left: Co K-edge XANES spectra of Co-N-C precatalyst (black), Co-N-C in electrolyte (grey), after 5 CVs activation (light grey) and under OER with various duration (red, 1, 3, 5 hr). Co standard samples: Co foil (purple), CoO (pink),  $\text{Co}_3\text{O}_4$  (brown),  $\text{Co}_2\text{O}_3$  (orange), CoPc (green) are showed in dashed lines. Right: The enlargement image of the red dashed box in left image, for determination of the change of the oxidation state. (b) Left: K-edge energies (at 50% level) of XANES spectra in Fig. (a), and cobalt references compounds containing Co(0), Co(II), or Co(III), showed in black squares (with CoPc shown in green square). Right: The enlarged graph of left image with apparent oxidation state higher than +3.2.

For the Co-based system, the XAS analysis of the dry Co-N-C sample revealed a five-coordinate Co(+2) ion surrounded by three N, one C, and one O atoms (Figure 3.22, Tables 3.7 and 3.8), the same as the description of Co-N-C pre-catalyst in Chapter 2. Upon immersion into a KOH electrolyte, two of the coordinated N atoms were replaced by three new O atoms from water or hydroxide ions, with a concomitant oxidation of Co from +2 to +3 (Figures 3.23 and 3.24). As illustrated in Figures 3.23 and 3.24, the XANES spectra of Co evolved after CVs activation, which

introduced a second metal ion (i.e., Ni and Co), and extended electrolysis (at 1 mA/cm<sup>2</sup>). The Co ions were oxidized to a higher oxidation state upon CVs activation, compared to the samples in KOH electrolyte. The oxidation state is even higher in the extended electrolysis. In terms of *operando* EXAFS (Figures 3.22a and 3.22b, Tables 3.7 and 3.8), the first coordinated shells (1.5–2 Å) were attributed to the presence of C, O, and N, while the second scattering shells (2–3.5 Å) were attributed to the single-scattering paths of Co-Ni and Co-Co, as well as long range metal carbon interactions. After CVs activation and extended electrolysis, second shell metal-metal coordination interactions were observed (Figures 3.22a and 3.22b, Tables 3.7 and 3.8). The CN of Co-Co (0.3-0.5) was higher than that of Co-Ni (0.2-0.3) and Co-Fe-N-C in Chapter 2 (0.2-0.3), suggesting a higher affinity of Co ion to the Co-N-C unit than Ni and Fe ions (Tables 3.7 and 3.8). Formation of CoOOH, metallic Co clusters and any type of related oxides were excluded because of the discrepancy in spectroscopic features (Figure 3.25). For both Co-Ni and Co-Co, the coordination structure was quite stable under OER conditions (Figure 3.22, Tables 3.7 and 3.8). The evolution in both CN and apparent distances of Co-Co and Co-Ni during OER was similar to that of Co-Fe-N-C (Table 2.1, Chapter 2). Thus, the formation of the three different DACs from the same Co single-atom pre-catalyst follows a similar mechanism, as depicted in Figure 3.22c.

Due to the low concentration of distal Ni atoms of Co-Ni-N-C, only *ex situ* XAS analysis for distal Ni atoms in the activated samples was conducted. The Ni XANES result displayed an oxidation state at around +3, as shown in Figure 3.26a, in which corresponding EXAFS result elucidated a CN value about 4 in the first-shell Ni-O (Figure 3.26b and Table 3.11). The lower CN value compared to a normal 6 CN might be owing to the dehydration of OH<sup>-</sup>/H<sub>2</sub>O group with absence of electrolyte contacting for *ex situ* samples. This dehydration also resulted a decreased length of second shell metal-metal interaction (Ni-Co path). The CN of Ni-Co path is around 1, further validating the formation of double atom pairs.

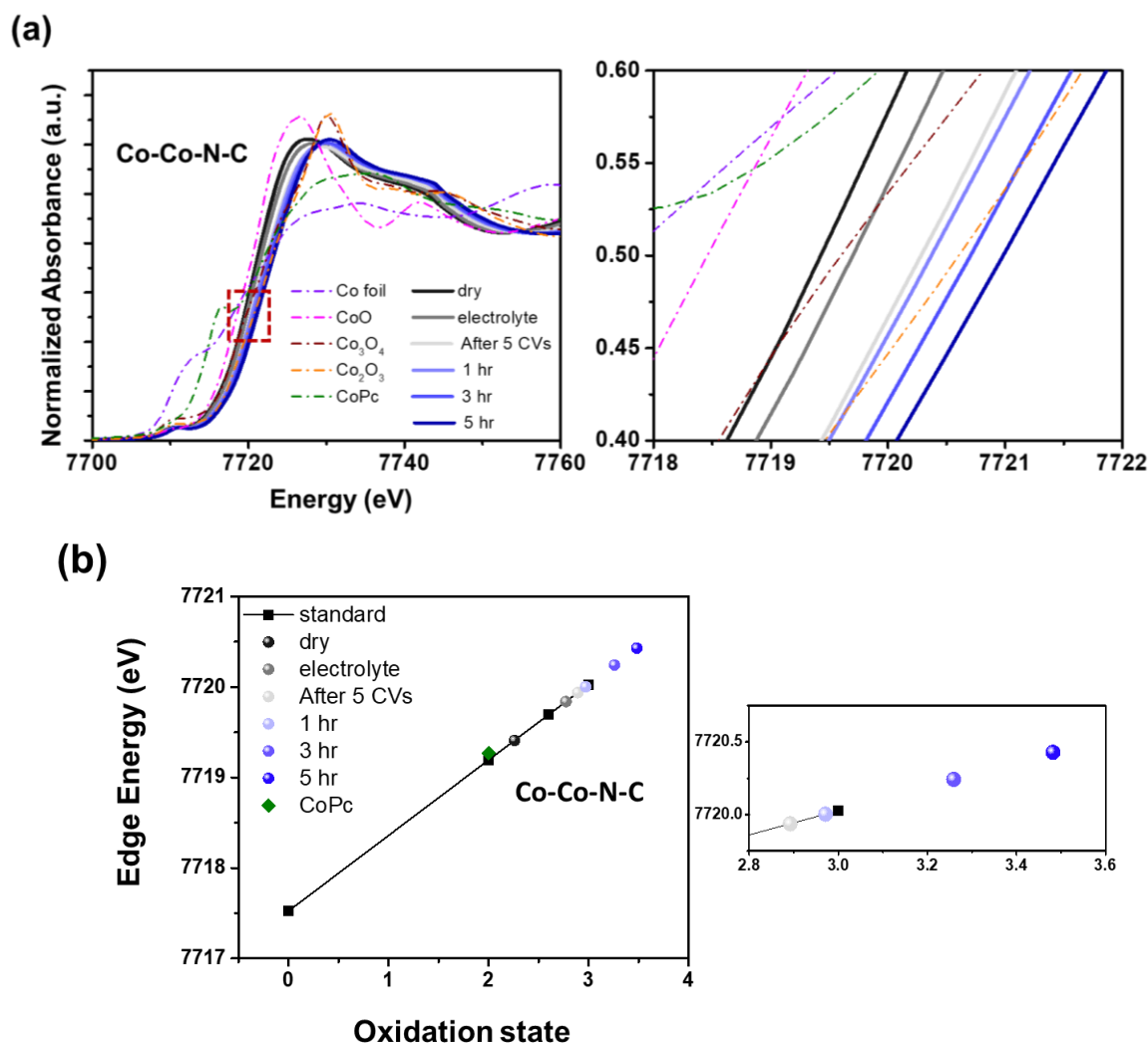


**Figure 3.24** *Operando* XANES of Co-Co-N-C. (a) Left: Co K-edge XANES spectra of Co-N-C precatalyst (black), Co-N-C in electrolyte (grey), after 5 CVs activation (light grey) and under OER with various duration (blue, 1, 3, 5 hr). Co standard samples: Co foil (purple), CoO (pink),  $\text{Co}_3\text{O}_4$  (brown),  $\text{Co}_2\text{O}_3$  (orange), CoPc (green) are showed in dashed lines. Right: The enlargement image of the dark red dashed box in left image, for determination of the change of the oxidation state. (b) Left: K-edge energies (at 50% level) of XANES spectra in Fig. (a), and cobalt references compounds containing Co(0), Co(II), or Co(III), showed in black squares (with CoPc shown in green square). Right: The enlarged graph of left image with apparent oxidation state between +2.8-3.6.

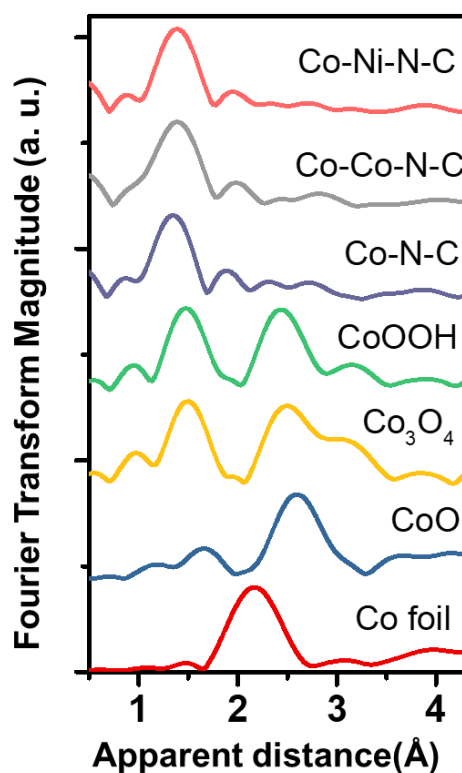


**Figure 3.25** Fourier transform Co K-edge EXAFS spectra of as-prepared Co-N-C, Co-Ni-N-C and Co-Co-N-C in comparison with various Co reference samples.

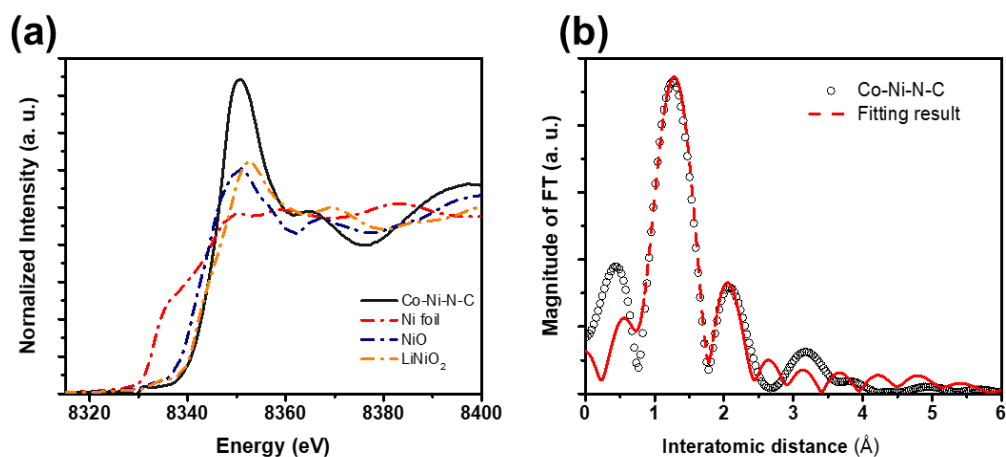


**Figure 3.26** *Ex situ* XAS of distal Ni atoms in Co-Ni-N-C. (a) Ni K-edge XANES spectra of Co-Ni-N-C (black). Ni standard samples: Ni foil (red), NiO (blue), LiNiO<sub>2</sub> (orange) are showed in dashed lines. (b) Fourier transform Ni K-edge EXAFS spectra of Co-Ni-N-C. The fitting result is shown in red solid curve.

### 3.4.3 Operando XAS study of Fe-Ni-N-C and Fe-Co-N-C

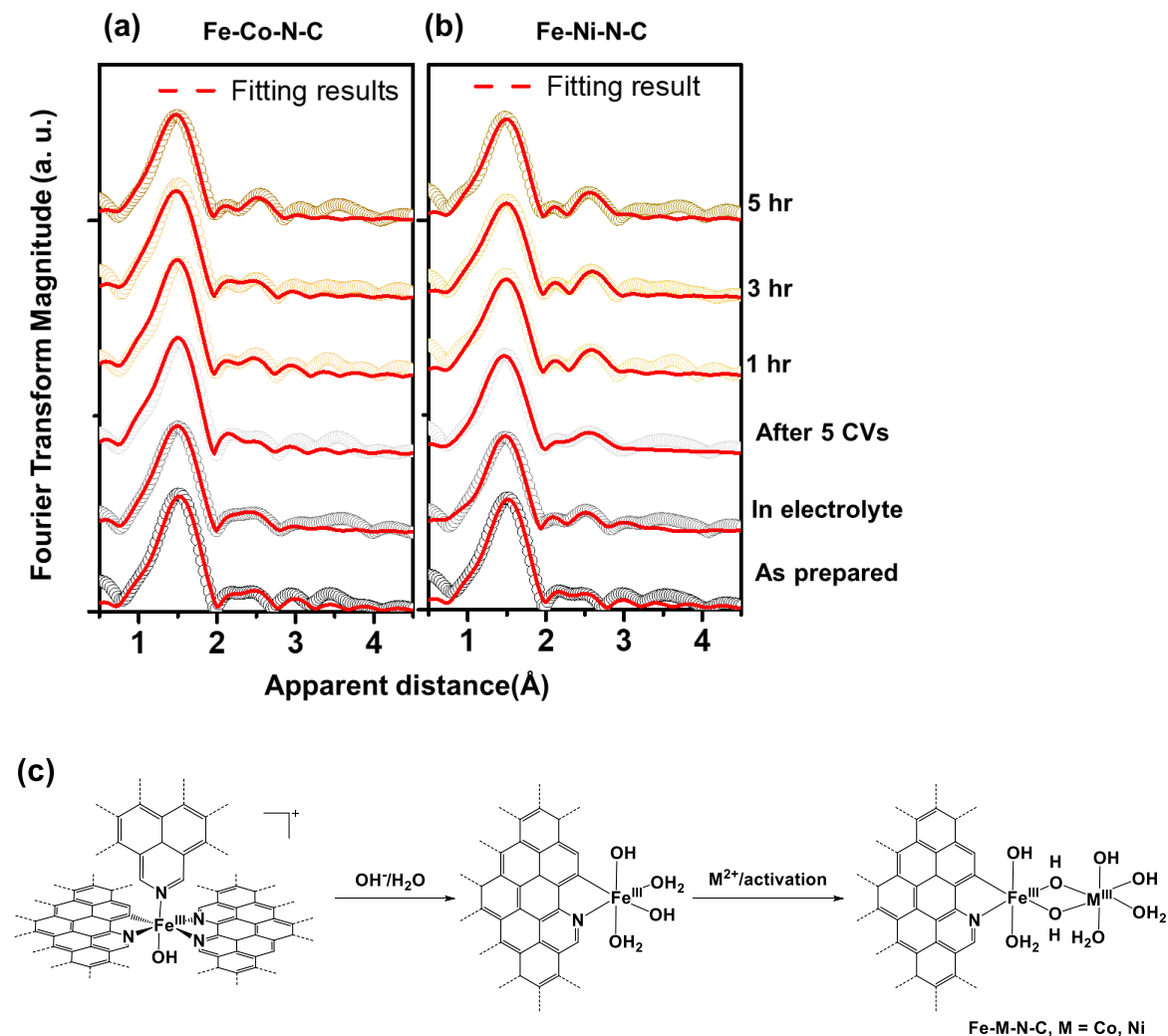


**Figure 3.27** Fourier transform of *operando* Fe K-edge EXAFS spectra w/o phase correction for as-prepared Fe-N-C and the catalyst after 5 CVs activation as well as under OER for various durations (1, 3, 5 hr) in (a) Co containing and (b) Ni containing Fe free KOH. The fitting results are showed in red solid curves. (c) Proposed model for the formation of Fe-based double-atom catalysts.



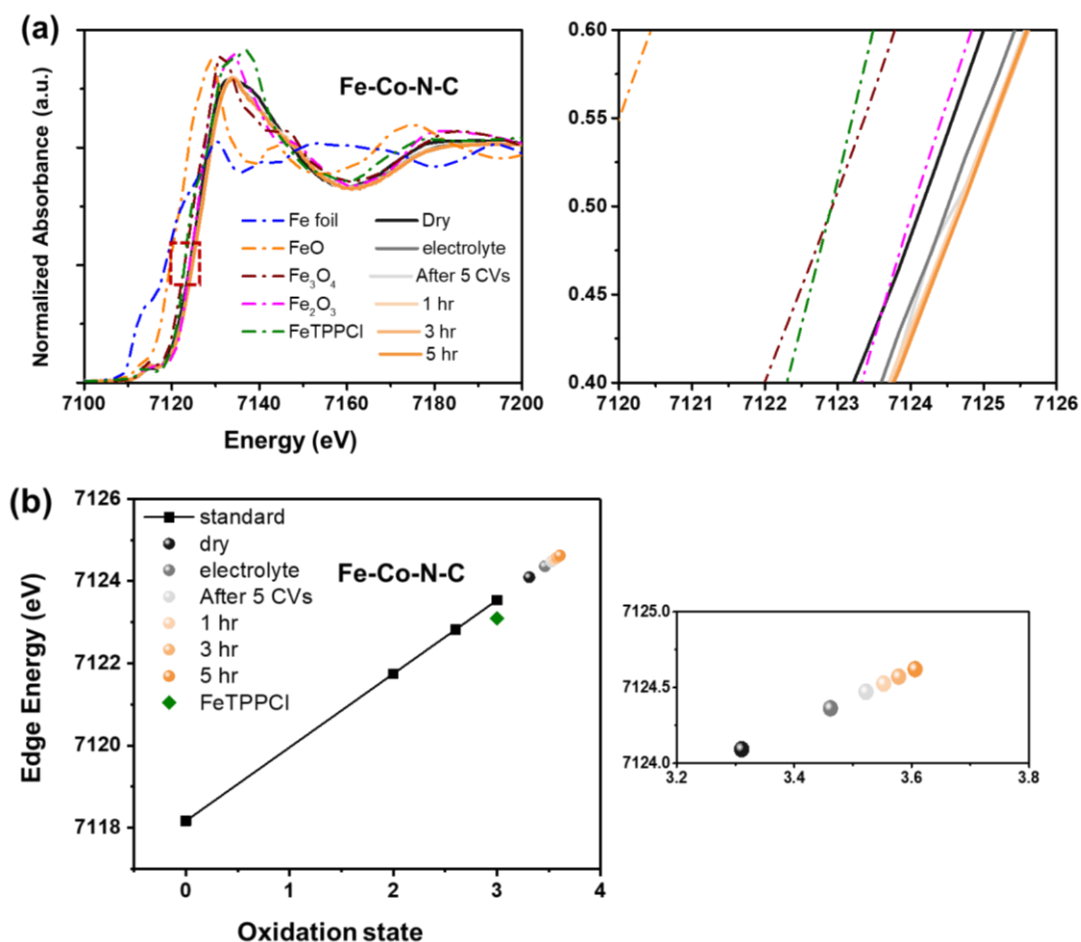


**Figure 3.28** Operando XANES of Fe-Co-N-C. (a) Left: Fe K-edge XANES spectra of Fe-N-C precatalyst (black), Fe-N-C in electrolyte (grey), after 5 CVs activation (light grey) and under OER with various duration (orange, 1, 3, 5 hr). Fe standard samples: Fe foil (blue), FeO (orange),  $\text{Fe}_3\text{O}_4$  (brown),  $\text{Fe}_2\text{O}_3$  (pink), FeTPPCI (green) are shown in dashed lines. Right: The enlargement image of the dark red dashed box in left image, for determination of the change of the oxidation state. (b) Left: K-edge energies (at 50% level) of XANES spectra in Figure (a), and iron references compounds containing Fe(0), Fe(II), or Fe(III), showed in black squares (with FeTPPCI shown in green square). Right: The enlarged graph of left image with apparent oxidation state between +3.2-3.8.

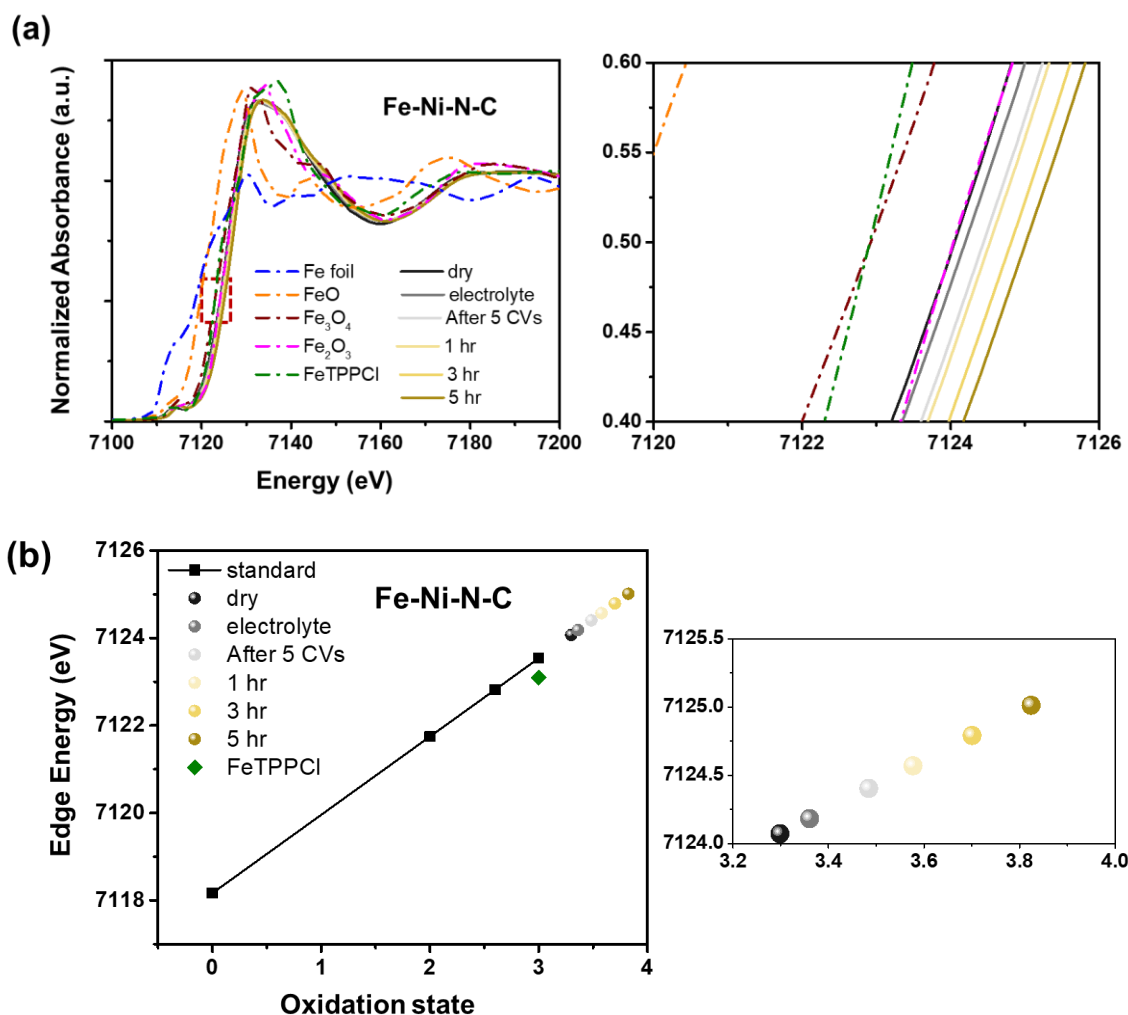


**Figure 3.29** Operando XANES of Fe-Ni-N-C. (a) Left: Fe K-edge XANES spectra of Fe-N-C precatalyst (black), Fe-N-C in electrolyte (grey), after 5 CVs activation (light grey) and under OER with various duration (yellow, 1, 3, 5 hr). Fe standard samples: Fe foil (blue), FeO (orange), Fe<sub>3</sub>O<sub>4</sub> (brown), Fe<sub>2</sub>O<sub>3</sub> (pink), FeTPPCI (green) are showed in dashed lines. Right: The enlargement image of the dark red dashed box in left image, for determination of the change of the oxidation state. (b) Left: K-edge energies (at 50% level) of XANES spectra in Figure (a), and iron references compounds containing Fe(0), Fe(II), or Fe(III), showed in black squares (with FeTPPCI shown in green square). Right: The enlarged graph of left image with apparent oxidation state between +3.2-4.0.

Moving to the Fe-based catalysts, the structure of dry Fe-N-C is slightly different from those of Co-N-C and Ni-N-C, with Fe being coordinated by 1 C, 4 N and 1 O donors (Figure 3.27, Tables 3.9 and 3.10). The oxidation state of Fe in Fe-N-C was about +3 (Figures 3.28 and 3.29). Upon immersion into alkaline electrolyte, three N donors are replaced by three O donors (Figure 3.27, Tables 3.9 and 3.10), and the resulting coordination structure of Fe now resembles those of Co-

N-C and Ni-N-C in KOH (Figures 3.18b, 3.22c, and 3.27c). The formation of Fe-Co-N-C and Fe-Ni-N-C was confirmed by *operando* EXAFS (Figures 3.27a and 3.27b, Tables 3.9 and 3.10). A scattering path corresponding to Fe-Co ( $\sim 3.0$  Å, CN = 0.2) or Fe-Ni ( $\sim 2.8$  Å, CN = 0.3) was observed upon activation of Fe-N-C in Co- or Ni-containing KOH (Figures 3.27a and 3.27b, Tables 3.9 and 3.10). The formation of Fe-based oxides or nanoparticles could be excluded by comparing the spectra of Fe-Co-N-C and Fe-Ni-N-C to those of Fe-based metal or metal oxides (Figure 3.30). The oxidation states of Fe in Fe-Co-N-C were slightly changed when immersed in KOH and in further CVs activation and extended electrolysis (Figure 3.28); while the Fe in Fe-Ni-N-C was obviously oxidized after CVs activation and the oxidation state of Fe was even close to +4 under extended electrolysis (Figure 3.29). Similar to Figures 3.18b and 3.22c, Figure 3.27c presents a general scheme describing the *in situ* formation of Fe-Co-N-C, and Fe-Ni-N-C.

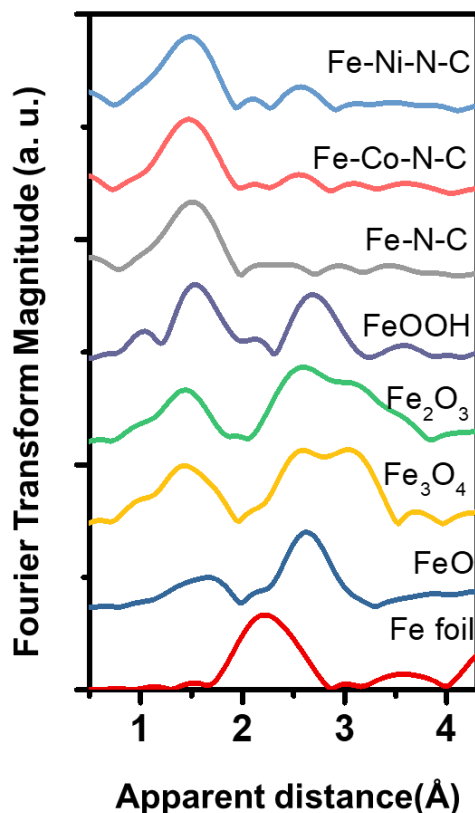


**Figure 3.30** Fourier transform Fe K-edge EXAFS spectra of as-prepared Fe-N-C, Fe-Ni-N-C and Fe-Co-N-C in comparison with various Fe reference samples.

Similar as Co-Ni-N-C, *ex situ* XAS experiments were conducted for distal metals of activated Fe-based samples, as showed in Figures 3.31 and 3.32, and Table 3.11. The oxidation state of both Ni in Fe-Ni-N-C and Co in Fe-Co-N-C were close to +3 after 3 hours electrochemical activation. The EXAFS results clarified a similar behavior as Co-Ni-N-C sample. The CN values of first shell were smaller than 6 (due to possible dehydration of the *ex situ* samples) and the second shell of M-M path yielded a similar CN value of around 1, which can be referred to the double atom structures as well.

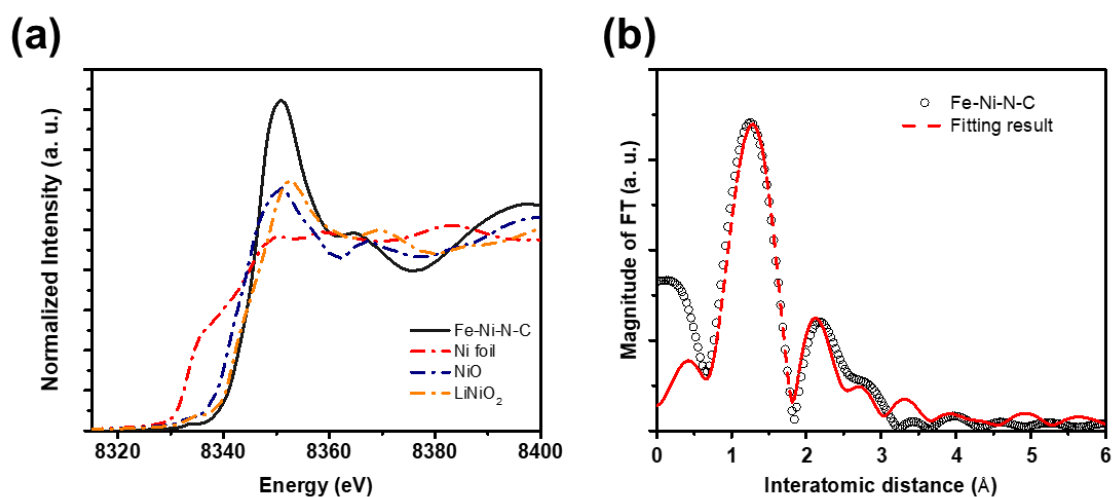


**Figure 3.31** *Ex situ* XAS of distal Ni atoms in Fe-Ni-N-C. (a) Ni K-edge XANES spectra of Fe-Ni-N-C (black). Ni standard samples: Ni foil (red), NiO (blue), LiNiO<sub>2</sub> (orange) are showed in dashed lines. (b) Fourier transform Ni K-edge EXAFS spectra of Fe-Ni-N-C. The fitting result is shown in red dashed curve.

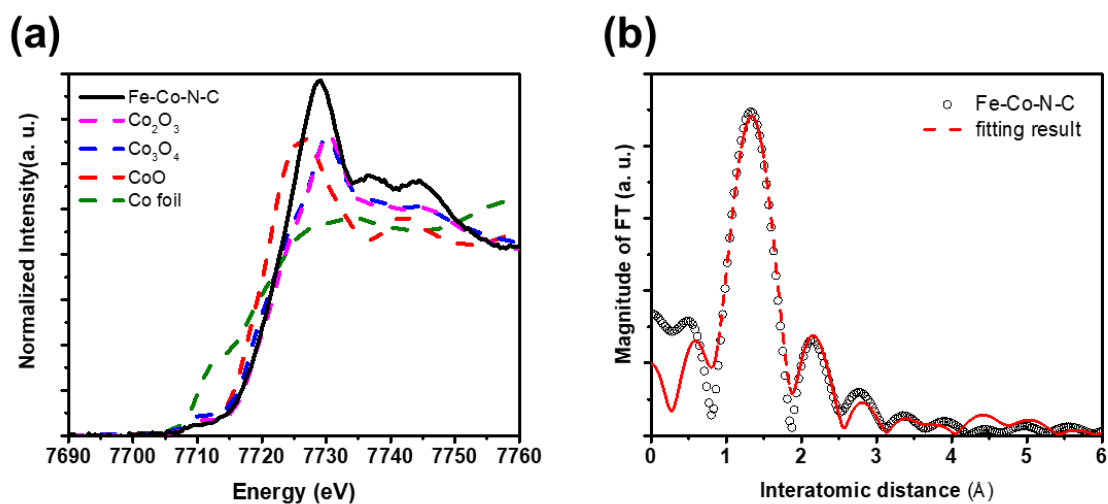


**Figure 3.32** *Ex situ* XAS of distal Co atoms in Fe-Co-N-C. (a) Co K-edge XANES spectra of Fe-Co-N-C (black). Co standard samples: Co foil (green), CoO (red), Co<sub>3</sub>O<sub>4</sub> (blue) and Co<sub>2</sub>O<sub>3</sub> (pink) are showed in dashed lines. (b) Fourier transform Co K-edge EXAFS spectra of Fe-Co-N-C. The fitting result is shown in red dashed curve.

**Table 3.5** Structural parameters of Ni-N-C and Ni-Fe-N-C extracted from *operando* Ni K-edge EXAFS refinement for as-prepared Ni-N-C and after 5 CVs activation with Fe as well as under OER for various duration. The filled area indicates the first shell coordination parameters.

condition	path	R (Å)	N	$\Delta E$	$\sigma^2$ (Å <sup>2</sup> )	R factor
As-prepared	Ni-C	1.84(4)	0.76(4)	3.4(7)	0.0095(7)	2.293
	Ni-N	1.88(5)	3.09(5)	-6.3(4)	0.0095(-)	
	Ni-O	2.07(3)	1.47(3)	-8.7(5)	0.0095(-)	
	Ni-C1	2.95(9)	3.98(9)	0.6(6)	0.0115(4)	
	Ni-C2	3.03(7)	3.44(7)	13.4(9)	0.0115(-)	
	Ni-Fe	-	-	-	-	
In electrolyte	Ni-C	1.83(4)	0.89(4)	9.3(7)	0.0095(7)	2.799
	Ni-N	1.83(4)	1.33(4)	-3.3(5)	0.0095(-)	
	Ni-O	1.91(9)	2.56(3)	-6.8(4)	0.0095(-)	
	Ni-C1	2.80(8)	3.96(9)	4.1(6)	0.0122(4)	
	Ni-C2	2.91(7)	3.99(6)	16.7(9)	0.0122(-)	
	Ni-Fe	-	-	-	-	
After 5 CVs activation	Ni-C	1.81(5)	1.05(6)	-13.6(6)	0.0111(8)	2.238
	Ni-N	1.75(8)	0.96(9)	10.2(7)	0.0111(-)	
	Ni-O	1.82(6)	2.98(9)	-12.5(3)	0.0111(-)	
	Ni-C1	2.87(5)	3.48(4)	-10.1(6)	0.0127(4)	
	Ni-C2	2.97(9)	3.63(7)	16.3(3)	0.0127(-)	
	Ni-Fe	2.89(4)	0.22(5)	10.8(3)	0.0044(5)	
1 hr	Ni-C	1.78(9)	1.05(8)	-13.6(-)	0.0111(-)	2.087
	Ni-N	1.78(5)	0.96(5)	10.2(-)	0.0111(-)	
	Ni-O	1.83(4)	3.29(6)	-12.5(-)	0.0111(-)	
	Ni-C1	2.83(6)	3.48(7)	-10.1(-)	0.0127(-)	
	Ni-C2	3.19(8)	3.63(6)	16.3(-)	0.0127(-)	
	Ni-Fe	2.99(7)	0.25(9)	19.5(9)	0.0056(7)	
3 hr	Ni-C	1.79(4)	1.05(-)	-13.6(-)	0.0111(-)	1.628
	Ni-N	1.78(5)	0.96(-)	10.2(-)	0.0111(-)	
	Ni-O	1.83(5)	3.29(6)	-12.5(-)	0.0111(-)	
	Ni-C1	2.83(6)	3.48(-)	-10.1(-)	0.0127(-)	
	Ni-C2	3.19(6)	3.63(-)	16.3(-)	0.0127(-)	
	Ni-Fe	2.99(7)	0.33(6)	18.4(8)	0.0046(5)	
5 hr	Ni-C	1.70(7)	1.05(-)	-13.6(-)	0.0111(-)	2.181
	Ni-N	1.75(4)	0.96(-)	10.2(-)	0.0111(-)	
	Ni-O	1.85(4)	3.13(8)	-12.5(-)	0.0111(-)	
	Ni-C1	2.83(6)	3.48(-)	-10.1(-)	0.0127(-)	
	Ni-C2	3.19(6)	3.63(-)	16.3(-)	0.0127(-)	
	Ni-Fe	2.97(8)	0.43(8)	19.8(3)	0.0032(6)	

**Table 3.6** Structural parameters of *operando* Fe K-edge EXAFS refinement for Ni-Fe-N-C under OER for various duration.

condition	path	R (Å)	N	$\Delta E$	$\sigma^2$ (Å <sup>2</sup> )	R factor
1 hr	Fe-O	2.13(6)	4.18(6)	1.0(5)	0.0110(5)	5.61
	Fe-Ni	3.41(7)	1.05(9)	3.3(8)	0.0020(9)	
2 hr	Fe-O	2.18(8)	4.70(8)	0.2(8)	0.0124(3)	6.94
	Fe-Ni	3.20(6)	1.06(4)	-9.4(5)	0.0043(5)	
3hr	Fe-O	2.15(5)	4.73(7)	1.8(7)	0.0118(3)	3.44
	Fe-Ni	3.23(8)	0.91(6)	-1.8(8)	0.0057(7)	
4hr	Fe-O	2.05(8)	5.18(7)	-6.2(6)	0.0112(9)	6.23
	Fe-Ni	2.94(6)	0.94(9)	0.2(9)	0.0087(8)	
5hr	Fe-O	2.07(9)	6.09(6)	5.1(6)	0.0127(3)	6.41
	Fe-Ni	2.79(3)	1.03(7)	-16.1(7)	0.0059(4)	
Post activation (12 hr)	Fe-O	1.99(7)	6.05(3)	-4.1(7)	0.0101(3)	7.24
	Fe-Ni	3.01(9)	1.02(7)	-8.9(8)	0.0029(3)	

**Table 3.7** Structural parameters of Co-N-C and Co-Ni-N-C extracted from *operando* Co K-edge EXAFS refinement for as-prepared Co-N-C and after 5 CVs activation with Ni as well as under OER for various duration. The filled area indicates the first shell coordination parameters.

condition	path	R (Å)	N	$\Delta E$	$\sigma^2$ (Å <sup>2</sup> )	R factor
As-prepared	Co-C	1.88(8)	0.42(4)	11.7(8)	0.0089(6)	2.031
	Co-N	1.90(6)	3.14(8)	-11.2(7)	0.0089(-)	
	Co-O	2.13(6)	1.20(6)	-9.9(4)	0.0089(-)	
	Co-C1	2.89(7)	3.91(5)	1.0(3)	0.0122(5)	
	Co-C2	3.08(4)	3.72(9)	-14.5(8)	0.0122(-)	
	Co-Ni	-	-	-	-	
In electrolyte	Co-C	1.86(3)	0.72(4)	3.2(6)	0.0090(6)	1.151
	Co-N	1.91(3)	1.21(8)	-8.2(6)	0.0090(-)	
	Co-O	1.97(6)	3.18(7)	-2.6(7)	0.0090(-)	
	Co-C1	2.82(8)	3.84(9)	8.5(6)	0.0120(8)	
	Co-C2	2.91(5)	3.86(4)	-3.6(3)	0.0120(-)	
	Co-Ni	-	-	-	-	
After 5 CVs activation	Co-C	1.86(8)	0.72(7)	5.2(6)	0.0090(9)	2.372
	Co-N	1.87(4)	0.83(8)	3.2(8)	0.0090(-)	
	Co-O	1.94(3)	3.97(9)	-3.8(4)	0.0090(-)	
	Co-C1	2.82(5)	3.86(4)	-7.1(6)	0.0120(4)	
	Co-C2	2.91(6)	3.85(9)	7.2(5)	0.0120(-)	
	Co-Ni	2.72(9)	0.17(7)	8.9(4)	0.0143(3)	
1 hr	Co-C	1.86(3)	0.72(-)	5.2(-)	0.0090(-)	2.915
	Co-N	1.88(4)	0.83(-)	3.2(-)	0.0090(-)	
	Co-O	1.93(7)	4.33(4)	-3.8(-)	0.0090(-)	
	Co-C1	2.84(8)	3.86(-)	-7.1(-)	0.0120(-)	
	Co-C2	2.92(4)	3.85(-)	7.2(-)	0.0120(-)	
	Co-Ni	2.75(3)	0.19(6)	-10.5(9)	0.0143(8)	
3 hr	Co-C	1.86(5)	0.72(-)	5.2(-)	0.0090(-)	2.980
	Co-N	1.90(7)	0.83(-)	3.2(-)	0.0090(-)	
	Co-O	1.93(3)	4.34(4)	-3.8(-)	0.0090(-)	
	Co-C1	2.87(4)	3.86(-)	-7.1(-)	0.0120(-)	
	Co-C2	2.94(7)	3.85(-)	7.2(-)	0.0120(-)	
	Co-Ni	2.71(7)	0.23(8)	-10.7(6)	0.0089(5)	
5 hr	Co-C	1.88(4)	0.72(-)	5.2(-)	0.0090(-)	7.450
	Co-N	1.87(9)	0.83(-)	3.2(-)	0.0090(-)	
	Co-O	1.93(4)	4.57(5)	-3.8(-)	0.0090(-)	
	Co-C1	2.93(6)	3.86(-)	-7.1(-)	0.0120(-)	
	Co-C2	3.07(3)	3.85(-)	7.2(-)	0.0120(-)	
	Co-Ni	2.72(9)	0.30(4)	-4.1(3)	0.0125(8)	



**Table 3.8** Structural parameters of Co-N-C and Co-Co-N-C extracted from *operando* Co K-edge EXAFS refinement for as-prepared Co-N-C and after 5 CVs activation with Co as well as under OER for various duration. The filled area indicates the first shell coordination parameters.

condition	path	R (Å)	N	$\Delta E$	$\sigma^2$ (Å <sup>2</sup> )	R factor
As-prepared	Co-C	1.82(9)	0.68(4)	-9.6(9)	0.0085(7)	7.743
	Co-N	1.89(3)	3.22(3)	-14.6(5)	0.0085(-)	
	Co-O	2.26(7)	0.83(5)	12.5(3)	0.0085(-)	
	Co-C1	2.93(6)	3.91(5)	-0.0(6)	0.0114(6)	
	Co-C2	3.16(5)	3.74(5)	-8.6(9)	0.0114(-)	
	Co-Co	-	-	-	-	
In electrolyte	Co-C	1.83(9)	0.86(3)	-12.5(7)	0.0087(7)	4.293
	Co-N	1.83(4)	1.01(3)	-11.3(7)	0.0087(-)	
	Co-O	1.89(8)	3.21(4)	17.5(9)	0.0087(-)	
	Co-C1	2.96(6)	3.99(8)	1.9(5)	0.0114(5)	
	Co-C2	3.19(7)	3.71(6)	-7.9(6)	0.0114(-)	
	Co-Co	-	-	-	-	
After 5 CVs activation	Co-C	1.82(8)	0.68(3)	10.5(7)	0.0087(9)	2.389
	Co-N	1.83(8)	0.91(5)	-2.1(6)	0.0087(-)	
	Co-O	1.87(7)	3.41(5)	-9.8(5)	0.0087(-)	
	Co-C1	2.97(6)	3.94(6)	2.1(6)	0.0122(4)	
	Co-C2	3.16(3)	3.70(7)	-16.3(9)	0.0122(-)	
	Co-Co	3.01(3)	0.19(9)	-18.1(8)	0.0051(6)	
1 hr	Co-C	1.83(3)	0.68(-)	11.7(-)	0.0087(-)	3.451
	Co-N	1.83(7)	0.91(-)	-1.4(-)	0.0087(-)	
	Co-O	1.87(5)	3.99(5)	-9.2(-)	0.0087(-)	
	Co-C1	2.95(7)	3.94(-)	6.0(-)	0.0122(-)	
	Co-C2	3.18(9)	3.70(-)	-18.0(-)	0.0122(-)	
	Co-Co	3.05(4)	0.25(6)	-18.7(6)	0.0057(6)	
3 hr	Co-C	1.82(3)	0.68(-)	11.7(-)	0.0087(-)	3.653
	Co-N	1.83(8)	0.91(-)	-1.4(-)	0.0087(-)	
	Co-O	1.87(5)	4.32(6)	-9.2(-)	0.0087(-)	
	Co-C1	2.97(6)	3.94(-)	6.0(-)	0.0122(-)	
	Co-C2	3.16(8)	3.70(-)	-16.2(-)	0.0122(-)	
	Co-Co	3.07(3)	0.46(4)	-7.8(4)	0.0078(6)	
5 hr	Co-C	1.85(4)	0.68(-)	11.7(-)	0.0087(-)	2.727
	Co-N	1.85(8)	0.91(-)	-1.4(-)	0.0087(-)	
	Co-O	1.87(5)	4.56(5)	-9.2(-)	0.0087(-)	
	Co-C1	2.95(7)	3.94(-)	6.0(-)	0.0122(-)	
	Co-C2	3.20(7)	3.70(-)	-17.1(-)	0.0122(-)	
	Co-Co	3.03(7)	0.58(3)	-7.1(9)	0.0074(6)	

**Table 3.9** Structural parameters of Fe-N-C and Fe-Co-N-C extracted from *operando* Fe K-edge EXAFS refinement for as-prepared Fe-N-C and after 5 CVs activation with Co as well as under OER for various duration. The filled area indicates the first shell coordination parameters.

condition	path	R (Å)	N	$\Delta E$	$\sigma^2$ (Å <sup>2</sup> )	R factor
As-prepared	Fe-C	1.75(4)	0.68(6)	-7.4(9)	0.0090(6)	1.332
	Fe-N	1.98(9)	4.19(8)	-3.7(3)	0.0090(-)	
	Fe-O	2.03(5)	1.17(3)	-16.4(5)	0.0090(-)	
	Fe-C1	2.76(4)	3.30(5)	19.9(4)	0.0105(5)	0.0105(-)
	Fe-C2	3.02(6)	4.09(6)	5.9(7)	0.0105(-)	
	Fe-Co	-	-	-	-	
In electrolyte	Fe-C	1.76(4)	0.77(6)	-4.2(8)	0.0086(5)	3.133
	Fe-N	1.79(6)	0.91(4)	-10.5(4)	0.0086(-)	
	Fe-O	1.99(5)	3.94(5)	3.5(3)	0.0086(-)	
	Fe-C1	2.77(3)	3.93(5)	11.1(5)	0.0120(7)	0.0120(-)
	Fe-C2	3.01(7)	3.52(6)	19.4(6)	0.0120(-)	
	Fe-Co	-	-	-	-	
After 5 CVs activation	Fe-C	1.73(6)	0.74(3)	-14.6(5)	0.0090(4)	2.206
	Fe-N	1.77(8)	0.85(5)	-5.4(7)	0.0090(-)	
	Fe-O	1.99(9)	4.25(9)	-6.4(4)	0.0090(-)	
	Fe-C1	2.82(7)	3.97(5)	-20.3(7)	0.0120(6)	0.0120(-)
	Fe-C2	2.96(8)	3.52(4)	-14.2(6)	0.0120(-)	
	Fe-Co	3.05(6)	0.17(7)	11.2(9)	0.0080(8)	
1 hr	Fe-C	1.74(6)	0.74(-)	-14.6(-)	0.0090(-)	3.804
	Fe-N	1.77(9)	0.85(-)	-5.4(-)	0.0090(-)	
	Fe-O	1.98(8)	4.29(8)	-6.4(-)	0.0090(-)	
	Fe-C1	2.88(8)	3.97(-)	-20.3(-)	0.0120(-)	0.0120(-)
	Fe-C2	2.98(5)	3.52(-)	-14.2(-)	0.0120(-)	
	Fe-Co	3.04(5)	0.16(4)	15.0(6)	0.0031(6)	
3 hr	Fe-C	1.75(5)	0.74(-)	-14.6(-)	0.0090(-)	2.815
	Fe-N	1.82(9)	0.85(-)	-5.4(-)	0.0090(-)	
	Fe-O	1.99(8)	4.00(4)	-6.4(-)	0.0090(-)	
	Fe-C1	2.87(7)	3.97(-)	-20.3(-)	0.0120(-)	0.0120(-)
	Fe-C2	2.99(5)	3.52(-)	-14.2(-)	0.0120(-)	
	Fe-Co	3.05(4)	0.16(5)	18.4(4)	0.0092(4)	
5 hr	Fe-C	1.75(7)	0.74(-)	-14.6(-)	0.0090(-)	0.453
	Fe-N	1.77(9)	0.85(-)	-5.4(-)	0.0090(-)	
	Fe-O	1.96(9)	3.82(7)	-6.4(-)	0.0090(-)	
	Fe-C1	2.99(7)	3.97(-)	-20.3(-)	0.0120(-)	0.0120(-)
	Fe-C2	3.05(5)	3.52(-)	-14.2(-)	0.0120(-)	
	Fe-Co	3.08(5)	0.17(5)	15.9(4)	0.0093(3)	

**Table 3.10** Structural parameters of Fe-N-C and Fe-Ni-N-C extracted from *operando* Fe K-edge EXAFS refinement for as-prepared Fe-N-C and after 5 CVs activation with Ni as well as under OER for various duration. The filled area indicates the first shell coordination parameters.

condition	path	R (Å)	N	ΔE	σ <sup>2</sup> (Å <sup>2</sup> )	R factor
As-prepared	Fe-C	1.83(6)	0.63(4)	-7.9(5)	0.0078(4)	1.134
	Fe-N	2.01(7)	4.01(4)	-6.4(6)	0.0078(-)	
	Fe-O	2.06(4)	1.25(3)	-12.3(6)	0.0078(-)	
	Fe-C1	2.71(5)	3.92(9)	5.7(4)	0.0120(6)	
	Fe-C2	2.92(8)	4.01(7)	16.4(8)	0.0120(-)	
	Fe-Ni	-	-	-	-	
In electrolyte	Fe-C	1.75(6)	0.59(5)	-11.1(7)	0.0078(4)	0.922
	Fe-N	1.81(8)	1.32(8)	-4.6(5)	0.0078(-)	
	Fe-O	1.97(8)	3.03(9)	-7.0(6)	0.0078(-)	
	Fe-C1	2.98(4)	3.97(6)	3.4(9)	0.0120(6)	
	Fe-C2	3.00(6)	3.78(5)	15.1(9)	0.0120(-)	
	Fe-Ni	-	-	-	-	
After 5 CVs activation	Fe-C	1.75(5)	0.57(3)	-12.5(7)	0.0078(3)	1.157
	Fe-N	1.81(4)	0.62(7)	-5.9(6)	0.0078(-)	
	Fe-O	1.97(8)	3.14(9)	-7.4(3)	0.0078(-)	
	Fe-C1	3.02(5)	3.97(6)	-9.0(7)	0.0120(7)	
	Fe-C2	3.11(6)	3.62(4)	1.2(4)	0.0120(-)	
	Fe-Ni	2.70(7)	0.18(8)	-16.8(9)	0.0057(5)	
1 hr	Fe-C	1.75(4)	0.57(-)	-12.5(-)	0.0078(-)	1.126
	Fe-N	1.81(7)	0.62(-)	-5.9(-)	0.0078(-)	
	Fe-O	1.97(4)	3.21(4)	-7.4(-)	0.0078(-)	
	Fe-C1	3.02(6)	3.97(-)	-9.0(-)	0.0120(-)	
	Fe-C2	3.11(3)	3.62(-)	1.2(-)	0.0120(-)	
	Fe-Ni	2.73(8)	0.18(3)	7.4(5)	0.0068(3)	
3 hr	Fe-C	1.75(4)	0.57(-)	-12.5(-)	0.0078(-)	1.276
	Fe-N	1.81(4)	0.62(-)	-5.9(-)	0.0078(-)	
	Fe-O	1.97(9)	3.26(5)	-7.4(-)	0.0078(-)	
	Fe-C1	3.02(8)	3.97(-)	-9.0(-)	0.0120(-)	
	Fe-C2	3.11(7)	3.62(-)	1.2(-)	0.0120(-)	
	Fe-Ni	2.77(7)	0.23(3)	23.6(4)	0.0067(9)	
5 hr	Fe-C	1.75(6)	0.57(-)	-12.5(-)	0.0078(-)	1.528
	Fe-N	1.81(5)	0.62(-)	-5.9(-)	0.0078(-)	
	Fe-O	1.97(7)	3.39(4)	-7.4(-)	0.0078(-)	
	Fe-C1	3.02(3)	3.97(-)	-9.0(-)	0.0120(-)	
	Fe-C2	3.11(8)	3.62(-)	1.2(-)	0.0120(-)	
	Fe-Ni	2.75(4)	0.25(4)	19.5(6)	0.0086(9)	

**Table 3.11** Structural parameters of distal atoms in Co-Ni-N-C, Fe-Ni-N-C, and Fe-Co-N-C after electrochemical activation.

condition	path	R (Å)	N	$\Delta E$	$\sigma^2$ (Å <sup>2</sup> )	R factor
Co-Ni-N-C	Ni-O	1.91(6)	4.33(3)	-11.6(5)	0.0107(5)	4.446
	Ni-Co	2.42(4)	1.03(6)	11.3(5)	0.0095(8)	
condition	path	R (Å)	N	$\Delta E$	$\sigma^2$ (Å <sup>2</sup> )	R factor
Fe-Ni-N-C	Ni-O	1.92(7)	4.28(7)	-4.8(7)	0.0136(8)	7.618
	Ni-Fe	2.48(9)	0.82(4)	-14.3(5)	0.0095(4)	
condition	path	R (Å)	N	$\Delta E$	$\sigma^2$ (Å <sup>2</sup> )	R factor
Fe-Co-N-C	Co-O	1.98(5)	4.34(5)	-5.2(8)	0.0098(4)	8.165
	Co-Fe	2.41(6)	0.94(4)	-7.8(7)	0.0074(6)	

### 3.5 Comparison of intrinsic OER activity

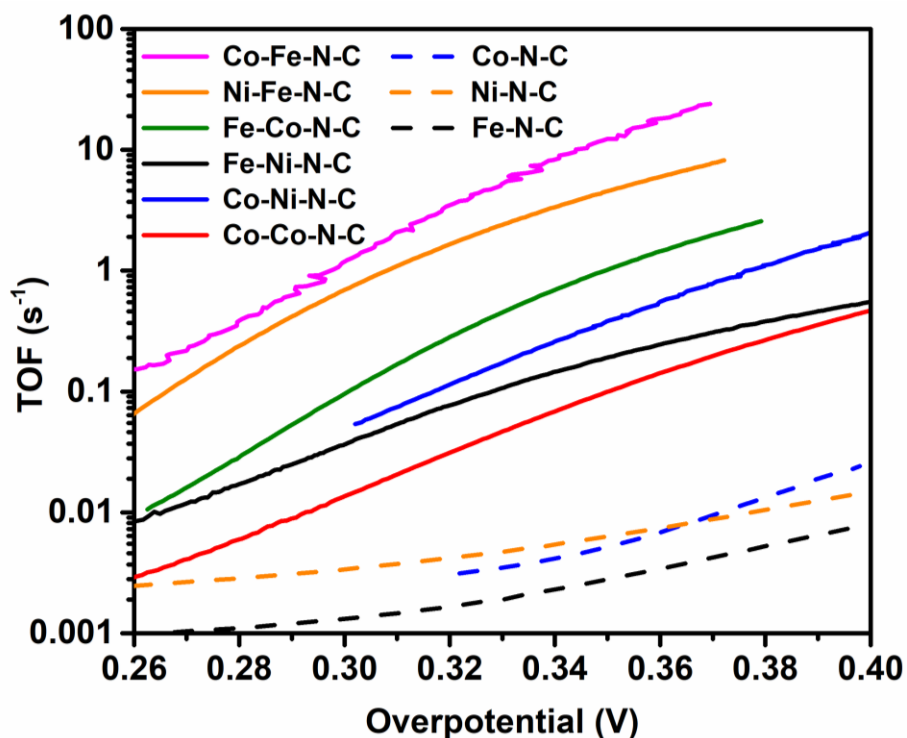


**Figure 3.33** Potential dependent TOFs of different atomically dispersed catalysts. The performance of SACs was obtained from the first LSV curve of these catalysts in 1M Fe-free KOH. For DACs, solid lines; for SACs, dashed lines.

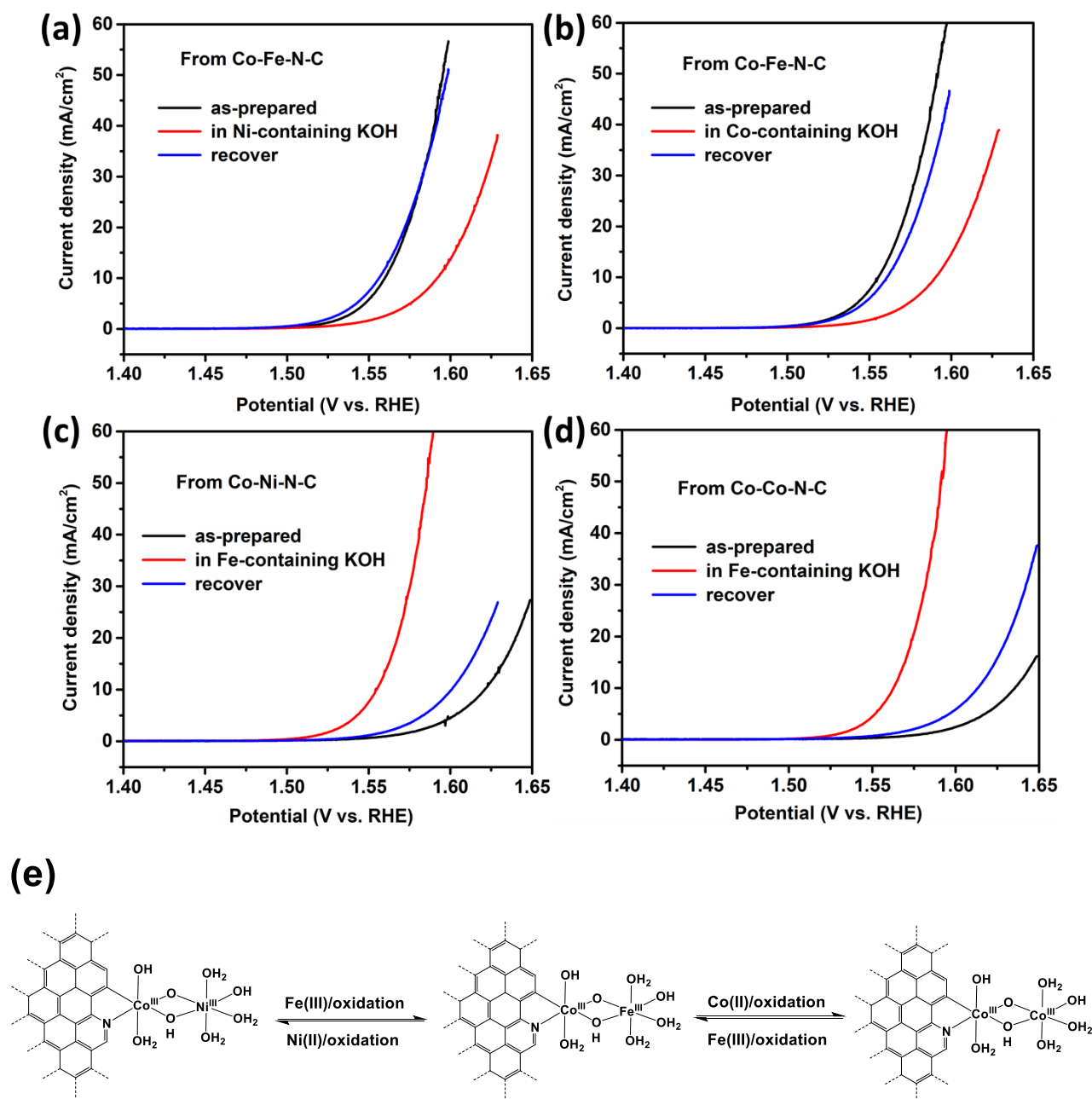


**Figure 3.34** Dynamic formation and interconversion of Co-based double-atoms. The LSVs of as-prepared double-atom catalysts (Co-M-N-C, M represents distal metal) were recorded as black curve. The as-prepared catalysts were first treated with KOH containing another metal impurities (absence of M ions) for 2h, the LSVs were shown as red curves. Then the catalysts were treated with fresh M ions containing KOH (absence of other metal impurities) for 2h, the final LSVs were shown as blue curves. The starting materials and the metal impurities in KOH are (a) Co-Fe-N-C, Ni containing KOH; (b) Co-Fe-N-C, Co containing KOH; (c) Co-Ni-N-C, Fe containing KOH; (d) Co-Co-N-C, Fe containing KOH, respectively. (e) The general scheme of interconversion of Co-based double-atoms.

Taking the double atom units as the active sites, the TOFs of the various DACs can be compared, together with those of the single-atom pre-catalysts (Figure 3.33). The activity has the following order: Co-Fe-N-C > Ni-Fe-N-C > Fe-Co-N-C > Co-Ni-N-C > Fe-Ni-N-C > Co-Co-N-C > Co-N-C > Ni-N-C > Fe-N-C. Furthermore, the TOFs of Co-Fe-N-C and Ni-Fe-N-C are comparable to those of the most active Co-Fe and Ni-Fe oxides (see Table 2.1 in Chapter 2 for details), e.g. being close to or higher than  $1 \text{ s}^{-1}$  at an overpotential of 300 mV. In all cases, adsorption of a second metal led to significantly improved activity compared to the single atom pre-catalysts. It is remarkable that addition of Fe to Co-N-C or Ni-N-C resulting in a nearly 1000-fold increases of the TOFs. Adding Ni or Co to Fe-N-C also generated hundreds of times of increase of the TOFs. A similar promotional effect is known for  $\text{CoFeO}_x$  and  $\text{NiFeO}_x$ ,<sup>30-31</sup> validating the DACs as molecular models of metal oxide OER catalysts. Significantly, the activity of Co-Fe-N-C compared to Fe-Co-N-C, as well as that of Ni-Fe-N-C compared to Fe-Ni-N-C, is very different. The catalysts where Fe is not directly linked to a N-doped carbon support are much more active than the catalysts where Fe is linked to the N-C support. This difference indicates a strong dependence of the activity on the coordination environments of the metal ions.

The DACs can interconverted to each other in certain conditions. Taking Co based double atoms as examples. The OER activity of Co-Fe-N-C significantly degraded in Ni or Co containing but Fe free KOH (Figures 3.34a and 3.34b). After 2h, the activity was close to that of Co-Ni-N-C or Co-Co-N-C. It is interesting that the activity could be recovered when the deactivated catalysts were electrolyzed in a fresh KOH containing Fe. Likewise, the as-prepared Co-Ni-N-C or Co-Co-N-C can be first transformed to Co-Fe-N-C in normal KOH (containing Fe), then recovered the original performance in a newly prepared Fe-free electrolyte (Figures 3.34c and 3.34d). These experiments demonstrated that the adsorbed distal metal ions are only stable when the electrolyte containing certain amount of metal ions impurity. The adsorption and desorption of the distal metal ions is a process of dynamic equilibrium (Figure 3.34e).

### 3.6 Conclusions

Various non-noble metal double-atom electrocatalysts supported on N-doped carbon can be generated from corresponding single-atom pre-catalysts via *in situ* electrochemical activation in KOH containing certain metal ions impurities. Thus, double-atom catalysis is ubiquitous in alkaline OER. This general synthesis provides five analogous bimetallic catalysts containing Co, Fe, or Ni,

in addition to Co-Fe-N-C that was mentioned in Chapter 2. Among them, the Co-Fe-N-C and Ni-Fe-N-C catalysts exhibit TOFs at the higher end of the values reported for known OER catalysts in alkaline medium. The atomic dispersity of these catalysts is confirmed by AC HAADF-STEM and XAS. The *operando* XAS further revealed the evolution of oxidation state and coordination environment of the double-atoms under catalytic conditions. All these DACs have molecule-like bimetallic active sites, connected through oxygen bridge, which resembles the possible key active centers of bimetallic heterogeneous catalysts. Due to the well-defined structure, these DACs are promising models for investigating OER mechanisms of corresponding heterogeneous catalysts in atomic level.

### 3.7 Experimental Section

All the chemicals (including metal salts and organic ligands) were purchased from Sigma-Aldrich unless otherwise noted. The solvents include ultra-pure water (18.2 MΩ/cm), ethanol (Fluka), and isopropanol (Fluka).

#### 3.7.1 Catalyst synthesis

Synthesis of the Ni-N-C pre-catalyst

0.5 mmol Ni(OAc)<sub>2</sub>·4H<sub>2</sub>O (OAc = acetate, 125 mg) was dissolved in 30 mL ethanol. An ethanol solution (20 mL) of 1,10-phenanthroline (Phen, 1.5 mmol, 270 mg) was added dropwise and the reaction mixture was sonicated for 30 min. 4 g of Mg(OH)<sub>2</sub> were then added and the reaction mixture was further sonicated for 30 min. The mixture was then refluxed at 60 °C for 4 h. The ethanol solvent was removed by rotary evaporation and the remaining solids were dried overnight in air and finely ground. The powder was calcinated at 700 °C for 2 h under a nitrogen atmosphere (ramping rate: 2 °C/min). A black solid was obtained. It was stirred in a 1 M HNO<sub>3</sub> solution at room temperature for 3 h to remove the MgO support and residual nickel nanoparticles. The solid was further washed with ultra-pure water until the filtrate became neutral. The solid was dried in air at room temperature overnight.

Synthesis of the Fe-N-C pre-catalyst

A solution of ethanol (30 mL) was degassed by N<sub>2</sub> for 30 mins to remove air. 0.5 mmol anhydrous Fe(OAc)<sub>2</sub> (87 mg, Alfa Aesar) was added the ethanol solution. An ethanol solution (20 mL,

degassed by  $N_2$ ) of 1,10-phenanthroline (Phen, 1.5 mmol, 270 mg) was added dropwise and the reaction mixture was sonicated for 30 min. Then 4 g  $Mg(OH)_2$  were added and the reaction mixture was further sonicated for 30 min. The mixture was then refluxed at 60 °C for 4 h. The ethanol solvent was removed by rotary evaporation. The remaining solids were dried overnight in air and finely ground. The powder was calcinated at 700 °C for 2 h under a nitrogen atmosphere (ramping rate: 2 °C/min). A black solid was obtained. It was stirred in a 1 M  $HNO_3$  solution at room temperature for 3 h to remove the MgO support and residual iron nanoparticles. The solid was further washed with ultra-pure water until the filtrate became neutral. The solid was dried in air at room temperature overnight.

#### Preparation of Ni-containing (Fe-depleted) KOH<sup>31</sup>

The Fe impurities in normal KOH solutions can be removed by treating with high-purity  $Ni(OH)_2$ . In a clean 50 mL polypropylene centrifuge tube, 2 g of  $Ni(NO_3)_2 \cdot 6H_2O$  (99.99%) was dissolved in 5 mL of ultrapure water. 20 mL of 1 M KOH solution was added to give a  $Ni(OH)_2$  precipitate. The suspension was agitated and centrifuged, and the supernatant was decanted. The  $Ni(OH)_2$  precipitate was washed with ultrapure water for three times by centrifugation. The solid was dispersed in 10 mL of 1 M KOH by centrifugation, and the supernatant was decanted. This solid was used as the Fe-absorber. The normal KOH solutions could be cleaned by adding to this  $Ni(OH)_2$ . The cleaning procedure involves dispersing  $Ni(OH)_2$  in the KOH solution, mechanically agitated over-night, followed by at least 3 h of resting.

#### Preparation of Co-containing (Fe-depleted) KOH<sup>30</sup>

In a clean 50 mL polypropylene centrifuge tube, 0.8-0.9 g  $Co(NO_3)_2 \cdot 6H_2O$  (99.99%) were added to a 0.1 M solution of normal KOH (40 mL), and then the reaction mixture was mechanically agitated to give a  $Co(OH)_2$  precipitate. The  $Co(OH)_2$  was washed three times with ultrapure water by centrifugation. It was then washed with 10 mL of 1 M KOH solution. Adding a normal solution of KOH to this  $Co(OH)_2$  yielded a Co-containing but Fe-depleted KOH solution, similar to the Ni-containing but Fe-depleted KOH solution described above.

### 3.7.2 Common Physical Characterizations

Powder XRD measurements were carried out on an X'Pert Philips diffractometer in Bragg-Brentano geometry with monochromatic  $CuK\alpha$  radiation (0.1541 nm) and a fast Si-PIN multi-strip



detector. The step size was 0.02 degree s<sup>-1</sup>. TEM was performed on an FEI Talos-S operated at 200 kV high tension. STEM-EDX mapping was used for elemental characterization, with simultaneously acquired HAADF-STEM images showing atomic number and thickness contrast. For atomic resolution imaging, the measurements were performed on an FEI Titan Themis 60-300 operated at 200 kV with an aberration-corrected electron probe and using HAADF-STEM conditions. Samples for TEM were prepared by drop-drying the samples from their diluted ethanol suspensions onto carbon-coated copper grids. XPS measurements were performed on a PHI5000 VersaProbe II XPS system by Physical Electronics (PHI) with a detection limit of 1 atomic percent. Monochromatic X-rays were generated by an Al K $\alpha$  source (1486.7 eV). The diameter of the analyzed area is 10  $\mu$ m. Raman spectrum was recorded on a LabRAM high resolution Raman spectrometer. The power of laser was set as 0.1% in order to alleviate the damage of carbon matrix caused by stronger laser beam. ICP-AES results were obtained by a Nexlon 350 (Perkin Elmer) machine. Before dissolving in ultra-pure nitric acid (65%, Merck KGaA), all the samples were put in muffle oven and then heated at 600 °C for 12 h in air to remove carbon support and make sure all of the metal ions were exposed to be digested by nitric acid. The *operando* XAS were recorded at SP8 (Japan) 12B2 Taiwan beamline of National Synchrotron Radiation Research Center (NSRRC). The electron storage ring was operated at 8.0 GeV with a constant current of ~100 mA. The *operando* XAS measurement was performed at the desired condition with a special cell designed for these experiments, and the data were collected in fluorescence mode.

### 3.7.3 XAS measurements

#### (1) XAS data collection

The XAS data were collected in the fluorescence mode which were recorded at beamline 01C1 of Taiwan beamline of National Synchrotron Radiation Research Center (NSRRC). The electron storage ring was operated at 3.0 GeV with a constant current of ~400 mA. The data were also collected at SP8 (Japan) 12B2 Taiwan beamline of National Synchrotron Radiation Research Center (NSRRC). The electron storage ring was operated at 8.0 GeV with a constant current of ~100 mA. The incident beam energy was monochromatized using a Si (111) double crystal monochromator. The scan range was kept in an energy range of 7000-7700 eV for Fe K-edge, 7600-8500 eV for Co K-edge, and 8200-9000 eV for Ni K-edge.

Similar as in Chapter 2, the *operando* XAS measurements were performed at the desired condition with a special electrochemical cell (EC) designed for these experiments, and the data were collected in fluorescence mode. During the measurements, the oxygen and hydrogen could be detected with close to 100% FE. Additionally, the activity trend of the catalysts was similar to that in EC for normal OER performance measurements. Thus, our XAS measurements can be considered as '*operando* experiments'.

## (2) XAS data analysis

### XANES analysis in oxidation state

For determining the oxidation states of central metal ions of each sample, several metal oxides and complexes were used as references to extract the standard edge energy of each reference. According to representative studies for determining the edge energy,<sup>35</sup> the edge energy is determined by the energy position located at 50% absorbance of edge-jump. Although the edge energy for nitrogen-coordinated metal ions may be slightly different from those of oxygen-coordinated ones, the change in edge energy caused by nitrogen coordination is relatively small compared to the changes resulted from a change in oxidation states.

An  $E_0$  values of 7112.0, 7709.0 and 8333 eV were used to calibrate all data with respect to the first inflection point of the absorption K-edge of Fe, Co and Ni foil, respectively. The backscattering amplitude and phase shift functions for specific atom pairs were calculated ab initio using the FEFF8 code. X-ray absorption data were analyzed using standard procedures, including pre-edge and post-edge background subtraction, normalization with respect to edge height, Fourier transformation, and nonlinear least-squares curve fitting. The normalized  $k^3$ -weighted EXAFS spectra,  $k^3\chi(k)$ , were Fourier-transformed in a  $k$  range from 1.5 to 11 Å<sup>-1</sup>, to evaluate the contribution of each bond pair to the Fourier transform (FT) peak. The experimental Fourier spectra were obtained by performing an inverse Fourier transformation with a Hanning window function with  $r$  between 0.8–2 Å for first coordinated shell and 1.8–3.1 Å for second coordinated shell. The  $S_0^2$  (amplitude reduction factor) values of the Fe, Co and Ni were fixed at 0.88, to determine the structural parameters of each bond pair. The R-value (%) is the yardstick with which to judge whether a fitting is proper, and is expressed by the following equation:

$$R = \frac{\sum\{k^n \chi_{obs}(k) - k^n \chi_{cal}(k)\}^2}{\sum\{k^n \chi_{obs}(k)\}^2} \quad (\text{Eq. 3.1})$$

### Constrained EXAFS fitting

To fulfill the degree of freedom for achieving a reasonable fitting process, we conducted the fitting for first- and second-shell individually. For constrained fitting of the EXAFS data, according a study of Charnock<sup>36</sup>, we assumed the Debye-Waller factor would be identical in the same coordinated shell. That is, in the first shell fitting, the Debye-Waller factors of M-N, M-O, and M-C paths were constrained to be an identical value, while the coordination number, atomic distance and energy shift were available for fitting. After obtaining the structural parameters of the first-shell, we set all parameters of first-shell according to the fitting results and then conducted the sequentially second-shell fitting with a constrained value of Debye-Waller factor for the M-C paths in the second-shell.

As for the samples in *operando* conditions, in additional to a similar fitting process that we conducted in the dry samples with the construction of Debye-Waller factor, the first- and second-shells are still fitted individually. Because the structural parameters for samples under OER for various durations are likely similar to those of the “activated” samples (after 5 CVs activation), some parameters including the Debye-Waller factor and energy shift for those samples were set to the extracted values from “activated” samples. In other words, we proposed the CNs of M-N and M-C paths in the first-shell and M-C1 and M-C2 paths in the second-shell for samples under OER for various durations are identical to those of “activated” samples, while the CN values for M-O (@ first-shell) and M-M (@second-shell) were available for extracting appropriate values. Slight changes of interatomic distances in M-N and M-C paths of the first-shell and M-C1 and M-C2 paths of the second-shell, oxidation states, and the overall CNs were expected, and these parameters were subject to fitting.

#### 3.7.4 Electrochemical characterization

The catalyst ink was prepared by mixing of 1 mL water, 0.25 mL isopropanol, 0.01 mL 5 wt% Nafion solution and 3 mg catalysts. The ink was sonicated for at least 2 h. Then 40  $\mu$ L of the ink was uniformly loaded onto a carbon cloth electrode (CC, plasma treated, 0.25 cm<sup>2</sup>), respectively. The electrodes were dried in a 75 °C oven for 30 mins before measurements.

The electrochemical measurements were performed in a three-electrode electrochemical cell, in which Pt wire and Ag/AgCl electrode (saturated KCl,  $E(\text{Ag}/\text{AgCl}) = 0.197$  V vs. SHE, standard

hydrogen electrode) were used as counter and reference electrode, respectively. The working electrode and reference electrode were separated with counter electrode by a glass frit. 1M KOH standard solution (Merck KGaA, pH = 13.6) and polypropylene beakers were adapted in order to make our measurements rigorous. All potentials were reported versus the reversible hydrogen electrode (RHE) unless otherwise specified by using the Eq. 3.2. The solution was stirred by a magnetic stirring bar in all of the electrochemical measurements. All of the electrochemical results were compensated with solution resistance. The polarization curves were recorded by the LSV, and the scan rate was 1 mV/s. The activation curves were measured in chronopotential mode with a current density of 2 mA/cm<sup>2</sup> in normal KOH, and 1 mA/cm<sup>2</sup> in Fe-depleting KOH. Applying lower current density is aiming to avoid too high initial overpotential, in which the carbon support is severely oxidized. Five CV scans were carried out before galvanic static activation. The TOFs were calculated by Eq. 3.3, where  $J$  is the anodic current density at certain overpotential,  $A$  is the geometrical surface area of the electrode,  $F$  is the Faraday constant (96485 C/mol), and  $m$  is the loadings of dimeric active sites (see main text for the details).

$$E_{(RHE)} = E_{(Ag/AgCl)} + 0.197 \text{ V} + 0.0592 \times 13.6 \text{ V} \quad (\text{Eq. 3.2})$$

$$TOF = \frac{J \times A}{4 \times F \times m} \quad (\text{Eq. 3.3})$$

The O<sub>2</sub> FE of the catalysts was measured in an H-type electrochemical cell, which is continuously flowed with He gas (flow rate = 12 mL/min) and connected to an online gas chromatograph (GC). The carrier gas of GC is He as well. The working electrode and reference electrode were separated from the counter electrode by an anion exchange membrane. The working electrolyte is KOH containing with a certain amount of metal ion impurities. The double-atom catalysts generated from 3 h of electrochemical activation from the corresponding single-atom precatalysts were used for measurements. For determination of FE, the gas sample in the quantitative loop was gathered and analyzed. Each points were analyzed for at least three times to get the averaged values with the error bars. The FE is calculated as Eq. 3.4, where  $A_m$  is the integrated area of the O<sub>2</sub> peak of measured samples,  $A_s$  is the integrated area of the O<sub>2</sub> peak of the standard samples. A nickel foam electrode activated in KOH with Fe impurities was employed as the standard samples (assuming its FE is 100%) for calibration of integrated O<sub>2</sub> peak area at different current.

$$FE = \frac{A_m}{A_s} \times 100\% \quad (\text{Eq. 3.4})$$

### 3.8 Contributions

L. Bai performed the synthesis, the majority of characterization, and electrochemical tests. C.-S. Hsu performed the *operando* X-ray absorption experiments. D. T. L. Alexander and L. Bai performed the spherical aberration corrected HAADF-STEM measurements. All authors analyzed the data. H. M. Chen and X. Hu directed the research.

The following staffs from EPFL were acknowledged for experimental assistance: Mr. Weiyan Ni (XRD and Raman spectra), Dr. Jun Gu (setup for FE measurements), Dr. Wu Lan and Prof. Jeremy Luterbacher (N<sub>2</sub> physical adsorption), Dr. Pierre Mettraux (XPS), and Dr. Natalia Gasilova (ICP-AES). Dr. Yen-Fa Liao (NSRRC) is acknowledged for help with *operando* XAS.

### 3.9 References of Chapter 3

1. Bai, L.; Hsu, C.-S.; Alexander, D.; Chen, H. M.; Hu, X., Double-atom catalysts provide a molecular platform for oxygen evolution. *ChemRxiv, preprint* **2019**. <https://doi.org/10.26434/chemrxiv.11341961.v1>
2. Suen, N. T.; Hung, S. F.; Quan, Q.; Zhang, N.; Xu, Y. J.; Chen, H. M., Electrocatalysis for the oxygen evolution reaction: recent development and future perspectives. *Chem. Soc. Rev.* **2017**, *46*, 337-365.
3. Song, F.; Bai, L.; Moysiadou, A.; Lee, S.; Hu, C.; Liardet, L.; Hu, X., Transition Metal Oxides as Electrocatalysts for the Oxygen Evolution Reaction in Alkaline Solutions: An Application-Inspired Renaissance. *J. Am. Chem. Soc.* **2018**, *140*, 7748-7759.
4. Dau, H.; Limberg, C.; Reier, T.; Risch, M.; Roggan, S.; Strasser, P., The Mechanism of Water Oxidation: From Electrolysis via Homogeneous to Biological Catalysis. *ChemCatChem* **2010**, *2*, 724-761.
5. Hunter, B. M.; Gray, H. B.; Muller, A. M., Earth-Abundant Heterogeneous Water Oxidation Catalysts. *Chem. Rev.* **2016**, *116*, 14120-14136.
6. Han, L.; Dong, S.; Wang, E., Transition-Metal (Co, Ni, and Fe)-Based Electrocatalysts for the Water Oxidation Reaction. *Adv. Mater.* **2016**, *28*, 9266-9291.
7. Dionigi, F.; Strasser, P., NiFe-Based (Oxy)hydroxide Catalysts for Oxygen Evolution Reaction in Non-Acidic Electrolytes. *Adv. Energy Mater.* **2016**, *6*, 1600621.
8. Zhu, K.; Zhu, X.; Yang, W., Application of In Situ Techniques for the Characterization of NiFe-Based Oxygen Evolution Reaction (OER) Electrocatalysts. *Angew. Chem. Int. Ed.* **2019**, *58*, 1252-1265.
9. Hu, C.; Zhang, L.; Gong, J., Recent progress made in the mechanism comprehension and design of electrocatalysts for alkaline water splitting. *Energy Environ. Sci.* **2019**, *12*, 2620-2645.

10. Bayatsarmadi, B.; Zheng, Y.; Vasileff, A.; Qiao, S. Z., Recent Advances in Atomic Metal Doping of Carbon-based Nanomaterials for Energy Conversion. *Small* **2017**, *13*, 1700191.
11. Zhu, C.; Fu, S.; Shi, Q.; Du, D.; Lin, Y., Single-Atom Electrocatalysts. *Angew. Chem. Int. Ed.* **2017**, *56*, 13944-13960.
12. Sultan, S.; Tiwari, J. N.; Singh, A. N.; Zhumagali, S.; Ha, M.; Myung, C. W.; Thangavel, P.; Kim, K. S., Single Atoms and Clusters Based Nanomaterials for Hydrogen Evolution, Oxygen Evolution Reactions, and Full Water Splitting. *Adv. Energy Mater.* **2019**, *9*, 1900624.
13. Chen, Y.; Ji, S.; Chen, C.; Peng, Q.; Wang, D.; Li, Y., Single-Atom Catalysts: Synthetic Strategies and Electrochemical Applications. *Joule* **2018**, *2*, 1242-1264.
14. Zhao, D.; Zhuang, Z.; Cao, X.; Zhang, C.; Peng, Q.; Chen, C.; Li, Y., Atomic site electrocatalysts for water splitting, oxygen reduction and selective oxidation. *Chem. Soc. Rev.* **2020**, *49*, 2215-2264.
15. Li, Q.; Chen, W.; Xiao, H.; Gong, Y.; Li, Z.; Zheng, L.; Zheng, X.; Yan, W.; Cheong, W. C.; Shen, R.; Fu, N.; Gu, L.; Zhuang, Z.; Chen, C.; Wang, D.; Peng, Q.; Li, J.; Li, Y., Fe Isolated Single Atoms on S, N Codoped Carbon by Copolymer Pyrolysis Strategy for Highly Efficient Oxygen Reduction Reaction. *Adv. Mater.* **2018**, *30*, e1800588.
16. Ren, W.; Tan, X.; Yang, W.; Jia, C.; Xu, S.; Wang, K.; Smith, S. C.; Zhao, C., Isolated Diatomic Ni-Fe Metal-Nitrogen Sites for Synergistic Electroreduction of CO<sub>2</sub>. *Angew. Chem. Int. Ed.* **2019**, *58*, 6972-6976.
17. Hou, Y.; Qiu, M.; Kim, M. G.; Liu, P.; Nam, G.; Zhang, T.; Zhuang, X.; Yang, B.; Cho, J.; Chen, M.; Yuan, C.; Lei, L.; Feng, X., Atomically dispersed nickel-nitrogen-sulfur species anchored on porous carbon nanosheets for efficient water oxidation. *Nat. Commun.* **2019**, *10*, 1392.
18. Liu, W.; Zhang, L.; Yan, W.; Liu, X.; Yang, X.; Miao, S.; Wang, W.; Wang, A.; Zhang, T., Single-atom dispersed Co-N-C catalyst: structure identification and performance for hydrogenative coupling of nitroarenes. *Chem. Sci.* **2016**, *7*, 5758-5764.
19. Cychosz, K. A.; Guillet-Nicolas, R.; Garcia-Martinez, J.; Thommes, M., Recent advances in the textural characterization of hierarchically structured nanoporous materials. *Chem. Soc. Rev.* **2017**, *46*, 389-414.
20. Jiang, K.; Siahrostami, S.; Zheng, T.; Hu, Y.; Hwang, S.; Stavitski, E.; Peng, Y.; Dynes, J.; Gangisetty, M.; Su, D.; Attenkofer, K.; Wang, H., Isolated Ni single atoms in graphene nanosheets for high-performance CO<sub>2</sub> reduction. *Energy Environ. Sci.* **2018**, *11*, 893-903.
21. Liu, W.; Chen, Y.; Qi, H.; Zhang, L.; Yan, W.; Liu, X.; Yang, X.; Miao, S.; Wang, W.; Liu, C.; Wang, A.; Li, J.; Zhang, T., A Durable Nickel Single-Atom Catalyst for Hydrogenation Reactions and Cellulose Valorization under Harsh Conditions. *Angew. Chem. Int. Ed.* **2018**, *57*, 7071-7075.
22. Gu, J.; Hsu, C.-S.; Bai, L.; Chen, H. M.; Hu, X., Atomically dispersed Fe<sup>3+</sup> sites catalyze efficient CO<sub>2</sub> electroreduction to CO. *Science* **2019**, *364*, 1091-1094.
23. Tan, B. J.; Klabunde, K. J.; Sherwood, P. M., X-ray photoelectron spectroscopy studies of solvated metal atom dispersed catalysts. Monometallic iron and bimetallic iron-cobalt particles on alumina. *Chem. Mater.* **1990**, *2*, 186-191.

24. Ju, W.; Bagger, A.; Hao, G. P.; Varela, A. S.; Sinev, I.; Bon, V.; Roldan Cuenya, B.; Kaskel, S.; Rossmeisl, J.; Strasser, P., Understanding activity and selectivity of metal-nitrogen-doped carbon catalysts for electrochemical reduction of CO<sub>2</sub>. *Nat. Commun.* **2017**, *8*, 944.
25. Yang, H. B.; Hung, S.-F.; Liu, S.; Yuan, K.; Miao, S.; Zhang, L.; Huang, X.; Wang, H.-Y.; Cai, W.; Chen, R.; Gao, J.; Yang, X.; Chen, W.; Huang, Y.; Chen, H. M.; Li, C. M.; Zhang, T.; Liu, B., Atomically dispersed Ni(i) as the active site for electrochemical CO<sub>2</sub> reduction. *Nat. Energy* **2018**, *3*, 140-147.
26. Fei, H.; Dong, J.; Arellano-Jimenez, M. J.; Ye, G.; Dong Kim, N.; Samuel, E. L.; Peng, Z.; Zhu, Z.; Qin, F.; Bao, J.; Yacaman, M. J.; Ajayan, P. M.; Chen, D.; Tour, J. M., Atomic cobalt on nitrogen-doped graphene for hydrogen generation. *Nat. Commun.* **2015**, *6*, 8668.
27. Wang, G.; Wang, H.; Lu, X.; Ling, Y.; Yu, M.; Zhai, T.; Tong, Y.; Li, Y., Solid-state supercapacitor based on activated carbon cloths exhibits excellent rate capability. *Adv. Mater.* **2014**, *26*, 2676-2682.
28. Lu, X.; Yim, W. L.; Suryanto, B. H.; Zhao, C., Electrocatalytic oxygen evolution at surface-oxidized multiwall carbon nanotubes. *J. Am. Chem. Soc.* **2015**, *137*, 2901-2907.
29. Tian, Z.; Wang, C.; Yue, J.; Zhang, X.; Ma, L., Effect of a potassium promoter on the Fischer–Tropsch synthesis of light olefins over iron carbide catalysts encapsulated in graphene-like carbon. *Catal. Sci. Tech.* **2019**, *9*, 2728-2741.
30. Burke, M. S.; Kast, M. G.; Trotochaud, L.; Smith, A. M.; Boettcher, S. W., Cobalt-iron (oxy)hydroxide oxygen evolution electrocatalysts: the role of structure and composition on activity, stability, and mechanism. *J. Am. Chem. Soc.* **2015**, *137*, 3638-3648.
31. Trotochaud, L.; Young, S. L.; Ranney, J. K.; Boettcher, S. W., Nickel-iron oxyhydroxide oxygen-evolution electrocatalysts: the role of intentional and incidental iron incorporation. *J. Am. Chem. Soc.* **2014**, *136*, 6744-6753.
32. Friebel, D.; Louie, M. W.; Bajdich, M.; Sanwald, K. E.; Cai, Y.; Wise, A. M.; Cheng, M. J.; Sokaras, D.; Weng, T. C.; Alonso-Mori, R.; Davis, R. C.; Bargar, J. R.; Nørskov, J. K.; Nilsson, A.; Bell, A. T., Identification of highly active Fe sites in (Ni,Fe)OOH for electrocatalytic water splitting. *J. Am. Chem. Soc.* **2015**, *137*, 1305-1313.
33. Smith, R. D. L.; Pasquini, C.; Loos, S.; Chernev, P.; Klingan, K.; Kubella, P.; Mohammadi, M. R.; González-Flores, D.; Dau, H., Geometric distortions in nickel (oxy)hydroxide electrocatalysts by redox inactive iron ions. *Energy Environ. Sci.* **2018**, *11*, 2476-2485.
34. Carta, D.; Loche, D.; Mountjoy, G.; Navarra, G.; Corrias, A., NiFe<sub>2</sub>O<sub>4</sub> nanoparticles dispersed in an aerogel silica matrix: an X-ray absorption study. *J. Phys. Chem. C* **2008**, *112*, 15623-15630.
35. Miyazato, I.; Takahashi, L.; Takahashi, K., Automatic oxidation threshold recognition of XAFS data using supervised machine learning. *Mol. Syst. Des. Eng.* **2019**, *4*, 1014-1018.
36. Charnock, J., Biological applications of EXAFS spectroscopy. *Radiat. Phys. Chem.* **1995**, *45*, 385-391.

# Chapter 4 Double-Atom Catalysts Provide a Molecular Platform for Heterogeneous Oxygen Evolution Electrocatalysis

The results presented in this chapter were partly reformatted from a published preprint<sup>1</sup>:

**L. Bai**, C. S. Hsu, D. T. L. Alexander, H. M. Chen, X. Hu: Double-Atom Catalysts Provide a Molecular Platform for Oxygen Evolution. ChemRxiv. Preprint (2019). Link:

<https://doi.org/10.26434/chemrxiv.11341961.v1>



## 4.1 Introduction

Understanding the reaction mechanism is crucial to get deep insight of the catalysts and catalytic processes. From the investigation, we will know the information like key reaction intermediates, rate-determining step (RDS), the properties of transfer of protons/hydroxyl ions and electrons.<sup>2-4</sup> The essential points, like which kinds of active sites, key intermediates and reaction processes are beneficial to high catalytic activity, will be understood.<sup>2-5</sup> Such information can also help to guide and improve the theoretical calculation, and ultimately provide the guidelines for further development of more advanced catalysts.

Previously, most of mechanistic understandings of electrocatalytic reactions, like OER (oxygen evolution reaction), were based on spectroscopic evidences and computational methods.<sup>2-6</sup> For examples, the mechanisms of OER catalyzed by Co-, Ni-, Fe-based oxides have been studied by various spectroscopic methods and density functional theory (DFT) calculations.<sup>2,5,6</sup> Since the real experimental condition can be quite different from assumed idealized situation in theoretical calculation, the proposed reaction mechanism and estimated energy barrier from DFT calculation remains high uncertainty. As mentioned in Section 1.4.2, Chapter 1, eletrokinetic analysis can provide essential information including RDS, the properties of protons/hydroxyl ions and electrons transfer and so on.<sup>7-9</sup> By combining with *in-situ/operando* spectroscopy, we are able to understand how the key intermediates are generated and converted to the final products. For instances, Nocera et al. did electrokinetic studies for electrodeposited Co, Ni, and Mn OER catalysts.<sup>10-12</sup> By combining with their earlier spectroscopic results, the detailed reaction mechanisms were proposed. Very recently, Hu and coworkers combined *in situ* X-ray absorption spectroscopy (XAS), *in situ* Raman, and electrokinetic analysis to study the OER mechanism of CoOOH in alkaline condition.<sup>13</sup> They discovered that the dominating resting state of the catalyst is Co(IV)O<sub>2</sub>, while Co superoxide species is an active intermediate, which is concurrently formed during the oxidation of CoOOH to CoO<sub>2</sub>. Different from conventional O-O bond formation via OH<sup>-</sup> attack to metal-oxo (M=O) center, the RDS of the catalyst is releasing of dioxygen from the superoxide intermediate.

Moreover, despite many efforts for investigating active sites and reaction mechanisms of heterogeneous OER catalysts, their heterogeneous nature makes it difficult to deduce conclusive mechanistic information.<sup>4-6</sup> This difficulty is more obvious for bimetallic OER catalysts, as manifested in the many research discrepancies with respect to the active sites, the oxidation

states, and the reaction pathways.<sup>4,6</sup> Development of OER catalysts with well-defined structure, such as atomically dispersed catalysts, is highly indispensable.

From Chapter 2 and Chapter 3, we have already known that double-atom catalysis is ubiquitous in alkaline OER. Six non-noble metal double-atom catalysts (DACs) could be prepared by *in situ* electrochemical activation of Co, Fe, Ni-based single-atom precatalysts in KOH containing certain metal ions impurities. These DACs have well-defined bimetallic coordination structures, which are resembles the possible key active motifs of various bimetallic oxides/oxyhydroxides. The molecular nature of the active sites and the dynamic stability of the DACs makes them attractive platforms to study the mechanism of OER in atomic level.

Actually, the DACs are quite suitable candidates for investigating reaction mechanisms via electrokinetic analysis. For the catalysts mentioned in Chapter 2 and Chapter 3, although both double-atom and single-atom units co-exist in the activated catalysts, the double-atom units exhibit significantly higher intrinsic activity, so they dominate the apparent activity and its kinetic behavior. Additionally, the double-atom sites are fully exposed to electrolyte, the loadings of which are also not high. Thus, the barrier of charge transfer and the overlapping diffusion region can be minimized.<sup>14</sup>

Pursuant to the aim of using the DACs to identify reaction mechanisms, this Chapter will apply a classical quasi-Langmuir model for the electrokinetic analysis (see the following sections for details).<sup>9,10,15</sup> The in-depth electrokinetic investigations of these catalysts revealed a generally uniform bimetallic catalytic cycle, yet having certain characteristics that depend significantly on the nature of the metal ions. The obtained mechanistic information may reflect the real catalytic mechanisms of the corresponding heterogeneous OER catalysts, highlighting the role of DACs as a molecular model to get atomic insight of the heterogeneous OER catalysis. While some of the catalytic cycles are also similar to those of some reported homogeneous bimetallic complexes, the double-atom OER catalysts are able to bridge the homogeneous and heterogeneous OER catalysis.

## 4.2 Methods for electrokinetic analysis

The mechanism of OER in the Tafel region can be described by a quasi-Langmuir model.<sup>9,10,15</sup> In this model, the surface concentration of key intermediate (resting state) is less than 10%, which

fits the general condition of Langmuir isotherm adsorption. This assumption is reasonable when the applied potential is moderate (e.g. in the Tafel region). Generally, the key process of OER involves a pre-equilibrium (quasi-equilibrium) step (PES) and an RDS. In alkaline condition, the key steps were depicted as Figure 4.1. The PES can either be a single electrochemical step (in most case  $n_2 = 1$ ) or combined consecutive electrochemical steps ( $n_2 > 1$ ). For the RDS, the transferred electrons  $n_4$  can be either 1 (single electron transfer step) or 0 (pure chemical step). The overall rate of the OER is related to these two steps, while the processes after RDS will not restrict the final reaction rate.<sup>16</sup>

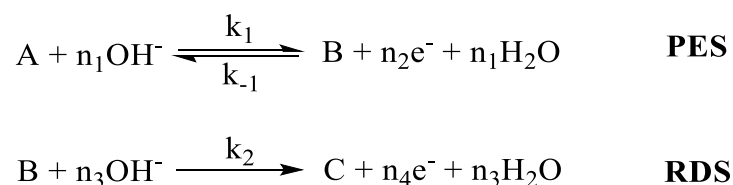


**Figure 4.1** General key process in alkaline OER, describing by quasi-Langmuir model.

Some of the previous study suggested that all of the steps (if have) before RDS were considered as PES.<sup>7,9,15,16</sup> Such assumption is not accurate if the initial step(s) are relatively fast or the adsorption of certain intermediates are saturated. For examples, for some OER catalysts in alkaline condition, the adsorption of  $OH^-$  to form  $M-OH$  is usually fast and nearly completed before OER onset (Figure 4.2).<sup>8</sup> Similar precatalytic processes were also observed for homogeneous OER catalysts.<sup>17,18</sup> In those cases, the behavior of the steps before the OER onset can be described by Nernst equation (Eq. 4.1). Here,  $x$  is the number of protons (hydroxyl ions) being transferred while  $y$  is the number of electrons being transferred at the same time.

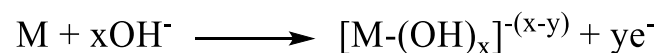


**Figure 4.2** General process of adsorption of  $OH^-$ . M represent the general metal centers.

$$E = E_0 - \frac{RT}{yF} \ln \left( \frac{[M][OH^-]^x}{[M-(OH)_x]} \right) \quad (4.1)$$

The ratio of  $[M]/[M-(OH)_x]$  is a constant value in certain potential. Therefore, Eq. 4.1 can be rearranged as:

$$E = E'_0 - \frac{2.303RTx}{Fy} \lg([OH^-]) \quad (4.2)$$

The ratio of  $x/y$  can be determined by the slope of potential -  $\log [OH^-]$  curves.

For the model presented in Figure 4.1,  $k_1$  and  $k_{-1}$  are the rate constants of the forward and reverse reaction of PES, respectively.  $k_2$  is rate constants of RDS. The steady-state velocity of oxygen evolution can be expressed as follows by using Butler-Volmer equation (the details of applying Butler-Volmer equation to elementary steps of multiple electron transfer electrochemical reactions were described in Appendix 1 of this Thesis):

$$v = k_2 \theta_B a_{OH^-}^{n_3} \exp\left(\frac{n_2 \alpha_2 \eta_2 F}{RT}\right) \quad (4.3)$$

$\alpha_2$  is the transfer coefficient of RDS,  $\eta_2$  is the overpotential relative to equilibrium potential of RDS (noted that it is not equal to apparent overpotential relative to OER equilibrium potential),  $F$  is the Faraday constant,  $R$  is the universal gas constant,  $T$  is the thermodynamic temperature.  $\theta_B$  represents the partial surface coverage of intermediate  $B$ .  $\theta_B$  can be defined in terms of the surface coverage of the resting state  $A$  ( $\theta_A$ ). The relationship between  $\theta_B$  and  $\theta_A$  can be deduced from the equilibrium equation:

$$v_a = k_1 \theta_A a_{OH^-}^{n_1} \exp\left(\frac{n_2 \alpha_1 \eta_1 F}{RT}\right) \quad (4.4)$$

$$v_{-a} = k_{-1} \theta_B \exp\left(-\frac{n_2 (1-\alpha_1) \eta_1 F}{RT}\right) \quad (4.5)$$

$v_a$  and  $v_{-a}$  are the reaction rate of the forward and reverse reaction of PES, respectively. For the quasi-equilibrium condition:

$$v_a = v_{-a} \quad (4.6)$$

$\eta_1$  is the overpotential relative to equilibrium potential of PES. Since both  $\eta_1$  and  $\eta_2$  are hard to determine, we use applied potential  $E$  and standard rate constants (denoted with superscript 0, the detailed derivation of the equations is referred to Appendix 1) to rearrange the above equations. Then we have:

$$\theta_B = K_1^0 \theta_A a_{OH^-}^{n_1} \exp\left(\frac{n_2 EF}{RT}\right) \quad (4.7)$$

$$K_1^0 = \frac{k_1^0}{k_{-1}^0}. \quad (4.8)$$

$$v = k_2^0 \theta_B a_{OH^-}^{n_3} \exp\left(\frac{n_4 \alpha_2 EF}{RT}\right) \quad (4.9)$$

Substituting the expression of  $\theta_B$  (Eq. 4.7) for Eq. 4.9, the steady-state velocity of OER can be expressed as:

$$v = k_2^0 K_1^0 \theta_A a_{OH^-}^{n_1+n_3} \exp\left(\frac{(n_2+n_4 \alpha_2)EF}{RT}\right) \quad (4.10)$$

If Langmuir conditions are assumed, the surface coverage of A ( $\theta_A$ ) would not be expected to change appreciably over the potential range, and may be considered a potential-independent constant. The catalytic current density ( $j$ ) of OER is:

$$j = 4Fv = k^0 a_{OH^-}^{n_1+n_3} \exp\left(\frac{(n_2+n_4 \alpha_2)EF}{RT}\right) \quad (4.11)$$

$$k^0 = 4Fk_2^0 K_1^0 \theta_A \quad (4.12)$$

The Tafel slope,  $\left(\frac{\partial E}{\partial \log j}\right)_{pH}$  or  $\left(\frac{\partial \eta}{\partial \log j}\right)_{pH}$ , of OER can be expressed as:

$$\left(\frac{\partial E}{\partial \log j}\right)_{pH} = \left(\frac{\partial \eta}{\partial \log j}\right)_{pH} = \frac{2.303RT}{(n_2+n_4 \alpha_2)F} \quad (4.13)$$

According to Marcus theory, the transfer coefficient  $\alpha$  is related to the activation driving force  $\Delta G$  and the reorganization energy  $\lambda$  (Eq. 4.14).<sup>16</sup>

$$\alpha = \frac{1}{2} \times \left(1 + \frac{\Delta G}{\lambda}\right) \quad (4.14)$$

The activation driving force is related to the overpotential. When the overpotential is not high, the driving force is much smaller than the reorganization energy. Ideally the transfer coefficient is 0.5 in this case, when the diffuse double layer effects were eliminated (a concentrations of electrolyte bigger than 0.5 M is sufficient to eliminate diffuse double layer effects).

Another factor that influences the transfer coefficient is the charge transfer barrier across the catalyst film. Typically, only a fraction,  $x$  ( $0 < x < 1$ ), of the applied potential  $E$  between electrode and electrolyte is effective for interfacial electron transfer, while the other part is required to overcome the electronic resistance across the film.<sup>9,19,20</sup> Therefore, the actual applied potential is  $xE$ . Eq. 4.11 is modified as:

$$j = k^0 a_{OH^-}^{n_1+n_3} \exp\left(\frac{(n_2+n_4 \alpha_2)xEF}{RT}\right) \quad (4.15)$$

The Tafel slope is now diverted as:

$$\left(\frac{\partial E}{\partial \log j}\right)_{pH} = \left(\frac{\partial \eta}{\partial \log j}\right)_{pH} = \frac{2.303RT}{(n_2+n_4\alpha_2)xF} \quad (4.16)$$

Thus the Tafel slope is increasing if there are significant charge transfer barrier across the catalyst films.

For atomically dispersed catalysts (DACs in this Thesis), nearly all of the active sites are highly exposed. The supporting N-doped carbon layer also possesses outstanding conductivity. Therefore, the charge transfer barrier across the catalyst film can be minimized. The transfer coefficient of RDS can be considered as close to 0.5. The explicit transfer coefficient value is also an advantage to unambiguously study the electrokinetics of DACs.

To study the order dependence of proton concentration ( $[H^+]$ ) or hydroxyl ions concentration ( $[OH^-]$ ) on the reaction rate, according to Eq. 4.11, in principle we can directly measure current density at a certain potential  $E$  (relative to Standard Hydrogen Electrode, SHE, the standard condition) with changing the  $[OH^-]$ . However, the current density may not locate in Tafel region, making the determination inaccurate. Typically, we first measure the variation of the potential with changing  $[OH^-]$  at a constant current density (in Tafel region). Then the order of  $[OH^-]$  can be determined by Eq. 4.17.

$$\left(\frac{\partial \log j}{\partial \log [OH^-]}\right)_E = -\frac{\left(\frac{\partial E}{\partial \log [OH^-]}\right)_j}{\left(\frac{\partial E}{\partial \log j}\right)_{pH}} \quad (4.17)$$

The relationship is also correct when the  $E$  is substituted by  $\eta$  (Eq. 4.18), the  $\left(\frac{\partial \log j}{\partial \log [OH^-]}\right)_\eta$  is pH-dependence degree in Reversible Hydrogen Electrode (RHE) scale:

$$\left(\frac{\partial \log j}{\partial \log [OH^-]}\right)_\eta = -\frac{\left(\frac{\partial \eta}{\partial \log [OH^-]}\right)_j}{\left(\frac{\partial \eta}{\partial \log j}\right)_{pH}} \quad (4.18)$$

The equation can be rearranged as below:

$$\left(\frac{\partial \log j}{\partial \log [OH^-]}\right)_\eta = -\frac{-\left(\frac{\partial E_{eq}}{\partial \log [OH^-]}\right)_j + \left(\frac{\partial E}{\partial \log [OH^-]}\right)_j}{\left(\frac{\partial E}{\partial \log j}\right)_{pH}} \quad (4.19)$$

Since  $Tafel\ slope = \left(\frac{\partial \eta}{\partial \log j}\right)_{pH} = \left(\frac{\partial E}{\partial \log j}\right)_{pH}$ , and the equilibrium potential of OER changed as -59 mV/dec with  $[OH^-]$  (-59 mV/pH). Thus, we have:

$$\left(\frac{\partial \log j}{\partial \log [\text{OH}^-]}\right)_\eta = -\frac{59 \text{ mV/dec} + \left(\frac{\partial E}{\partial \log [\text{OH}^-]}\right)_j}{\left(\frac{\partial E}{\partial \log j}\right)_{pH}} \quad (4.20)$$

And finally we found that the relationship between pH-dependence degree and the order of  $[\text{OH}^-]/[\text{H}^+]$  is depicted as Eq. 4.21. The pH-dependence degree is actually a function of  $[\text{OH}^-]$  and Tafel slope.

$$\left(\frac{\partial \log j}{\partial \log [\text{OH}^-]}\right)_\eta = \left(\frac{\partial \log j}{\partial \log [\text{OH}^-]}\right)_E - \frac{59 \text{ mV/dec}}{\left(\frac{\partial E}{\partial \log j}\right)_{pH}} \quad (4.21)$$

It should be noted that in some of previous studies, researchers judged whether the protons and electrons are coupled or decoupled by examining the pH-dependence degree.<sup>21-23</sup> They suggested if  $\left(\frac{\partial \log j}{\partial \log [\text{OH}^-]}\right)_\eta$  is equal to zero, the OER should proceed via proton coupled electron transfer (PCET) process, vice versa. Since this parameter depends on both reaction order of  $[\text{OH}^-]$  and Tafel slope, a non-zero value does not necessary mean decoupled  $\text{H}^+/\text{OH}^-$  transfer with electrons, at least for the OER catalysts whose catalytic behavior can be described by quasi-Langmuir model.

In the following content, the electrokinetics of various DACs mentioned in Chapter 2 and Chapter 3 will be systematically studied and compared by using this modified quasi-Langmuir model. The results will also be combined with *in-situ/operando* XAS data (from Chapter 2 and Chapter 3) to determine the involved key intermediates, as well as how the intermediates are generated and the destiny of these intermediates. The combined study will finally provide detailed information of reaction mechanisms of each double-atom OER catalysts.

## 4.3 Electrokinetic analysis and reaction mechanisms of double-atom catalysts

### 4.3.1 Electrokinetic analysis and reaction mechanisms of Co-based double atoms

#### (1) Co-Fe-N-C

First considering Co-Fe-N-C that was mentioned in Chapter 2, the Tafel slope of this catalyst was close to 40 mV/dec (Figures 4.3a and 4.3b). The values kept nearly unchanged in KOH with concentration from 0.5 M to 2 M. According to Eq. 4.11 and Eq. 4.13, this Tafel slope corresponds to a reaction that has a PES involving one-electron transfer, followed by a RDS that also involves

a one-electron transfer, if the transfer coefficient of RDS is 0.5 ( $n_2 = n_4 = 1$ , the theoretical Tafel slope is  $2.303RT/1.5F = 40$  mV/dec). The details of associating observed Tafel slope values to certain reaction processes are provided in Appendix 1 of this Thesis (the same for following contents). To probe the involvement of hydroxyl ions in these two steps, we measured the catalytic activity at different concentrations of  $\text{OH}^-$  (Figure 4.3a-b). When the potential at 1 mA/cm<sup>2</sup> (vs. Ag/AgCl or SHE) was plotted against the logarithm of  $[\text{OH}^-]$ , a slope of about -80 mV/dec was obtained (Figure 4.3c). According to Eq. 4.17,<sup>10</sup> the current density has a second order dependence on the concentration of  $\text{OH}^-$  (Table 4.1). Thus, the PES and RDS involve the transfer of two hydroxyl ions in total (Table 4.1). The overall rate of the reaction is:

$$v_{\text{Co-Fe}} = k_{\text{Co-Fe}}^0 a_{\text{OH}^-}^2 \exp\left(\frac{3EF}{2RT}\right) \quad (4.22)$$

The redox potentials of Co(II)/Co(III) in Co-Fe-N-C were measured at different  $\text{OH}^-$  concentrations (Figures 4.3d and 4.3e). The potentials shifted by about -69 mV per unit of log  $[\text{OH}^-]$ , close to a Nernstian behavior (Figure 4.3f). This result suggests that the Co(II) to Co(III) transformation is accompanied by one  $\text{OH}^-$  transfer (Table 4.1).

Combining the electrokinetic data and *operando* XAS results, a plausible reaction mechanism was proposed for Co-Fe-N-C (Figure 4.4). Beyond the OER onset potential, the Co(II) is oxidized to Co(III), with a concurrent one proton loss from one of the aqua ligands ( $\text{S}_0 \rightarrow \text{S}_1$ ). According to Figure 2.10 in Chapter 2, the freshly activated sample entered the catalytic cycle at this stage ( $\text{S}_1$ ). The next step is the oxidation of an M(III)-OH to M(IV)=O, where the M can be either Co or Fe. According to electrokinetics, this is the PES. Both Co(IV)=O and Fe(IV)=O have been previously proposed as intermediates for OER catalyzed by Co-Fe oxyhydroxides.<sup>24-27</sup> The assignment of either intermediate was based on the change of oxidation states of either metal from XAS data. Following this procedure and considering the significant oxidation of Co(III) during OER revealed by XAS data (Figure 2.10 in Chapter 2), we tentatively assign Co as the site of oxo formation ( $\text{S}_2$ ). It should be noted that spectroscopic evidences for Co(IV)=O are known for Co oxides<sup>24,28-31</sup> and molecular Co complexes.<sup>32-34</sup> The RDS is the hydroxide attack on the Co(IV)=O to give Co(III)-OOH ( $\text{S}_3$ ). While the combination of two M(IV)=O to form a peroxo dimer was proposed for a spinel Co oxide<sup>35</sup> and some molecular dinuclear Co complexes<sup>32,34</sup>, this pathway is ruled out because it would give a different Tafel slope (30 mV/dec) than the observed value. Another PCET gives Co(III)-OO $\cdot$  ( $\text{S}_4$ ), which releases  $\text{O}_2$  and regenerates the Co(II)-Fe(III) upon internal electron transfer from the superoxo group ( $\text{S}_0$ ).



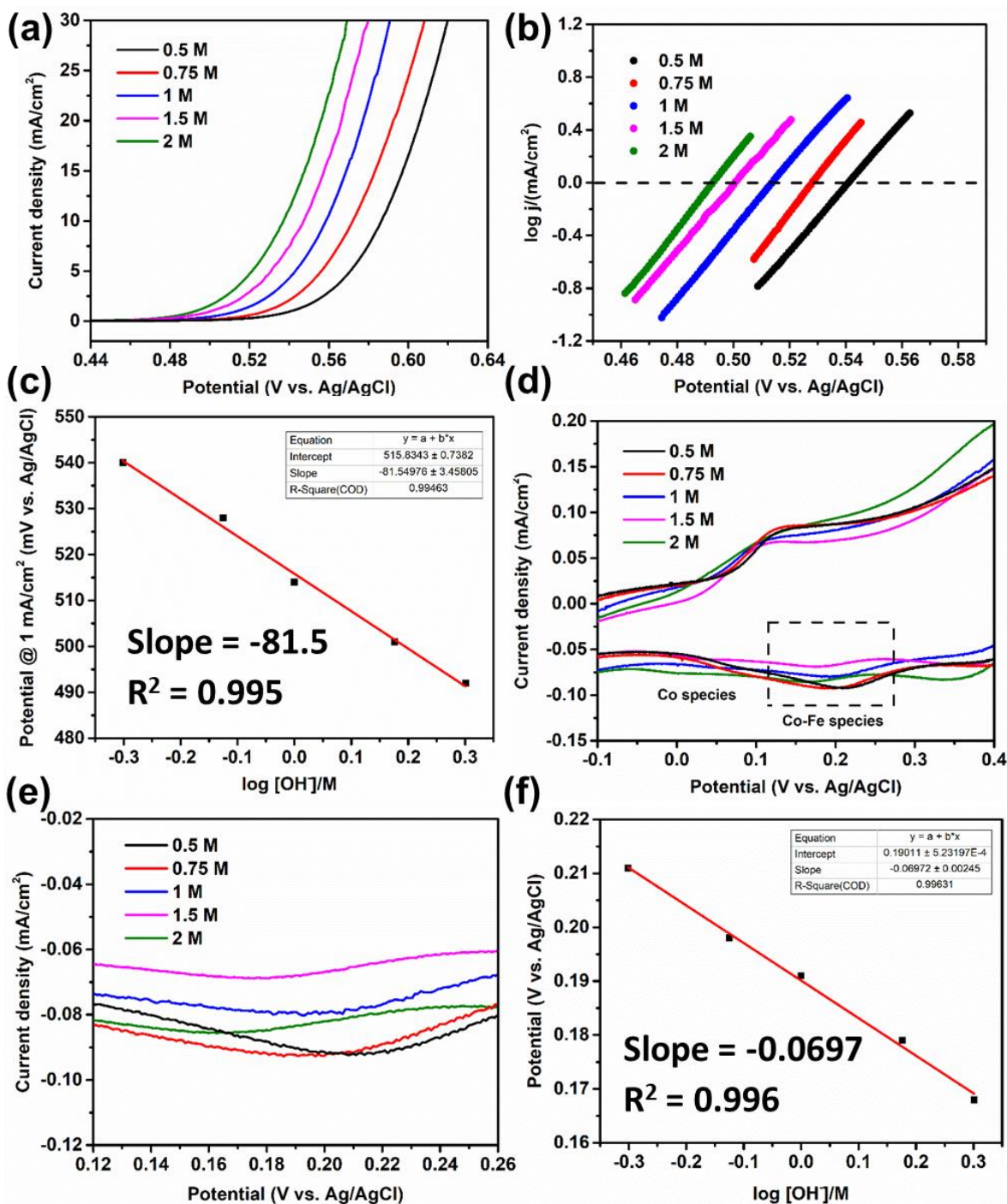


**Figure 4.3 Kinetic study of Co-Fe-N-C.** (a) Linear scan voltammetry curves (LSVs) and (b) the corresponding Tafel plots of Co-Fe-N-C in KOH with different concentrations. Commercial KOH that contains Fe impurities was used to prepare the electrolyte. (c) Plots of the overpotential at 1 mA/cm<sup>2</sup> against to the logarithm of the concentrations of OH<sup>-</sup>. (d) The cyclic voltammetry scans (CVs) of Co-Fe-N-C in the region of Co(II)/Co(III) transformation and (e) the enlarged graph of the square with dashed line in (d), (f) correlation of the redox potential to the logarithm of the concentration of OH<sup>-</sup> by a linear fitting.

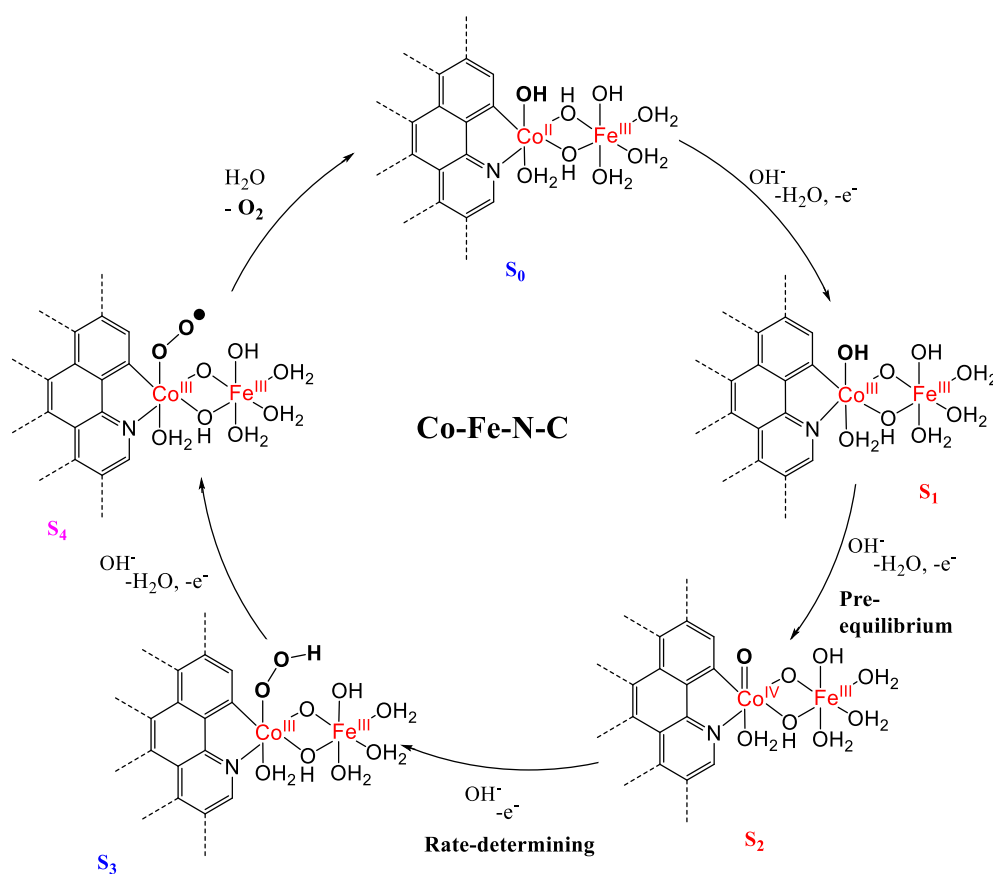


**Figure 4.4** Possible OER mechanisms of Co-Fe-N-C in alkaline condition. S<sub>0</sub> represents the initial state (just after releasing oxygen), S<sub>1</sub> represents the state before OER onset, S<sub>2</sub> represents the resting state (before RDS), S<sub>3</sub> and S<sub>4</sub> represent the possible product of RDS and the deduced species after RDS, respectively. The red mark indicates the states supported by both electrokinetic and spectroscopic evidences; the blue mark indicates the states proposed from electrokinetic data; the pink mark indicates the states hypothesized.

## (2) Co-Ni-N-C

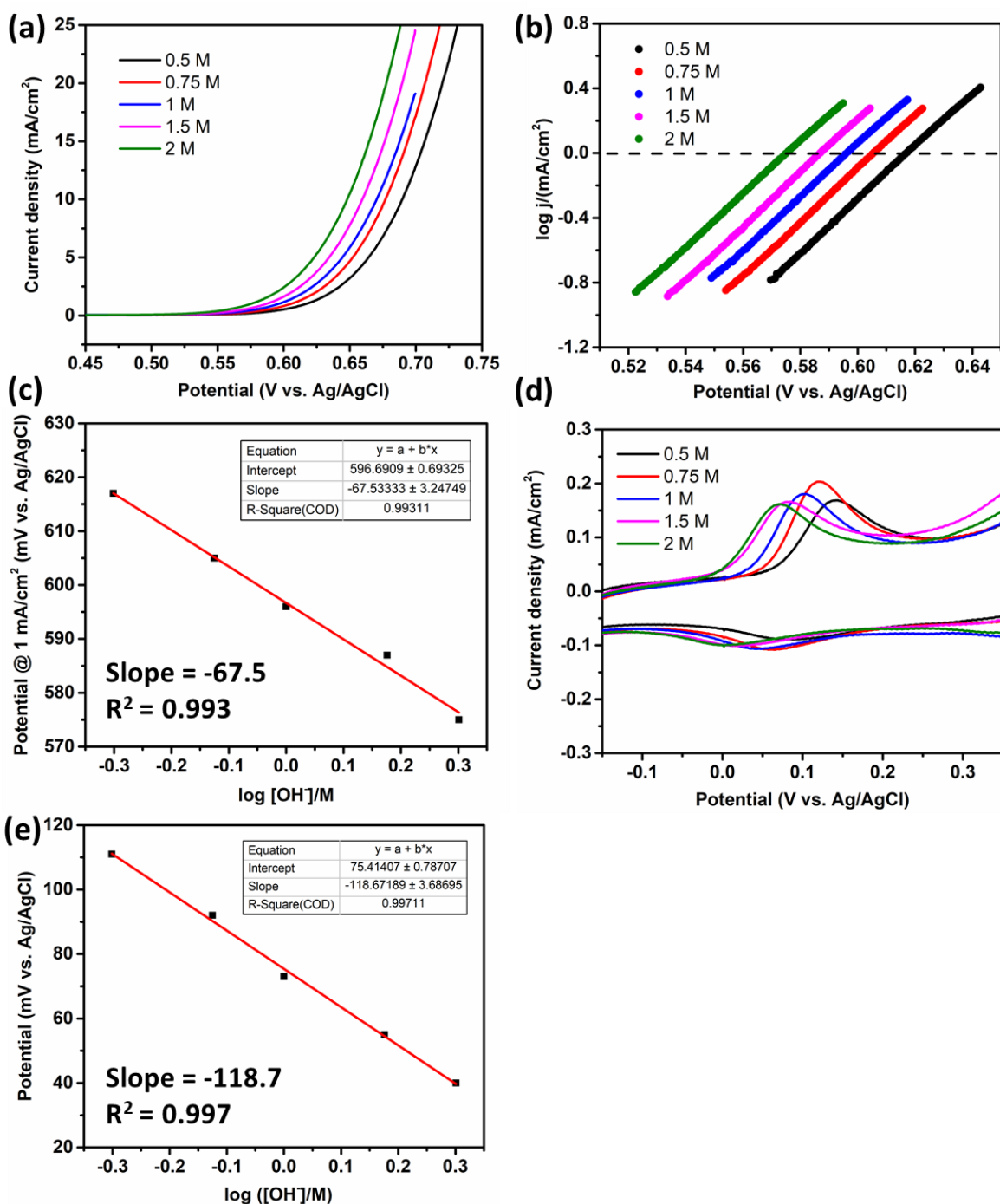


**Figure 4.5** Kinetic study of Co-Ni-N-C. (a) LSVs of Co-Ni-N-C in different concentration of KOH. The KOH solution contains Ni but is depleted of Fe. (b) Corresponding Tafel plots derived from (a). (c) Plots of the overpotential at  $1 \text{ mA}/\text{cm}^2$  against to the logarithm of the concentrations of  $\text{OH}^-$ . (d) The CVs of Co-Ni-N-C in the region of Co(II)/Co(III) transformation and (e) Correlation of the redox potential of Co(II)/Co(III) to the logarithm of the concentration of  $\text{OH}^-$  by a linear fitting.

Turning to the Co-Ni-N-C catalyst, it has a Tafel slope of about 60 mV/dec (Table 4.1; Figures 4.5a and 4.5b), nearly unchanged with KOH concentrations, which suggests that there is a PES involving one electron transfer followed by a pure chemical RDS ( $n_2 = 1$ ,  $n_4 = 0$ , the theoretical Tafel slope is  $2.303RT/F = 59$  mV/dec).<sup>12,36</sup> By using Eq. 4.17, the current density has only a first-order dependence on the concentrations of  $\text{OH}^-$  (Table 4.1 and Figure 4.5c), indicating that only one hydroxide transfer occurred during the PES and RDS in total. The overall rate of the reaction is:

$$v_{\text{Co-Ni}} = k_{\text{Co-Ni}}^0 a_{\text{OH}^-}^1 \exp\left(\frac{EF}{RT}\right) \quad (4.23)$$

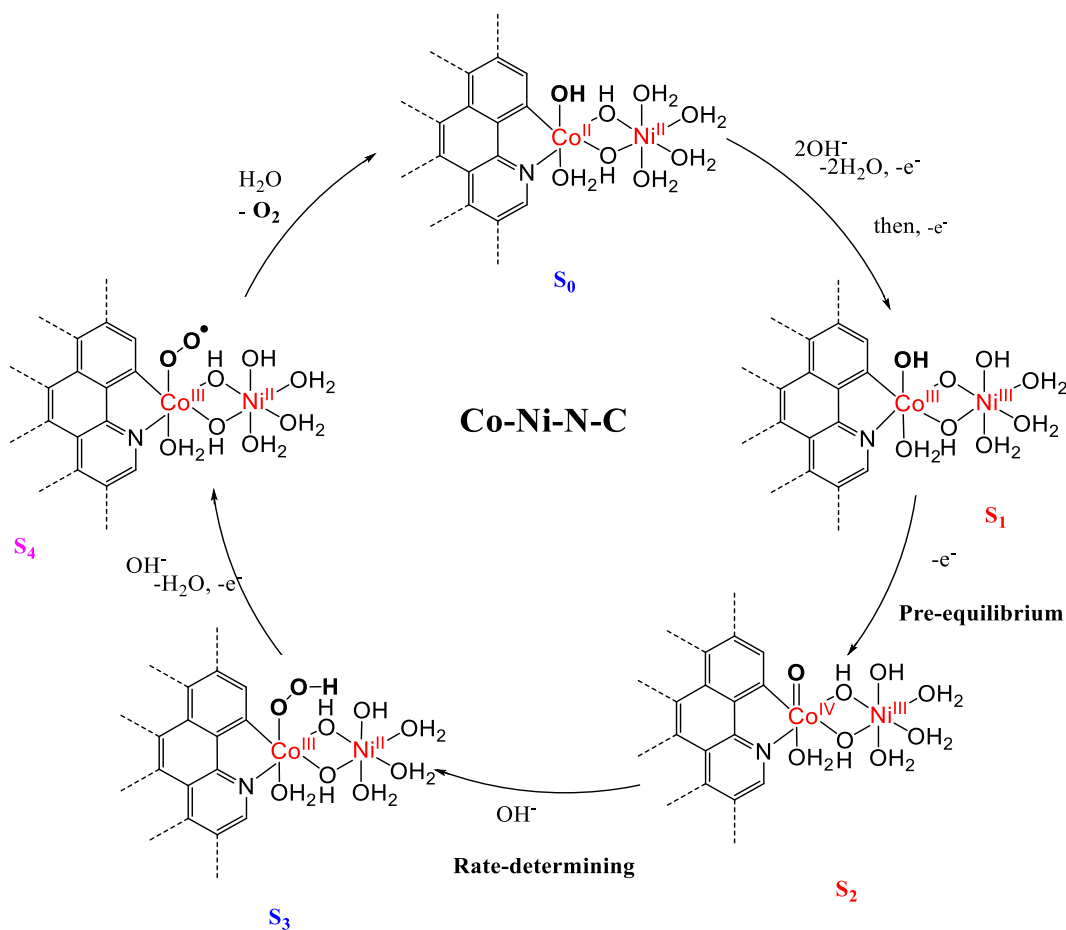


**Figure 4.6** Possible OER mechanisms of Co-Ni-N-C in alkaline condition.  $S_0$  represents the initial state (just after releasing oxygen),  $S_1$  represents the state before OER onset,  $S_2$  represents the resting state (before RDS),  $S_3$  and  $S_4$  represent the possible product of RDS and the deduced species after RDS, respectively. The red mark indicates the states supported by both electrokinetic and spectroscopic evidences; the blue mark indicates the states proposed from electrokinetic data; the pink mark indicates the states hypothesized.

The Co(II)/Co(III) potentials shifted by -119 mV per unit of  $\log [\text{OH}^-]$  (Table 4.1, Figures 4.5d and 4.5e), indicating that the oxidation was accompanied by the loss of 2 protons. These data suggest a slightly different mechanism (Figure 4.6): the Co(II) is first oxidized to Co(III) while two protons were removed by the  $\text{OH}^-$ . The Ni(II) is then oxidized to Ni(III) ( $\text{S}_0 \rightarrow \text{S}_1$ ). Although the redox peaks of Ni(II) to Ni(III) were not observed due to the very low loading of Ni (about 5% relative to Co), the Ni K-edge XANES spectrum of activated Co-Ni-N-C indicated that Ni was oxidized to a +3 oxidation state before the onset of OER (Figure 3.26a, Chapter 3). The PES is the oxidation of Co(III)-OH to Co(IV)=O ( $\text{S}_1 \rightarrow \text{S}_2$ ). This proposal is in agreement with the oxidation of Co(III) observed by *operando* XAS (Figure 3.23, Chapter 3). Because no external proton transfer is involved, we proposed that one proton was transferred internally from the Co-(III)-OH to the bridging O in Co-O-Ni.<sup>37</sup> The RDS is the attack  $\text{OH}^-$  to the Co(IV)=O ( $\text{S}_2 \rightarrow \text{S}_3$ ). This step requires no external electron transfer, because the nearby Ni(III) site can take one electron from Co(II)-OOH to form Ni(II), concurrently generating Co(III)-OOH. The catalytic cycle is completed by further 1 e oxidation and oxygen release ( $\text{S}_3 \rightarrow \text{S}_4 \rightarrow \text{S}_0$ ).

### (3) Co-Co-N-C

Lastly considering Co-Co-N-C, the Tafel slop is also about 60 mV/dec, independent of  $[\text{OH}^-]$ , similar as that of Co-Ni-N-C (Table 4.1, Figures 4.5a-b and 4.7a-b). By using similar method, we calculated the current density has a second-order dependence on the concentrations of  $\text{OH}^-$  (Table 4.1, Figure 4.7c), and the Co(II)/Co(III) potentials shifted by about -70 mV per unit of  $\log [\text{OH}^-]$  (Table 4.1, Figures 4.7d and 4.7e). Thus, the oxidation of Co(II) is accompanied by one proton loss, the PES is a concerted proton-electron transfer, and the RDS involves one  $\text{OH}^-$  transfer (Table 4.1). The overall rate of the reaction is:

$$v_{\text{Co-Co}} = k_{\text{Co-Co}}^0 a_{\text{OH}^-}^2 \exp\left(\frac{EF}{RT}\right) \quad (4.24)$$

In the proposed mechanism (Figure 4.8), the two Co(II) centers are oxidized independently to Co(III) with loss of two protons ( $\text{S}_0 \rightarrow \text{S}_1$ ). Similarly to Co-Ni-N-C, the PES is the oxidation of a Co(III)-OH to Co(IV)=O ( $\text{S}_1 \rightarrow \text{S}_2$ ), as Co(IV) were detected by XAS (Figure 3.24 in Chapter 3). The RDS is the  $\text{OH}^-$  attack on the Co(IV)=O, and the nearby (second) Co(III) center can take 1 electron so no external electron transfer is involved in the RDS ( $\text{S}_2 \rightarrow \text{S}_3$ ). Further oxidation and  $\text{O}_2$  release

regenerate the catalyst ( $S_3 \rightarrow S_4 \rightarrow S_0$ ). This mechanism is similar to the dual-site mechanism proposed for Co oxides/oxyhydroxides<sup>12,28,36</sup>, suggesting the double-atom Co-Co-N-C catalyst as a suitable molecular model of Co oxides.

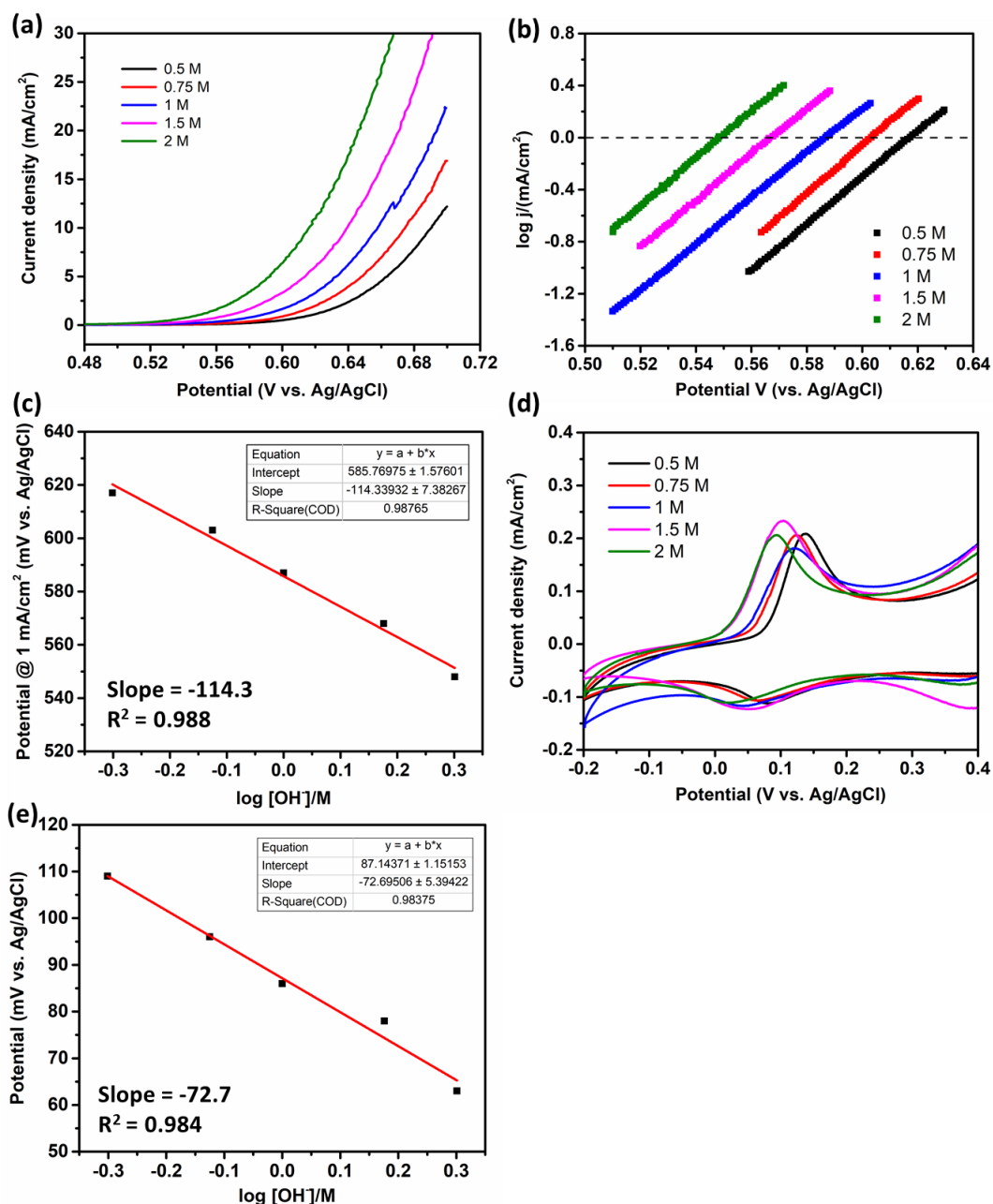


**Figure 4.7** Kinetic study of Co-Co-N-C. (a) LSVs of Co-Co-N-C in different concentration of KOH. The KOH solution contains Co but is depleted of Fe. (b) Corresponding Tafel plots derived from (a). (c) Plot of the overpotential at  $1 \text{ mA}/\text{cm}^2$  against to the logarithm of the concentrations of  $\text{OH}^-$ . (d) The CVs in the region of  $\text{Co(II)}/\text{Co(III)}$

transformation and (e) correlation of the redox potential of Co(II)/Co(III) to the logarithm of the concentration of OH<sup>-</sup> by a linear fitting.

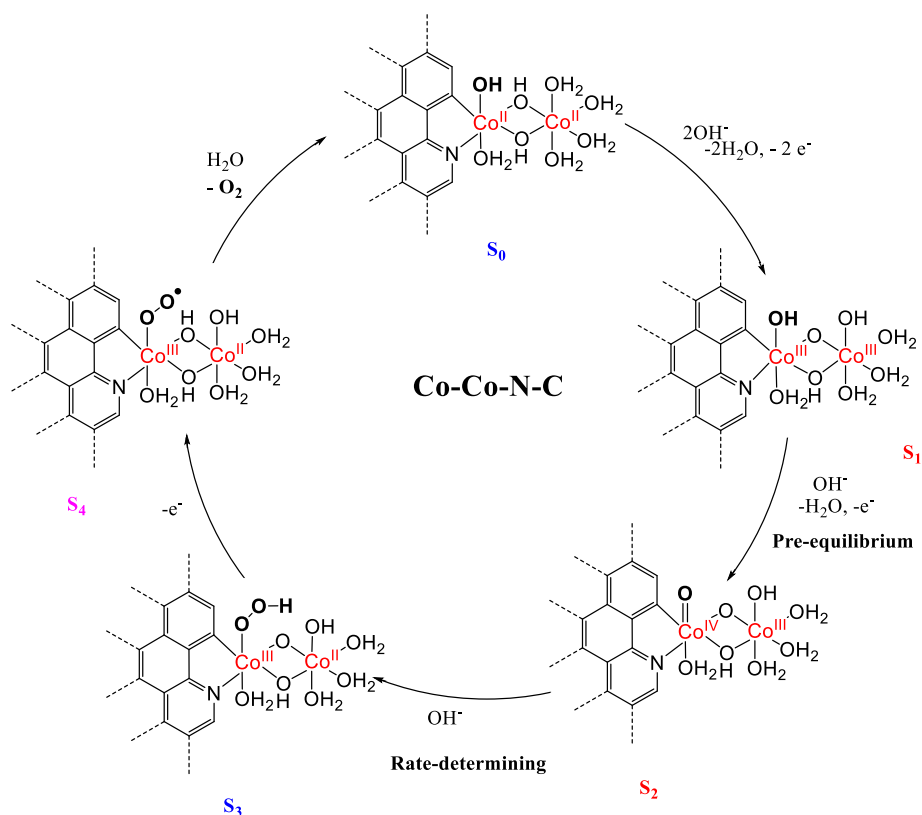


**Figure 4.8** Possible OER mechanisms of Co-Co-N-C in alkaline condition. S<sub>0</sub> represents the initial state (just after releasing oxygen), S<sub>1</sub> represents the state before OER onset, S<sub>2</sub> represents the resting state (before RDS), S<sub>3</sub> and S<sub>4</sub> represent the possible product of RDS and the deduced species after RDS, respectively. The red mark indicates the states supported by both electrokinetic and spectroscopic evidences; the blue mark indicates the states proposed from electrokinetic data; the pink mark indicates the states hypothesized.

#### 4.3.2 Electrokinetic analysis and reaction mechanisms of Ni-based double atoms

The Tafel slope of Ni-Fe-N-C is close to 40 mV/dec (Table 4.1, Figures 4.9a and 4.9b), independent of the concentration of OH<sup>-</sup> as well. The results suggested that the reaction has a PES involving one-electron transfer, followed by an RDS that also involves one-electron transfer. Based on the order of the current density on the concentration of OH<sup>-</sup> (Eq. 4.17), the PES and RDS involve the transfer of two hydroxyl ions in total (Table 4.1, Figure 4.9c). The overall rate of the reaction is:

$$v_{Ni-Fe} = k_{Ni-Fe}^0 a_{OH^-}^2 \exp\left(\frac{3EF}{2RT}\right) \quad (4.25)$$

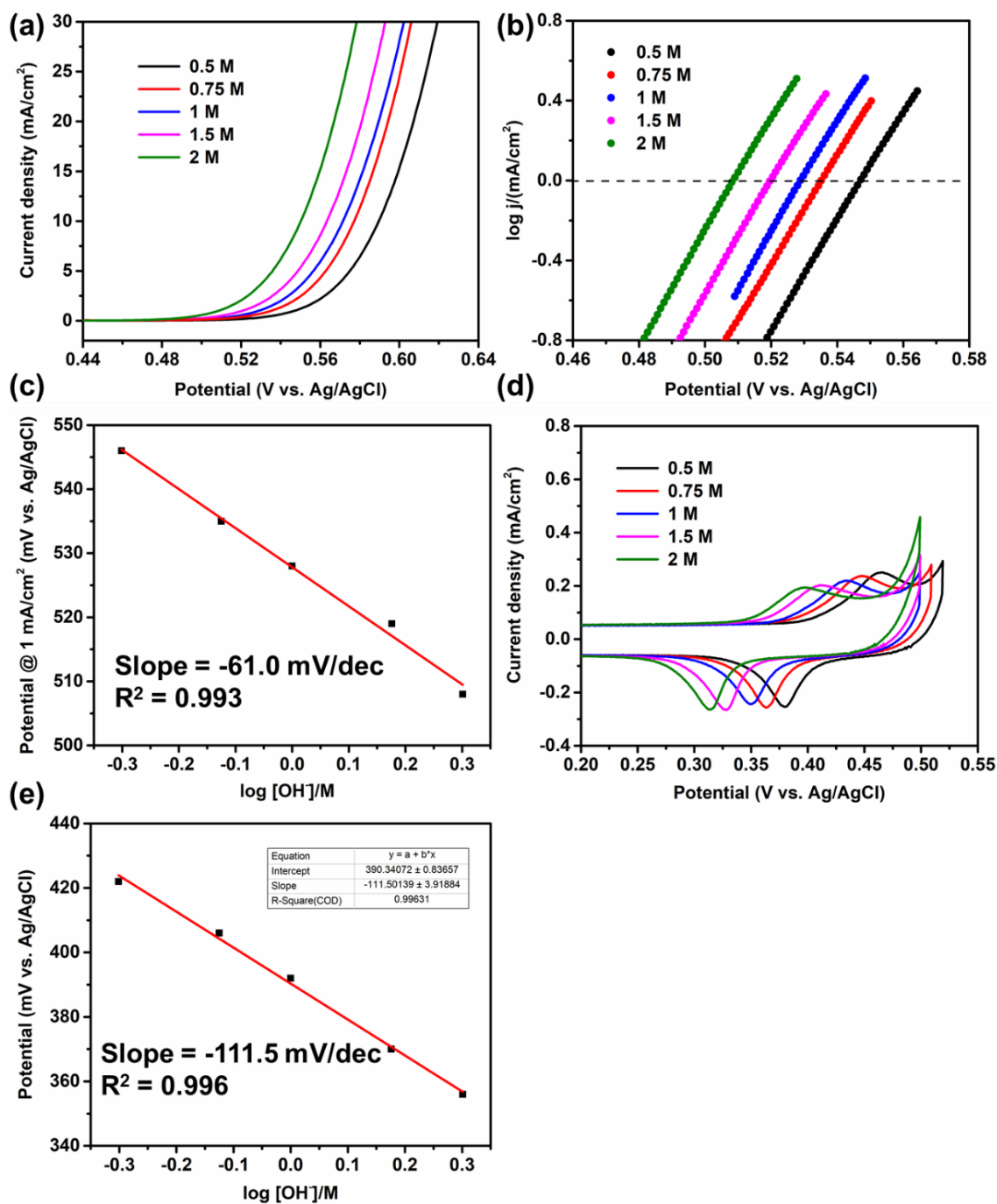


**Figure 4.9** Kinetic study of Ni-Fe-N-C. (a) LSVs of Ni-Fe-N-C in different concentration of KOH. Commercial KOH which contains Fe impurities was used to prepare the electrolyte. (b) Corresponding Tafel plots derived from (a). (c) Plot of the overpotential at 1  $\text{mA}/\text{cm}^2$  against to the logarithm of the concentrations of  $\text{OH}^-$ . (d) The CVs in the region of Ni(II)/Ni(III) transformation and (e) correlation of the redox potential of Ni(II)/Ni(III) to the logarithm of the concentration of  $\text{OH}^-$  by a linear fitting.



Therefore, the general reaction kinetics related to PES and RDS is the same as that of Co-Fe-N-C. We further found that the redox potentials of Ni(II)/Ni(III) in Ni-Fe-N-C are shifted by about -112 mV per unit of  $\log [\text{OH}^-]$ , indicating that the Ni(II) to Ni(III) transformation was accompanied by two  $\text{OH}^-$  transfer (Table 4.1, Figures 4.9d and 4.9e). The redox peaks related to Fe were not observed.

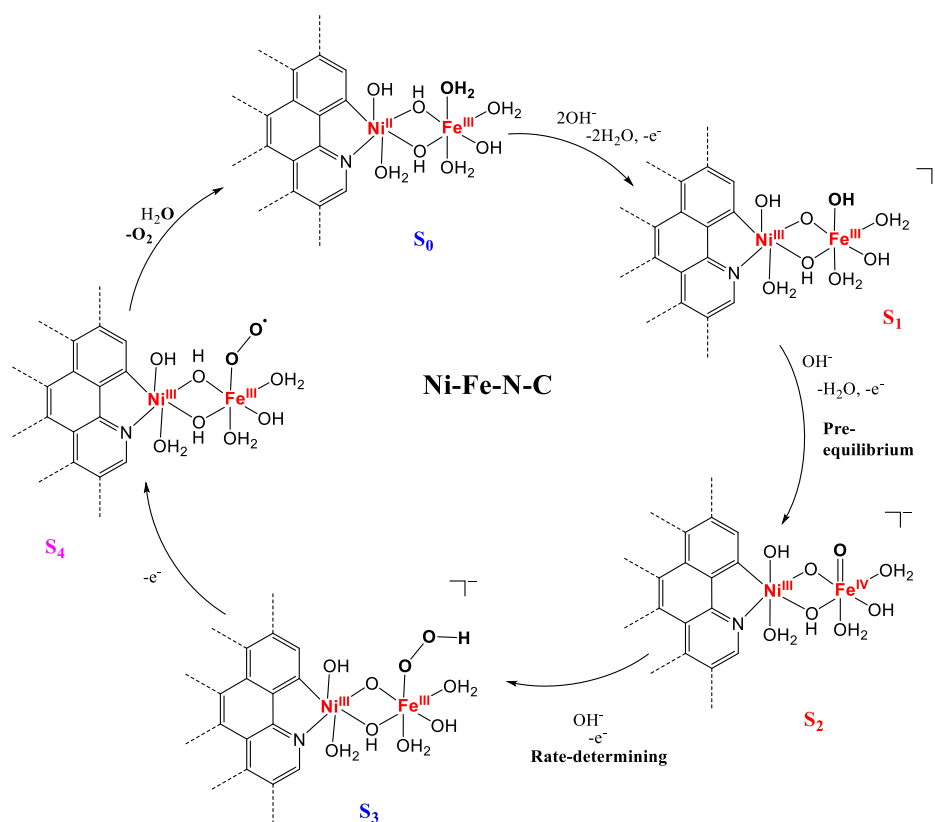


**Figure 4.10** Possible OER mechanisms of Ni-Fe-N-C in alkaline condition.  $S_0$  represents the initial state (just after releasing oxygen),  $S_1$  represents the state before OER onset,  $S_2$  represents the resting state (before RDS),  $S_3$  and  $S_4$  represent the possible product of RDS and the deduced species after RDS, respectively. The red mark indicates the states supported by both electrokinetic and spectroscopic evidences; the blue mark indicates the states proposed from electrokinetic data; the pink mark indicates the states hypothesized.

Combining with *operando* XAS data (Figures 3.17 and 3.21 in Chapter 3), a plausible reaction mechanism can be proposed for Ni-Fe-N-C (Figure 4.10). At the onset of OER, a Ni(II) ion is oxidized to Ni(III), accompanied by the loss of two protons ( $S_0 \rightarrow S_1$ ). The Ni ion appears to remain as Ni(III) during catalysis (Figure 3.17 in Chapter 3), whereas XANES spectra of Fe K-edge

suggested Fe is oxidized to higher than +3 oxidation state when certain amount of Ni-Fe double-atoms are generated (Figure 3.21 in Chapter 3). Such result is also consistent with previous studies of NiFeO<sub>x</sub> that suggested the oxidation of Fe(III) to Fe(IV) occurs at potentials less positive than that of Ni(III) to Ni(IV).<sup>38,39</sup> Noted that Fe(IV)=O has also been observed for homogeneous Fe complexes.<sup>40,41</sup> Therefore, we proposed that the next step is the oxidation of Fe(III)-OH to Fe(IV)=O, which is the PES (S<sub>1</sub>→S<sub>2</sub>). The RDS is the hydroxide attack on the Fe(IV)=O to give Fe(III)-OOH (S<sub>2</sub>→S<sub>3</sub>). Another PCET yields Fe(III)-OO·, which releases O<sub>2</sub> and regenerate the Ni(II)-Fe(III) (S<sub>3</sub>→S<sub>4</sub>→S<sub>0</sub>). This mechanism is similar to the mechanism proposed in several studies of NiFeO<sub>x</sub>.<sup>38,39</sup>

### 4.3.3 Electrokinetic analysis and reaction mechanisms of Fe-based double atoms

#### (1) Fe-Ni-N-C

Similar methods and experiments were also performed for Fe-Ni-N-C and Fe-Co-N-C. The Fe-Ni-N-C has a Tafel slope of 60 mV/dec (Table 4.1, Figures 4.11a and 4.11b), so different from that of Ni-Fe-N-C (close to 40 mV/dec, Figures 4.9a and 4.9b). The reaction has a PES involving one electron transfer, followed by a pure chemical RDS. The catalytic current was calculated as first order on the concentration of hydroxyl ions (Figure 4.11c), so that the PES and RDS involve 1 proton transfer in total (Table 4.1). The overall rate of Fe-Ni-N-C is:

$$v_{Fe-Ni} = k_{Fe-Ni}^0 a_{OH}^1 \exp\left(\frac{EF}{RT}\right) \quad (4.26)$$

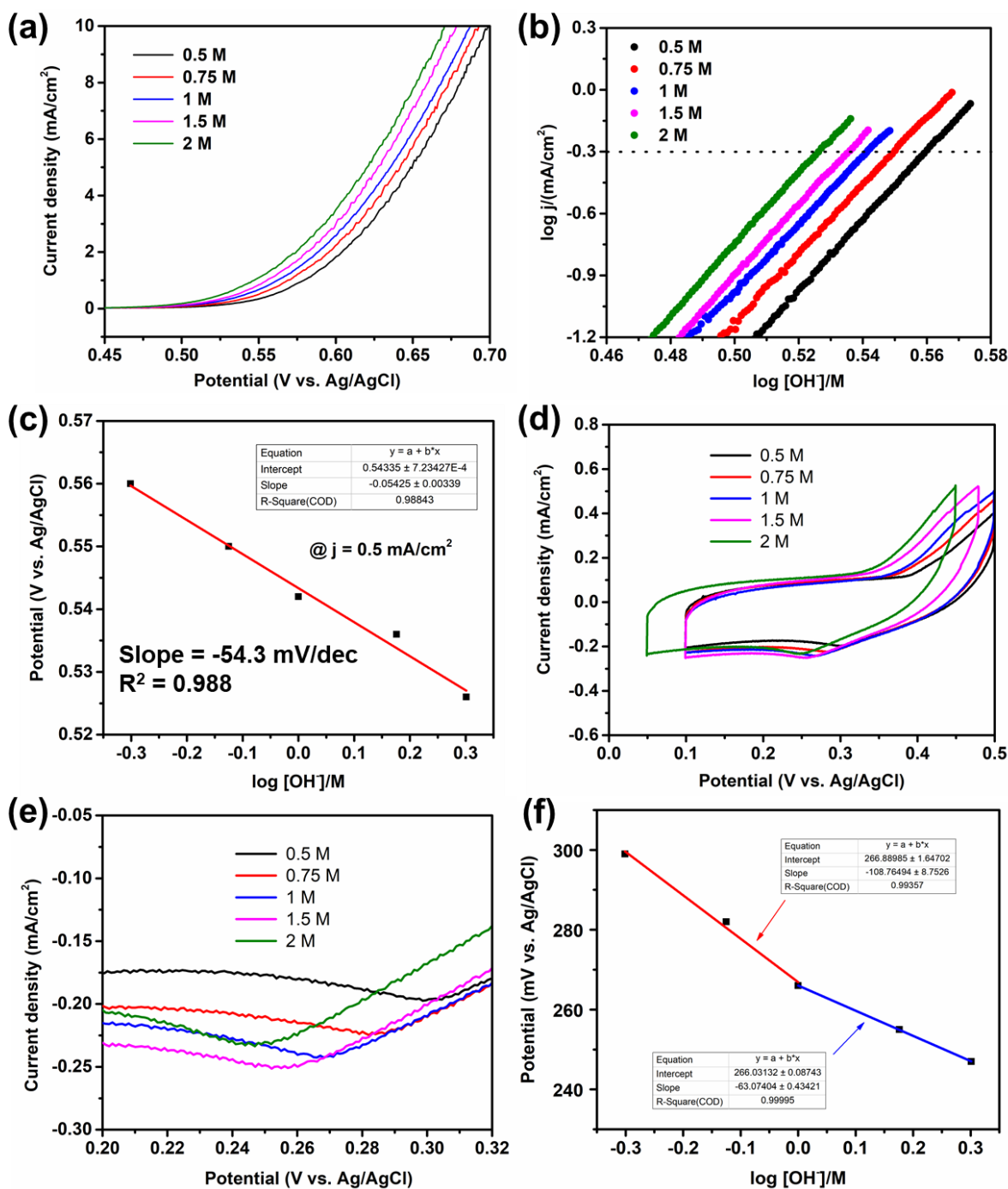


**Figure 4.11** Kinetic study of Fe-Ni-N-C. (a) LSVs of Fe-Ni-N-C in different concentration of KOH. The KOH solution contains Ni but is depleted of Fe. (b) The corresponding Tafel plots derived from (a). (c) Plot of the overpotential at 0.5 mA/cm<sup>2</sup> against the logarithm of the concentrations of OH<sup>-</sup>. (d) The CVs in the region of Ni(II)/Ni(III) transformation and (e) the enlarged graph of the square with dashed line in (d). (f) Correlation of the redox potential of Ni(II)/Ni(III) to the logarithm of the concentration of OH<sup>-</sup> by a linear fitting.

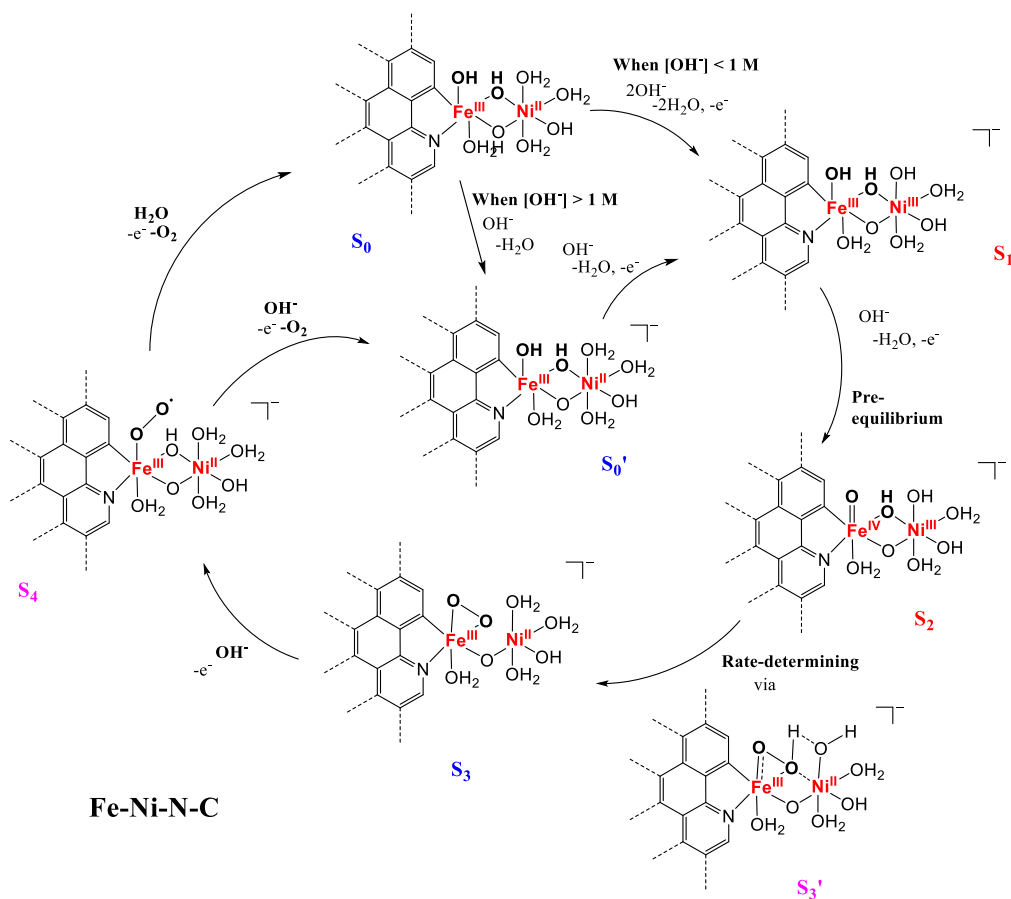


**Figure 4.12** Possible OER mechanisms of Fe-Ni-N-C in alkaline condition.  $S_0$  represents the initial state (just after releasing oxygen),  $S_1$  represents the state before OER onset,  $S_2$  represents the resting state (before RDS),  $S_3$  and  $S_4$  represent the possible product of RDS and the deduced species after RDS, respectively. The red mark indicates the states supported by both electrokinetic and spectroscopic evidences; the blue mark indicates the states proposed from electrokinetic data; the pink mark indicates the states hypothesized.  $S_x'$  represents the proposed intermediate states before or after  $S_x$ .

According to *operando* XAS (Figure 3.29 in Chapter 3), oxidation of Fe(III) ions occurred after electrochemical activation and during OER. These data are consistent with the oxidation of Fe(III)-OH to Fe(IV)=O as a PES ( $S_1 \rightarrow S_2$ ), and attack of a bridging  $\text{OH}^-$  on the Fe(IV)=O as a RDS ( $S_2 \rightarrow S_3' \rightarrow S_3$ ). A recent computational study proposed a similar mechanism for OER catalyzed by  $\text{NiFeO}_x$ , and suggested that the hydrogen atom of the resulting Fe-OOH group would be transferred to a nearby Ni-O site.<sup>42</sup> The Fe(II)/Fe(III) oxidation peak could not be detected by CVs, probably because its potential was very negative. The oxidation state of Ni was close to +3 after electrochemical activation (Figure 3.31a in Chapter 3). Additionally, we also observed a small

reductive peak corresponding to Ni(III)/Ni(II) in the CV of Fe-Ni-N-C (Figures 4.11d and 4.11e). The oxidation peak of Ni(II)/Ni(III) might be hidden underneath the background capacitive current (similar as the case of Co-Fe-N-C, Figure 4.3d-e). When the concentration of OH<sup>-</sup> is below 1 M, the number of transferred hydroxyl ions is two for the Ni(II)/Ni(III) couple (S<sub>0</sub>→S<sub>1</sub>). This number decreases to 1 when the concentration of OH<sup>-</sup> is higher than 1 M (Figure 4.11f, S<sub>0</sub>→S<sub>0'</sub>→S<sub>1</sub>). The change is likely due to the lower proton number in the Ni(II) form of the catalyst in more basic electrolyte.<sup>10,43</sup> Considering these data, we proposed the following mechanism for Fe-Ni-N-C (Figure 4.12). Before the onset of OER, Ni(II) is oxidized to Ni(III), accompanied by either 1 or 2 OH<sup>-</sup> transfer (S<sub>0</sub>→S<sub>0'</sub>→S<sub>1</sub> or S<sub>0</sub>→S<sub>1</sub>). The PES is the oxidation of Fe(III)-OH to Fe(IV)=O (S<sub>1</sub>→S<sub>2</sub>), while the RDS is the intramolecular reaction between Fe(IV)=O and bridging OH<sup>-</sup> (S<sub>2</sub>→S<sub>3'</sub>→S<sub>3</sub>). A subsequent PCET step generates [Fe(III)-OO<sup>-</sup>] (S<sub>3</sub>→S<sub>4</sub>). The oxygen is released by either water ([OH<sup>-</sup>] < 1 M, S<sub>4</sub>→S<sub>0</sub>) or OH<sup>-</sup> attack to [Fe(III)-OO<sup>-</sup>] ([OH<sup>-</sup>] > 1 M, S<sub>4</sub>→S<sub>0'</sub>).

## (2) Fe-Co-N-C

Unlike the above case of Fe-Ni-N-C vs. Ni-Fe-N-C, the Fe-Co-N-C catalyst has a similar Tafel slope to that for Co-Fe-N-C (i.e., 40 mV/dec, Table 4.1, Figures 4.13a and 4.13b). Moreover, the current density has a second-order dependence on the concentrations of OH<sup>-</sup>, again similar to Co-Fe-N-C (Table 4.1, Figure 4.13c). Thus, the reaction has a PES involving one-electron transfer, followed by a RDS that also involves a one-electron transfer. The PES and RDS involve the transfer of two hydroxyl ions in total (Table 4.1). The overall rate of the reaction is similar as Eq. 4.22 (the case of Co-Fe-N-C):

$$v_{Fe-Co} = k_{Fe-Co}^0 a_{OH^-}^2 \exp\left(\frac{3EF}{2RT}\right) \quad (4.27)$$

The Co of activated Fe-Co-N-C had an oxidation state of close to +3 (Figure 3.32a in Chapter 3). The Co(II)/Co(III) oxidation peak could not be detected due to a low loading of Co (about 10% relative to Fe), so we could not measure the number of protons loss associated with this oxidation (Figure 4.13d). Based on similar metal composition and electrokinetics to Co-Fe-N-C, we assumed one proton was lost during this oxidation (S<sub>0</sub>→S<sub>1</sub>). Although currently we don't know whether Co was further oxidized to Co(IV) during OER, the oxidation of Fe(III) to a higher oxidation state, presumably Fe(IV), was observed in XAS (Figure 3.28 in Chapter 3). Thus, we proposed a mechanism based on Fe as the active site (Figure 4.14). The PES is the formation of Fe(IV)=O (S<sub>1</sub>→S<sub>2</sub>), and the RDS is the attack of OH<sup>-</sup> on Fe(IV)=O to form Fe(III)-OOH (S<sub>2</sub>→S<sub>3</sub>). The

mechanism is therefore analogous to that of Co-Fe-N-C, except that the positions of Fe and Co are exchanged.

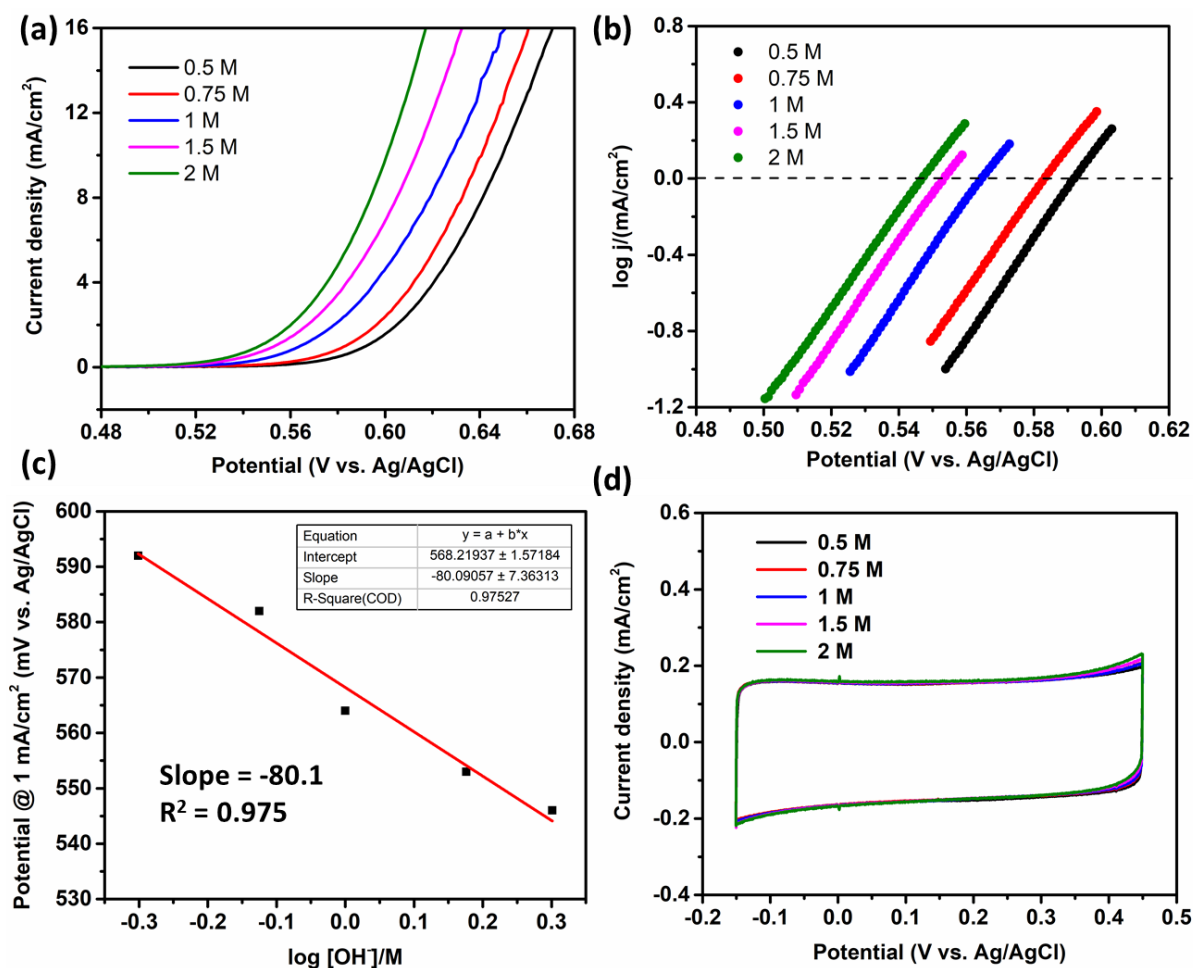


**Figure 4.13** Kinetic study of Fe-Co-N-C. (a) LSVs of Fe-Co-N-C in different concentration of KOH. The KOH solution contains Co but is depleted of Fe. (b) The corresponding Tafel plots derived from (a). (c) Plot of the overpotential at 1  $\text{mA}/\text{cm}^2$  against the logarithm of the concentrations of  $\text{OH}^-$ . (d) CVs in the range from -0.15 V to 0.45 V vs. Ag/AgCl in KOH with concentration range from 0.5 to 2 M. No obvious redox peaks of Co(II)/Co(III) were observed.

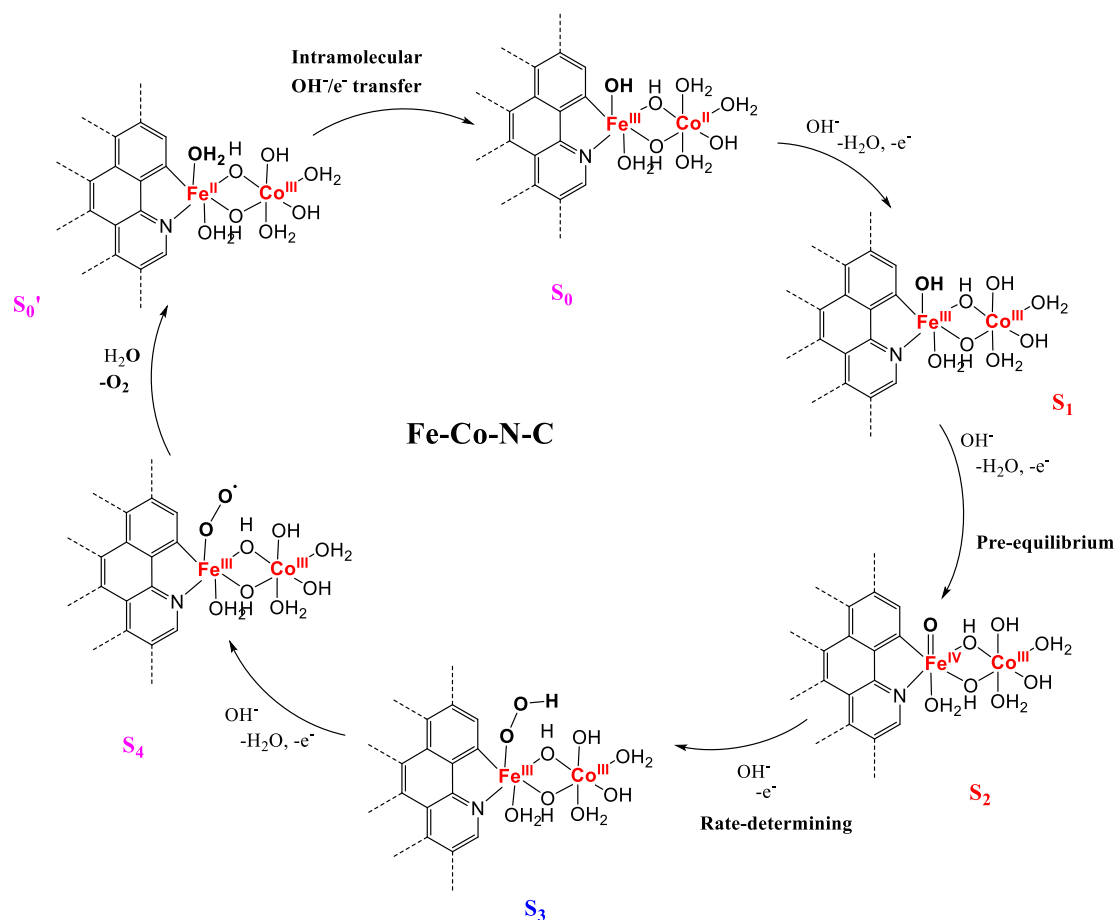


**Figure 4.14** Possible OER mechanisms of Fe-Co-N-C in alkaline condition.  $S_0$  represents the initial state (just after releasing oxygen),  $S_1$  represents the state before OER onset,  $S_2$  represents the resting state (before RDS),  $S_3$  and  $S_4$  represent the possible product of RDS and the deduced species after RDS, respectively. The red mark indicates the states supported by both electrokinetic and spectroscopic evidences; the blue mark indicates the states proposed from electrokinetic data; the pink mark indicates the states hypothesized.  $S_x'$  represents the proposed intermediate states before  $S_x$ .

#### 4.4 Comparisons and discussions of the reaction mechanisms

We first compared the reaction mechanisms of Co-based DACs. The mechanistic divergence of Co-Fe-N-C, Co-Ni-N-C, and Co-Co-N-C might be understood by considering the difference of electronic properties of Fe, Ni, and Co. Fe incorporation largely decreases the redox potential of Co(III)-OH to Co(IV)=O, enabling catalysis at a much lower overpotential. In comparison, Ni or a second Co ion have a similar, but less efficient function. The second metal may promote the O-O

bond formation in the RDS as well. Our results are in agreement with previous studies showing the promotional effects of Fe<sup>24,26,27</sup>, Co<sup>28,44</sup>, and Ni<sup>45</sup> on the OER activity of Co oxides.

**Table 4.1.** Electro-kinetics parameters of different double-atom catalysts

	Tafel Slope <sup>a</sup>	Order on [OH <sup>-</sup> ]	n of e <sup>-</sup> /OH <sup>-</sup> in pre-equilibrium	n of e <sup>-</sup> /OH <sup>-</sup> in RDS	n of e <sup>-</sup> /OH <sup>-</sup> in pre-catalytic redox <sup>b</sup>
<b>Co-Fe-N-C</b>	39(40)	2	1/1	1/1	1/1 for Co(II)/Co(III)
<b>Co-Ni-N-C</b>	58(59)	1	1/0	0/1	1/2 for Co(II)/Co(III) <sup>c</sup>
<b>Co-Co-N-C</b>	57(59)	2	1/1	0/1	2/2 for Co(II)/Co(III)
<b>Ni-Fe-N-C</b>	36(40)	2	1/1	1/1	1/2 for Ni(II)/Ni(III)
<b>Fe-Co-N-C</b>	40(40)	2	1/1	1/1	Probable 1/1 for Co(II)/Co(III) <sup>d</sup>
<b>Fe-Ni-N-C</b>	61(59)	1	1/1	0/0	1/2 or 1/1 for Ni(II)/Ni(III) <sup>e</sup>

- The ideal Tafel slope is provided in the parentheses.
- The redox peaks of Fe(II)/Fe(III) is not in the electrochemical windows of this study.
- Due to the low loading of Ni, the redox peak of Ni(II)/Ni(III) cannot be observed.
- Due to the low loading of Co, the redox peak of Co(II)/Co(III) cannot be observed.
- The transferred OH<sup>-</sup> is 2 for KOH from 0.5 to 1 M, while the transferred OH<sup>-</sup> is 1 for KOH from 1 to 2 M.

The kinetic differences of these three catalysts can be traced back to an electronic origin. The different Lewis acidity of metals results in different numbers of proton transfer associated with a given electron transfer step. The different redox potentials of M(II)/M(III) couples lead to either internal (for Co and Ni) or external (for Fe) electron transfer in the RDS. The combination of these effects gives rise to different Tafel slope values.

Despite the divergence in these details, the overarching mechanism appears the same for all three of the Co-based DACs: Co(IV)=O is the active intermediate and hydroxide attack on the Co(IV)=O is the O-O bond forming step. The second metal decreases the potential of the Co(III)-OH/Co(IV)=O couple as well as modulates the order of electron/hydroxide transfers. While the bimetallic promotion is essential, the high TOFs of Co-Fe-N-C compared to other Co-Fe oxides also suggests that the N-doped carbon support (N-C) serves an important function.<sup>46-49</sup>

In both Fe-Ni-N-C and Ni-Fe-N-C (Ni-Fe based DACs), the Fe site is where O-O bond formation occurs. Regardless of the coordination environment, the potential of Fe(III)-OH to Fe(IV)=O oxidation appears to be lower than the Ni(III)-OH to Ni(IV)=O counterpart. This result is in line with some recent studies of NiFe oxyhydroxides, which suggested Fe as the site of O-O



bond formation.<sup>38,39,50-52</sup> While the mechanisms of Ni-Fe-N-C and Fe-Ni-N-C all invoke the formation of Fe(IV)=O and a consequent OH<sup>-</sup> attack, the sources of OH<sup>-</sup> were different. For Fe-Ni-N-C the OH<sup>-</sup> probably comes from a bridging hydroxyl ligand, while for the other two catalysts the OH<sup>-</sup> comes from the electrolyte. This difference might be a result of different nucleophilicity of the bridging hydroxyl ligands in these catalysts.

For Co-Fe based DACs, going from Co-Fe-N-C to Fe-Co-N-C, the metal that mediates O-O bond formation switches from Co to Fe. We proposed that the N-doped carbon support facilitates the oxidation of the metal ions covalently linked to it to form the corresponding M(IV)=O species. This result suggests both Co and Fe sites can mediate O-O bond formation in CoFe-based electrocatalysts, depending on the coordination environment. Indeed, mechanisms involving both Co and Fe active sites have been proposed for CoFe oxides.<sup>24-27</sup>

Due to the molecular nature of the active sites of the DACs, we also compared their mechanisms to those of molecular bimetallic OER catalysts<sup>18</sup>. For examples, in the classic Ru-O-Ru blue dimer catalyst<sup>53,54</sup>, consecutive PCETs to the (OH<sub>2</sub>)Ru(III)-O-Ru(III)(OH<sub>2</sub>) catalyst yields a O=Ru(V)-O-Ru(V)=O intermediate. The O-O bond forming step is a nucleophilic attack of water to one of the Ru(V)=O, during which one electron is transfer to each Ru(V), while one proton is transfer to the other Ru(V)=O to form (HOO)Ru(IV)-O-Ru(IV)(OH) (2e<sup>-</sup>/1H<sup>+</sup> process). Intramolecular PCET from the latter then gives a (·OO)Ru(IV)-O-Ru(III)(OH<sub>2</sub>), which then releases dioxygen to give the starting catalyst. In this mechanism a second Ru(V)=O unit serves as an acceptor for accepting two electrons and two protons in total. This mode of bimetallic cooperation is not seen in our DACs, probably because for first-row transition metal M-O-M dimers, the potential to generate an O=M-O-M=O unit is actually higher than OER potentials. However, the mechanism of O-O bond formation of the blue dimer is similar to those of our DACs. Also, the intramolecular proton/electron transfer processed were also observed for some DACs of this Thesis, like Co-Ni-N-C, Co-Co-N-C, and Fe-Ni-N-C. Turning to first-row transition metal bimetallic catalysts, a Co(III)-(OH)<sub>2</sub>-Co(III) was reported to serve as a homogeneous catalyst for OER.<sup>34</sup> It was proposed that two PCETs from Co(III)-(OH)<sub>2</sub>-Co(III) gives a Co(III)-(O·)<sub>2</sub>-Co(III) intermediate containing two oxyl radicals. Radical-radical coupling of the bis-μ-oxyl ligands then yields a Co(III)-(peroxo)-Co(III) intermediate, which upon oxidation gives O<sub>2</sub>. A DFT study suggests that for first-row transition metal M-(OH)<sub>2</sub>-M dimers, both the water/OH<sup>-</sup> nucleophilic attack and radical coupling mechanisms have similar computational overpotentials.<sup>54</sup> For our DACs, we can rule out the radical coupling mechanism based on electrokinetic data.

Although the mechanisms of molecular OER catalysts have been thoroughly investigated, including those involving bimetallic cooperation, few studies are conducted on bimetallic complexes containing first-row transition metal ions because they have the tendency to decompose to metal oxide nanoparticles.<sup>18</sup> Our bimetallic catalysts are atomically dispersed species imbedded in an N-doped carbon support. Unlike molecular catalysts including those immobilized on surface, they do not have discrete organic ligands so that they are more stable. No molecular equivalents of these catalysts are known. On the other hand, these atomically dispersed catalysts differ from traditional heterogeneous catalysts in that they have molecular-like active sites, which similar to molecular catalysts facilitate mechanistic studies. In this context, the atomically dispersed catalysts described in this work combine the strengths of both homogeneous and heterogeneous catalysts. Mechanistic studies of these catalysts, the first of which is presented here, provide a new means to apply knowledge of molecular catalysis for the understanding of heterogeneous catalysis.

## 4.5 Conclusions

The molecular nature of the active sites in several non-noble metal DACs facilitates the atomic level insight of the OER mechanisms. The deduction of reaction mechanisms was based on using data from XAS and electrokinetic measurements. In all the catalysts, the O-O bond forming step appears to be the nucleophilic attack of OH<sup>-</sup> on a M(IV)=O unit. However, depending on the nature of the metal ions and their coordination environment, and the identity of the M, the number of protons and electrons that transfer in each step, as well as the source of OH<sup>-</sup>, vary. These subtleties originate from the different redox potentials and Lewis acidity of the different metal ions, especially when they are coordinated to different ligands. The much higher activity of DACs compared to their single-atom counterparts is a result of bimetallic cooperation, which is evident from the mechanisms. Not only do these results provide blueprints for the mechanistic studies of mixed metal oxide OER catalysts, but also our work introduces a new class of easily accessed, molecularly defined, and earth-abundant OER electrocatalysts. By bridging the transitionally separated molecular and solid-state catalysts, these DACs offer an attractive platform for fundamental studies of heterogeneous OER electrocatalysts.

## 4.6 Experimental Section

All the catalysts were deposited on carbon-cloth electrode for the electrokinetic analysis. The procedure of electrode preparation is the same as the description in Section 3.7.4, Chapter 3.

The electrochemical measurements were performed in a three-electrode electrochemical cell, in which Pt wire and Ag/AgCl electrode (saturated KCl,  $E(\text{Ag}/\text{AgCl}) = 0.197 \text{ V vs. SHE}$ ) were used as the counter and the reference electrode, respectively. The working electrode and the reference electrode were separated with counter electrode by a glass frit. The solution was stirred by a magnetic stirring bar in all of the electrochemical measurements. All of the electrochemical results were compensated with solution resistance. The polarization curves were recorded by the LSV, and the scan rate was  $1 \text{ mV/s}$ . Electrokinetic studies were performed in KOH (containing certain metal ions impurities) with concentration ranging from  $0.5 \text{ M}$  to  $2 \text{ M}$ . The  $0.5 \text{ M}$  and  $0.75 \text{ M}$  KOH were prepared by diluting  $1 \text{ M}$  KOH standard solution, while  $1.5 \text{ M}$  and  $2 \text{ M}$  KOH were prepared by further adding desired amount of KOH flakes (Sigma Aldrich) in  $1 \text{ M}$  KOH standard solution. For Co or Ni containing but Fe-free KOH, the normal KOH with different concentration were first prepared, and then treated with  $\text{Co}(\text{OH})_2$  or  $\text{Ni}(\text{OH})_2$ , as the same procedures mentioned in Section 3.7.1, Chapter 3. The LSVs of investigated electrodes were obtained sequentially in  $0.5 \text{ M}$ ,  $0.75 \text{ M}$ ,  $1 \text{ M}$ ,  $1.5 \text{ M}$  and  $2 \text{ M}$  KOH. The Tafel plots were derived from LSVs and linearly fitted, as  $(\partial E/\partial j)_{\text{pH}}$ . The relationship between the potential at a constant current density (here is  $1$  or  $0.5 \text{ mA/cm}^2$ ) and the concentration of hydroxyl ions  $((\partial E/\partial \log[\text{OH}^-])_j)$ , were obtained by calculating the potential at  $1$  or  $0.5 \text{ mA/cm}^2$ . The order dependence on the hydroxyl ions  $((\partial j/\partial \log[\text{OH}^-])_E)$  in  $0.5$ - $2 \text{ M}$  KOH can be determined according to Eq. 4.17. This parameter should not be directly read from LSVs since it is hard to ensure that in a certain potential, all the current densities are in Tafel region for KOH with different concentrations. To investigate redox peaks of each DACs, the scan rate was set to  $50 \text{ mV/s}$  in order to obtain a high signal to background ratio.

## 4.7 Contributions

L. Bai performed all the experiments for electrokinetic analysis. X. Hu directed the study.

## 4.8 References of Chapter 4

- (1) Bai, L.; Hsu, C.-S.; Alexander, D.; Chen, H. M.; Hu, X., Double-atom catalysts provide a molecular platform for oxygen evolution. *ChemRxiv*, preprint **2019**. <https://doi.org/10.26434/chemrxiv.11341961.v1>
- (2) Song, J.; Wei, C.; Huang, Z. F.; Liu, C.; Zeng, L.; Wang, X.; Xu, Z. J. A review on fundamentals for designing oxygen evolution electrocatalysts. *Chem. Soc. Rev.* **2020**, *49*, 2196-2214.
- (3) Suen, N. T.; Hung, S. F.; Quan, Q.; Zhang, N.; Xu, Y. J.; Chen, H. M. Electrocatalysis for the oxygen evolution reaction: recent development and future perspectives. *Chem. Soc. Rev.* **2017**, *46*, 337-365.
- (4) Song, F.; Bai, L.; Moysiadou, A.; Lee, S.; Hu, C.; Liardet, L.; Hu, X. Transition Metal Oxides as Electrocatalysts for the Oxygen Evolution Reaction in Alkaline Solutions: An Application-Inspired Renaissance. *J. Am. Chem. Soc.* **2018**, *140*, 7748-7759.
- (5) Hu, C.; Zhang, L.; Gong, J. Recent progress made in the mechanism comprehension and design of electrocatalysts for alkaline water splitting. *Energy Environ. Sci.* **2019**, *12*, 2620-2645.
- (6) Zhu, K.; Zhu, X.; Yang, W. Application of In Situ Techniques for the Characterization of NiFe-Based Oxygen Evolution Reaction (OER) Electrocatalysts. *Angew. Chem. Int. Ed.* **2019**, *58*, 1252-1265.
- (7) Fang, Y.-H.; Liu, Z.-P. Tafel Kinetics of Electrocatalytic Reactions: From Experiment to First-Principles. *ACS Catal.* **2014**, *4*, 4364-4376.
- (8) Zhang, J.; Tao, H. B.; Kuang, M.; Yang, H. B.; Cai, W.; Yan, Q.; Mao, Q.; Liu, B. Advances in Thermodynamic-Kinetic Model for Analyzing the Oxygen Evolution Reaction. *ACS Catal.* **2020**, *10*, 8597-8610.
- (9) Lyons, M. E. G.; Brandon, M. P. A comparative study of the oxygen evolution reaction on oxidised nickel, cobalt and iron electrodes in base. *J. Electroanal. Chem.* **2010**, *641*, 119-130.
- (10) Bediako, D. K.; Surendranath, Y.; Nocera, D. G. Mechanistic studies of the oxygen evolution reaction mediated by a nickel-borate thin film electrocatalyst. *J. Am. Chem. Soc.* **2013**, *135*, 3662-3674.
- (11) Huynh, M.; Bediako, D. K.; Nocera, D. G. A functionally stable manganese oxide oxygen evolution catalyst in acid. *J. Am. Chem. Soc.* **2014**, *136*, 6002-6010.
- (12) Surendranath, Y.; Kanan, M. W.; Nocera, D. G. Mechanistic studies of the oxygen evolution reaction by a cobalt-phosphate catalyst at neutral pH. *J. Am. Chem. Soc.* **2010**, *132*, 16501-16509.
- (13) Moysiadou, A.; Lee, S.; Hsu, C. S.; Chen, H. M.; Hu, X. Mechanism of Oxygen Evolution Catalyzed by Cobalt Oxyhydroxide: Cobalt Superoxide Species as a Key Intermediate and Dioxygen Release as a Rate-Determining Step. *J. Am. Chem. Soc.* **2020**, *142*, 11901-11914.
- (14) Streeter, I.; Baron, R.; Compton, R. G. Voltammetry at nanoparticle and microparticle modified electrodes: theory and experiment. *J. Phy. Chem. C* **2007**, *111*, 17008-17014.

- (15) Bockris, J. O. M. Kinetics of activation controlled consecutive electrochemical reactions: anodic evolution of oxygen. *J. Chem. Phys.* **1956**, *24*, 817-827.
- (16) Bard, A. J.; Faulkner, L. R.; Leddy, J.; Zoski, C. G.: *Electrochemical methods: fundamentals and applications*; Wiley New York, 1980; Vol. 2.
- (17) Karkas, M. D.; Verho, O.; Johnston, E. V.; Akemark, B. Artificial photosynthesis: molecular systems for catalytic water oxidation. *Chem. Rev.* **2014**, *114*, 11863-12001.
- (18) Garrido-Barros, P.; Gimbert-Surinach, C.; Matheu, R.; Sala, X.; Llobet, A. How to make an efficient and robust molecular catalyst for water oxidation. *Chem. Soc. Rev.* **2017**, *46*, 6088-6098.
- (19) Chung, D. Y.; Park, S.; Lopes, P. P.; Stamenkovic, V. R.; Sung, Y.-E.; Markovic, N. M.; Strmcnik, D. Electrokinetic Analysis of Poorly Conductive Electrocatalytic Materials. *ACS Catal.* **2020**, *10*, 4990-4996.
- (20) Vrubel, H.; Moehl, T.; Gratzel, M.; Hu, X. Revealing and accelerating slow electron transport in amorphous molybdenum sulphide particles for hydrogen evolution reaction. *Chem. Commun.* **2013**, *49*, 8985-8987.
- (21) Zhang, P.; Li, L.; Nordlund, D.; Chen, H.; Fan, L.; Zhang, B.; Sheng, X.; Daniel, Q.; Sun, L. Dendritic core-shell nickel-iron-copper metal/metal oxide electrode for efficient electrocatalytic water oxidation. *Nat. Commun.* **2018**, *9*, 381.
- (22) Huang, Z.-F.; Song, J.; Du, Y.; Xi, S.; Dou, S.; Nsanzimana, J. M. V.; Wang, C.; Xu, Z. J.; Wang, X. Chemical and structural origin of lattice oxygen oxidation in Co–Zn oxyhydroxide oxygen evolution electrocatalysts. *Nat. Energy* **2019**, *4*, 329-338.
- (23) Grimaud, A.; Diaz-Morales, O.; Han, B.; Hong, W. T.; Lee, Y.-L.; Giordano, L.; Stoerzinger, K. A.; Koper, M. T. M.; Shao-Horn, Y. Activating lattice oxygen redox reactions in metal oxides to catalyze oxygen evolution. *Nat. Chem.* **2017**, *9*, 457-465.
- (24) Hung, S. F.; Chan, Y. T.; Chang, C. C.; Tsai, M. K.; Liao, Y. F.; Hiraoka, N.; Hsu, C. S.; Chen, H. M. Identification of Stabilizing High-Valent Active Sites by *Operando* High-Energy Resolution Fluorescence-Detected X-ray Absorption Spectroscopy for High-Efficiency Water Oxidation. *J. Am. Chem. Soc.* **2018**, *140*, 17263-17270.
- (25) Enman, L. J.; Stevens, M. B.; Dahan, M. H.; Nellist, M. R.; Toroker, M. C.; Boettcher, S. W. *Operando* X-Ray Absorption Spectroscopy Shows Iron Oxidation Is Concurrent with Oxygen Evolution in Cobalt-Iron (Oxy)hydroxide Electrocatalysts. *Angew. Chem. Int. Ed.* **2018**, *57*, 12840-12844.
- (26) Smith, R. D. L.; Pasquini, C.; Loos, S.; Chernev, P.; Klingan, K.; Kubella, P.; Mohammadi, M. R.; Gonzalez-Flores, D.; Dau, H. Spectroscopic identification of active sites for the oxygen evolution reaction on iron-cobalt oxides. *Nat. Commun.* **2017**, *8*, 2022.
- (27) Gong, L.; Chng, X. Y. E.; Du, Y.; Xi, S.; Yeo, B. S. Enhanced Catalysis of the Electrochemical Oxygen Evolution Reaction by Iron(III) Ions Adsorbed on Amorphous Cobalt Oxide. *ACS Catal.* **2018**, *8*, 807-814.
- (28) Zhang, M.; de Respinis, M.; Frei, H. Time-resolved observations of water oxidation intermediates on a cobalt oxide nanoparticle catalyst. *Nat. Chem.* **2014**, *6*, 362-367.

- (29) Favaro, M.; Yang, J.; Nappini, S.; Magnano, E.; Toma, F. M.; Crumlin, E. J.; Yano, J.; Sharp, I. D. Understanding the Oxygen Evolution Reaction Mechanism on CoOx using *Operando* Ambient-Pressure X-ray Photoelectron Spectroscopy. *J. Am. Chem. Soc.* **2017**, *139*, 8960-8970.
- (30) Kanan, M. W.; Yano, J.; Surendranath, Y.; Dinca, M.; Yachandra, V. K.; Nocera, D. G. Structure and valency of a cobalt– phosphate water oxidation catalyst determined by in situ X-ray spectroscopy. *J. Am. Chem. Soc.* **2010**, *132*, 13692-13701.
- (31) Wang, H. Y.; Hung, S. F.; Chen, H. Y.; Chan, T. S.; Chen, H. M.; Liu, B. In *Operando* Identification of Geometrical-Site-Dependent Water Oxidation Activity of Spinel Co<sub>3</sub>O<sub>4</sub>. *J. Am. Chem. Soc.* **2016**, *138*, 36-39.
- (32) Ullman, A. M.; Brodsky, C. N.; Li, N.; Zheng, S. L.; Nocera, D. G. Probing Edge Site Reactivity of Oxidic Cobalt Water Oxidation Catalysts. *J. Am. Chem. Soc.* **2016**, *138*, 4229-4236.
- (33) Wasylenko, D. J.; Ganesamoorthy, C.; Borau-Garcia, J.; Berlinguette, C. P. Electrochemical evidence for catalytic water oxidation mediated by a high-valent cobalt complex. *Chem. Commun.* **2011**, *47*, 4249-4251.
- (34) Ishizuka, T.; Watanabe, A.; Kotani, H.; Hong, D.; Satonaka, K.; Wada, T.; Shiota, Y.; Yoshizawa, K.; Ohara, K.; Yamaguchi, K.; Kato, S.; Fukuzumi, S.; Kojima, T. Homogeneous Photocatalytic Water Oxidation with a Dinuclear Co(III)-Pyridylmethylamine Complex. *Inorg. Chem.* **2016**, *55*, 1154-1164.
- (35) Wang, H. Y.; Hung, S. F.; Hsu, Y. Y.; Zhang, L.; Miao, J.; Chan, T. S.; Xiong, Q.; Liu, B. In Situ Spectroscopic Identification of  $\mu$ -OO Bridging on Spinel Co<sub>3</sub>O<sub>4</sub> Water Oxidation Electrocatalyst. *J. Phys. Chem. Lett.* **2016**, *7*, 4847-4853.
- (36) Gerken, J. B.; McAlpin, J. G.; Chen, J. Y.; Rigsby, M. L.; Casey, W. H.; Britt, R. D.; Stahl, S. S. Electrochemical water oxidation with cobalt-based electrocatalysts from pH 0-14: the thermodynamic basis for catalyst structure, stability, and activity. *J. Am. Chem. Soc.* **2011**, *133*, 14431-14442.
- (37) Halck, N. B.; Petrykin, V.; Krtil, P.; Rossmeisl, J. Beyond the volcano limitations in electrocatalysis--oxygen evolution reaction. *Phys. Chem. Chem. Phys.* **2014**, *16*, 13682-13688.
- (38) Friebe, D.; Louie, M. W.; Bajdich, M.; Sanwald, K. E.; Cai, Y.; Wise, A. M.; Cheng, M. J.; Sokaras, D.; Weng, T. C.; Alonso-Mori, R.; Davis, R. C.; Bargar, J. R.; Norskov, J. K.; Nilsson, A.; Bell, A. T. Identification of highly active Fe sites in (Ni,Fe)OOH for electrocatalytic water splitting. *J. Am. Chem. Soc.* **2015**, *137*, 1305-1313.
- (39) Goldsmith, Z. K.; Harshan, A. K.; Gerken, J. B.; Vörös, M.; Galli, G.; Stahl, S. S.; Hammes-Schiffer, S. Characterization of NiFe oxyhydroxide electrocatalysts by integrated electronic structure calculations and spectroelectrochemistry. *Proc. Natl. Acad. Sci. USA* **2017**, *114*, 3050-3055.
- (40) Kroll, N.; Speckmann, I.; Schoknecht, M.; Gulzow, J.; Diekmann, M.; Pfrommer, J.; Stritt, A.; Schlangen, M.; Grohmann, A.; Horner, G. O-O Bond Formation and Liberation of Dioxygen Mediated by N5 -Coordinate Non-Heme Iron(IV) Complexes. *Angew. Chem. Int. Ed.* **2019**, *58*, 13472-13478.
- (41) Fillol, J. L.; Codola, Z.; Garcia-Bosch, I.; Gomez, L.; Pla, J. J.; Costas, M. Efficient water oxidation catalysts based on readily available iron coordination complexes. *Nat. Chem.* **2011**, *3*, 807-813.

- (42) Martirez, J. M. P.; Carter, E. A. Unraveling Oxygen Evolution on Iron-Doped beta-Nickel Oxyhydroxide: The Key Role of Highly Active Molecular-like Sites. *J. Am. Chem. Soc.* **2019**, *141*, 693-705.
- (43) Diaz-Morales, O.; Ferrus-Suspedra, D.; Koper, M. T. M. The importance of nickel oxyhydroxide deprotonation on its activity towards electrochemical water oxidation. *Chem. Sci.* **2016**, *7*, 2639-2645.
- (44) Pham, H. H.; Cheng, M.-J.; Frei, H.; Wang, L.-W. Surface Proton Hopping and Fast-Kinetics Pathway of Water Oxidation on Co<sub>3</sub>O<sub>4</sub> (001) Surface. *ACS Catal.* **2016**, *6*, 5610-5617.
- (45) Bajdich, M.; Garcia-Mota, M.; Vojvodic, A.; Norskov, J. K.; Bell, A. T. Theoretical investigation of the activity of cobalt oxides for the electrochemical oxidation of water. *J. Am. Chem. Soc.* **2013**, *135*, 13521-13530.
- (46) Bai, L.; Hsu, C. S.; Alexander, D. T. L.; Chen, H. M.; Hu, X. A Cobalt-Iron Double-Atom Catalyst for the Oxygen Evolution Reaction. *J. Am. Chem. Soc.* **2019**, *141*, 14190-14199.
- (47) Fei, H.; Dong, J.; Feng, Y.; Allen, C. S.; Wan, C.; Voloskiy, B.; Li, M.; Zhao, Z.; Wang, Y.; Sun, H.; An, P.; Chen, W.; Guo, Z.; Lee, C.; Chen, D.; Shakir, I.; Liu, M.; Hu, T.; Li, Y.; Kirkland, A. I.; Duan, X.; Huang, Y. General synthesis and definitive structural identification of MN<sub>4</sub>C<sub>4</sub> single-atom catalysts with tunable electrocatalytic activities. *Nat. Catal.* **2018**, *1*, 63-72.
- (48) Guan, J.; Duan, Z.; Zhang, F.; Kelly, S. D.; Si, R.; Dupuis, M.; Huang, Q.; Chen, J. Q.; Tang, C.; Li, C. Water oxidation on a mononuclear manganese heterogeneous catalyst. *Nat. Catal.* **2018**, *1*, 870-877.
- (49) Chen, S.; Duan, J.; Jaroniec, M.; Qiao, S. Z. Three-dimensional N-doped graphene hydrogel/NiCo double hydroxide electrocatalysts for highly efficient oxygen evolution. *Angew. Chem. Int. Ed.* **2013**, *52*, 13567-13570.
- (50) Lee, S.; Banjac, K.; Lingenfelder, M.; Hu, X. Oxygen Isotope Labelling Experiments Reveal Different Reaction Sites for the Oxygen Evolution Reaction on Nickel and Nickel Iron Oxides. *Angew. Chem. Int. Ed.* **2019**, *58*, 10295 –10299.
- (51) Chen, J. Y.; Dang, L.; Liang, H.; Bi, W.; Gerken, J. B.; Jin, S.; Alp, E. E.; Stahl, S. S. *Operando* Analysis of NiFe and Fe Oxyhydroxide Electrocatalysts for Water Oxidation: Detection of Fe(4)(+) by Mossbauer Spectroscopy. *J. Am. Chem. Soc.* **2015**, *137*, 15090-15093.
- (52) Ahn, H. S.; Bard, A. J. Surface Interrogation Scanning Electrochemical Microscopy of Ni(1-x)Fe(x)OOH (0 < x < 0.27) Oxygen Evolving Catalyst: Kinetics of the "fast" Iron Sites. *J. Am. Chem. Soc.* **2016**, *138*, 313-318.
- (53) Liu, F.; Concepcion, J. J.; Jurss, J. W.; Cardolaccia, T.; Templeton, J. L.; Meyer, T. J. Mechanisms of water oxidation from the blue dimer to photosystem II. *Inorg. Chem.* **2008**, *47*, 1727-1752.
- (54) Mavros, M. G.; Tsuchimochi, T.; Kowalczyk, T.; McIsaac, A.; Wang, L. P.; Voorhis, T. V. What can density functional theory tell us about artificial catalytic water splitting? *Inorg. Chem.* **2014**, *53*, 6386-6397.

# Chapter 5 Spectroscopic and electrokinetic evidence for a bifunctional mechanism of the oxygen evolution reaction

The results presented in this chapter were published in:

**L. Bai**+, S. Lee+, X. Hu\* Spectroscopic and electrokinetic evidence for a bifunctional mechanism of the oxygen evolution reaction. *Angew. Chem. Int. Ed.* 2020, DOI: <https://doi.org/10.1002/anie.202011388>

Reprinted (adapted) with permission from [1]. Copyright 2020 Wiley-VCH.

An early version of the results were also published as a preprint:

**L. Bai**+, S. Lee+, X. Hu\* Spectroscopic and electrokinetic evidence for a bifunctional mechanism of the oxygen evolution reaction. Chemrxiv, preprint, link: <https://doi.org/10.26434/chemrxiv.12661514.v2>



## 5.1 Introduction

As depicted in Section 1.4.1, Chapter 1, for oxygen evolution reaction (OER) catalyzed by metal oxides and oxyhydroxides, the most commonly assumed mechanism involves four consecutive proton-coupled electron transfer (PCET) processes, where the O-O bond forming step is nucleophile attack of water or hydroxide on a metal-oxo species (Figure 1.6a, Chapter 1).<sup>2,3</sup> Density functional theory (DFT) computations revealed a scaling relationship between the adsorption energies of  $\text{OH}^*$ ,  $\text{O}^*$ , and  $\text{OOH}^*$ .<sup>3,4</sup> In particular, the difference of the adsorption energies of  $\text{*OH}$  and  $\text{*OOH}$  is always 3.2 eV for nearly all metal oxides.<sup>3,4</sup> This scaling relationship poses an upper limit on the performance of OER catalysts, which has a theoretical overpotential of about 0.4 eV, with the uncertainty of 0.2 V.<sup>3,4</sup>

To break the performance limit imposed by the scaling relationship, a change of catalytic mechanism is required.<sup>5,6</sup> A “bifunctional” mechanism has recently been proposed.<sup>6-9</sup> This mechanism involves two catalytic sites, often based on two different metal ions, which work in a cooperative manner (Figure 1.9, Chapter 1). One site provides the electrophilic  $\text{M=O}$  entity, while the other side provides a hydrogen atom acceptor (A). Although the direct nucleophilic attack of an  $\text{OH}^-$  on the  $\text{M=O}$  to form the  $\text{M-OOH}$  intermediate is energetically too unfavourable, a concerted hydrogen atom transfer to the neighbouring acceptor significantly lowers the energetics. Up until now, however, the bifunctional mechanism is supported by DFT computations only.<sup>6-9</sup> Our group previously developed an  $\text{FeOOH-NiOOH}$  composite catalyst, where nanoclusters of  $\gamma$ - $\text{FeOOH}$  covalently linked to a  $\gamma$ - $\text{NiOOH}$  support. This catalyst is significantly more active than conventional Ni-Fe oxyhydroxides and related layered double hydroxides ( $\text{NiFeO}_x\text{H}_y$  and  $\text{NiFe LDH}$ ), which were the benchmark OER catalysts in alkaline medium.<sup>9</sup> According to DFT computations, the structure of  $\text{FeOOH-NiOOH}$  could enable a bifunctional mechanism where the O-O bond forming step is a nucleophilic attack of  $\text{OH}^-$  on a  $\text{Fe=O}$  moiety coupled with a concerted hydrogen atom transfer to a nearby terrace O site on the  $\gamma$ - $\text{NiOOH}$  support.

In this Chapter, we present experimental evidences including *operando* Raman spectroscopy and electrokinetic data to support this bifunctional mechanism. We compared the OER performance and catalytic behavior of two model catalysts,  $\text{FeOOH-NiOOH}$  and  $\text{NiFe LDH}$ . The data support two distinct mechanisms for the two catalysts.  $\text{FeOOH-NiOOH}$  operates by a bifunctional mechanism where the rate-determining O-O bond forming step is the  $\text{OH}^-$  attack on a  $\text{Fe=O}$  coupled with a hydrogen atom transfer to a deprotonated  $\text{Ni}^{\text{III}}\text{-O}$  site, whereas  $\text{NiFe LDH}$

operates by a conventional mechanism of four consecutive PCET steps. The experimental validation of the bifunctional mechanism stimulates both the mechanistic understanding and the design principles of OER catalysts.

## 5.2 Basic characterization

FeOOH-NiOOH was prepared by dipping a clean nickel foam (NF) in a solution of FeCl<sub>3</sub>, drying in air at 80 °C, followed by multiple cyclic voltammetry (CV) scans activation in a Fe-containing KOH.<sup>9</sup> While the previous work assigned the support as pure NiOOH<sup>9</sup>, we found in the present study that some Fe ions were incorporated in the lattice of NiOOH, which resulted in a positive shift of the Ni(OH)<sub>2</sub>/NiOOH oxidation potential during the formation of FeOOH-NiOOH (Figure 5.1a).<sup>10-12</sup> Since the precursor Fe<sup>3+</sup> solution is oxidative and acidic, Ni<sup>2+</sup> is generated when dipping NF in Fe<sup>3+</sup> solution<sup>13</sup>. Then the Fe doped NiO<sub>x</sub>H<sub>y</sub> (NiFeO<sub>x</sub>H<sub>y</sub>) is formed on the surface of NF during the drying process. The excess Fe is transformed to γ-FeOOH after drying (Figure 5.1b-c).

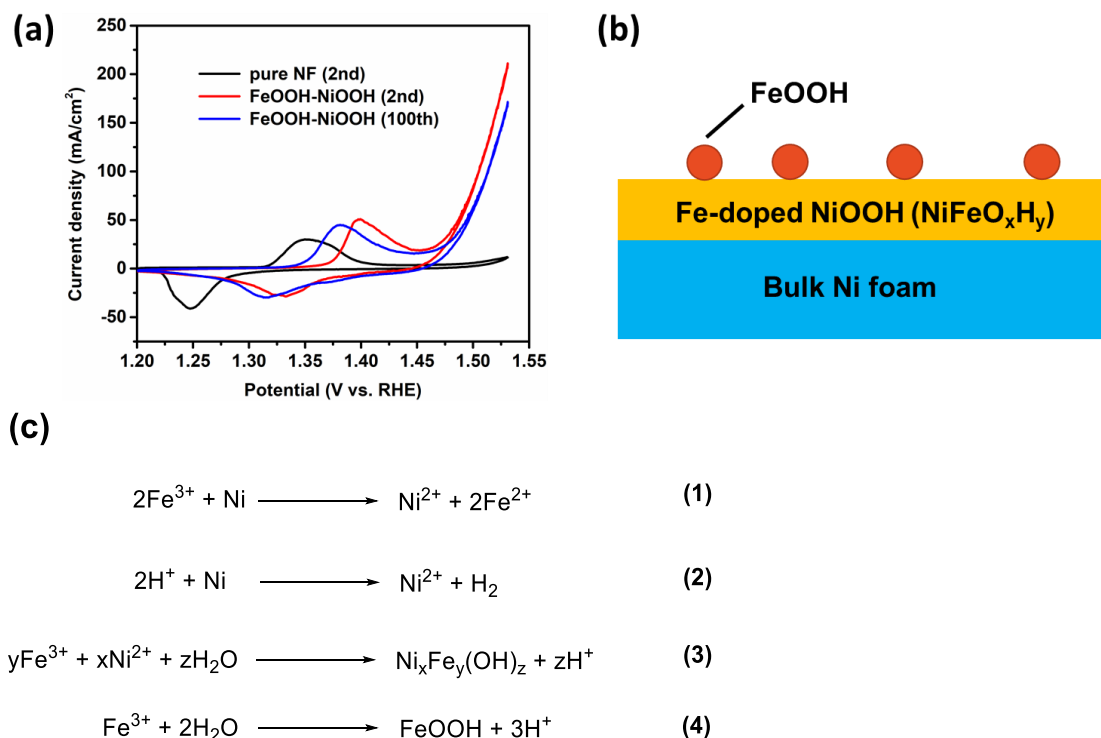


**Figure 5.1** Possible generation process of FeOOH-NiOOH (a) 2nd (red) and 100th (blue) CVs of as-prepared FeOOH-NiOOH and 2nd of pure NF (black). (b) Illustrated scheme for the composition of FeOOH-NiOOH. (c) Possible reactions for generating Fe-doped NiOOH and FeOOH. The 2<sup>nd</sup> CV was adopted since the 1<sup>st</sup> CV contains big background signals.

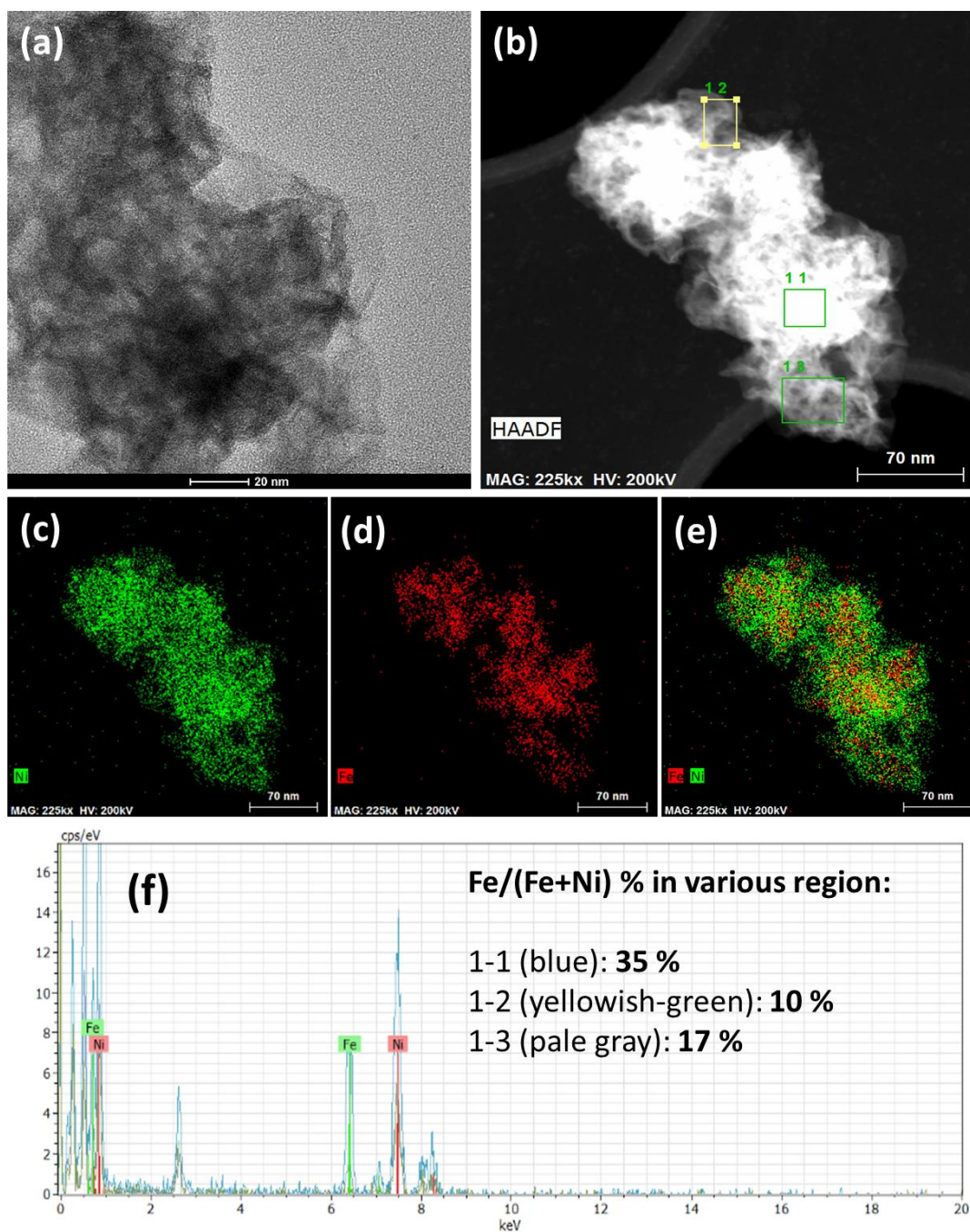


**Figure 5.2** Microscopic characterization of FeOOH-NiOOH. (a) TEM, (b) HAADF-STEM, (c-e) corresponding EDX mapping images of Ni, Fe and overlay of Ni and Fe. (f) EDX spectra of three different regions in (b), the Fe content in three different regions is indicated.

In FeOOH-NiOOH, the distribution of Fe was not uniform, according to transimission electron microscopy (TEM), high-angle annular scanning transimission electron microscopy (HAADF-

STEM), and corresponding energy dispersed X-ray (EDX) mapping images and spectrum (Figure 5.2).

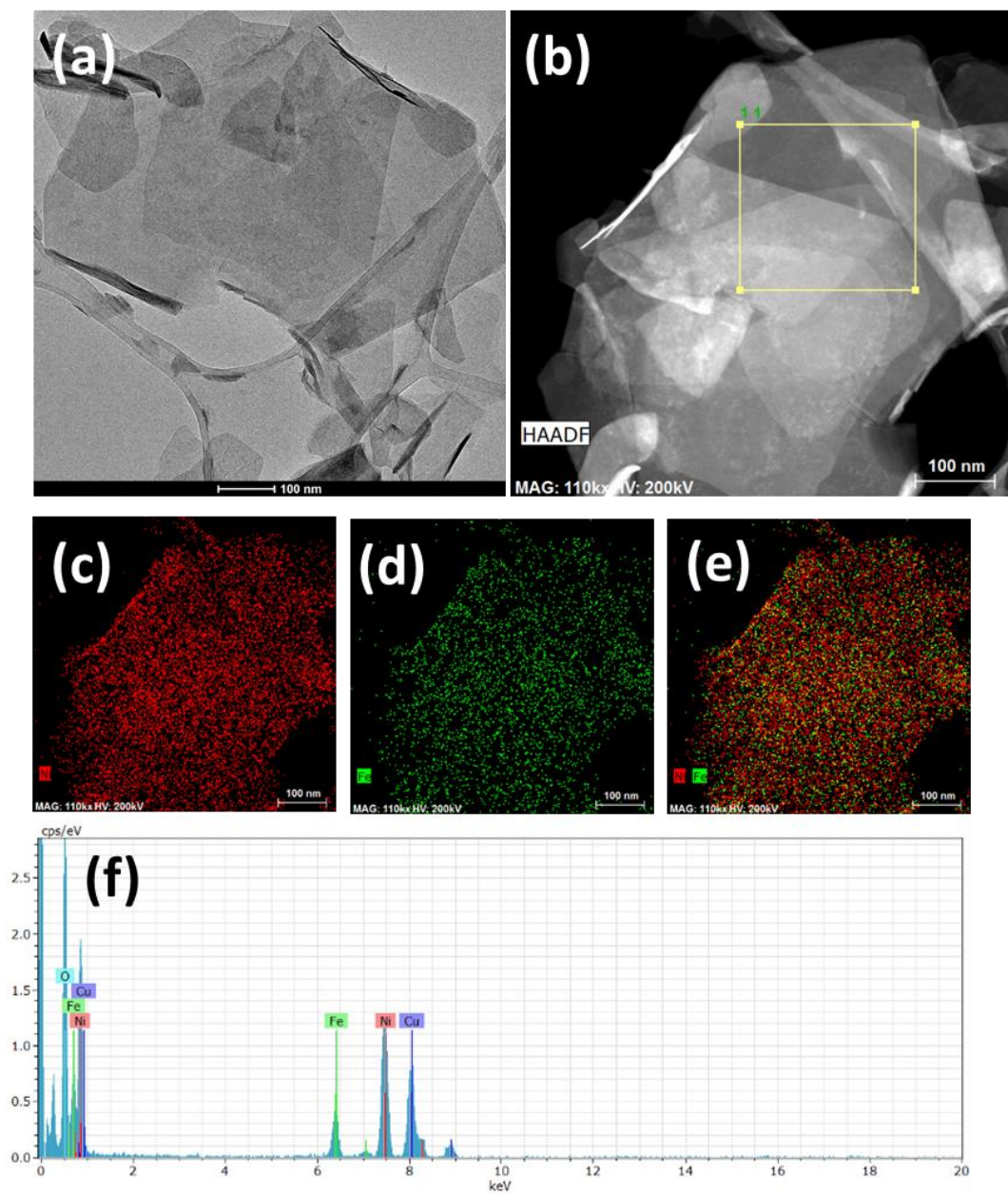


**Figure 5.3** Microscopic characterization of NiFe LDH. (a) TEM, (b) HAADF-STEM, (c-e) corresponding EDX mapping images of Ni, Fe and overlay of Ni and Fe. (f) EDX spectrum of the region in (b), the Fe content is  $22 \pm 2$  %.

NiFe LDH was synthesized according to a reported hydrothermal reaction method.<sup>14</sup> Layered structure was observed in TEM and HAADF-STEM images (Figures 5.3a and 5.3b). Unlike



FeOOH-NiOOH, both Ni and Fe ions appeared to be uniformly distributed in NiFe LDH, and the Fe content was about 22% (Figures 5.3c-5.3f).

### 5.3 Activity comparison for OER

The activity of FeOOH-NiOOH and NiFe LDH was compared with similar Fe loadings (see Figure 5.13 for details). Previous study indicated that some FeOOH was generated on pure NF during multiple CVs activation.<sup>9</sup> To avoid the interference of the formation of FeOOH-NiOOH species on NF during OER test, the activity of NiFe LDH was tested on a carbon-cloth (CC) electrode. Both catalysts were activated by multiple CV scans (Figures 5.1a and 5.4). The activation of FeOOH-NiOOH was related to the incorporation of Fe ions and formation of FeOOH as reported previously.<sup>9</sup> The activation of NiFe LDH was related to a morphology change that increased the surface area, which was indicated by the increase of areas of the redox peaks assigned to Ni(OH)<sub>2</sub> to NiOOH transition (Figure 5.4). Moreover, TEM and HAADF-STEM images (Figures 5.5a and 5.5b) showed that the initial large lamellar structure cracked into small layers upon activation, while the Fe/(Ni+Fe) ratio remained unchanged (Figures 5.3f and 5.5f).

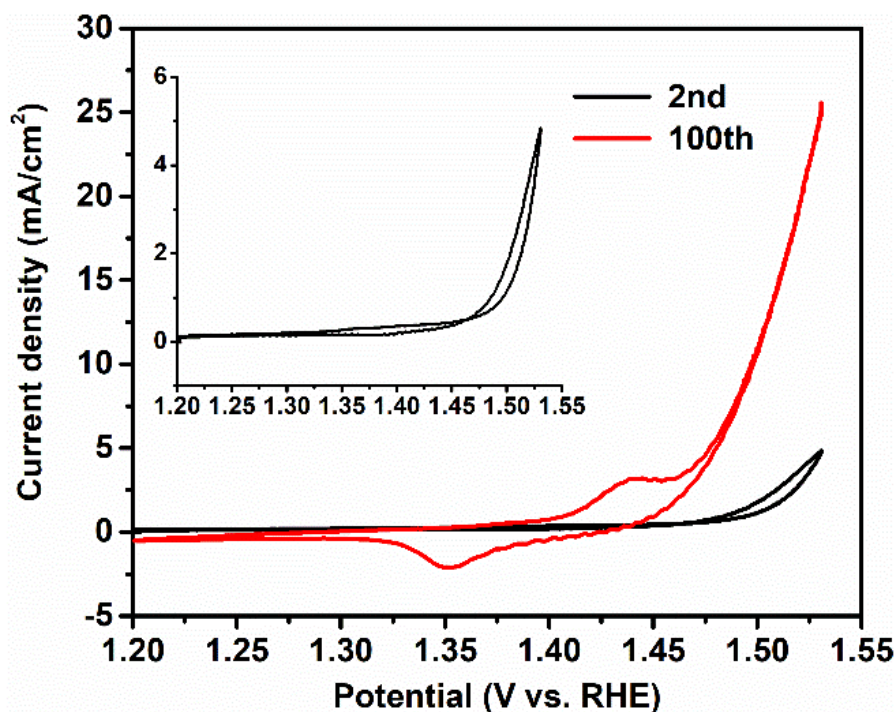


**Figure 5.4** 2<sup>nd</sup> and 100<sup>th</sup> CVs of NiFe LDH in 1 M KOH. Inset is the enlarged graph of the initial 2<sup>nd</sup> CV.

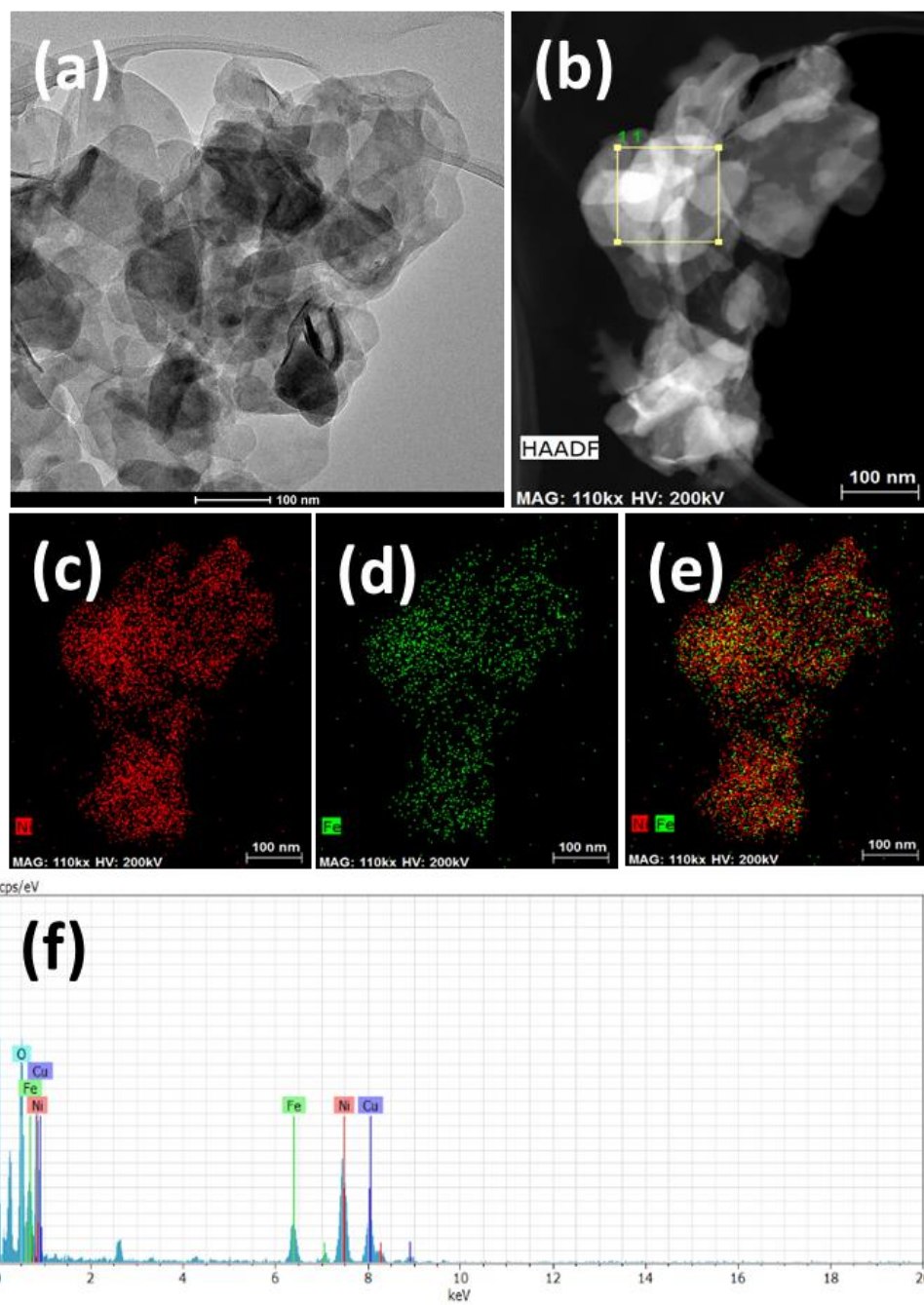


**Figure 5.5** Microscopic characterization of NiFe LDH after multiple CVs activation. (a) TEM, (b) HAADF-STEM, (c-e) corresponding EDX mapping images of Ni, Fe and overlay of Ni and Fe. (f) EDX spectrum of the region in (b), the Fe content is  $21 \pm 2$  %.

The activity of FeOOH-NiOOH is significantly more active than that of NiFe LDH, both in apparent geometric activity (Figure 5.6a) and in electrochemical active surface area (ECSA)-averaged activity (Figure 5.6b). The turnover frequencies (TOFs) were also compared assuming a bimetallic Ni-Fe active site for both catalysts (Figure 5.6c). The FeOOH-NiOOH has TOFs that are about 10 times higher than those of NiFe LDH. Albeit FeOOH-NiOOH also contains Fe-doped NiOOH species, the above data (Figure 5.6) indicates a difference in the active sites of FeOOH-NiOOH and NiFe LDH, and confirms that the Fe-doped NiOOH support had no noticeable contribution to the measured activity of FeOOH-NiOOH.

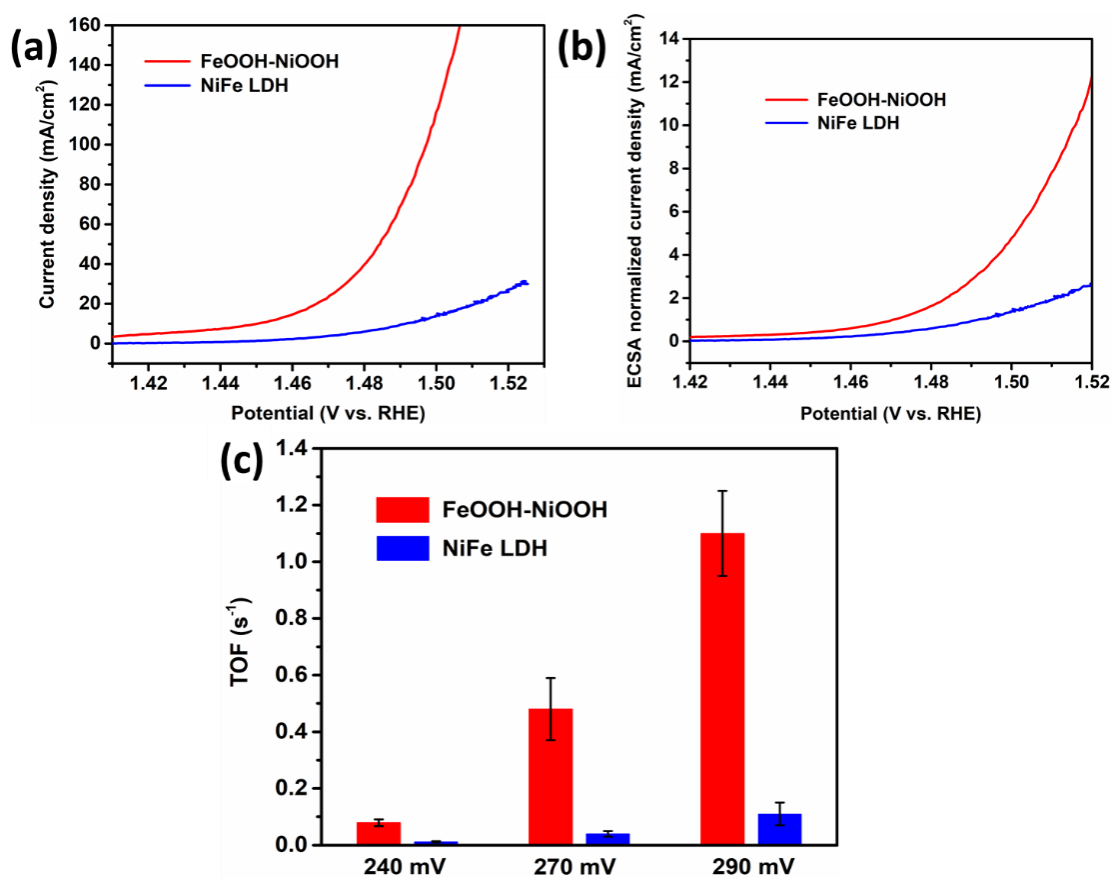


**Figure 5.6** Electrocatalytic activity comparison of FeOOH-NiOOH and NiFe LDH. (a) Linear scan voltammetry (LSV) curves and (b) ECSA normalized activity of FeOOH-NiOOH (red) and NiFe LDH (blue) in 1 M KOH. (c) Comparison of TOFs of FeOOH-NiOOH (red) and NiFe LDH (blue) at various overpotentials. Three independent experiments showed that the double layer capacitance of FeOOH-NiOOH is  $1.97 \pm 0.23 \text{ mF}/\text{cm}^2$ , while that of NiFe LDH is  $0.78 \pm 0.11 \text{ mF}/\text{cm}^2$ . The specific capacitance of electrode based on  $\text{NiFeO}_x$  is assumed as  $0.081 \text{ mF}/\text{cm}^2$ , according to the literature.<sup>15</sup>

## 5.4 Operando Raman Spectroscopy

### 5.4.1 Potential and position dependent *operando* Raman Spectroscopy

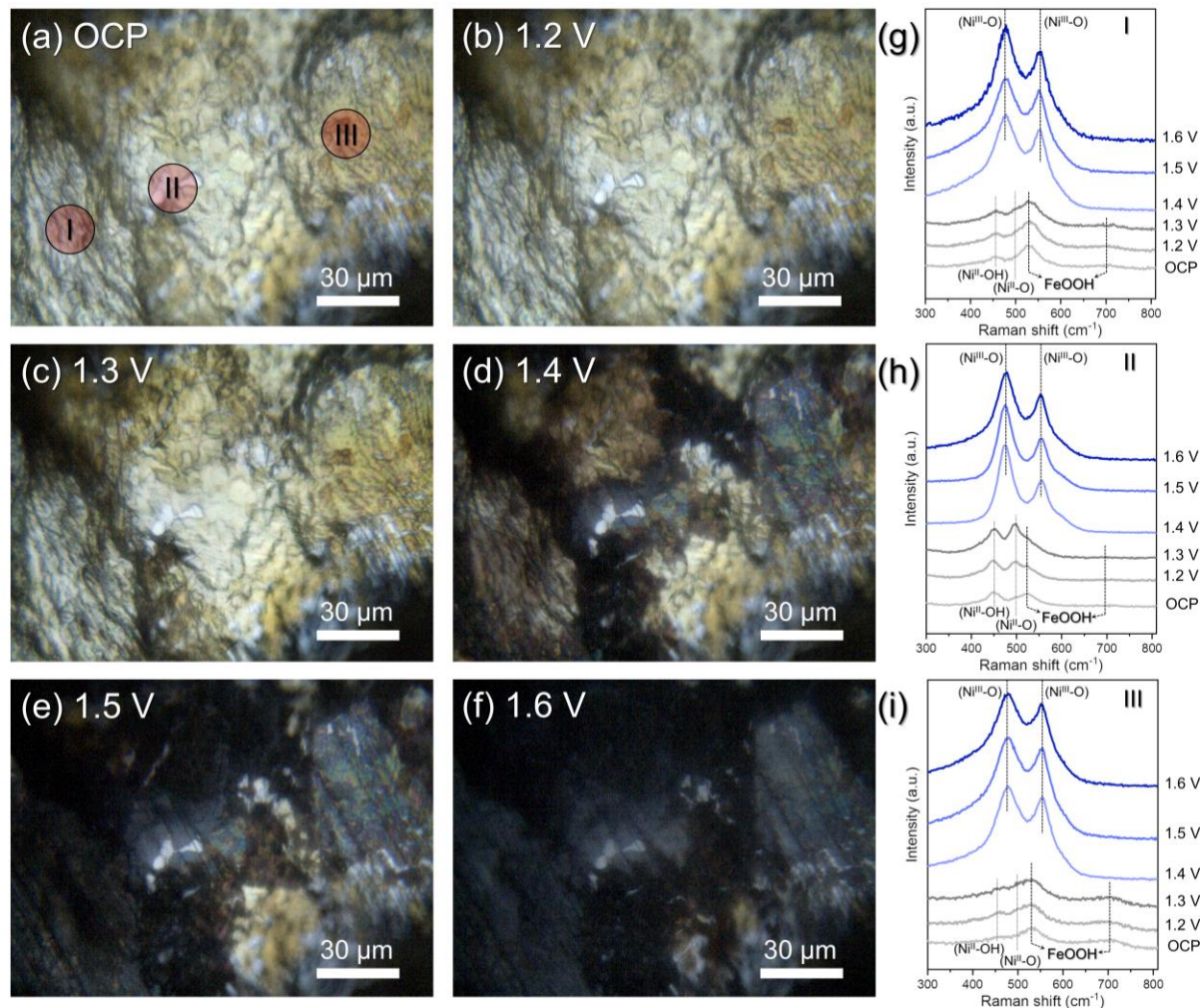


**Figure 5.7** *Operando* Raman spectroscopic analysis of FeOOH-NiOOH. (a-f) Optical microscopy images of FeOOH-NiOOH at different applied potentials and (g-i) the corresponding *operando* Raman spectra obtained from three different spots as indicated in the (a).

Raman spectroscopy is sensitive to the catalyst/electrolyte solution interface, which reflects the information of the change of the phase and oxidation state of the materials.<sup>16</sup> Since the predicted bifunctional OER mechanism involves interfacial catalysis, therefore *operando* Raman spectroscopy is suitable for monitoring the different dynamic behavior of the two model catalysts. Figure 5.7 shows *operando* Raman optical microscopy images and spectra of FeOOH-NiOOH,



recorded from the open circuit potential (OCP) to 1.6 V (vs. Reversible Hydrogen Electrode, RHE) with an interval of 0.1 V. The surface morphology of FeOOH-NiOOH can be viewed by microscope objective of Raman. Due to existence of FeOOH, the surface looks brownish-yellow at OCP compared with bare NF (Figure 5.8), which is silver-white.<sup>9,17</sup> The Raman signals were collected from three different beam spots (I, II, and III in Figure 5.7a). Consistent with previous XAS results<sup>9</sup>, surface  $\gamma$ -FeOOH species were identified by two main Raman bands at 526  $\text{cm}^{-1}$  and 690  $\text{cm}^{-1}$  (Figure 5.7g-i).<sup>9,13,18</sup> At 1.4 V and above, two strong Raman bands at around 480 and 560  $\text{cm}^{-1}$  were observed (Figure 5.7g-i). These two bands correspond to the Ni-O bending and stretching vibrations of NiOOH, respectively.<sup>12,19-22</sup> Their appearance indicated the presence of NiOOH at these potentials, again consistent with previous XAS data.<sup>9</sup> At the three chosen spots on the surface, the relative intensities of the 480  $\text{cm}^{-1}$  and 560  $\text{cm}^{-1}$  bands ( $I_B/I_S$ ) and the half-widths of the two bands vary, indicating different local environments around the Ni-O bonds. Fe-incorporation into NiOOH causes structural defects and disorder of lattice, which leads to a lower  $I_B/I_S$ .<sup>12,19,22</sup> Accordingly, the amount of Fe dopant in the NiOOH at the three spots follows the order of: III > I > II. In summary, the potential-dependent Raman spectra vary at three different spots of the surface (Figure 5.7g-i), indicating a surface heterogeneity, which is consistent with TEM and EDX mapping images (Figure 5.2) showed that Fe ions were not uniformly distributed on the surface.

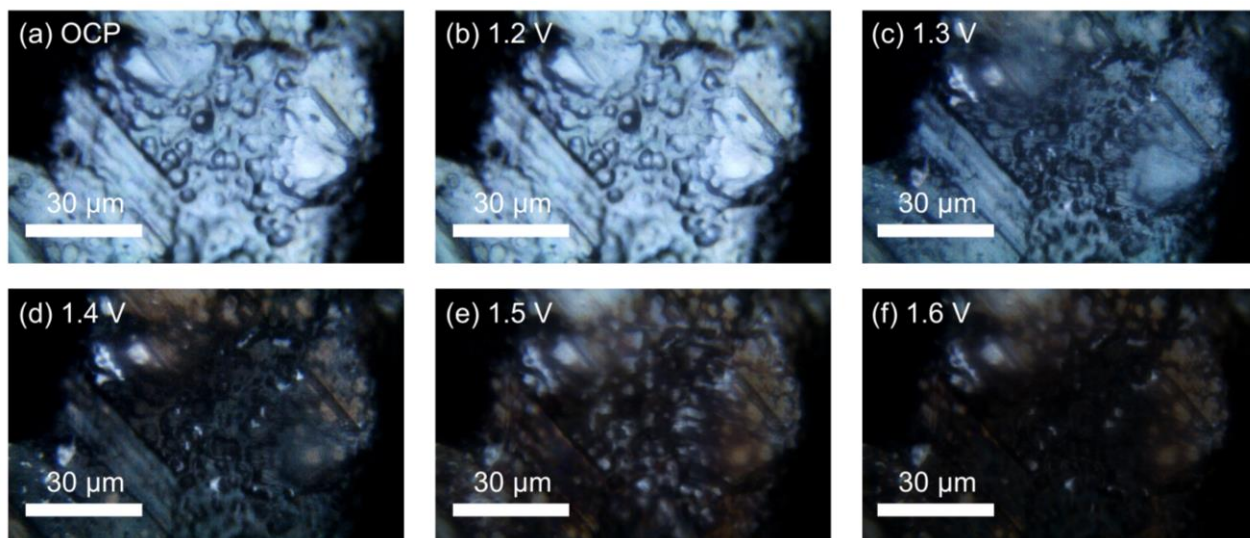


**Figure 5.8** Optical microscopy images of bare NF at different applied potentials.

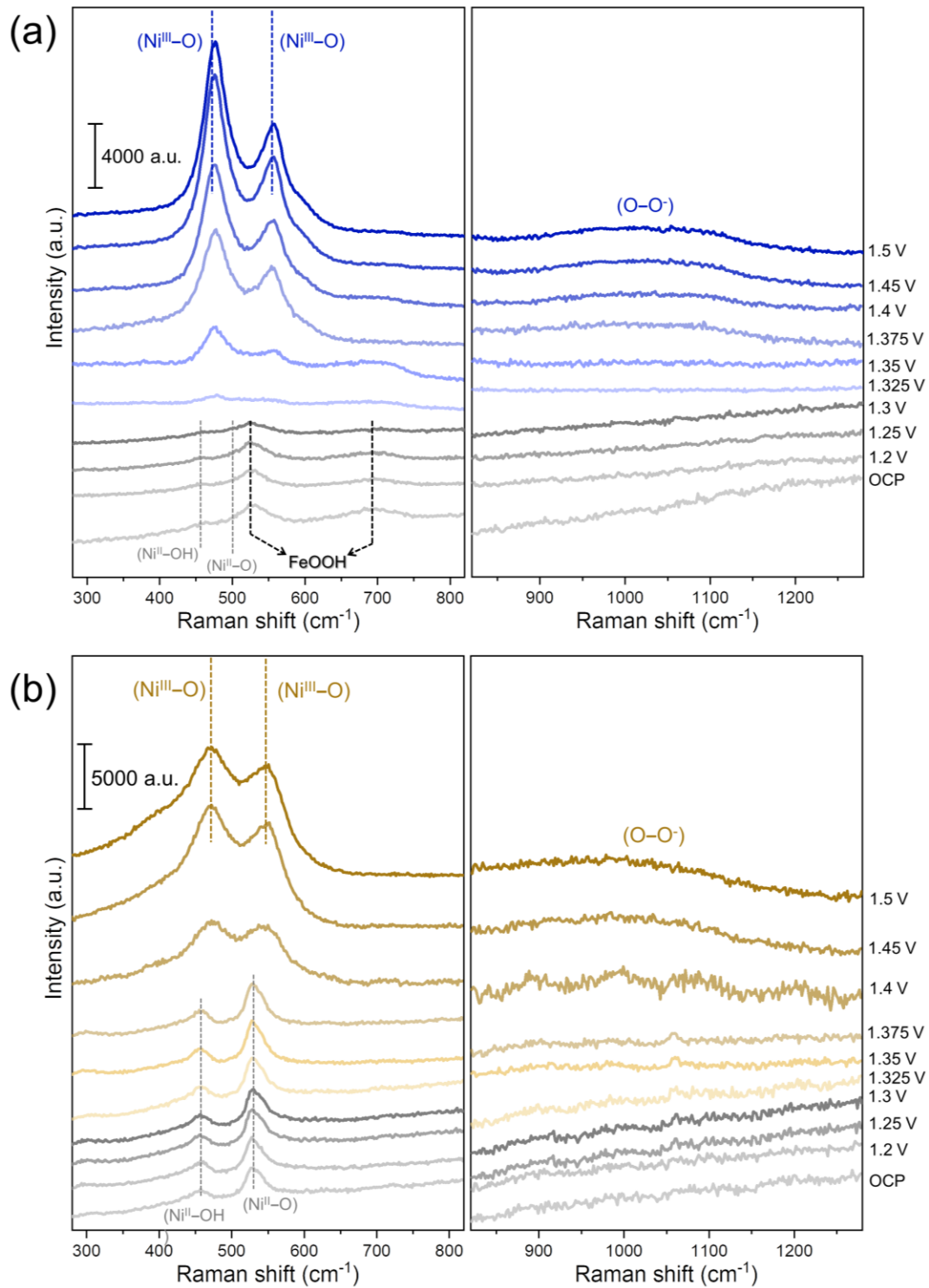


**Figure 5.9** Operando Raman spectra of (a) FeOOH-NiOOH and (b) NiFe LDH recorded at different applied potentials.

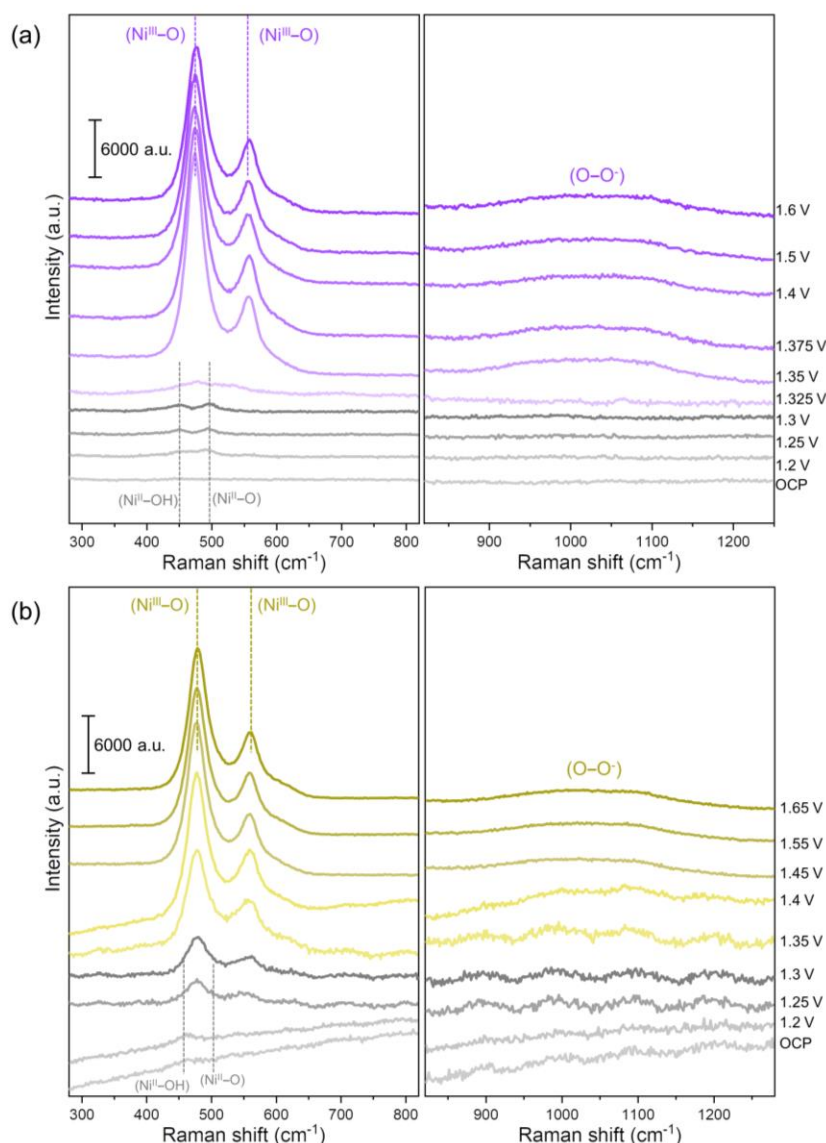


**Figure 5.10** *Operando* Raman spectra of (a) bare NF and (b)  $\text{Ni}(\text{OH})_2$  recorded in the potential range of 1.2 V to 1.6 V and 1.65 V respectively.

We directly compared the representative *operando* Raman spectra of  $\text{FeOOH-NiOOH}$  (region I) and  $\text{NiFe LDH}$  from OCP to 1.5 V (Figure 5.9). The *operando* Raman spectra of pure NF and pure  $\text{Ni}(\text{OH})_2$  were also investigated as the references (Figure 5.10). At OCP, Ni is mostly in the +2 oxidation state (in the form of  $\text{Ni}(\text{OH})_2$ ) for all the samples (Figures 5.9 and 5.10). For  $\text{NiFe LDH}$ , there are no spectral features corresponding to  $\gamma\text{-FeOOH}$  (Figure 5.9). Compared to  $\text{Ni}(\text{OH})_2$  and pure NF,  $\text{NiFe LDH}$  exhibited a peak corresponding to  $\text{Ni}^{\text{II}}\text{-O}$  vibration at around  $525\text{ cm}^{-1}$  but not  $500\text{ cm}^{-1}$ , which originates from the structural disorder induced by Fe doping (Figures 5.9b

and Figure 5.10).<sup>18,22,23</sup>. In NiFe LDH, the two Raman bands of Ni<sup>III</sup>-O (from NiOOH) began to grow from 1.375 V and the growth was completed at around 1.45 V (Figure 5.9b). For FeOOH-NiOOH, a broad band in the frequency range of 900 to 1150 cm<sup>-1</sup>, which is attributed to Ni-OO<sup>-</sup>,<sup>19-21,24</sup> was observed from 1.375 V (Figure 5.9a). In the case of NiFe LDH, on the contrary, the broad band in higher frequency range of 900 to 1150 cm<sup>-1</sup>, due to Ni-OO<sup>-</sup>,<sup>19-21,24</sup> appeared from about 1.4 V (Figure 5.9b). These results suggested Ni in FeOOH-NiOOH is earlier oxidized compared to Ni in NiFe LDH, consistent with CVs in Figure 5.1a and Figure 5.4. The emergence of Raman peaks corresponding to NiOOH and Ni-OO<sup>-</sup> was clearly earlier in the reference Ni(OH)<sub>2</sub> and bare NF samples (Figure 5.10). The results were in accordance with previous literatures that Fe doping anodically shifted the oxidation potential of Ni<sup>II</sup>/Ni<sup>III</sup>. Additionally, the I<sub>B</sub>/I<sub>S</sub> of NiFe LDH (1.18) was significantly lower than that of FeOOH-NiOOH (1.72), bare NF (1.91), and Ni(OH)<sub>2</sub> (2.2), indicative of both FeOOH-NiOOH and NiFe LDH has the Fe incorporation in the lattice of NiOOH, while NiFe LDH has the highest structural disorder among the four samples (Figures 5.9 and 5.10).

The above *operando* Raman spectra revealed the presence of surface  $\gamma$ -FeOOH in FeOOH-NiOOH, but not in NiFe LDH. Otherwise, the two catalysts have a similar component, Fe-doped  $\gamma$ -NiOOH. Bulk  $\gamma$ -FeOOH is a poor OER catalyst,<sup>25,26</sup> whereas the surface  $\gamma$ -FeOOH here is responsible for remarkable OER activity (Figures 5.1a and 5.6). In addition, *operando* Raman of pure FeOOH showed no obvious changes in peaks associated with  $\gamma$ -FeOOH at increasing potential from OCP to 1.8 V (Figure 5.11). These results suggest FeOOH-NiOOH should have a mechanism that involves more than  $\gamma$ -FeOOH alone. The doping of Fe in NiOOH causes structural disorder in the lattice of NiOOH, which could be inferred by the I<sub>B</sub>/I<sub>S</sub> of the Raman spectra of NiOOH.<sup>12,19,22</sup> The lower structural disorder of FeOOH-NiOOH compared to NiFe LDH is consistent with most Fe ions being on the surface in FeOOH-NiOOH but in the bulk of NiFe LDH.

A previous study reported that FeOOH was not a stable OER catalyst in alkaline medium and would be dissolved at high overpotentials.<sup>25</sup> We found that the Fe loadings of FeOOH-NiOOH indeed decreased after activation by multiple CVs (Figure 5.13b). However, after activation, both the loading of Fe and the OER activity remained stable in an 18 h electrolysis at 10 mA/cm<sup>2</sup> (Figures 5.13b and 5.12a). The Raman spectra were measured after 1 h, 2 h, 3 h and 18 h of constant current electrolysis, showing no obvious changes of the peaks associated with  $\gamma$ -FeOOH (Figure 5.12b). The improved stability of FeOOH in FeOOH-NiOOH compared to bare FeOOH is probably due to the covalent interaction with the NiOOH substrate.

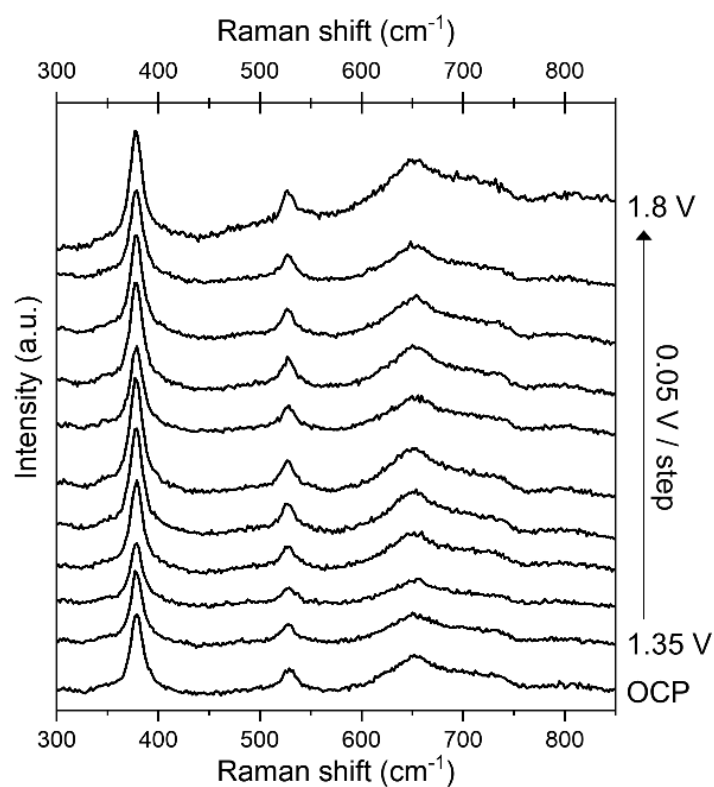


**Figure 5.11** Operando Raman spectra of pure  $\gamma$ -FeOOH recorded in the potential range of OCP, 1.35 V to 1.8 V.

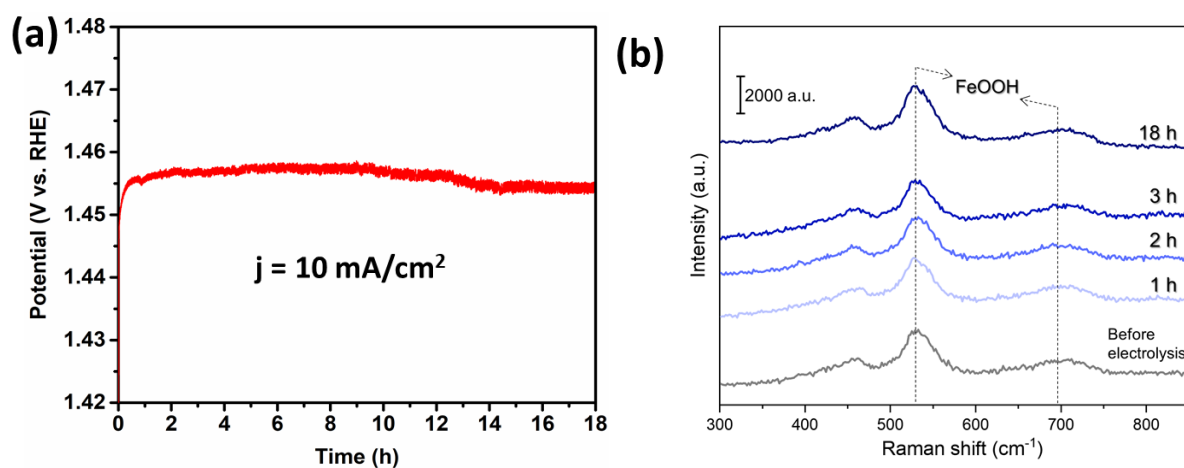


**Figure 5.12** (a) Chronopotential electrolysis of FeOOH-NiOOH at  $10 \text{ mA/cm}^2$ . The potential is corrected by ohmic loss. (b) Raman spectra of FeOOH-NiOOH before and after 1h, 2h, 3h and 18h of electrolysis at a constant current of  $10 \text{ mA cm}^{-2}$  in 1 M KOH. The spectra were recorded by reducing the generated Ni(III) to Ni(II).

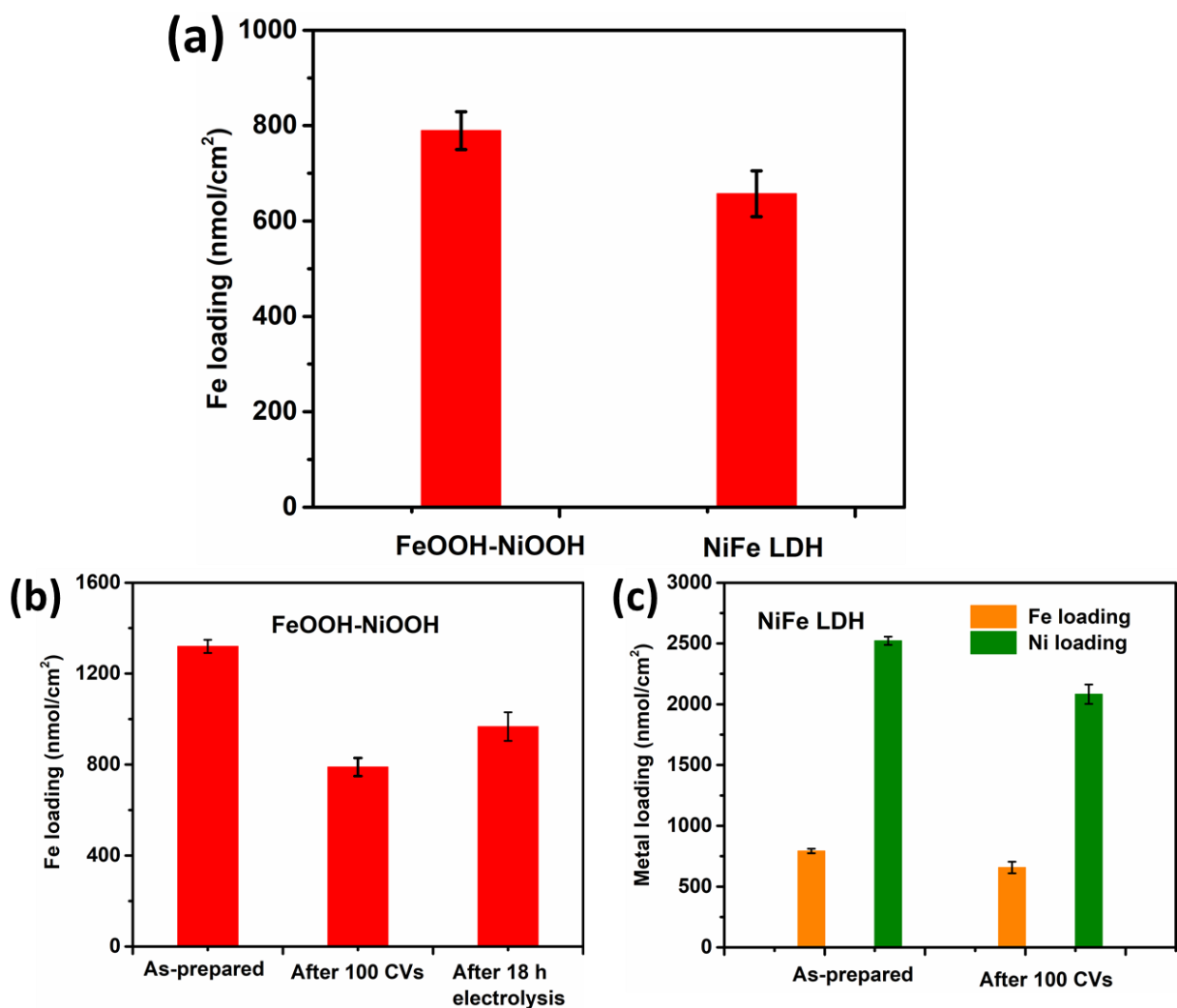


**Figure 5.13** Inductively coupled plasma atomic emission spectrometry (ICP-AES) measurements. (a) Fe loadings of FeOOH-NiOOH and NiFe LDH after 100 CVs activation. (b) Variation of Fe loadings of FeOOH-NiOOH at different conditions. The slight increase of Fe loadings after 18 h electrolysis is probably due to redeposition of Fe on nickel foam substrate. (c) Variation of Fe and Ni loadings of as prepared NiFe LDH and NiFe LDH after 100 CVs. The loading of both Ni and Fe slightly decreased due to the detachment of materials during reaction. The ratio of Fe/(Ni+Fe) is  $23 \pm 1$  % for both as-prepared and activated samples, which is consistent with the results obtained from EDX spectra in Figure 5.3f and Figure 5.5f.

#### 5.4.2 <sup>18</sup>O isotope labeling and exchange experiments

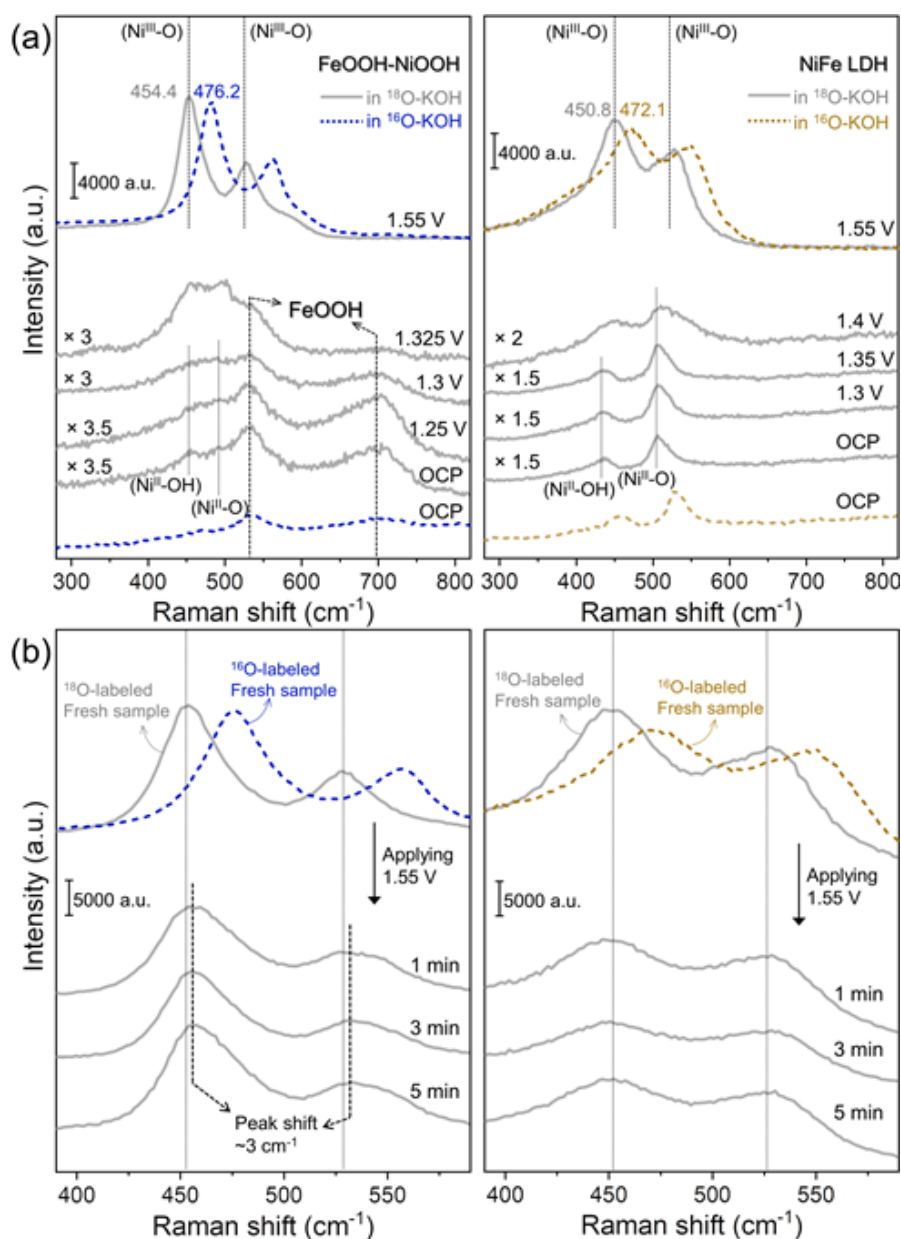


**Figure 5.14** *Operando* Raman spectra of FeOOH-NiOOH (left column) and NiFe LDH (right column) obtained at various potentials for oxygen isotope labeling and exchange experiments. (a) Oxygen isotope labelling experiments in 1 M KOH-H<sub>2</sub><sup>18</sup>O solution and (b) subsequent isotope exchange experiments. The <sup>18</sup>O-labeled samples were monitored at 1.55 V in 1 M KOH-H<sub>2</sub><sup>16</sup>O solution. For ease of comparison of peak shift in between the two solutions, <sup>16</sup>O-labeled peaks of each sample are indicated respectively.

We conducted <sup>18</sup>O isotope labeling and exchange experiments on FeOOH-NiOOH and NiFe LDH, to investigate whether lattice oxygen is involved in OER catalysis. The as-prepared, <sup>16</sup>O-labeled, samples were first immersed in a <sup>18</sup>O-KOH solution. For FeOOH-NiOOH at OCP to about 1.3 V,



the peak of FeOOH remained at the same position whereas the peaks of Ni<sup>II</sup>-O, Ni<sup>II</sup>-OH appeared to be shifted, but the shift could not be quantified due to an overlap of peaks (Figure 5.14a, left). For NiFe LDH in <sup>18</sup>O-KOH solution, same as reported previously<sup>19,20</sup>, the peaks of Ni<sup>II</sup>-O, Ni<sup>II</sup>-OH at OCP to about 1.35 V red-shifted by about 22 cm<sup>-1</sup>, indicating the exchange of lattice <sup>16</sup>O with <sup>18</sup>O of the electrolyte (Figure 5.14a, right). Upon formation of NiOOH, and more obviously at 1.55 V, the Ni<sup>III</sup>-O bands were observed at around 455 and 535 cm<sup>-1</sup> for both FeOOH-NiOOH and NiFe LDH, red-shifted by about 22 cm<sup>-1</sup> relative to those of <sup>16</sup>O-labeled samples. This shift further indicates lattice oxygen exchange from <sup>16</sup>O to <sup>18</sup>O. For FeOOH-NiOOH, the Raman peaks of  $\gamma$ -FeOOH did not shift during this process up to 1.325 V. At higher potentials the peaks were hidden by those of high intensity Ni<sup>III</sup>-O bands (Figure 5.14a, left). To probe whether lattice O in FeOOH was exchanged during OER, an FeOOH-NiOOH sample was first subjected to a <sup>18</sup>O-KOH solution at 1.55 V where OER was occurring, and then the Raman spectrum was collected at 1.25 V. We found that the Raman peaks of  $\gamma$ -FeOOH still remained at the same positions of a <sup>16</sup>O-labeled sample (Figure 5.15). Thus, the lattice oxygens of  $\gamma$ -FeOOH do not exchange with the electrolyte even under OER.

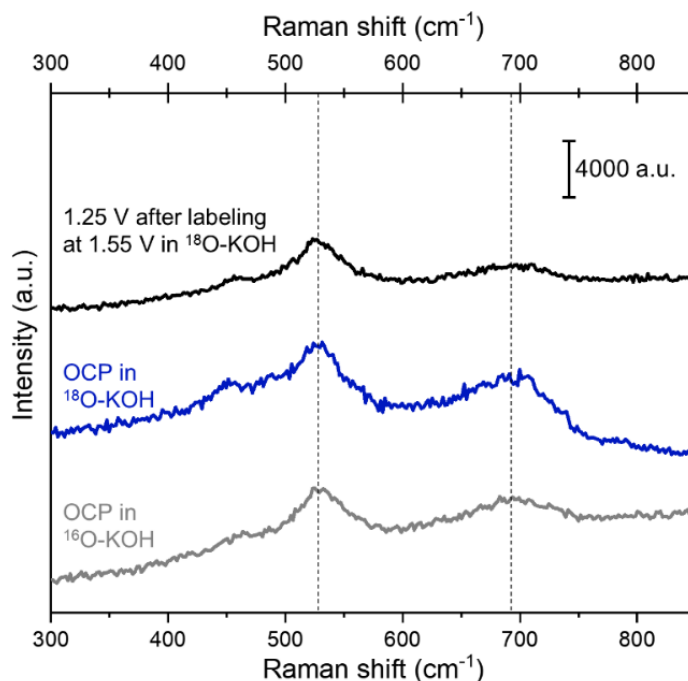


**Figure 5.15** Operando Raman spectra of FeOOH-NiOOH obtained at OCP in <sup>18</sup>O-KOH before labeling process (blue) and at 1.25 V after the activation for labeling by <sup>18</sup>OH<sup>-</sup> at 1.55 V (black). The <sup>16</sup>O-labeled peaks at OCP in <sup>16</sup>O-KOH are indicated in grey at the bottom.



The  $^{18}\text{O}$ -labeled samples of FeOOH-NiOOH and NiFe LDH were immediately placed back in a 1 M  $^{16}\text{O}$ -KOH solution and potentiostatically charged at 1.55 V. For FeOOH-NiOOH, the peaks corresponding to  $\text{Ni}^{\text{III}}$ -O vibrational modes were shifted by about  $3\text{ cm}^{-1}$  to high frequencies (Figure 5.14b, left). For NiFe LDH, no shift of peaks related to  $\text{Ni}^{\text{III}}$ -O was observed (Figure 5.14b, right). As a reference, similar isotope labelling (Figure 5.16a) and exchange (Figure 5.16b) experiments were performed for bare NF, a shift of  $18\text{ cm}^{-1}$  was observed (Figure 5.16b).

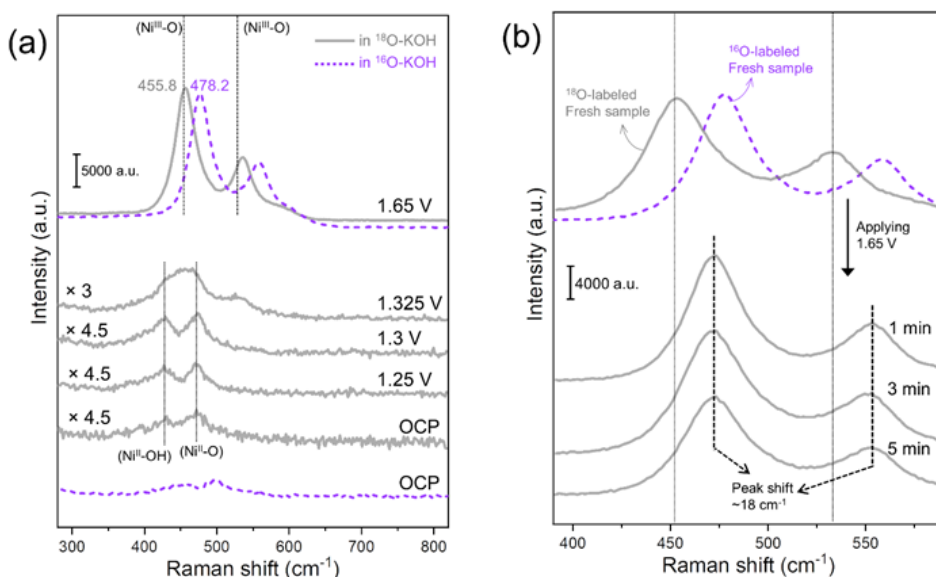


**Figure 5.16** Operando Raman spectra of bare NF obtained at various given potentials for oxygen isotope labeling (a) in 1 M KOH- $\text{H}_2^{18}\text{O}$  solution and (b) subsequent isotope exchange experiment. The  $^{18}\text{O}$ -labeled fresh sample was monitored at 1.65 V in 1 M KOH- $\text{H}_2^{16}\text{O}$  solution. For ease of comparison of the peak shift of the sample in between the two solutions,  $^{16}\text{O}$ -labeled peaks were indicated in purple dashed curves.

As reported previously,<sup>19,20</sup> the lattice oxygen of NiOOH or Fe-doped NiOOH can exchange with O from the  $\text{OH}^-$  electrolyte without applying potential, when Ni is at the +2 oxidation state (as in  $\text{Ni}(\text{OH})_2$ ). However, in the case of Ni is oxidized to +3 or above, the lattice  $^{18}\text{O}$  and  $^{18}\text{O}$ - $^{18}\text{O}^-$  of pure  $\text{Ni}(\text{OH})_2$  and NiFe LDHs containing small amount of Fe (< 4.7%) could be replaced to  $^{16}\text{O}$  and  $^{16}\text{O}$ - $^{16}\text{O}^-$  to a certain degree in  $^{16}\text{OH}^-$  solution, with oxidative applied potential (relevant to OER condition). Once the Fe content reaches 4.7% and above, the lattice O and O- $\text{O}^-$  in the  $^{18}\text{O}$ -labelled form were no longer exchanged back to  $^{16}\text{O}$ -labelled form during OER electrolysis.<sup>19</sup> The lattice O of NiOOH in FeOOH-NiOOH can also be exchanged at the  $\text{Ni}^{\text{II}}$  stage. Noticing that under OER potentials, a  $3\text{ cm}^{-1}$  isotopic shift of FeOOH-NiOOH indicates partial O exchange. Compared to bulk pure NF ( $18\text{ cm}^{-1}$  shift), the degree of lattice oxygen exchange was about 16%. Noticing

that the Fe content of FeOOH-NiOOH is higher than 10% (Figure 5.2f). The most possible explanation for this partial lattice oxygen exchange is some of Ni(III) is reduced to Ni(II) during OER catalysis (see the following contents for detailed explanations). Thus, the different O exchange behavior reflects a mechanistic difference between FeOOH-NiOOH and NiFe LDH.

## 5.5 Analysis of the electrokinetics

### 5.5.1 Analysis of Tafel slope and reaction order of hydroxyl ions concentration

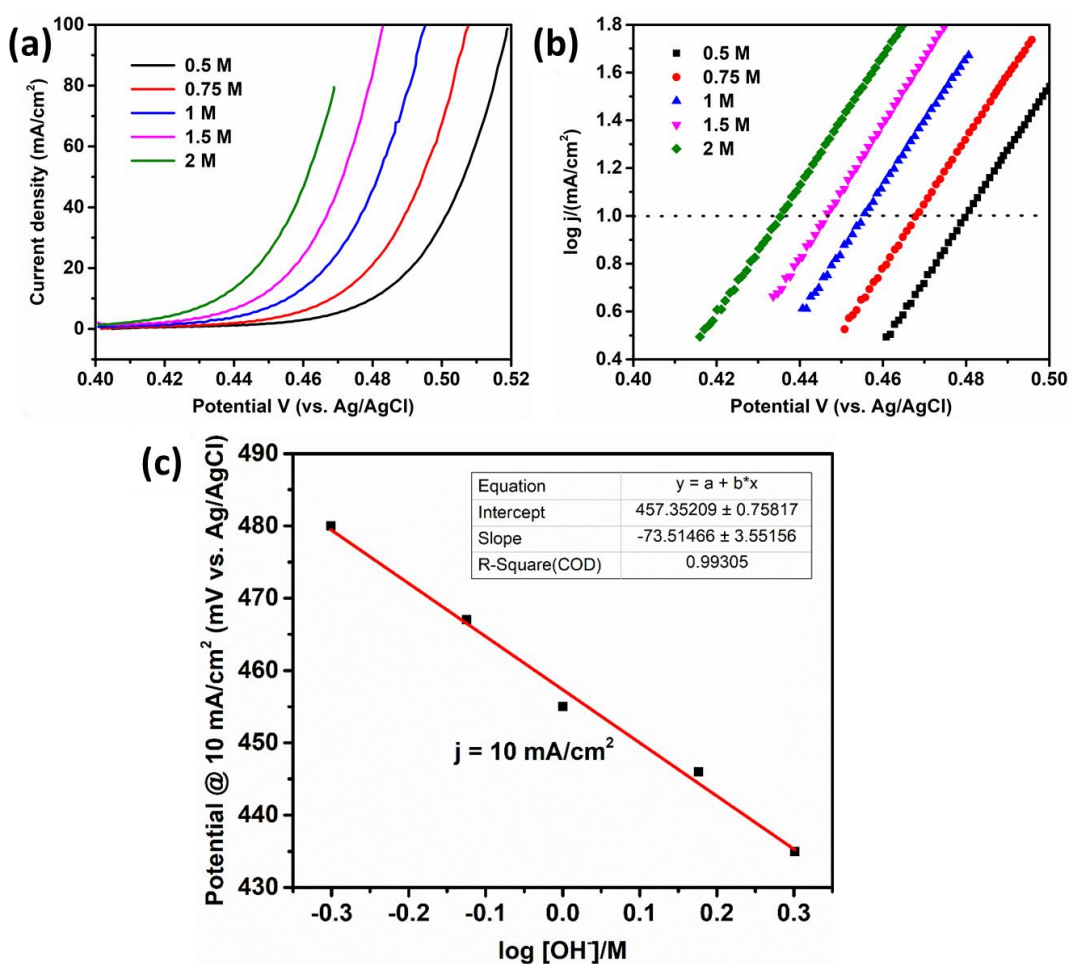


**Figure 5.17** Electrokinetic analysis of FeOOH-NiOOH. (a) LSVs and (b) corresponding Tafel plots in different concentrations of KOH. (c) The change of constant potential at a certain current density (10 mA/cm²) based on the logarithm of [OH⁻]. The linear fitting of the data points gives the  $(\partial E / \partial \log [\text{OH}^-])_j$  values, as the slope of the fitting plot.

To better understand the different catalytic process of OER, the electrokinetic behaviors of FeOOH-NiOOH and NiFe LDH was analyzed and compared. The analysis was conducted according to the same methods depicted in Section 4.3, Chapter 4. FeOOH-NiOOH exhibited a similar Tafel Slope of  $38 \pm 2$  mV/dec in 0.5 M to 2 M KOH (Figures 5.17a and 5.17b, Table 5.1). The potentials vs. Ag/AgCl (or Standard Hydrogen Electrode, SHE) at 10 mA/cm<sup>2</sup> linearly depended on the log of the concentration of hydroxyl ions (Figure 5.17c), with a slope of -74 mV/dec. The rate order of [OH<sup>-</sup>] in 0.5-2 M KOH was determined according to (Eq. 5.1).

$$\left( \frac{\partial \log j}{\partial \log [\text{OH}^-]} \right)_E = - \frac{\left( \frac{\partial E}{\partial \log [\text{OH}^-]} \right)_j}{\left( \frac{\partial E}{\partial \log j} \right)_{pH}} \quad (5.1)$$

The denominator of (Eq. 5.1) is the Tafel slope and the numerator is the slope in Figure 5.17c. Accordingly, the order of [OH<sup>-</sup>] was  $1.8 \pm 0.1$ .

Similar analysis was performed for NiFe LDH (Figures 5.18a and 5.18b). The Tafel slopes of NiFe LDH are 42 to 48 mV/dec, depends on the concentration of hydroxyl ions (Figures 5.18a and 5.18b, Table 5.1). The Tafel slope decreased with increasing [OH<sup>-</sup>]. The Tafel slope in 2 M KOH is close to 40 mV/dec, similar to that of FeOOH-NiOOH. The potentials vs. Ag/AgCl (or SHE) at 1 mA/cm<sup>2</sup> linearly depended on the log of the concentration of hydroxyl ions (Figure 5.18c), with a slope of -80 mV/dec. According to (Eq. 5.1), the rate order of [OH<sup>-</sup>] was also close to two.

**Table 5.1** Tafel slope (mV/dec) of FeOOH-NiOOH and NiFe LDH in KOH with different concentrations.

[OH <sup>-</sup> ]	0.5M	0.75M	1M	1.5M	2M
FeOOH-NiOOH	39±1	38±1	38±2	37±1	37±1
NiFe LDH	47±2	46±3	43±2	43±2	42±2

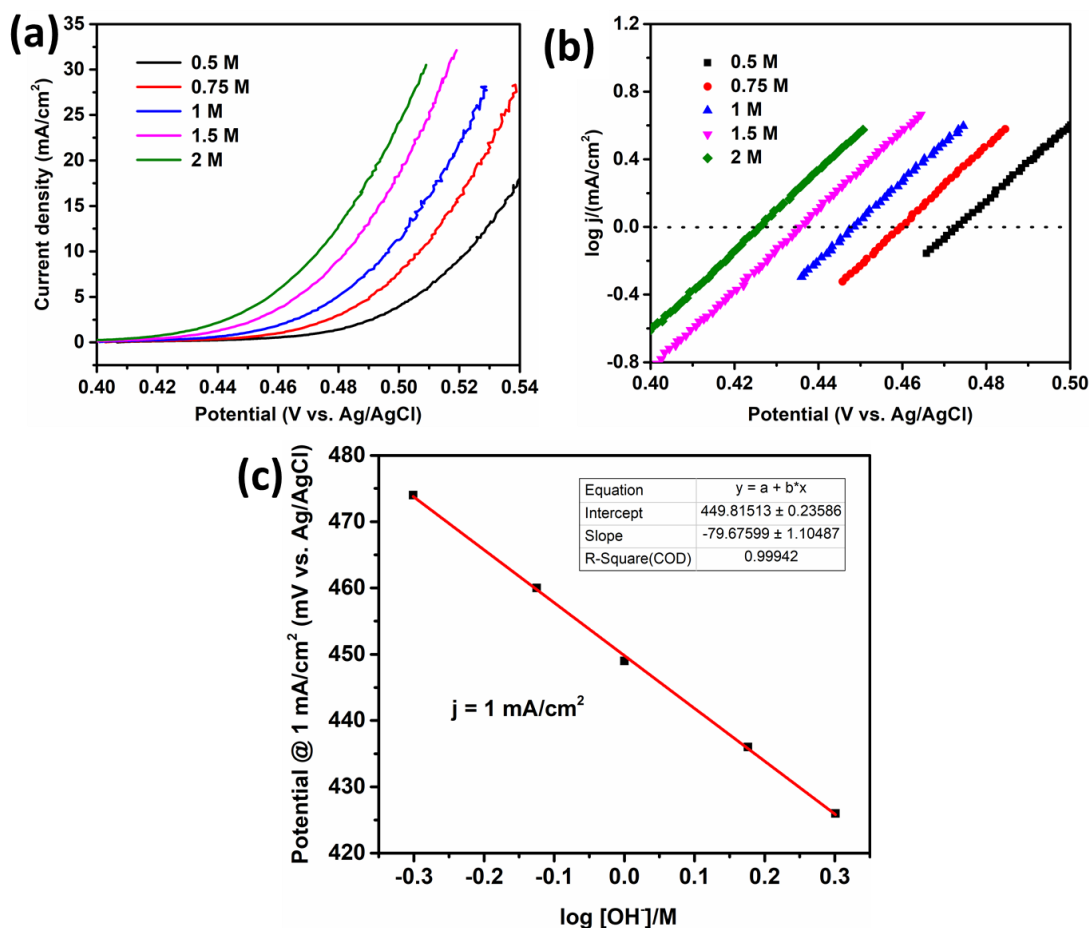


**Figure 5.18** Electrokinetic analysis of NiFe LDH. (a) LSVs and (b) corresponding Tafel plots in different concentrations of KOH. (c) The change of constant potential at a certain current density ( $1 \text{ mA/cm}^2$ ) based on the logarithm of  $[\text{OH}^-]$ . The linear fitting of the data points gives the  $(\partial E / \partial \log [\text{OH}^-])_j$  values, as the slope of the fitting plot.

The redox potentials of the precatalytic  $\text{Ni(II)/Ni(III)}$  shifted negatively by ca. 100 mV when the  $[\text{OH}^-]$  increased by 10 fold, indicating a  $3\text{OH}^-/2\text{e}^-$  process (Figure 5.19) for both  $\text{FeOOH-NiOOH}$  and NiFe LDH. The results showed that the (Fe-doped) NiOOH is deprotonated during  $\text{Ni}^{\text{II}}/\text{Ni}^{\text{III}}$  transformation steps. The deprotonated NiOOH is possible to act as a proton or hydrogen acceptor (see Section 5.5.2 for details).

Similar to Section 4.2, Chapter 4, we employed a quasi-equilibrium (quasi-Langmuir) model to describe the OER kinetics, in which the key steps are described by one pre-equilibrium step (PES) plus one rate-determining step (RDS).<sup>27,28</sup> The RDS limits the OER velocity while the PES determines the concentration of the resting states. The overall OER rate and catalytic behavior

are controlled by both steps. The other steps are fast and do not restrict overall reaction rate. This model is suitable for catalysts in the intermediate applied overpotential (Tafel region), where the concentration of the resting state is not high (see Section 4.2, Chapter 4 and Appendix I for details).

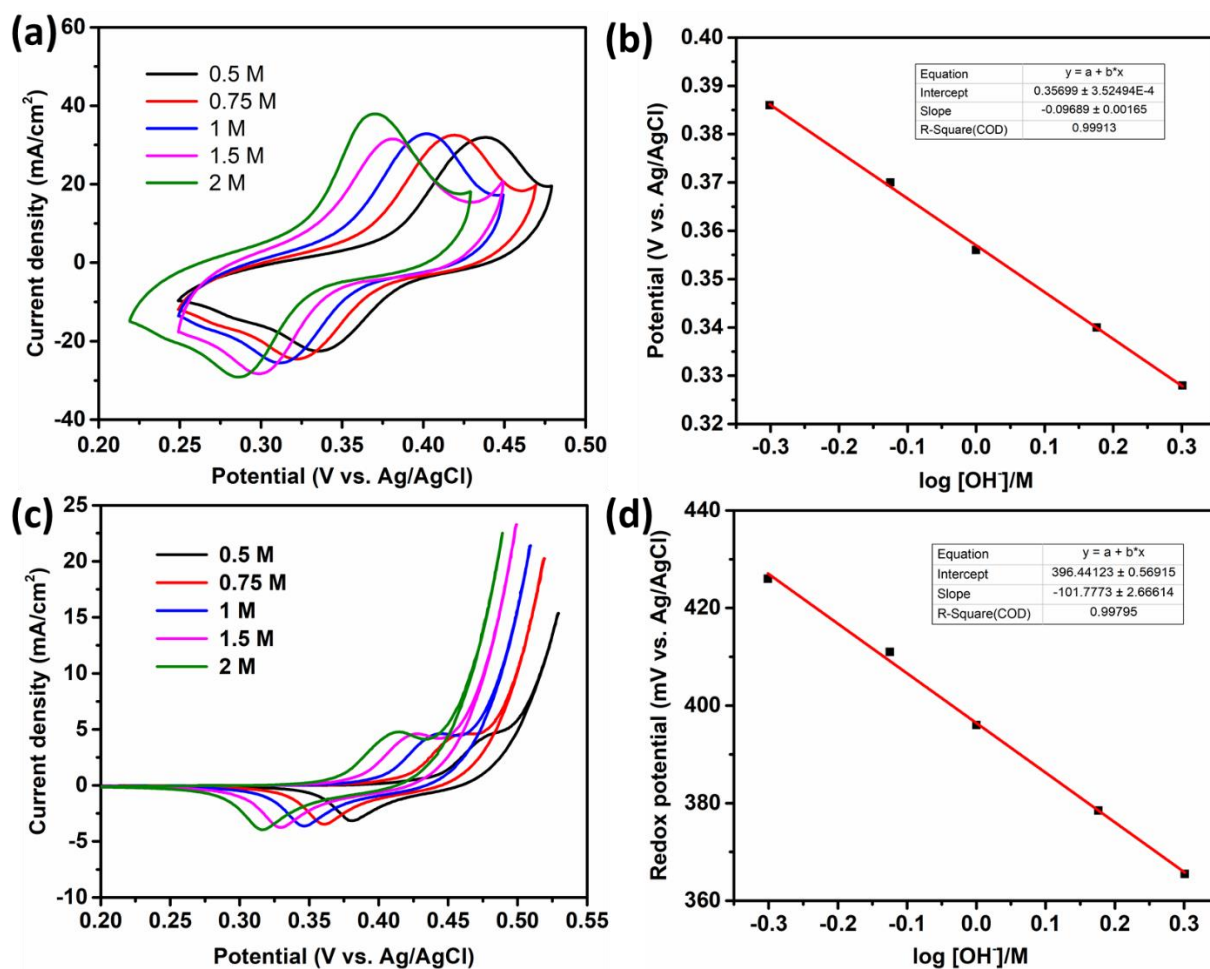


**Figure 5.19** Ni(II)/Ni(III) redox peaks of FeOOH-NiOOH and NiFe LDH. (a) and (b) is for FeOOH-NiOOH; (c) and (d) is for NiFe LDH. (a, c) CVs at various concentrations of KOH. (b, d) The relationship of Ni(II)/Ni(III) redox potential based on the logarithm of the concentration of hydroxyl ions. Ni(II)/Ni(III) redox potential is derived from (a, c) by averaging the potential of oxidative and reductive peaks. (b) is derived from (a) while (d) is derived from (c). For the NiFe LDH in 0.5 M KOH, the oxidative peaks position is determined by looking for the point corresponding to lowest value of the first derivative of the forward CV scan (potential region: 0.45-0.52 V vs. Ag/AgCl).

For the conventional mechanism involving four PCET steps (see Figure 1.6a, Chapter 1 for details, see also Figure 5.22a for simplified scheme), if the formation of M=O is the PES, and the

nucleophilic attack of  $\text{OH}^-$  on a  $\text{M}=\text{O}$  is the RDS (Figure 1.6a, Chapter 1; Figure 5.22a), the predicted Tafel slope is 40 mV/dec and the predicted rate order in  $[\text{OH}^-]$  is two, assuming there is no charge transfer barrier.<sup>28,29</sup> For the bifunctional mechanism (see Figure 1.9, Chapter 1 for details, see also Figure 5.22b for simplified scheme), if the formation of  $\text{M}=\text{O}$  is the PES, and the nucleophilic attack of  $\text{OH}^-$  on a  $\text{M}=\text{O}$  coupled with a hydrogen atom transfer is the RDS (Figure 1.9, Chapter 1; Figure 5.22b), the predicted Tafel slope is also 40 mV/dec and the predicted rate order in  $[\text{OH}^-]$  is also two. The experimental values for both  $\text{FeOOH-NiOOH}$  and  $\text{NiFe LDH}$ , thus, agree with the predictions of both mechanisms. However, there are noticeable differences in the Tafel behaviors of  $\text{FeOOH-NiOOH}$  and  $\text{NiFe LDH}$ . The Tafel slopes of  $\text{FeOOH-NiOOH}$  are independent of  $[\text{OH}^-]$ . In contrast, the Tafel slopes of  $\text{NiFe LDH}$  decrease with increased  $[\text{OH}^-]$ , suggesting a charge transfer barrier across the bulk film, which is more pronounced at lower  $[\text{OH}^-]$  (for a detailed description, see Section 4.2, Chapter 4 and Appendix I).<sup>30,31</sup> The absence of charge transfer barrier in  $\text{FeOOH-NiOOH}$  would be consistent with surface-dominated catalysis, as indicated by the results of *operando* Raman spectroscopy.

The activity of  $\text{NiFe LDH}$  was very different in 1 M  $\text{KOH}$ ,  $\text{NaOH}$ ,  $\text{LiOH}$  (Figure 5.20a), indicating a cation effect. There are various explanations for the cation effect in OER. Such as enlarged Ni-O bonds<sup>32</sup>; expanded layer distance of LDH by cation insertion<sup>33</sup>; or special interaction between cations and active oxygen species<sup>34</sup>. In any cases, cation effect indicates the bulk Ni or Fe sites are involved in catalysis.

On the contrary, the cation effect was not obvious for  $\text{FeOOH-NiOOH}$  (Figure 5.20b). Noted that  $\text{FeOOH-NiOOH}$  also contains a certain amount of Fe-doped  $\text{NiOOH}$  or  $\text{NiFeO}_x\text{H}_y$  species. Therefore, there should be other active sites existed via an OER mechanism different from  $\text{NiFe LDH}$  or  $\text{NiFeO}_x\text{H}_y$ . Moreover, these sites should be more active; else, the cation effect should be dominated. The small cation effect observed for  $\text{FeOOH-NiOOH}$  is again consistent with behavior of surface electrocatalysis.

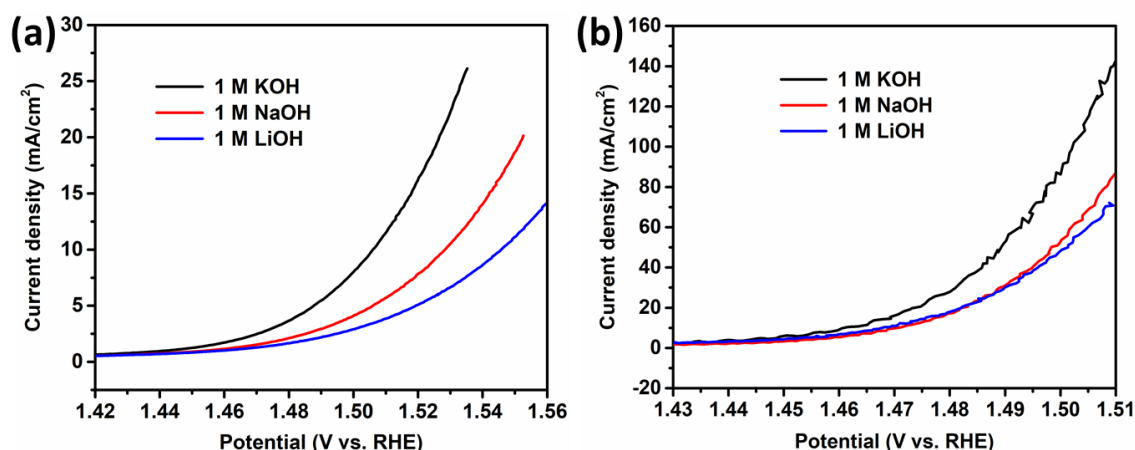


**Figure 5.20** Cation effect of NiFe LDH and FeOOH-NiOOH. (a) Comparison of LSVs of NiFe LDH in 1 M KOH (black), 1 M NaOH (red) and 1 M LiOH (blue). (b) Comparison of LSVs of FeOOH-NiOOH in 1 M KOH (black), 1 M NaOH (red) and 1 M LiOH (blue).

### 5.5.2 Analysis of H-D isotope effect

Hydrogen/deuterium (H/D) exchange affects both thermodynamics and kinetics of PCET type reactions.<sup>35,36</sup> Accordingly, both thermodynamic isotope effect (TIE) and the kinetic isotope effect (KIE) exist.<sup>35,36</sup> The TIE originates from a change in the reaction thermodynamics due to different vibrational zero-point energies (ZPEs) of chemical bonds involving hydrogen and deuterium.<sup>35,37</sup> In the present case, H/D TIE effect should be observed in PES involving proton or hydrogen transfer. On the other hand, H/D KIE originates from the different activation barriers caused by the differences of ZPEs between H- and D-substituted analogues.<sup>35,36,38,39</sup> KIE is usually employed to probe the involvement of proton or hydrogen transfer in RDS.<sup>35,36,38,39</sup> The combination of TIE and KIE leads to the overall observed isotope effect (IE). The further details of H-D isotope effect is depicted in Appendix 2 of this Thesis.

The FeOOH-NiOOH had an H/D isotope effect of 1.4 to 2.0 for catalyzing OER, depending on the concentration of hydroxyl ions and the applied potential (Figure 5.21a). On the other hand, NiFe LDH had an H/D isotope effect of 2.0-2.4 (Figure 5.21b), and the isotope effect did not vary substantially at different potentials nor [OH<sup>-</sup>].

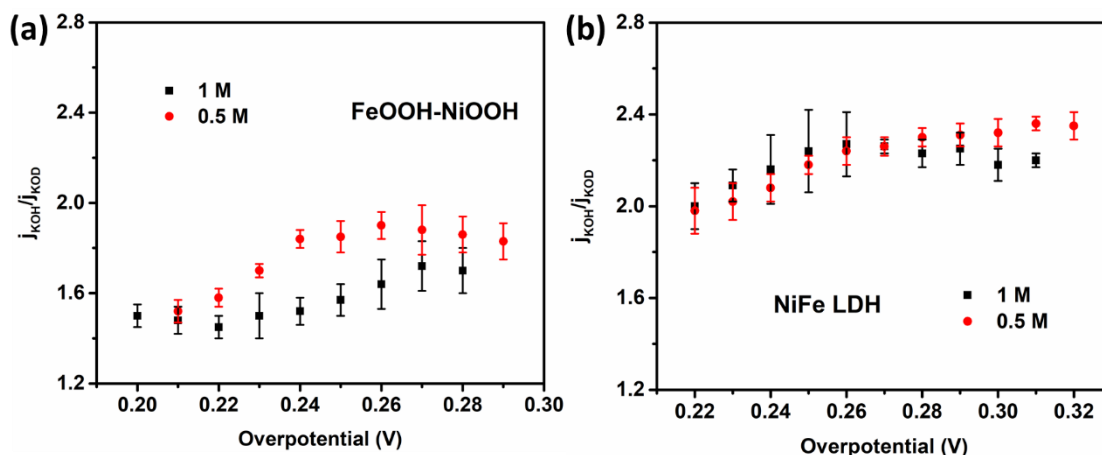


**Figure 5.21** H/D isotope effect analysis ( $j_{\text{KOH}}/j_{\text{KOD}}$  versus overpotential). (a) FeOOH-NiOOH and (b) NiFe LDH. Electrolyte concentrations: 1 M (black), 0.5 M (red). The error bar and the average values were deduced from three independent measurements.

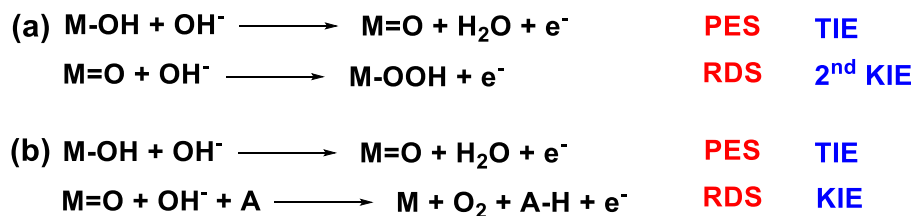


**Figure 5.22** Simplified scheme of OER mechanisms. (a) General key steps of the traditional PCET type OER mechanism in alkaline medium.<sup>3</sup> (b) General key steps of the bifunctional OER mechanism in alkaline medium.<sup>9</sup>

For the conventional PCET type OER mechanism (Figure 5.22a), there is direct proton transfer in the PES but not in RDS. Consequently, only TIE and secondary KIE are expected. Secondary KIE is typically below 1.3,<sup>38,40</sup> so TIE would dominate. The data for NiFe LDH (H/D IE of 2.0-2.4) fit this model. The IE is roughly independent of applied potential, characteristic of TIE.<sup>37,41</sup> Moreover, the IE is pH-independent, consistent with a PCET-type PES.<sup>37,41</sup>

For the bifunctional mechanism, the direct proton/hydrogen transfer is involved in both PES and RDS (Figure 5.22b), so that KIE becomes significant. In the Tafel region, the overall IE can be expressed as (Eq. 5.2) (see Appendix 2 of this Thesis for detailed derivation of this Equation).<sup>38</sup>

$$IE = \frac{k_0}{k'_0} \exp\left(\frac{(\alpha_2 - \alpha'_2)\eta F}{RT}\right) \quad (5.2)$$



$k_0$  and  $k_0'$  are the rate constants of H- and D-substituted reactants, respectively;  $\alpha_2$  and  $\alpha_2'$  are the transfer coefficients of RDS for H- and D-substituted reactants;  $R$ ,  $T$ ,  $\eta$ , and  $F$  are universal gas constant, thermodynamic temperature, overpotential, Faradaic constant, respectively. Typically  $\alpha_2$  is bigger than  $\alpha_2'$  due to a higher barrier of charge transfer after deuterium substitution.<sup>38</sup> In the Tafel region,  $k_0$  and  $k_0'$ ,  $\alpha_2$  and  $\alpha_2'$  can be considered as potential-independent. Therefore, the observed IE should increase with increasing overpotential. Moreover, if the generation of the hydrogen atom acceptor is pH-dependent, the KIE is expected to depend on pH as well.<sup>42</sup> The data for FeOOH-NiOOH fits this model. The observed IE indeed increases with applied overpotential, and decreases with  $[\text{OH}^-]$ .

Note that the overall IE of FeOOH-NiOOH, dominated by KIE, is lower than that of NiFe LDH, dominated by TIE. Accordingly, the TIE of FeOOH-NiOOH is lower than that of NiFe LDH, reflecting a difference in the nature of M=O in these two catalysts. The KIE of FeOOH-NiOOH is rather small likely due to the internal hydrogen transfer in RDS. Indeed, previous literatures suggested internal hydrogen or proton acceptor could minimize the H/H<sup>+</sup> transfer distance, thus significantly decreasing the H/D KIE.<sup>43,44</sup>

## 5.6 Possible OER mechanisms

Based on the data from both *operando* Raman spectroscopy and electrokinetic analysis, we proposed a catalytic cycle for FeOOH-NiOOH (Figure 5.23a). The as-prepared catalyst (A-I) is composed of  $\gamma$ -FeOOH clusters covalently linked to a Ni(OH)<sub>2</sub> support, which is slightly doped by Fe. At about 1.35 V, the support is oxidized to NiOOH via a  $3\text{OH}^-/2\text{e}^-$  process. The process is best described by oxidation of a dimeric Ni<sup>II</sup> unit into a dimeric Ni<sup>III</sup> unit accompanied by the loss of three protons from coordinated water or OH<sup>-</sup> groups (A-II). The Fe<sup>III</sup> center in FeOOH then undergoes a PCET to form an electrophilic Fe(IV)=O center (A-III), which is the PES of the catalytic cycle. Consequently and in the RDS, the Fe(IV)=O center, an external OH<sup>-</sup>, and the deprotonated Ni<sup>III</sup>-O moiety react in a concerted manner to give Fe<sup>II</sup>-Ni<sup>II</sup>-OH (A-IV), O<sub>2</sub> and an electron. Oxidations of Fe<sup>II</sup> and Ni<sup>II</sup> then regenerates the catalyst (A-II). The reaction mechanism described here is similar as previous DFT computation<sup>9</sup>, with small difference in detailed steps.

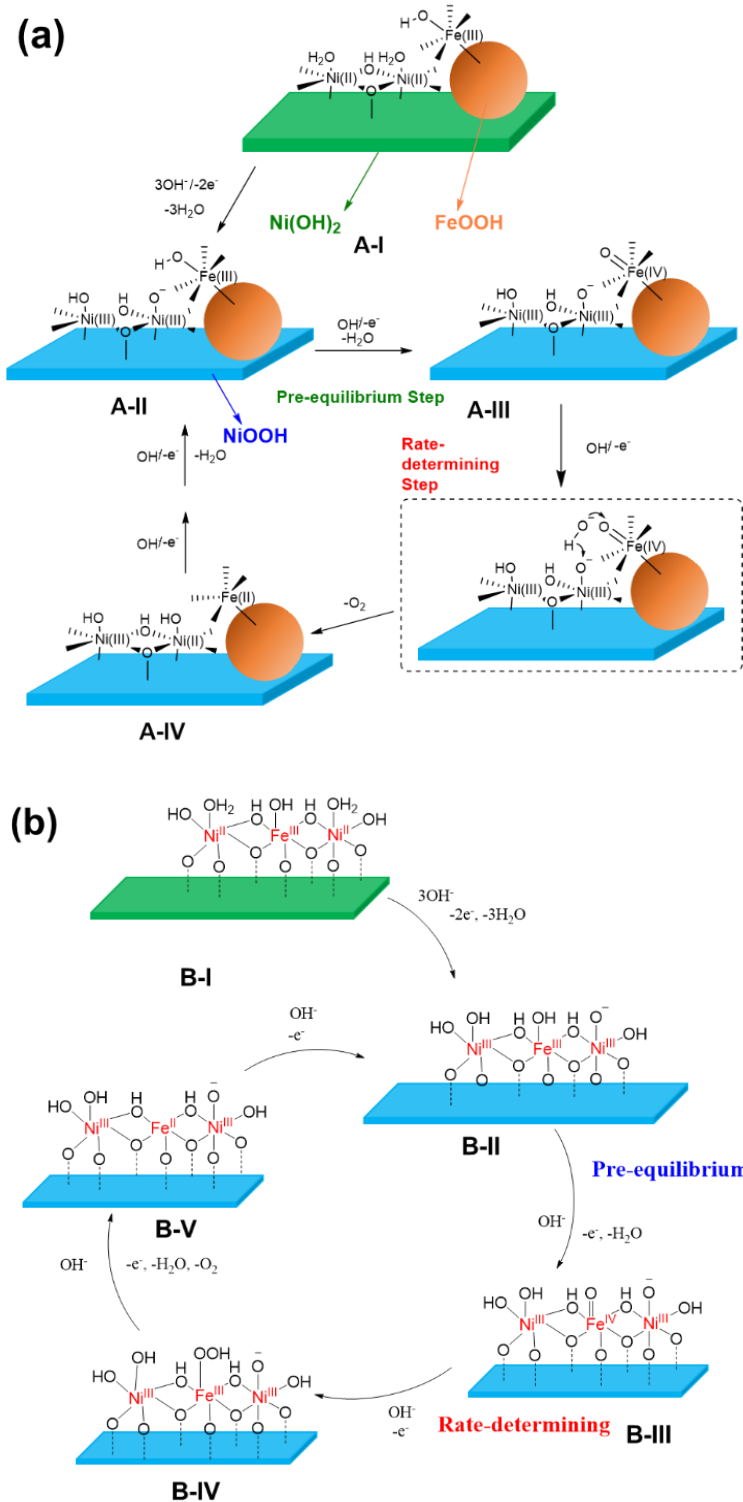


**Figure 5.23** Proposed OER reaction mechanisms of (a) FeOOH-NiOOH; (b) NiFe LDH (assuming Fe is the catalytic center).

For NiFe LDH (Figure 5.23b), the as-prepared catalyst is comprised of  $\text{Ni}(\text{OH})_2$  doped by  $\text{Fe}^{\text{III}}$  ions (B-I). A  $3\text{OH}^-/2\text{e}^-$  process generates Fe-doped  $\text{NiOOH}$  (B-II). Although there are debates on whether Ni or Fe site serves as the site of O-O bond formation<sup>26,45,46</sup>, a dimeric Fe-O-Ni active site would agree with most data. The catalytic cycle proceeds via a PES to form a  $\text{M}=\text{O}$  (B-III, assuming M is Fe, but the same result is obtained when M is Ni), followed by a RDS of  $\text{OH}^-$  attack on  $\text{M}=\text{O}$  to give  $\text{M-OOH}$  (B-IV). A further PCET oxidation gives  $\text{O}_2$  and M (B-V), which can then be oxidized back to the initial catalyst B-II. When M is Fe, the Fe ions shuffle between  $\text{Fe}^{\text{II}}$ ,  $\text{Fe}^{\text{III}}$ , and  $\text{Fe}^{\text{IV}}$  while the Ni ions remain as  $\text{Ni}^{\text{III}}$  during catalysis. When M is Ni, the Ni ions shuffle between  $\text{Ni}^{\text{II}}$ ,  $\text{Ni}^{\text{III}}$ , and  $\text{Ni}^{\text{IV}}$  while the Fe ions remain as  $\text{Fe}^{\text{III}}$ .

The results from O isotope exchange experiments (Figure 5.14) suggest the presence of transient  $\text{Ni}^{\text{II}}$  sites in  $\text{FeOOH-NiOOH}$  but not in NiFe LDH during OER. About 16% of lattice O in  $\text{FeOOH-NiOOH}$  exchanges with  $\text{OH}^-$  under OER, but such an exchange is absent in NiFe LDH. It is known that at  $\text{Ni}^{\text{II}}$  the lattice O of Fe-doped  $\text{NiOOH}$  or NiFe LDH can exchange with O from  $\text{OH}^-$  electrolyte without applied potential, but at  $\text{Ni}^{\text{III}}$  and above, the exchange does not occur even under OER.<sup>19,20</sup> These results are consistent with  $\text{FeOOH-NiOOH}$  operating via the bifunctional mechanism (Figure 5.23a) where a  $\text{Ni}^{\text{III}}\text{-O}$  site accepts a hydrogen atom in the RDS to become a  $\text{Ni}^{\text{II}}\text{-OH}$  site. They are also consistent with NiFe LDH operating via the conventional mechanism (Figure 5.23b) where the redox changes occur most probable at the Fe site.

## 5.7 Conclusions

*Operando* Raman spectroscopy and electrokinetic analysis were employed to study two active OER catalysts,  $\text{FeOOH-NiOOH}$  and NiFe LDH. Despite their similar chemical compositions, the two catalysts exhibited different electrochemical and spectroscopic features, implying that most of Fe species of  $\text{FeOOH-NiOOH}$  exist as surface  $\gamma\text{-FeOOH}$  clusters but they are doped in the lattice of  $\text{Ni}(\text{OH})_2/\text{NiOOH}$  in NiFe LDH. This difference results in a 10-fold higher OER activity of  $\text{FeOOH-NiOOH}$  compared to NiFe LDH. During OER, different O isotope exchange behaviors of the  $\text{NiOOH}$  component were observed for the two catalysts: about 16% of lattice O in  $\text{FeOOH-NiOOH}$  exchanged with the  $\text{OH}^-$  electrolyte whereas there was no exchange for NiFe LDH. These data suggest that  $\text{Ni}^{\text{II}}$  species are present in the catalytic cycle of  $\text{FeOOH-NiOOH}$ , but not in NiFe LDH. The two catalysts exhibited similar Tafel slopes and rate orders in  $[\text{OH}^-]$  under standard

conditions. However, they had different H/D isotope effects. FeOOH-NiOOH had an IE of 1.4 to 2.0, with a significant KIE component and depending on  $[\text{OH}^-]$  and overpotential. NiFe LDH had an IE of 2.0-2.4, which is mostly TIE and is independent of both  $[\text{OH}^-]$  and overpotential. The spectroscopic and kinetic data support two distinct mechanisms for the two catalysts. FeOOH-NiOOH operates by a bifunctional mechanism where the rate-determining O-O bond forming step is the concerted  $\text{OH}^-$  attack on a  $\text{Fe}=\text{O}$  coupled with a hydrogen atom transfer to a nearby  $\text{Ni}^{\text{III}}-\text{O}$  site. On the contrary, NiFe LDH operates by a conventional mechanism of four consecutive PCET steps, and the rate-determining O-O bond forming step is the attack of  $\text{OH}^-$  on a  $\text{Fe}=\text{O}$  unit.

The data described here constitutes the first experimental evidences for the bifunctional mechanism which has hitherto only theoretical computation supports. The superior activity of FeOOH-NiOOH demonstrates the potential of bifunctional catalysts to overcome the performance limit of conventional catalysts imposed by the scaling relationship. The bifunctional mechanism provides an opportunity to individually fine-tune two components of an OER catalyst for optimized activity, adding a new design principle. For examples, analogous to the present FeOOH-NiOOH catalyst, the FeOOH component might be replaced by another material with a lower energy barrier to form an electrophilic  $\text{M}=\text{O}$  unit, while the NiOOH component might be replaced by another hydrogen atom acceptor, including even suitable organic materials.

## 5.8 Experimental Sections

### 5.8.1 Chemicals and the synthesis of the catalysts

KOD (30% in  $\text{D}_2\text{O}$ ) is purchased from ABCR; ethanol (99.5%) is purchased from Fluka; 1 M KOH standard solution is purchased from Merck KGaA. All other chemicals were purchased from Sigma-Aldrich. The electrolytes were prepared by using ultra-pure water ( $18.2 \text{ M}\Omega/\text{cm}$ ).

**Pretreatment of nickel foam (NF)** The NF was first cleaned by sonicating in acetone for 30 mins to remove the organic impurities. Then the NF was dried and dipped in 15% HCl for 30 mins with sonication. The electrode was washed by ultra-pure water and dried in room temperature. Noted that the electrode should be used within two hours, else the surface generated nickel hydroxide would decrease the adsorption ability of the catalysts (FeOOH).

**Synthesis of FeOOH-NiOOH<sup>9</sup>** A cleaned NF electrode was dipped in 10 mM FeCl<sub>3</sub> solution with stirring for 15 mins. After that, the electrode was directly dried in 75 °C oven over night. The FeOOH-NiOOH was formed during the drying period.

**Synthesis of NiFe LDH (20% Fe)** We used a method according to previous literature with modifications.<sup>14</sup> Typically, Ni(NO<sub>3</sub>)<sub>2</sub>·6H<sub>2</sub>O (2.0 mmol, 582 mg), Fe(NO<sub>3</sub>)<sub>3</sub>·9H<sub>2</sub>O (0.5 mmol, 202 mg), NH<sub>4</sub>F (10 mmol, 371 mg) and urea (25 mmol, 1.50 g) were dissolved in H<sub>2</sub>O (40 ml) with vigorous stirring. The mixed solution was stirred for 30 mins and then transferred to a 50 mL Teflon-lined stainless steel autoclave. The autoclave was heated at 120 °C for 16 h. After cooling down to room temperature, the yellowish solid was washed by ultrapure water for 3 times and ethanol for 1 time, and then naturally dried on a watch glass. If no special indication, the NiFe LDH samples mentioned in SI and main-text have 20% Fe content.

**Synthesis of Ni(OH)<sub>2</sub>** The bulk Ni(OH)<sub>2</sub> was synthesized through a hydrothermal method.<sup>47</sup> 0.10 M of Ni(NO<sub>3</sub>)<sub>2</sub>·6H<sub>2</sub>O and 0.15 M of urea were dissolved in 80 mL of deionized water that was already boiled to remove dissolved CO<sub>2</sub> in it. The mixed solution was sonicated for 30 mins to make it homogeneous. Then, the resulting solution was transferred to a 50 mL Teflon-lined stainless steel autoclave and heated at 190 °C for 48 h. The as-obtained green product was collected by centrifugation as it washed with ultrapure water for 3 times and ethanol for 1 time.

**Synthesis of γ-FeOOH** The material was synthesized according to previous literature with modifications.<sup>9</sup> Typically, 20 mL of 0.02 M Fe(NO<sub>3</sub>)<sub>3</sub> solution was sealed in a glass container, which was then maintained at 75 °C for 24 h. After centrifuging and washing with water for 3 times and ethanol for 1 time, yellowish-brown powder was obtained as γ-FeOOH.

**Preparation of Fe-free KOH** The Fe-free KOH was prepared for *operando* Raman experiments of pure NF and pure Ni(OH)<sub>2</sub> (see below). The Fe impurities in normal KOH solutions can be removed by treating with high-purity Ni(OH)<sub>2</sub>.<sup>10</sup> In a clean 50 mL polypropylene centrifuge tube, 2 g of Ni(NO<sub>3</sub>)<sub>2</sub>·6H<sub>2</sub>O (99.99%) was dissolved in 5 mL of ultrapure water. 20 mL of 1 M KOH solution was added to give a Ni(OH)<sub>2</sub> precipitate. The suspension was agitated and centrifuged, and the supernatant was decanted. The Ni(OH)<sub>2</sub> precipitate was washed with ultrapure water for three times by centrifugation. The solid was dispersed in 10 mL of 1 M KOH by centrifugation, and the supernatant was decanted. This solid was used as the Fe-absorber. The normal KOH solutions could be cleaned by adding to this Ni(OH)<sub>2</sub>. The cleaning procedure involves dispersing Ni(OH)<sub>2</sub> in the KOH solution, mechanically agitated over-night, followed by at least 3 h of resting.

### 5.8.2 Characterizations

TEM was performed on an FEI Talos instrument that operated at 200 kV high tension. EDX mapping was used for determining the distribution of the elemental compositions. The images were collected in HAADF-STEM mode and the mapping was performed in ESpirit software. Samples for TEM were prepared by drop-drying the samples from their diluted ethanol suspensions onto carbon-coated copper grids. Suspension of FeOOH-NiOOH was collected by sonicating the electrode in ethanol for 1h. ICP-AES results were obtained by a Nexlon 350 (Perkin Elmer) machine. All the samples were dissolved by ultra-pure nitric acid (65%, Merck KGaA) then diluted by 30 times.

Raman spectroscopic experiments were performed at a Raman spectroscopy (inVia confocal Raman microscope, Renishaw) with a 63x water immersion objective (Leica-Microsystems) for both *operando* and *ex situ* analysis. A transparent Teflon film (0.001 in thickness, McMaster Carr) was applied to cover the lens of the objective in order to prevent direct contact with electrolyte. The wavelength of the laser excitation source was 532 nm with a laser power of ~0.5 mW at a grating of 1800 l mm<sup>-1</sup>. Charge coupled device (CCD) detector was used to collect the scattered light from electrode surface. Prior to use, peak position of Raman spectrum was calibrated based on 520±0.5 cm<sup>-1</sup> peak of silicon. Each spectrum was recorded with a resolution of ~1 cm<sup>-1</sup> by setting up the measurement condition such that 30 consecutive scans and exposure time of 2 sec to laser at a beam spot were applied. All Raman experiments were carried out with a custom-made electrochemical cell in which a platinum wire and a custom-made double-junction Ag/AgCl served as counter and reference electrodes respectively. Prior to each experiment, the cell was dipped in an acid bath to remove all traces of metals and other dirt, and subsequently it was rinsed with acetone, alcohol and distilled water. For FeOOH-NiOOH samples, they were pressed with a hydraulic machine at 5 tons to make them flat and thin enough to fit the electrochemical Raman cell. For other powder-type samples (LDHs), the same catalyst ink as used in electrochemical measurements was drop-casted on a thin Au foil and then dried. The catalyst deposited Au was employed for subsequent *operando* Raman spectroscopy experiments.

### 5.8.3 Electrochemical test conditions

FeOOH-NiOOH (geometric area: 0.2-0.3 cm<sup>2</sup>) was directly used for electrochemical measurements. For NiFe LDH samples, the catalyst ink was prepared by mixing of 1 mL water, 0.25 mL isopropanol, 0.01 mL 5 wt% Nafion solution and 3 mg materials. The ink was sonicated for at least 2 h. Then 160 µL/cm<sup>2</sup> of the ink was uniformly loaded onto a carbon cloth electrode (CC, plasma treated, geometric area: 0.2-0.3 cm<sup>2</sup>). The electrodes were dried in a 75 °C oven for 30 mins before measurements.

All of the electrochemical measurements in this study were independently repeated for at least three times. The electrochemical measurements were performed in a three-electrode electrochemical cell, in which Pt wire and Ag/AgCl electrode (saturated KCl, E(Ag/AgCl) = 0.197 V vs. SHE) were used as counter and reference electrode, respectively. The working electrode and reference electrode were separated with counter electrode by a glass frit. All potentials were reported versus RHE unless otherwise specified. Before measurements, all of the electrolyte were calibrated the point of 0 V versus RHE by standard hydrogen saturation calibration experiments. A glassy carbon electrode drop-casted by Pt/C was used as the working electrode. After bubbling with hydrogen for 30 mins, the electrode was subjected to LSV (scan rate: 2 mV/s), in which the current of both hydrogen evolution and hydrogen oxidation could be observed. The cross-point is 0 V vs. RHE. Based on Eq. 5.3, the pH values of various electrolytes can be measured. The solution was stirred by a magnetic stirring bar in all of the electrochemical measurements. The polarization curves were recorded by LSV, and the scan rate was 1 mV/s, with 95% IR correction. The data was collected from cathodic potential to anodic potential (forward scan). 3 LSV scans were obtained for each measurements and the third LSV was used for analysis. The first LSV was typically influenced by oxidative peak. The Tafel plots were derived from LSVs. To investigate redox peaks, the scan rate was set to 10 mV/s, with 90% IR correction. The activation process is performed from 1.20-1.53 V vs. RHE. The scan rate is 10 mV/s, with 90% IR correction. The TOFs were calculated by Eq. 5.4, where  $J$  is the anodic current density at certain overpotential,  $A$  is the geometrical surface area of the electrode,  $F$  is the Faraday constant (96485 C/mol), and  $m$  is the loadings of Fe (assumed to be active sites).

$$E(\text{RHE}) = E(\text{Ag/AgCl}) + 0.197 \text{ V} + 0.0592 \times \text{pH} \text{ V} \quad (5.3)$$

$$TOF = \frac{J \times A}{4 \times F \times m} \quad (5.4)$$

ECSA was calculated from double-layer capacitance (Eq. 5.5).<sup>48</sup> The  $C_s$  the specific capacitance of monolayer  $\text{NiFeO}_x$  ( $0.081 \text{ mF/cm}^2$ ),<sup>15</sup> while the  $C_{dl}$  are the double-layer capacitance of the working electrodes. The  $C_{dl}$  was measured according to Eq. 5.6, where  $j_a$  and  $j_c$  are charging and discharging current densities and  $u$  is the scan rate. The potential range of the measurements is from 1.00 to 1.10 V vs. RHE, where no catalytic current and Ni redox peaks were observed. The difference of charging and discharging current densities at 1.05 V was used for calculation. The scan rates were from 10 to 200 mV/s (10, 20, 50, 100, 150, and 200 mV/s).

$$ECSA = \frac{C_{dl}}{C_s} \quad (5.5)$$

$$C_{dl} = \frac{|j_a - j_c|}{2u} \quad (5.6)$$

Electrokinetic studies were performed in KOH with concentration from 0.5 M – 2 M. The 0.5 M and 0.75 M KOH were prepared by dilute 1 M KOH standard solution, while 1.5 M and 2 M KOH were prepared by further adding desired amount of KOH flakes in 1 M KOH standard solution. The LSVs of investigated electrodes were obtained sequentially in 0.5 M, 0.75 M, 1 M, 1.5 M and 2 M KOH. The Tafel plots were derived from LSVs and linear fitted, as  $(\partial E / \partial j)_{pH}$ . The relationship between the potential at a constant current and the concentration of hydroxyl ions  $((\partial E / \partial \log[OH^-]))$  were obtained by calculating the potential at a constant current ( $10 \text{ mA/cm}^2$  for  $\text{FeOOH-NiOOH}$ ;  $1 \text{ mA/cm}^2$  for  $\text{NiFe LDH}$ ) and  $\log [OH^-]$ , and then linear fitting. The order dependence on the hydroxyl ions  $((\partial j / \partial \log[OH^-])_E)$  in 0.5-2 M KOH can be determined according to Eq. 5.1. This parameter should not be directly read from LSVs since it is hard to ensure that in a certain potential, all the current densities are in Tafel region for KOH with different concentrations.

Cation effect of each catalysts was investigated in 1 M KOH, 1 M NaOH and 1 M LiOH. The point of 0 V (vs. RHE) of each electrolyte was calibrated by standard hydrogen saturation calibration method (see above). Noted that the apparent pH value of KOH, NaOH, LiOH is different, despite the same concentration. The pH values are 13.7, 13.5, 13.1 for 1 M KOH, NaOH, LiOH, respectively. The LSVs of investigated electrodes were obtained sequentially in 1 M KOH, 1 M NaOH and 1 M LiOH.

Hydrogen/deuterium (H/D) isotope experiments were performed in 0.5 M and 1 M electrolyte. KOD in  $\text{D}_2\text{O}$  solution were prepared by diluting 30% KOD with  $\text{D}_2\text{O}$  to desired concentrations. The pH of KOH was calibrated by standard hydrogen saturation calibration method. The pD of KOD were calculated by adding 0.87 based on pH of KOH with same concentration. This treatment is



according to the different  $pK_w$  values of  $H_2O$  (14.00) and  $D_2O$  (14.87). The isotope effect value is calculated by the ratio of the current density in KOH and KOD, in the same overpotential (Eq. 5.7). Noted that the theoretical potential of OER in water is 1.229 V vs. RHE, while that of OER in  $D_2O$  is 1.262 V vs. RDE (reversible deuterium electrode).<sup>38</sup> Therefore, the overpotential in KOH and in KOD is calculated as Eq. 5.8-5.9.

$$\text{Isotope effect value} = \frac{j_{KOH}}{j_{KOD}} \quad (5.7)$$

$$\eta_{KOH} = E(Ag/AgCl) + 0.197\text{ V} + 0.0592\text{ V} \times pH - 1.229\text{ V} \quad (5.8)$$

$$\eta_{KOD} = E(Ag/AgCl) + 0.197\text{ V} + 0.0592\text{ V} \times (pH + 0.87) - 1.262\text{ V} \quad (5.9)$$

## 5.9 Contributions

L. Bai performed the synthesis, the majority of characterization, and electrochemical measurements. S. Lee performed the *operando* Raman experiments. L. Bai and S. Lee contributed equally. X. Hu directed the research. All authors analyzed the data.

Dr. Natalia Gasilova (EPFL) is acknowledged for ICP-AES measurements.

## 5.10 References of Chapter 5

- (1) Bai, L.; Lee, S.; Hu, X. Spectroscopic and electrokinetic evidence for a bifunctional mechanism of the oxygen evolution reaction. *Angew. Chem. Int. Ed.* **2020**, DOI: <https://doi.org/10.1002/anie.202011388>.
- (2) Dau, H.; Limberg, C.; Reier, T.; Risch, M.; Roggan, S.; Strasser, P. The Mechanism of Water Oxidation: From Electrolysis via Homogeneous to Biological Catalysis. *ChemCatChem* **2010**, 2, 724-761.
- (3) Man, I. C.; Su, H.-Y.; Calle-Vallejo, F.; Hansen, H. A.; Martínez, J. I.; Inoglu, N. G.; Kitchin, J.; Jaramillo, T. F.; Nørskov, J. K.; Rossmeisl, J. Universality in Oxygen Evolution Electrocatalysis on Oxide Surfaces. *ChemCatChem* **2011**, 3, 1159-1165.
- (4) Koper, M. T. M. Thermodynamic theory of multi-electron transfer reactions: Implications for electrocatalysis. *J. Electroanal. Chem.* **2011**, 660, 254-260.
- (5) Busch, M. Water oxidation: From mechanisms to limitations. *Curr. Opin. Electrochem.* **2018**, 9, 278-284.

- (6) Busch, M.; Halck, N. B.; Kramm, U. I.; Siahrostami, S.; Krttil, P.; Rossmeisl, J. Beyond the top of the volcano? – A unified approach to electrocatalytic oxygen reduction and oxygen evolution. *Nano Energy* **2016**, 29, 126-135.
- (7) Halck, N. B.; Petrykin, V.; Krttil, P.; Rossmeisl, J. Beyond the volcano limitations in electrocatalysis--oxygen evolution reaction. *Phys. Chem. Chem. Phys.* **2014**, 16, 13682-13688.
- (8) Martirez, J. M. P.; Carter, E. A. Unraveling Oxygen Evolution on Iron-Doped beta-Nickel Oxyhydroxide: The Key Role of Highly Active Molecular-like Sites. *J. Am. Chem. Soc.* **2019**, 141, 693-705.
- (9) Song, F.; Busch, M. M.; Lassalle-Kaiser, B.; Hsu, C.-S.; Petkucheva, E.; Bensimon, M.; Chen, H. M.; Corminboeuf, C.; Hu, X. An Unconventional Iron Nickel Catalyst for the Oxygen Evolution Reaction. *ACS Cent. Sci.* **2019**, 5, 558-568.
- (10) Trotochaud, L.; Young, S. L.; Ranney, J. K.; Boettcher, S. W. Nickel-iron oxyhydroxide oxygen-evolution electrocatalysts: the role of intentional and incidental iron incorporation. *J. Am. Chem. Soc.* **2014**, 136, 6744-6753.
- (11) Stevens, M. B.; Trang, C. D. M.; Enman, L. J.; Deng, J.; Boettcher, S. W. Reactive Fe-Sites in Ni/Fe (Oxy)hydroxide Are Responsible for Exceptional Oxygen Electrocatalysis Activity. *J. Am. Chem. Soc.* **2017**, 139, 11361-11364.
- (12) Klaus, S.; Cai, Y.; Louie, M. W.; Trotochaud, L.; Bell, A. T. Effects of Fe Electrolyte Impurities on Ni(OH)<sub>2</sub>/NiOOH Structure and Oxygen Evolution Activity. *J. Phy. Chem. C* **2015**, 119, 7243-7254.
- (13) Yin, H.; Jiang, L.; Liu, P.; Al-Mamun, M.; Wang, Y.; Zhong, Y. L.; Yang, H.; Wang, D.; Tang, Z.; Zhao, H. Remarkably enhanced water splitting activity of nickel foam due to simple immersion in a ferric nitrate solution. *Nano Research* **2018**, 11, 3959-3971.
- (14) Xu, X.; Song, F.; Hu, X. A nickel iron diselenide-derived efficient oxygen-evolution catalyst. *Nat. Commun.* **2016**, 7, 12324.
- (15) Batchellor, A. S.; Boettcher, S. W. Pulse-Electrodeposited Ni–Fe (Oxy)hydroxide Oxygen Evolution Electrocatalysts with High Geometric and Intrinsic Activities at Large Mass Loadings. *ACS Catal.* **2015**, 5, 6680-6689.
- (16) Handoko, A. D.; Wei, F.; Jenndy; Yeo, B. S.; Seh, Z. W. Understanding heterogeneous electrocatalytic carbon dioxide reduction through *operando* techniques. *Nat. Catal.* **2018**, 1, 922-934.
- (17) Fu, D.; Keech, P. G.; Sun, X.; Wren, J. C. Iron oxyhydroxide nanoparticles formed by forced hydrolysis: dependence of phase composition on solution concentration. *Phys. Chem. Chem. Phys.* **2011**, 13, 18523-18529.
- (18) Chen, J.; Zheng, F.; Zhang, S.-J.; Fisher, A.; Zhou, Y.; Wang, Z.; Li, Y.; Xu, B.-B.; Li, J.-T.; Sun, S.-G. Interfacial Interaction between FeOOH and Ni–Fe LDH to Modulate the Local Electronic Structure for Enhanced OER Electrocatalysis. *ACS Catal.* **2018**, 8, 11342-11351.
- (19) Lee, S.; Bai, L.; Hu, X. Deciphering Iron-Dependent Activity in Oxygen Evolution Catalyzed by Nickel-Iron Layered Double Hydroxide. *Angew. Chem. Int. Ed.* **2020**, 59, 8072-8077.

- (20) Lee, S.; Banjac, K.; Lingenfelder, M.; Hu, X. Oxygen Isotope Labeling Experiments Reveal Different Reaction Sites for the Oxygen Evolution Reaction on Nickel and Nickel Iron Oxides. *Angew. Chem. Int. Ed.* **2019**, *58*, 10295-10299.
- (21) Trzesniewski, B. J.; Diaz-Morales, O.; Vermaas, D. A.; Longo, A.; Bras, W.; Koper, M. T.; Smith, W. A. In Situ Observation of Active Oxygen Species in Fe-Containing Ni-Based Oxygen Evolution Catalysts: The Effect of pH on Electrochemical Activity. *J. Am. Chem. Soc.* **2015**, *137*, 15112-15121.
- (22) Louie, M. W.; Bell, A. T. An investigation of thin-film Ni-Fe oxide catalysts for the electrochemical evolution of oxygen. *J. Am. Chem. Soc.* **2013**, *135*, 12329-12337.
- (23) Lu, Z.; Xu, W.; Zhu, W.; Yang, Q.; Lei, X.; Liu, J.; Li, Y.; Sun, X.; Duan, X. Three-dimensional NiFe layered double hydroxide film for high-efficiency oxygen evolution reaction. *Chem. Commun.* **2014**, *50*, 6479-6482.
- (24) Diaz-Morales, O.; Ferrus-Suspedra, D.; Koper, M. T. M. The importance of nickel oxyhydroxide deprotonation on its activity towards electrochemical water oxidation. *Chem. Sci.* **2016**, *7*, 2639-2645.
- (25) Zou, S.; Burke, M. S.; Kast, M. G.; Fan, J.; Danilovic, N.; Boettcher, S. W. Fe (Oxy)hydroxide Oxygen Evolution Reaction Electrocatalysis: Intrinsic Activity and the Roles of Electrical Conductivity, Substrate, and Dissolution. *Chem. Mater.* **2015**, *27*, 8011-8020.
- (26) Friebe, D.; Louie, M. W.; Bajdich, M.; Sanwald, K. E.; Cai, Y.; Wise, A. M.; Cheng, M. J.; Sokaras, D.; Weng, T. C.; Alonso-Mori, R.; Davis, R. C.; Bargar, J. R.; Nørskov, J. K.; Nilsson, A.; Bell, A. T. Identification of highly active Fe sites in (Ni,Fe)OOH for electrocatalytic water splitting. *J. Am. Chem. Soc.* **2015**, *137*, 1305-1313.
- (27) Bockris, J. O. M. Kinetics of activation controlled consecutive electrochemical reactions: anodic evolution of oxygen. *J. Chem. Phys.* **1956**, *24*, 817-827.
- (28) Lyons, M. E. G.; Brandon, M. P. A comparative study of the oxygen evolution reaction on oxidised nickel, cobalt and iron electrodes in base. *J. Electroanal. Chem.* **2010**, *641*, 119-130.
- (29) Fang, Y.-H.; Liu, Z.-P. Tafel Kinetics of Electrocatalytic Reactions: From Experiment to First-Principles. *ACS Catal.* **2014**, *4*, 4364-4376.
- (30) Vrubel, H.; Moehl, T.; Gratzel, M.; Hu, X. Revealing and accelerating slow electron transport in amorphous molybdenum sulphide particles for hydrogen evolution reaction. *Chem. Commun.* **2013**, *49*, 8985-8987.
- (31) Chung, D. Y.; Park, S.; Lopes, P. P.; Stamenkovic, V. R.; Sung, Y.-E.; Markovic, N. M.; Strmcnik, D. Electrokinetic Analysis of Poorly Conductive Electrocatalytic Materials. *ACS Catal.* **2020**, *10*, 4990-4996.
- (32) Michael, J. D.; Demeter, E. L.; Illes, S. M.; Fan, Q.; Boes, J. R.; Kitchin, J. R. Alkaline Electrolyte and Fe Impurity Effects on the Performance and Active-Phase Structure of NiOOH Thin Films for OER Catalysis Applications. *J. Phys. Chem. C* **2015**, *119*, 11475-11481.

- (33) Zaffran, J.; Stevens, M. B.; Trang, C. D. M.; Nagli, M.; Shehadeh, M.; Boettcher, S. W.; Caspary Toroker, M. Influence of Electrolyte Cations on Ni(Fe)OOH Catalyzed Oxygen Evolution Reaction. *Chem. Mater.* **2017**, *29*, 4761-4767.
- (34) Garcia, A. C.; Touzalin, T.; Nieuwland, C.; Perini, N.; Koper, M. T. M. Enhancement of Oxygen Evolution Activity of Nickel Oxyhydroxide by Electrolyte Alkali Cations. *Angew. Chem. Int. Ed.* **2019**, *58*, 12999-13003.
- (35) Parkin, G. Temperature-Dependent Transitions Between Normal and Inverse Isotope Effects Pertaining to the Interaction of H-H and C-H Bonds with Transition Metal Centers. *Acc. Chem. Res.* **2009**, *42*, 315-325.
- (36) Zhang, W.; Burgess, I. J. Kinetic isotope effects in proton coupled electron transfer. *J. Electroanal. Chem.* **2012**, *668*, 66-72.
- (37) Pasquini, C.; Zaharieva, I.; Gonzalez-Flores, D.; Chernev, P.; Mohammadi, M. R.; Guidoni, L.; Smith, R. D. L.; Dau, H. H/D Isotope Effects Reveal Factors Controlling Catalytic Activity in Co-Based Oxides for Water Oxidation. *J. Am. Chem. Soc.* **2019**, *141*, 2938-2948.
- (38) Sakaushi, K. Quantum electrocatalysts: theoretical picture, electrochemical kinetic isotope effect analysis, and conjecture to understand microscopic mechanisms. *Phys. Chem. Chem. Phys.* **2020**, *22*, 11219-11243.
- (39) Krishtalik, L. I. The mechanism of the proton transfer: an outline. *Biochimica et Biophysica Acta (BBA) - Bioenergetics* **2000**, *1458*, 6-27.
- (40) Gómez-Gallego, M.; Sierra, M. A. Kinetic Isotope Effects in the Study of Organometallic Reaction Mechanisms. *Chem. Rev.* **2011**, *111*, 4857-4963.
- (41) Moysiadou, A.; Lee, S.; Hsu, C. S.; Chen, H. M.; Hu, X. Mechanism of Oxygen Evolution Catalyzed by Cobalt Oxyhydroxide: Cobalt Superoxide Species as a Key Intermediate and Dioxygen Release as a Rate-Determining Step. *J. Am. Chem. Soc.* **2020**, *142*, 11901-11914.
- (42) Zhang, Y.; Zhang, H.; Ji, H.; Ma, W.; Chen, C.; Zhao, J. Pivotal Role and Regulation of Proton Transfer in Water Oxidation on Hematite Photoanodes. *J. Am. Chem. Soc.* **2016**, *138*, 2705-2711.
- (43) Liu, Y.; McCrory, C. C. L. Modulating the mechanism of electrocatalytic CO<sub>2</sub> reduction by cobalt phthalocyanine through polymer coordination and encapsulation. *Nat. Commun.* **2019**, *10*, 1683.
- (44) Li, W.; Li, F.; Yang, H.; Wu, X.; Zhang, P.; Shan, Y.; Sun, L. A bio-inspired coordination polymer as outstanding water oxidation catalyst via second coordination sphere engineering. *Nat. Commun.* **2019**, *10*, 5074.
- (45) Song, F.; Bai, L.; Moysiadou, A.; Lee, S.; Hu, C.; Liardet, L.; Hu, X. Transition Metal Oxides as Electrocatalysts for the Oxygen Evolution Reaction in Alkaline Solutions: An Application-Inspired Renaissance. *J. Am. Chem. Soc.* **2018**, *140*, 7748-7759.
- (46) Li, N.; Bediako, D. K.; Hadt, R. G.; Hayes, D.; Kempa, T. J.; von Cube, F.; Bell, D. C.; Chen, L. X.; Nocera, D. G. Influence of iron doping on tetravalent nickel content in catalytic oxygen evolving films. *Proc. Natl. Acad. Sci. USA* **2017**, *114*, 1486.

(47) Xu, L.; Wang, Z.; Chen, X.; Qu, Z.; Li, F.; Yang, W. Ultrathin layered double hydroxide nanosheets with Ni(III) active species obtained by exfoliation for highly efficient ethanol electrooxidation. *Electrochim. Acta* **2018**, 260, 898-904.

(48) McCrory, C. C.; Jung, S.; Peters, J. C.; Jaramillo, T. F. Benchmarking heterogeneous electrocatalysts for the oxygen evolution reaction. *J. Am. Chem. Soc.* **2013**, 135, 16977-16987.

# **Chapter 6 Conclusions and Outlooks**

The Chapter 2 and Chapter 3 of this Thesis declared that a series of double-atom catalysts (DACs) composed of Fe, Co, Ni could be prepared by *in situ* electrochemical activation of single-atom precatalysts in KOH containing certain metal ions impurities. In terms of the oxygen evolution reaction (OER) in 1M KOH, all of the DACs exhibited magnitudes higher intrinsic activity than the corresponding single-atom catalysts (SACs). Especially, Co-Fe and Ni-Fe double-atoms showed the performance comparable to the best-reported OER catalysts in alkaline condition. These DACs have atomically dispersed well-defined bimetallic active sites stabilized in N-doped carbon support, in which the two metals are connected via bridging oxygen. The coordination structures of the catalysts resemble the minimal key active motifs of many bimetallic heterogeneous OER catalysts. Thus the DACs can serve as molecular models to investigate OER reaction mechanisms and the evolution of the active sites in atomic level.

By combing the *operando* X-ray absorption spectroscopy (XAS) results from Chapter 2 and Chapter 3 and the electrokinetic analysis data from Chapter 4, the dynamic evolution of the active sites and the reaction mechanisms of different DACs can be learned. In all of the SACs, the formation of high-valent metal-oxygen ( $M(IV)=O$ ) was confirmed by *operando* XAS, which was also considered as pre-equilibrium step (PES), according to electrokinetic analysis. The rate-determining step (RDS) appeared to be the O-O bond forming step via nucleophilic attack of  $OH^-$  on a  $M(IV)=O$  unit. All of the DACs shared similar catalytic cycles, based on bimetallic cooperation. However, depending on the nature of the metal ions and their coordination environment, the number of protons/hydroxyl ions and electrons that transfer in each step, as well as the source of  $OH^-$  can be varied. These subtleties originate from the different redox potentials and Lewis acidity of the different metal ions, especially when they are coordinated to different ligands. The proposed reaction mechanisms in this Thesis are also similar to some experimental and theoretical mechanistic investigations of molecular homogeneous OER catalysts and mixed metal oxide/oxyhydroxide heterogeneous OER catalysts. The Thesis discovered that the catalytic center and the reaction process can be controlled in atomic level by tuning the local coordination environment. Thus, due to the uneven distribution of the active sites or coexisting of different active centers in the heterogeneous OER catalysts, the discrepancy of identification of the active centers and poor quality of electrokinetic data (e.g. deviation of Tafel slopes from theoretical values, not unity reaction orders) can happen. In summary, therefore, by bridging the transitionally separated molecular and solid-state catalysts, these easily accessed, molecularly defined, and earth-abundant double-atom OER electrocatalysts provide blueprints for the mechanistic studies

of heterogeneous mixed metal oxide OER catalysts in atomic level, which in turn facilitate the further development of more advanced OER electrocatalysts.

This Thesis investigated the DACs composed of Ni-Fe, Co-Fe, and Co-Ni. It is anticipated that other DACs, based on Co-Mn, Co-V, Ni-V, and so on, can be prepared by similar methods or other synthetic procedure. In this way, the active centers and reaction mechanisms of these heterogeneous bimetallic OER catalysts<sup>1-3</sup> could also be investigated in atomic level. Introducing a third type of metal to bimetallic OER catalysts, the resulted "trimetallic" OER catalysts have better OER performance compared to bimetallic ones.<sup>4-6</sup> However, the direct identification of active sites and illustration of reaction mechanisms are rather difficult for these mixed multi-metal OER catalysts. Therefore, it would be quite interesting if an atomically dispersed sub-nano clusters composed of multi-metals could be developed, in order to study the multi-metal OER catalysts in molecular level.

The research results from Chapter 2 to Chapter 4 suggested that double-atom catalysis is ubiquitous in alkaline OER. Some 'so-called' SACs actually transform to DACs under OER catalytic conditions. Up until now, many single-atom OER catalysts<sup>7-10</sup> have been reported to have outstanding performance for OER.<sup>7-10</sup> These catalysts were prepared by different methods and had different core structures. Despite the results of this Thesis do not signify that all of the SACs are not stable or have structural and compositional change during OER catalysis, the researchers should check if SACs are transformed to other real active species during or after reaction. Since metal ions impurities (e.g. Fe) in electrolyte may have huge impact for the apparent performance,<sup>11-13</sup> the activity in impurity-depleting condition (e.g. Fe-free) should be evaluated to determine the real activity of the SACs. The similar caution should also be taken in terms of other electrocatalysis, like hydrogen evolution reaction (HER), oxygen reduction reaction (ORR), CO<sub>2</sub> reduction reaction (CRR), and so on.

In addition to employing atomically dispersed catalysts as model systems for molecular level insight of OER catalysis, this Thesis also adopted experimental methods, including *operando* Raman spectroscopy and electrokinetic analysis, to validate a novel bifunctional OER mechanism. In this mechanism, the O-O bond formation step is facilitated through a nucleophilic attack of OH<sup>-</sup> on a M=O moiety coupled with a concerted hydrogen atom transfer to a nearby hydrogen acceptor. This mechanism has been considered to have the potential to break the overpotential limit caused by scaling relationship of conventional proton-coupled electron transfer (PCET) OER mechanism. Up until now, the mechanism has only been proposed by theoretical calculations. In Chapter 5,



two model OER catalysts, FeOOH-NiOOH composite catalyst and NiFe layered double hydroxide (LDH) were investigated. Despite their similar chemical compositions, the spectroscopic and electrokinetic data support two distinct mechanisms for the two catalysts. FeOOH-NiOOH operates by a bifunctional mechanism where the rate-determining O-O bond forming step is the concerted  $\text{OH}^-$  attack on a  $\text{Fe}=\text{O}$  site coupled with a hydrogen atom transfer to a  $\text{Ni}^{\text{III}}-\text{O}$  site. On the contrary, NiFe LDH operates by a conventional mechanism of four consecutive PCET steps, and the rate-determining O-O bond forming step is the attack of  $\text{OH}^-$  on a  $\text{Fe}=\text{O}$  unit. Due to the promoted O-O bond formation step in bifunctional mechanism, the intrinsic activity of FeOOH-NiOOH is 10 times higher compared to conventional NiFe LDH catalyst. The data described here constitute the first experimental evidences for the bifunctional mechanism which has hitherto only computational supports. The superior activity of FeOOH-NiOOH demonstrates the potential of bifunctional OER catalysts to overcome the performance limit of conventional catalysts imposed by the scaling relationship.

In recent years, some OER catalysts fabricated on nickel foam (NF) electrode were developed and exhibited very high performance for alkaline OER.<sup>14-16</sup> The overpotential to reach  $10 \text{ mA/cm}^2$  is even below 200 mV.<sup>17-18</sup> However, it should be noted that the activity of these OER catalysts is highly dependent on the substrates.<sup>19</sup> When other inert substrates like glassy carbon electrode were employed, the activities were inferior compared to the catalysts on NF, even by normalizing to the loading of catalyst and electrochemical active surface area (ECSA).<sup>20-21</sup> Thus, it would be intriguing to investigate whether the high performance is originated from the bifunctional OER mechanisms, since NiOOH from NF is a good hydrogen acceptor.

The bifunctional mechanism provides an opportunity to individually fine-tune two components of an OER catalyst for optimized activity, adding a new design principle. For example, analogous to the present FeOOH-NiOOH catalyst, the FeOOH component might be replaced by another material with a low energy barrier to form an electrophilic  $\text{M}=\text{O}$  unit, while the NiOOH component might be replaced by another better hydrogen atom acceptor. It is expected that in this way, OER catalysts with higher intrinsic activity can be developed.

Overall, by combining *in-situ/operando* spectroscopy and electrokinetic analysis, this Thesis not only reveals the dynamic information of the active centers, but also elucidates the reaction mechanisms of OER catalysis in atomic level. For the first time, the Thesis has introduced double-atom catalysis concept in alkaline OER, and employed them as molecular models to deeply investigate OER catalysis. The Thesis has also proved the existence of bifunctional OER

mechanisms by experimental methods. It is anticipated that the similar research methods can be applied to other electrochemical reactions, in order to have a comprehensive atomic-level insight of the active sites and reaction processes.

## References of Chapter 6

1. Fan, K.; Chen, H.; Ji, Y.; Huang, H.; Claesson, P. M.; Daniel, Q.; Philippe, B.; Rensmo, H.; Li, F.; Luo, Y.; Sun, L., Nickel-vanadium monolayer double hydroxide for efficient electrochemical water oxidation. *Nat. Commun.* **2016**, *7*, 11981.
2. Song, F.; Hu, X., Ultrathin Cobalt–Manganese Layered Double Hydroxide Is an Efficient Oxygen Evolution Catalyst. *J. Am. Chem. Soc.* **2014**, *136*, 16481-16484.
3. Liardet, L.; Hu, X., Amorphous Cobalt Vanadium Oxide as a Highly Active Electrocatalyst for Oxygen Evolution. *ACS Catal.* **2018**, *8*, 644-650.
4. Zhang, B.; Zheng, X.; Voznyy, O.; Comin, R.; Bajdich, M.; García-Melchor, M.; Han, L.; Xu, J.; Liu, M.; Zheng, L., Homogeneously dispersed multimetal oxygen-evolving catalysts. *Science* **2016**, *352*, 333-337.
5. Jiang, J.; Sun, F.; Zhou, S.; Hu, W.; Zhang, H.; Dong, J.; Jiang, Z.; Zhao, J.; Li, J.; Yan, W.; Wang, M., Atomic-level insight into super-efficient electrocatalytic oxygen evolution on iron and vanadium co-doped nickel (oxy)hydroxide. *Nat. Commun.* **2018**, *9*, 2885.
6. Smith, R. D.; Prevot, M. S.; Fagan, R. D.; Zhang, Z.; Sedach, P. A.; Siu, M. K.; Trudel, S.; Berlinguette, C. P., Photochemical route for accessing amorphous metal oxide materials for water oxidation catalysis. *Science* **2013**, *340*, 60-63.
7. Zhu, C.; Fu, S.; Shi, Q.; Du, D.; Lin, Y., Single-Atom Electrocatalysts. *Angew. Chem. Int. Ed.* **2017**, *56*, 13944-13960.
8. Zhao, D.; Zhuang, Z.; Cao, X.; Zhang, C.; Peng, Q.; Chen, C.; Li, Y., Atomic site electrocatalysts for water splitting, oxygen reduction and selective oxidation. *Chem. Soc. Rev.* **2020**, *49*, 2215-2264.
9. Zhu, C.; Shi, Q.; Feng, S.; Du, D.; Lin, Y., Single-Atom Catalysts for Electrochemical Water Splitting. *ACS Energy Lett.* **2018**, *3*, 1713-1721.
10. Zhang, H.; Tian, W.; Duan, X.; Sun, H.; Liu, S.; Wang, S., Catalysis of a Single Transition Metal Site for Water Oxidation: From Mononuclear Molecules to Single Atoms. *Adv. Mater.* **2020**, *32*, e1904037.
11. Corrigan, D. A., The catalysis of the oxygen evolution reaction by iron impurities in thin film nickel oxide electrodes. *J. Electrochem. Soc.* **1987**, *134*, 377-384.

12. Burke, M. S.; Kast, M. G.; Trotochaud, L.; Smith, A. M.; Boettcher, S. W., Cobalt-iron (oxy)hydroxide oxygen evolution electrocatalysts: the role of structure and composition on activity, stability, and mechanism. *J. Am. Chem. Soc.* **2015**, *137*, 3638-3648.
13. Trotochaud, L.; Young, S. L.; Ranney, J. K.; Boettcher, S. W., Nickel-iron oxyhydroxide oxygen-evolution electrocatalysts: the role of intentional and incidental iron incorporation. *J. Am. Chem. Soc.* **2014**, *136*, 6744-6753.
14. Suen, N. T.; Hung, S. F.; Quan, Q.; Zhang, N.; Xu, Y. J.; Chen, H. M., Electrocatalysis for the oxygen evolution reaction: recent development and future perspectives. *Chem. Soc. Rev.* **2017**, *46*, 337-365.
15. Song, F.; Bai, L.; Moysiadou, A.; Lee, S.; Hu, C.; Liardet, L.; Hu, X., Transition Metal Oxides as Electrocatalysts for the Oxygen Evolution Reaction in Alkaline Solutions: An Application-Inspired Renaissance. *J. Am. Chem. Soc.* **2018**, *140*, 7748-7759.
16. Feng, C.; Faheem, M. B.; Fu, J.; Xiao, Y.; Li, C.; Li, Y., Fe-Based Electrocatalysts for Oxygen Evolution Reaction: Progress and Perspectives. *ACS Catal.* **2020**, *10*, 4019-4047.
17. Qian, M.; Cui, S.; Jiang, D.; Zhang, L.; Du, P., Highly Efficient and Stable Water-Oxidation Electrocatalysis with a Very Low Overpotential using FeNiP Substitutional-Solid-Solution Nanoplate Arrays. *Adv. Mater.* **2017**, *29*, 1704075.
18. Xu, X.; Song, F.; Hu, X., A nickel iron diselenide-derived efficient oxygen-evolution catalyst. *Nat. Commun.* **2016**, *7*, 12324.
19. Gu, H.; Shi, G.; Chen, H.-C.; Xie, S.; Li, Y.; Tong, H.; Yang, C.; Zhu, C.; Mefford, J. T.; Xia, H.; Chueh, W. C.; Chen, H. M.; Zhang, L., Strong Catalyst-Support Interactions in Electrochemical Oxygen Evolution on Ni-Fe Layered Double Hydroxide. *ACS Energy Lett.* **2020**, *5*, 3185-3194.
20. Lu, X.; Zhao, C., Electrodeposition of hierarchically structured three-dimensional nickel-iron electrodes for efficient oxygen evolution at high current densities. *Nat. Commun.* **2015**, *6*, 6616.
21. Morales-Guio, C. G.; Liardet, L.; Hu, X., Oxidatively Electrodeposited Thin-Film Transition Metal (Oxy)hydroxides as Oxygen Evolution Catalysts. *J. Am. Chem. Soc.* **2016**, *138*, 8946-8957.

# Appendix 1 The quasi-equilibrium model for electrokinetic study

## A1.1 Bultler-Volmer equation

For any elemental electrochemical reaction ( $xR \rightarrow yO + ne^-$ ), the catalytic current density can be described by Butler-Volmer equation<sup>1</sup>:

$$j = nF(C_R^x k_a^0 \exp\left(\frac{n\alpha FE}{RT}\right) - C_O^y k_c^0 \exp\left(-\frac{n(1-\alpha)FE}{RT}\right)) \quad (A-1)$$

In this equation,  $\alpha$  is the transfer coefficient of the reaction,  $E$  is the applied potential,  $F$  is the Faraday constant,  $R$  is the universal gas constant,  $T$  is the thermodynamic temperature. Noted that  $E$  value is relative to Standard Hydrogen Electrode (SHE), which is zero point.  $C_R$  and  $C_O$  are concentration of reactant and product, respectively.  $k_a^0$  and  $k_c^0$  are rate constant of forward and reverse reaction, respectively. The subscript  $a$  and  $c$  are related to anodic and cathodic reactions. The expression of  $k_a^0$  and  $k_c^0$  are depicted as below:

$$k_a^0 = P_a \exp\left(\frac{-\Delta\widetilde{G}_a^0(E=0)}{RT}\right) \quad (A-2)$$

$$k_c^0 = P_c \exp\left(\frac{-\Delta\widetilde{G}_c^0(E=0)}{RT}\right) \quad (A-3)$$

The  $\Delta\widetilde{G}_a^0(E=0)$  and  $\Delta\widetilde{G}_c^0(E=0)$  denote as standard Gibbs free energy of activation, which are related to the activation energies (energy barriers) to be overcome by the reduced (a) and oxidized (c) species in standard conditions.  $P_a$  and  $P_c$  are corresponding pre-exponential factors. Noted that both  $k_a^0$  and  $k_c^0$  are related to standard condition, which is independent of the concentration of reduced and oxidized species.

At the equilibrium potential ( $E_{eq}$ ), the forward and reverse reaction rate is equal ( $j_a = j_c$ ). Then,

$$C_{Req}^x k_a^0 \exp\left(\frac{n\alpha F E_{eq}}{RT}\right) = C_{Oeq}^y k_c^0 \exp\left(-\frac{n(1-\alpha) F E_{eq}}{RT}\right) \quad (A-4)$$

In this case the Butler-Volmer Equation is reformatted as:

$$j = j_0' \left( \frac{C_R^x}{C_{Req}^x} \exp\left(\frac{n\alpha F \eta}{RT}\right) - \frac{C_O^y}{C_{Oeq}^y} \exp\left(-\frac{n(1-\alpha) F \eta}{RT}\right) \right) \quad (A-5)$$

$$j_0' = nF C_{Req}^x k_a^0 \exp\left(\frac{n\alpha F E_{eq}}{RT}\right) = nF C_{Oeq}^y k_c^0 \exp\left(-\frac{n(1-\alpha) F E_{eq}}{RT}\right) \quad (A-6)$$

$$\eta = E - E_{eq} \quad (A-7)$$

$\eta$  is the applied overpotential. When the reaction is highly irreversible, the Eq. A-5 is reformatted as well-known Tafel equation,  $j_0$  is the exchange current density:

$$j = j_0 \exp\left(\frac{n\alpha F \eta}{RT}\right) \quad (A-8)$$

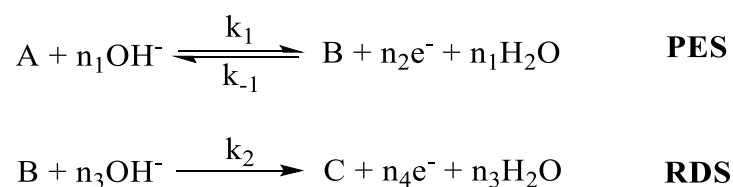
$$j_0 = nF C_R^x k_a^0 \exp\left(\frac{n\alpha F E_{eq}}{RT}\right) = nF k_a C_R^x \quad (A-9)$$

$$k_a = k_a^0 \exp\left(\frac{n\alpha F E_{eq}}{RT}\right) \quad (A-10)$$

## A1.2 Quasi-Langmuir model

The electrochemical reaction that involves multiple electron transfer can not be simply described by Butler-Volmer Equation.<sup>1</sup> Certain reasonable model should be established to accurately study the reaction kinetics. The mechanism of oxygen evolution reactions (OER) in the Tafel region can be described by a quasi-Langmuir model.<sup>2-4</sup> In this model, the surface concentration of key intermediate (resting state) is less than 10%, which fits the general condition of Langmuir isotherm adsorption. This assumption is reasonable when the applied potential is moderate (e.g. in the Tafel region). Generally, the key process of OER involves a pre-equilibrium (quasi-equilibrium) step (PES) and a rate-determining step (RDS). In alkaline condition, the reactions were depicted as Scheme A-

1. The PES can either be a single electrochemical step (in most case  $n_2 = 1$ ) or combined consecutive electrochemical steps ( $n_2 \geq 1$ ). For the RDS, the transferred electrons  $n_4$  can be either 1 or 0. The overall rate of the OER is related to these two steps, while the other steps such as the reversible redox processes (can be described by Nernst equation, see below) and the processes after RDS will not restrict the final reaction rate.<sup>1</sup>



**Scheme A-1.** General key process in alkaline OER.

$k_1$  and  $k_{-1}$  are the rate constants of the forward and reverse reaction of PES, respectively.  $k_2$  is rate constants of RDS. The steady-state velocity of oxygen evolution can be expressed as follows by using Butler-Volmer equation:

$$v = k_2 \theta_B a_{OH^-}^{n_3} \exp\left(\frac{n_4 \alpha_2 \eta_2 F}{RT}\right) \quad (A-11)$$

$\alpha_2$  is the transfer coefficient of RDS,  $\eta_2$  is the overpotential relative to equilibrium potential of RDS (it is not equal to apparent overpotential relative to OER equilibrium potential),  $F$  is the Faraday constant,  $R$  is the universal gas constant,  $T$  is the thermodynamic temperature.  $\theta_B$  represents the partial surface coverage of intermediate  $B$ .  $\theta_B$  can be defined in terms of the surface coverage of the resting state  $A$  ( $\theta_A$ ). The relationship between  $\theta_B$  and  $\theta_A$  can be deduced from the equilibrium equation:

$$v_a = k_1 \theta_A a_{OH^-}^{n_1} \exp\left(\frac{n_2 \alpha_1 \eta_1 F}{RT}\right) \quad (A-12)$$

$$v_{-a} = k_{-1} \theta_B \exp\left(-\frac{n_2 (1-\alpha_1) \eta_1 F}{RT}\right) \quad (A-13)$$

For the quasi-equilibrium condition:

$$v_a = v_{-a} \quad (A-14)$$

$\eta_1$  is the overpotential relative to equilibrium potential of PES. Since both  $\eta_1$  and  $\eta_2$  are hard to determine, we use applied potential  $E$  and standard rate constants (denoted with superscript 0, similar as Eq. A-10) to rearrange the above equation. Then we have:

$$\theta_B = K_1^0 \theta_A a_{OH^-}^{n_1} \exp\left(\frac{n_2 EF}{RT}\right) \quad (A-15)$$

$$K_1^0 = \frac{k_1^0}{k_{-1}^0}. \quad (A-16)$$

$$v = k_2^0 \theta_B a_{OH^-}^{n_3} \exp\left(\frac{n_4 \alpha_2 EF}{RT}\right) \quad (A-17)$$

Substituting the expression of  $\theta_B$  (Eq. A-15) for Eq. A-17, the steady-state velocity of OER can be expressed as:

$$v = k_2^0 K_1^0 \theta_A a_{OH^-}^{n_1+n_3} \exp\left(\frac{(n_2+n_4 \alpha_2) EF}{RT}\right) \quad (A-18)$$

If Langmuir conditions are assumed, the surface coverage of  $A$  ( $\theta_A$ ) would not be expected to change appreciably over the potential range, and may be considered a potential-independent constant. The catalytic current density of OER is:

$$j = 4Fv = k^0 a_{OH^-}^{n_1+n_3} \exp\left(\frac{(n_2+n_4 \alpha_2) EF}{RT}\right) \quad (A-19)$$

$$k^0 = 4Fk_2^0 K_1^0 \theta_A \quad (A-20)$$

The Tafel slope,  $\left(\frac{\partial E}{\partial \log j}\right)_{pH}$  or  $\left(\frac{\partial \eta}{\partial \log j}\right)_{pH}$ , of OER can be expressed as:

$$\left(\frac{\partial E}{\partial \log j}\right)_{pH} = \left(\frac{\partial \eta}{\partial \log j}\right)_{pH} = \frac{2.303RT}{(n_2+n_4 \alpha_2)F} \quad (A-21)$$

To study the order of proton concentration ( $[H^+]$ ) or hydroxyl ions concentration ( $[OH^-]$ ) on the reaction rate, according to Eq. A-18, in principle we can directly measure current density at a certain potential  $E$  (relative to Standard Hydrogen Electrode, SHE, the standard condition) with changing the  $[OH^-]$ . However, the current density may not locate in Tafel region, making the determination inaccurate. Typically, we first measure the variation of the potential with changing  $[OH^-]$  in a constant current density (in Tafel region). Then the order of  $[OH^-]$  can be determined by Eq. A-22.

$$\left(\frac{\partial \log j}{\partial \log [\text{OH}^-]}\right)_E = -\frac{\left(\frac{\partial E}{\partial \log [\text{OH}^-]}\right)_j}{\left(\frac{\partial E}{\partial \log j}\right)_{pH}} \quad (\text{A-22})$$

The relationship is also correct when the  $E$  is substituted by  $\eta$  (Eq. A-22), the  $\left(\frac{\partial \log j}{\partial \log [\text{OH}^-]}\right)_\eta$  is pH-dependence degree in Reversible Hydrogen Electrode (RHE) scale:

$$\left(\frac{\partial \log j}{\partial \log [\text{OH}^-]}\right)_\eta = -\frac{\left(\frac{\partial \eta}{\partial \log [\text{OH}^-]}\right)_j}{\left(\frac{\partial \eta}{\partial \log j}\right)_{pH}} \quad (\text{A-23})$$

The equation can be rearranged as below (Eq. A-24 and A-25), and finally the relationship of pH-dependence degree and the order of  $[\text{OH}^-]/[\text{H}^+]$  is depicted as Eq. A-26. The pH-dependence degree is actually a function of  $[\text{OH}^-]$  and Tafel slope.

$$\left(\frac{\partial \log j}{\partial \log [\text{OH}^-]}\right)_\eta = -\frac{-\left(\frac{\partial E_{eq}}{\partial \log [\text{OH}^-]}\right)_j + \left(\frac{\partial E}{\partial \log [\text{OH}^-]}\right)_j}{\left(\frac{\partial E}{\partial \log j}\right)_{pH}} \quad (\text{A-24})$$

Since  $Tafel\ slope = \left(\frac{\partial \eta}{\partial \log j}\right)_{pH} = \left(\frac{\partial E}{\partial \log j}\right)_{pH}$ , and the equilibrium potential of OER changed as -59 mV/dec with  $[\text{OH}^-]$  (-59 mV/pH). Thus we have:

$$\left(\frac{\partial \log j}{\partial \log [\text{OH}^-]}\right)_\eta = -\frac{59\text{ mV/dec} + \left(\frac{\partial E}{\partial \log [\text{OH}^-]}\right)_j}{\left(\frac{\partial E}{\partial \log j}\right)_{pH}} \quad (\text{A-25})$$

$$\left(\frac{\partial \log j}{\partial \log [\text{OH}^-]}\right)_\eta = \left(\frac{\partial \log j}{\partial \log [\text{OH}^-]}\right)_E - \frac{59\text{ mV/dec}}{\left(\frac{\partial E}{\partial \log j}\right)_{pH}} \quad (\text{A-26})$$

### A1.3 Typical examples for the application of the electrokinetic model

Here we presented some typical theoretical values of Tafel slope deduced from the modified quasi-Langmuir models.

(1) Tafel slope = 40 mV/dec



In this case, both the PES and RDS involve one electron transfer ( $n_2 = n_4 = 1$ , Scheme A-1). Ideally the transfer coefficient is 0.5 ( $\alpha_2 = 0.5$ ) when the diffuse double layer effects were eliminated (a concentrations of electrolyte bigger than 0.5 M is sufficient to eliminate diffuse double layer effects). According to Eq. A-21, the Tafel slope is  $2.303RT/1.5F = 40$  mV/dec. In this Thesis, double-atom catalysts like Co-Fe-N-C, Fe-Co-N-C, Ni-Fe-N-C, and Ni-Fe based heterogeneous OER catalysts like FeOOH-NiOOH and NiFe LDH fit well with this kinetic parameter.

(2) Tafel slope = 59 mV/dec

In this case, only PES involve one electron transfer and there is no apparent electron transfer in RDS ( $n_2 = 1$ ,  $n_4 = 0$ , Scheme A-1). According to Eq. A-21, the Tafel slope is  $2.303RT/F = 60$  mV/dec. In this Thesis, double-atom catalysts like Co-Ni-N-C, Co-Co-N-C and Fe-Ni-N-C fit well with this kinetic parameter.

(3) Tafel slope = 118 mV/dec

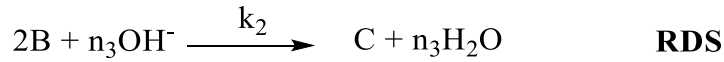
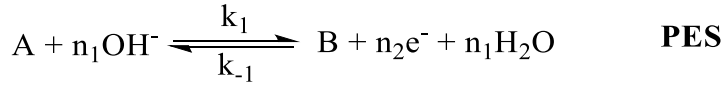
In this case, there are no PES before RDS, the reaction is limited by a single-electron transfer. Typically this happens when the first step is the RDS or all of the steps before RDS are irreversible and can not be considered as the PES. In terms of Scheme A-1, for example, A is completely transformed to B. According to Eq. A-8 or Eq. A-21 ( $n_2 = 0$ ,  $n_4 = 1$ , Scheme A-1), when the transfer coefficient is 0.5, the Tafel slope is  $2.303RT/0.5F = 118$  mV/dec. In this Thesis, the Tafel slopes of single-atom precatalysts like Ni-N-C and Fe-N-C are close to this value.

(4) Tafel slope = 24 mV/dec

In this case, the RDS involves one electron transfer, while the PES involves transfer of two electrons, or there are two one electron transfer PESs before RDS ( $n_2 = 2$ ,  $n_4 = 1$ , Scheme A-1). Considering the ideal transfer coefficient of  $\alpha_2$  is 0.5, according to Eq. A-

21, the Tafel slope is  $2.303RT/2.5F = 24$  mV/dec. No catalysts in this Thesis exhibited this kind of Tafel slope values.

(5) Tafel slope = 30 or 15 mV/dec



**Scheme A-2.** General key process in alkaline OER, in which O-O bond formation is the coupling of two M=O center (B).

To have such Tafel slopes, the OER mechanism should involve RDS as the coupling of two M=O center (Scheme A-2). This step does not have apparent electron transfer.

For this mechanism, the reaction rate is:

$$v = k_2^0 \theta_B^2 a_{OH^-}^{n_3} \quad (A-27)$$

For the PES, the reaction is in quasi-equilibrium, thus Eq. A-11 to A-13 are also suitable:

$$v_a = v_{-a} = k_1^0 \theta_A a_{OH^-}^{n_1} \exp\left(\frac{n_2 \alpha_1 EF}{RT}\right) = k_{-1}^0 \theta_B \exp\left(-\frac{n_2(1-\alpha_1)EF}{RT}\right) \quad (A-28)$$

Then we also have:

$$\theta_B = K_1^0 \theta_A a_{OH^-}^{n_1} \exp\left(\frac{n_2 EF}{RT}\right) \quad (A-29)$$

$$K_1^0 = \frac{k_1^0}{k_{-1}^0}. \quad (A-30)$$

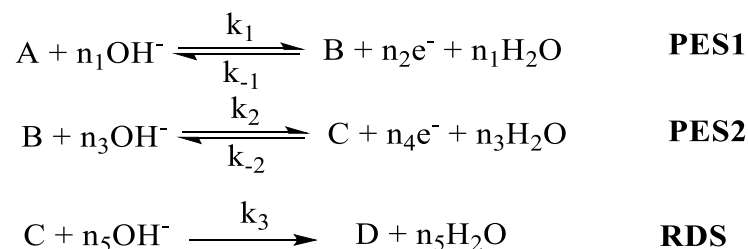
Substituting the expression of  $\theta_B$  (A-29) for Eq. A-27 and then reformat in the form of current density:

$$j = 4Fv = 4Fk_2^0 (K_1^0 \theta_A)^2 a_{OH^-}^{2n_1+n_3} \exp\left(\frac{2n_2 EF}{RT}\right) \quad (A-31)$$

The Tafel slope is:

$$\left(\frac{\partial E}{\partial \log j}\right)_{pH} = \left(\frac{\partial \eta}{\partial \log j}\right)_{pH} = \frac{2.303RT}{2Fn_2} \quad (\text{A-32})$$

Typically the PES involves one electron transfer, thus  $n_2 = 1$ , and the Tafel slope is 30 mV/dec. When two electrons transfer is involved in PES ( $n_2 = 2$ ), the Tafel slope change to 15 mV/dec. Another scenario is that the O-O bond formation involves the coupling of two different M=O centers. In this case, the Scheme A-2 is reformatted as Scheme A-3:



**Scheme A-3.** General key process in alkaline OER, in which O-O bond formation is the coupling of two different M=O center (C). In this case, the coupling is considered occurring at C internally.

For this mechanism, the reaction rate is:

$$v = k_3^0 \theta_C a_{\text{OH}^-}^{n_5} \quad (\text{A-33})$$

For two PESs:

$$v_a = v_{-a} = k_1^0 \theta_A a_{\text{OH}^-}^{n_1} \exp\left(\frac{n_2 \alpha_1 EF}{RT}\right) = k_{-1}^0 \theta_B \exp\left(-\frac{n_2(1-\alpha_1)EF}{RT}\right) \quad (\text{A-34})$$

$$v_b = v_{-b} = k_2^0 \theta_B a_{\text{OH}^-}^{n_1} \exp\left(\frac{n_3 \alpha_2 EF}{RT}\right) = k_{-2}^0 \theta_C \exp\left(-\frac{n_3(1-\alpha_2)EF}{RT}\right) \quad (\text{A-35})$$

Then we also have:

$$\theta_B = K_1^0 \theta_A a_{\text{OH}^-}^{n_1} \exp\left(\frac{n_2 EF}{RT}\right) \quad (\text{A-36})$$

$$K_1^0 = \frac{k_1^0}{k_{-1}^0}. \quad (\text{A-37})$$

$$\theta_C = K_2^0 \theta_B a_{OH^-}^{n_3} \exp\left(\frac{n_4 EF}{RT}\right) \quad (A-38)$$

$$K_2^0 = \frac{k_2^0}{k_{-2}^0}. \quad (A-39)$$

Emerging the above equations, we have:

$$\theta_C = K_1^0 K_2^0 \theta_A a_{OH^-}^{n_1+n_3} \exp\left(\frac{(n_2+n_4)EF}{RT}\right) \quad (A-40)$$

$$j = 4Fv = 4Fk_3^0 K_1^0 K_2^0 \theta_A a_{OH^-}^{n_1+n_3+n_5} \exp\left(\frac{(n_2+n_4)EF}{RT}\right) \quad (A-41)$$

The Tafel slope is:

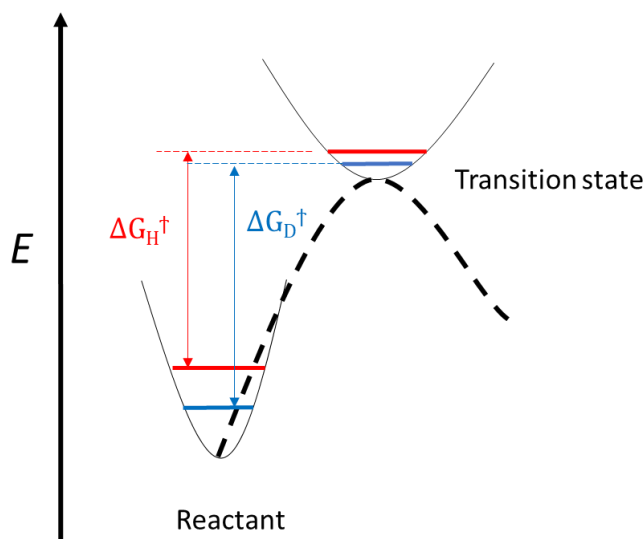
$$\left(\frac{\partial E}{\partial \log j}\right)_{pH} = \left(\frac{\partial \eta}{\partial \log j}\right)_{pH} = \frac{2.303RT}{(n_2+n_4)F} \quad (A-42)$$

Typically the generation of two different M=O involves two electrons in total ( $n_2 = n_4 = 1$ ), thus, the Tafel slope is still 30 mV/dec, the same as that of two same M=O center coupling. It should be noted that no OER catalysts in this Thesis exhibited this kind of Tafel slope values.

## Appendix 2 H-D isotope effect

H-D isotope effect (IE) is the change of the reaction rate of a chemical reaction when one of the H atoms in the reactants is replaced by a deuterium. In electrochemical reaction, the change of the reaction rate is reflected by the variation of current density. For OER in alkaline condition, the key reactants are hydroxyl ions and adsorbed \*OH and \*O species. Since H of adsorbed \*OH is rapidly exchanged with D, the H-D isotope effect can be investigated by measure the activity difference between KOH water solution and KOD heavy water solution (Eq. A-43).

$$IE = \frac{j_{KOH}}{j_{KOD}} \quad (\text{A-43})$$

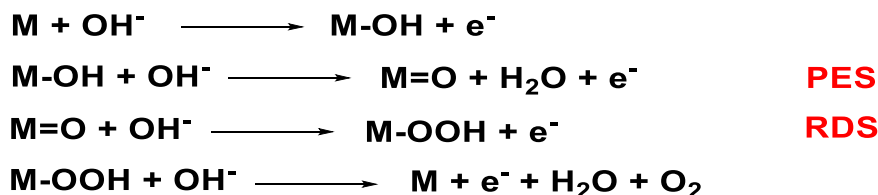


**Scheme A-4.** Illustration of H/D isotope effect via energy diagram.  $\Delta G_H^\ddagger$  and  $\Delta G_D^\ddagger$  represent the activation energy of original and deuterium-substituted reactants, respectively. Typically,  $\Delta G_H^\ddagger$  is smaller than  $\Delta G_D^\ddagger$ .

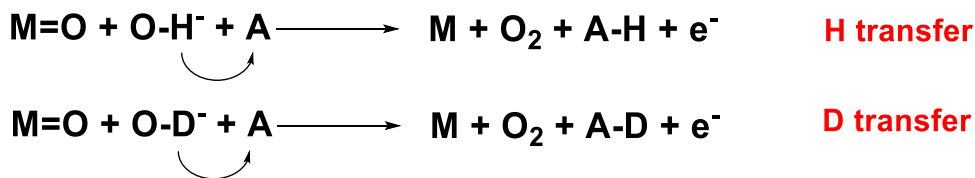
This change in reaction rate is a quantum mechanical effect. Compared to their lighter counterparts (like H), heavier isotopes (like D) will lead to lower vibration frequencies, or

viewed quantum mechanically, lower zero-point energy (ZPE).<sup>5-6</sup> With a lower ZPE, greater energetic input is required to reach the transition state, resulting in a higher activation energy for bond cleavage, consequently, a slower reaction rate (Scheme A-4).<sup>5-6</sup>

There are two types of KIE, the primary KIE and the secondary KIE.<sup>5-7</sup> Primary KIE is found when a bond to the isotopically-labeled atom is being formed or broken. For a multi-step reaction, the observation of a primary KIE is indicative of breaking/forming a bond to the isotopically-labeled atom at the RDS.<sup>5-6</sup> As the study in Chapter 5 of this Thesis for examples, the steps indicated in Scheme A-5 and A-6 involve direct H/D breaking, which should exhibit primary KIE.



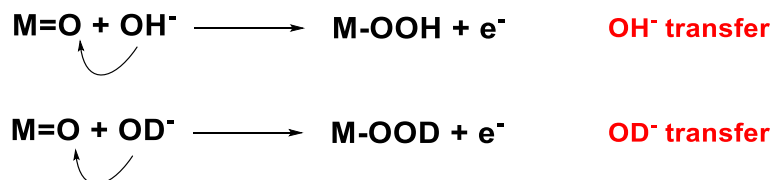
**Scheme A-5.** Representative key step of OER that involves primary isotope effect.



**Scheme A-6.** Representative key step of OER that involves primary isotope effect.

Secondary KIE is observed when no bond to the isotopically-labeled atom in the reactant is broken or formed, but a neighboring bond of isotopically-labeled atom is broken or formed.<sup>5, 7</sup> Take the reactions in Scheme A-7 as an example, neither direct O-H(D) break nor formation happens. Only an O-O bond close to H/D is formed. The observed isotope

effect is originated from difference of ZPE between O-OH<sup>•</sup> and O-OD<sup>•</sup>. Secondary KIEs tend to be much smaller than primary KIEs, typically in the range of 1.0-1.3.<sup>5, 7</sup>



**Scheme A-7.** Representative key step of OER that involves secondary isotope effect.

It should be noted that the exchange of H by D affects both the thermodynamics and the kinetics of PCET reactions.<sup>8-9</sup> Thus, the observed isotope effect can be divided as the thermodynamic isotope effect (TIE) and the kinetic isotope effect (KIE). The TIE is originated from a change in the reaction thermodynamics or shift of the equilibriums due to an increase in the vibrational ZPE of a certain bond involving hydrogen.<sup>8, 10</sup> According to the quasi-Langmuir models, H/D TIE effect should be observed in PES that involved proton/hydrogen transfer, while KIE is usually employed to determine whether proton/hydrogen transfer is involved in RDS.<sup>6-7, 9</sup> The overall isotope effect (IE) is the combination of TIE and KIE (Eq. A-44).

$$IE = KIE \times TIE \quad (\text{A-44})$$

In quasi-Langmuir model, the reaction rate is depicted as Eq. A-19 in Appendix 1, as below:

$$j = 4Fv = k^0 a_{\text{OH}^{\bullet}}^{n_1+n_3} \exp\left(\frac{(n_2+n_4\alpha_2)EF}{RT}\right) \quad (\text{A-19})$$

The isotope effect should be compared in the same overpotential since the equilibrium potential is different when hydrogen is substituted by deuterium. Thus, Eq. A-19 should be rearranged as below:

$$j = k_0 a_{\text{OH}^{\bullet}}^{n_1+n_3} \exp\left(\frac{(n_2+n_4\alpha_2)\eta F}{RT}\right) \quad (\text{A-45})$$

$$k_0 = k^0 \exp\left(\frac{(n_2+n_4\alpha_2)E_{eq}F}{RT}\right) \quad (A-46)$$

When hydrogen is substituted by deuterium, the reaction rate is changed but the reaction mechanism should remain unchanged. Thus, Eq. A-45 is modified as Eq. A-47:

$$j' = 4Fv' = k'_0 a_{OD^-}^{n_1+n_3} \exp\left(\frac{(n_2+n_4\alpha'_2)\eta F}{RT}\right) \quad (A-47)$$

Considering the reaction mechanism involved in this study, the isotope effect is:

$$IE = \frac{k_0}{k'_0} \exp\left(\frac{(\alpha_2-\alpha'_2)\eta F}{RT}\right) \quad (A-48)$$

The expression of the rate constant  $k_0$  and  $k'_0$  are as below:

$$k_0 = 4Fk_2^0 K_1^0 \theta_A \exp\left(\frac{(n_2+n_4\alpha_2)E_{eq}F}{RT}\right) \quad (A-49)$$

$$k'_0 = 4Fk_2^{0'} K_1^{0'} \theta'_A \exp\left(\frac{(n_2+n_4\alpha'_2)E'_{eq}F}{RT}\right) \quad (A-50)$$

From the above analysis, the apparent value of isotope effect can be deconvoluted into TIE and KIE:

$$IE = KIE \times TIE = \frac{k_2^0 K_1^0 \theta_A}{k_2^{0'} K_1^{0'} \theta'_A} \exp\left(\frac{(n_2+n_4\alpha_2)(E_{eq}-E'_{eq})F}{RT}\right) \exp\left(\frac{(\alpha_2-\alpha'_2)\eta F}{RT}\right) \quad (A-51)$$

$$TIE = \frac{K_1^0 \theta_A}{K_1^{0'} \theta'_A} \exp\left(\frac{(n_2+n_4\alpha_2)(E_{eq}-E'_{eq})F}{RT}\right) \quad (A-52)$$

$$KIE = \frac{k_2^0}{k_2^{0'}} \exp\left(\frac{(\alpha_2-\alpha'_2)\eta F}{RT}\right) \quad (A-53)$$

At moderate applied overpotentials, the surface concentration of key intermediate (resting state,  $\theta_B$ ) is less than 10%.<sup>2-4</sup> Hence  $\theta_A$  (as well as  $\theta'_A$ ) is regarded as a potential-independent constant. The equilibrium constant  $K_1^0$  and  $K_1^{0'}$  are also potential-independent parameters, Therefore, TIE is not potential-dependent. In the case that only secondary KIE exists in RDS, the difference between  $\alpha_2$  and  $\alpha'_2$  is typically small. Therefore, the observed isotope effect is dominated by TIE, which has a small change within increasing overpotentials.



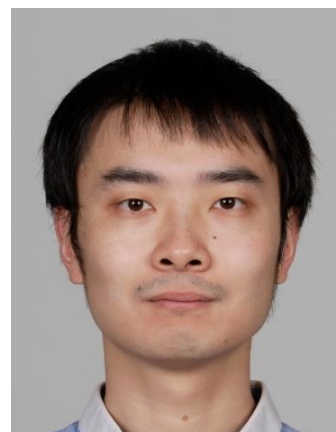
According to Eq. A-53, KIE is usually potential dependent. When the  $\alpha_2$  is bigger than  $\alpha_2'$ , KIE increases with increasing overpotential. Vice versa when the  $\alpha_2$  is smaller than  $\alpha_2'$ . Typically  $\alpha_2$  is bigger than  $\alpha_2'$  due to higher barrier of charge transfer in the situation of deuterium-substitution.<sup>7</sup> In the Tafel region,  $\alpha_2$  and  $\alpha_2'$  are not potential-dependent, the logarithm (or ln) of KIE or overall value of isotope effect is linear dependent on overpotential. Higher overpotential results higher isotope effect value.

At higher overpotentials, the KIE values may deviate from this relationship due to many reasons.<sup>7</sup> For examples, the transfer coefficient  $\alpha_2$  and  $\alpha_2'$  become potential-dependent at high overpotentials. The change of the RDS or overall reaction mechanisms, and the variation of surface coverage of resting state will also contribute to a deviation.

# References of the Appendix

1. Bard, A. J.; Faulkner, L. R.; Leddy, J.; Zoski, C. G., *Electrochemical methods: fundamentals and applications*. Wiley New York: 1980; Vol. 2.
2. Lyons, M. E. G.; Brandon, M. P., A comparative study of the oxygen evolution reaction on oxidised nickel, cobalt and iron electrodes in base. *J. Electroanal. Chem.* **2010**, *641*, 119-130.
3. Bockris, J. O. M., Kinetics of activation controlled consecutive electrochemical reactions: anodic evolution of oxygen. *J. Chem. Phys.* **1956**, *24*, 817-827.
4. Bediako, D. K.; Surendranath, Y.; Nocera, D. G., Mechanistic studies of the oxygen evolution reaction mediated by a nickel-borate thin film electrocatalyst. *J. Am. Chem. Soc.* **2013**, *135*, 3662-3674.
5. Gómez-Gallego, M.; Sierra, M. A., Kinetic Isotope Effects in the Study of Organometallic Reaction Mechanisms. *Chem. Rev.* **2011**, *111*, 4857-4963.
6. Krishtalik, L. I., Kinetic isotope effect in the hydrogen evolution reaction. *Electrochim. Acta* **2001**, *46*, 2949-2960.
7. Sakaushi, K., Quantum electrocatalysts: theoretical picture, electrochemical kinetic isotope effect analysis, and conjecture to understand microscopic mechanisms. *Phys. Chem. Chem. Phys.* **2020**, *22*, 11219-11243.
8. Parkin, G., Temperature-Dependent Transitions Between Normal and Inverse Isotope Effects Pertaining to the Interaction of H-H and C-H Bonds with Transition Metal Centers. *Acc. Chem. Res.* **2009**, *42*, 315-325.
9. Zhang, W.; Burgess, I. J., Kinetic isotope effects in proton coupled electron transfer. *J. Electroanal. Chem.* **2012**, *668*, 66-72.
10. Pasquini, C.; Zaharieva, I.; Gonzalez-Flores, D.; Chernev, P.; Mohammadi, M. R.; Guidoni, L.; Smith, R. D. L.; Dau, H., H/D Isotope Effects Reveal Factors Controlling Catalytic Activity in Co-Based Oxides for Water Oxidation. *J. Am. Chem. Soc.* **2019**, *141*, 2938-2948.

# Curriculum Vitae



## CONTACT INFORMATION

Gender: Male

Data of Birth: 12th, January, 1991

Place of Birth: Maanshan, Anhui Province, China

Nationality: Chinese

Address: BCH-3201, Laboratory of Inorganic Synthesis and Catalysis (LSCI), Institute of Chemistry and Chemical Engineering (ISIC), Ecole Polytechnique Fédérale de Lausanne (EPFL), EPFL-SB-ISIC-LSCI, Avenue Forel 2, 1015 Lausanne, Switzerland.

Telephone (office): +41 21 693 9877

Telephone (mobile): +41 78 681 3920

E-mail: [lichen.bai@epfl.ch](mailto:lichen.bai@epfl.ch) Website: <https://www.epfl.ch/labs/lsci/>

OrcID: <https://orcid.org/0000-0003-1452-6129>

Google Scholar: <https://scholar.google.com/citations?user=zTZ03u0AAAAJ&hl=en>

## EDUCATION

09/2016~02/2021 Ph.D. of Chemistry

Ecole Polytechnique Fédérale de Lausanne (EPFL), Switzerland

09/2013~06/2016 M.S. of Chemical Engineering and Technology (Fine Chemicals)

Dalian University of Technology (DUT), China

Major Grades: 92.9/100 Ranking: 1/39

09/2009~06/2013 B.S. of Chemical Engineering and Technology (Fine Chemicals)

Dalian University of Technology (DUT), China

Major Grades: 89.7/100 Ranking: 1/54

### **RESEARCH PROJECTS AND EXPERIENCES**

Ph.D. (Advisor: Prof. Xile Hu):

Title of Thesis: Atomic Level Insights of Non-Noble Metal Catalysts for the Oxygen Evolution Reaction

Project: Electrocatalytic oxygen evolution reaction (OER)

- Develop atomically dispersed catalysts (double-atom catalysts) for the OER
- Using various double-atom catalysts as model system to study OER mechanisms
- OER mechanisms study of bimetallic OER catalysts

M.S. (Advisor: Prof. Fei Li, Prof. Licheng Sun):

Title of Thesis: Iron-based Oxides for the Photo- and Electrochemical Oxidation of Water and Organics

Project 1: Electrocatalytic OER

- Fe-based electrocatalysts by electrodeposition, which is active in near-neutral conditions

Project 2: Photoelectrochemical cells (photanode)

- Immobilize molecular catalysts on hematite for photoelectrochemical oxidation of organic substrates

B.S. (Advisor: Prof. Fei Li):

Title of Thesis: Water Oxidation Catalyzed by Homogeneous Non-noble Metal

Project: molecular catalysts for electrocatalytic OER

- Mainly focus on Ru- and Cu-based molecular catalysts

### **AWARDS, FELLOWSHIPS AND SCHOLARSHIPS**

03/2021-08/2022 Early postdoctoral fellowship from Swiss National Science Foundation (SNSF)

2019 Chemistry travel award from Swiss Chemical Society (SCS) and Swiss Academy of Natural Sciences (SCNAT)

2017 Excellent Master Thesis of Liaoning Province, China

2016 Excellent Master Thesis of DUT, excellent Graduate Student (M. S.) of DUT

2013 Excellent Graduate Student (B. S.) of DUT

During M. S. (2013-2016) and B. S. (2009-2013), first class scholarship in every academic year.

### **PERSONAL SKILLS**

Language Levels: Chinese (Mother Tongue); English (B2-C1); French (A2-B1).

Technical Skills: transmission electron microscopy (TEM), including spherical aberration corrected scanning transmission electron microscopy (STEM) and energy loss spectroscopy (EELS) analysis; powdered X-ray diffraction (PXRD); gas chromatography (GC), UV-vis spectroscopy.

Have good knowledge of electrochemical methods and techniques, as well as common techniques of material synthesis.

### **SUMMARY OF ACADEMIC ACHIEVEMENTS**

Since 2016, Lichen Bai has published 15 papers in high-impact scientific journals (including *Science*, *J. Am. Chem. Soc.*, *Angew. Chem. Int. Ed.*, *Chem. Sci.*, etc.). Especially, in four of the publications, Lichen Bai is the first author or co-first author. Additionally, Lichen Bai has also published some papers in international academic conference. The research fields are related to electrocatalysis, energy materials, and spectroscopy. According to Google Scholar, Lichen Bai has > 1000 total citations, with an h-index of 12. More details can be find in Lichen Bai's academic account (ORCID, Google Scholar account) and the publication list.

### **SCIENTIFIC PUBLICATIONS**

#### **(A) Publications with peer review process**

1. **Bai L.**+, Lee S.+, Hu X.\* (2020): Spectroscopic and electrokinetic evidence for a bifunctional mechanism of the oxygen evolution reaction. **Angew. Chem. Int. Ed.**, accepted. DOI: <https://doi.org/10.1002/anie.202011388>.

2. Lee S., **Bai L.**, Hu X.\* (2020): Deciphering iron-dependent activity in oxygen evolution catalyzed by nickel iron layered double hydroxide. **Angew. Chem. Int. Ed.**, 59, 8072-8077.

3. Thalluri S. M., **Bai L.**, Lv C., Huang Z.\*, Hu X.\*, Liu L.\* (2020): Strategies for semiconductor/electrocatalyst coupling toward solar-driven water splitting. **Adv. Sci.**, 7, 1902102.
4. **Bai L.**, Hsu C.-S., Alexander D. T. L., Chen H. M.\*, Hu X.\* (2019): A Cobalt-Iron Double-Atom Catalyst for the Oxygen Evolution Reaction. **J. Am. Chem. Soc.**, 141, 14190-14199.
5. Gu J., Hsu C.-S., **Bai L.**, Chen H. M.\*, Hu X.\* (2019): Atomically dispersed Fe<sup>3+</sup> sites catalyze efficient CO<sub>2</sub> electroreduction to CO. **Science**, 364, 1091-1094.
6. Liu S., van Muyden A. P., **Bai L.**, Cui X., Fei Z., Li X.\*, Hu X.\*, Dyson P. J.\* (2019): Metal-sulfide catalysts derived from lignosulfonate and their efficient use in hydrogenolysis. **ChemSusChem**, 19, 3271-3277.
7. Liu S., **Bai L.**, van Muyden A. P., Huang Z., Cui X., Fei Z., Li X.\*, Hu X.\*, Dyson P. J.\* (2019): Oxidative Cleavage of  $\beta$ -O-4 Bonds in Lignin Model Compounds with a Single-atom Co Catalyst." **Green Chem.**, 21, 1974-1981.
8. Zhang Z., **Bai L.**, Hu X.\* (2019): Alkene Hydrosilylation Catalyzed by Easily Assembled Ni (II)-Carboxylate MOFs. **Chem. Sci.**, 10, 3791-3795.
9. Song F., **Bai L.**, Moysiadou A., Lee S., Hu C., Liardet L., Hu X.\* (2018): Transition metal oxides as electrocatalysts for the oxygen evolution reaction in alkaline solutions: an application-inspired renaissance. **J. Am. Chem. Soc.**, 140, 7748-7759.
10. Wang Y., Li F.\*, Zhou X., Yu F., Du J., **Bai L.**, Sun L. (2017): Highly efficient photoelectrochemical water splitting with an immobilized molecular Co<sub>4</sub>O<sub>4</sub> cubane catalyst. **Angew. Chem. Int. Ed.**, 56, 6911-6915.
11. Yu F., Li F.\*, Hu J., **Bai L.**, Zhu Y., Sun L. (2016): Electrocatalytic water oxidation by a macrocyclic Cu (II) complex in neutral phosphate buffer." **Chem. Commun.**, 52, 10377-10380.
12. **Bai L.**, Li F.\*, Wang Y., Li H., Jiang X., Sun L. (2016): Visible-light-driven selective oxidation of benzyl alcohol and thioanisole by molecular ruthenium catalyst modified hematite." **Chem. Commun.**, 52, 9711-9714.
13. Li F.\*+, **Bai L.**+, Li H., Wang Y., Yu F., Sun L. (2016): An iron-based thin film as a highly efficient catalyst for electrochemical water oxidation in a carbonate electrolyte. **Chem. Commun.**, 52, 5753-5756.
14. Wang Y., Li F.\*, Li H., **Bai L.**, Sun L. (2016): Photocatalytic water oxidation via combination of BiVO<sub>4</sub>-RGO and molecular cobalt catalysts." **Chem. Commun.**, 52, 3050-3053.
15. Li H., Li F.\*, Wang Y., **Bai L.**, Yu F., Sun L. (2016): Visible-Light-Driven Water Oxidation on a Photoanode by Supramolecular Assembly of Photosensitizer and Catalyst. **ChemPlusChem**, 81, 1056-1059.

### **(B) Publications without peer review process (preprints)**

1. **Bai L.**+, Lee S., Hu X.\* (2020): Spectroscopic and electrokinetic evidence for a bifunctional mechanism of the oxygen evolution reaction. **ChemRxiv. Preprint**, link: <https://doi.org/10.26434/chemrxiv.12661514.v2>. (This preprint manuscript has been published in *Angew. Chem. Int. Ed.* (see **A1**).
2. **Bai L.**, Hsu C.-S., Alexander D. T. L., Chen H. M.\*, Hu X.\* (2019): Double-Atom Catalysts Provide a Molecular Platform for Oxygen Evolution. **ChemRxiv., Preprint**, link: <https://doi.org/10.26434/chemrxiv.11341961.v1>.
3. **Bai L.**, Hsu C.-S., Alexander D. T. L., Chen H. M.\*, Hu X.\* (2019): A Cobalt-Iron Double-Atom Catalyst for the Oxygen Evolution Reaction. **ChemRxiv. Preprint**, link: <https://doi.org/10.26434/chemrxiv.8131235.v1>. (This preprint manuscript has been published in *J. Am. Chem. Soc.* (see **A4**).

### **(C) International conferences (poster presentations)**

1. **Bai L.**, Hsu C.-S., Alexander D. T. L., Chen H. M.\*, Hu X.\* (2019): A Cobalt-Iron Double-Atom Catalyst for the Oxygen Evolution Reaction. **IUPAC Conference 2019**, Paris, France. 1326pp (Poster presentation).
2. Gu J., Hsu C.-S., **Bai L.**, Chen H. M.\*, Hu X.\* (2019): Fe-N-C Catalyst with Atomically Dispersed Fe<sup>3+</sup> Sites for Efficient CO<sub>2</sub> Electroreduction to CO. **IUPAC Conference 2019**, Paris, France. 1279pp (Poster presentation).
3. **Bai L.**, Hu X.\* (2018): "A Cobalt-Iron Double-Atom Catalyst for the Oxygen Evolution Reaction." **NRG2018** (Winter School, Challenges & opportunities in energy research), Crans Montana, Switzerland. (Poster presentation).

**\* = Corresponding author, + = Contribute equally**